Can interferons help the body beat COVID-19? p. 125

Microbe-aided healing wins NOSTER & *Science* Microbiome Prize p. 152

Socially distanced quantum coupling p. 174

Science

$15
10 JULY 2020

AAAS

COGNITIVE MAPS

Bats navigate using a mental image of their world

pp. 142, 188, & 194

Innovative insights into the role of the human microbiome in controlling disease

Human gut microorganisms are making useful drugs right inside of us that fight disease.

Noster was incorporated in May 2020 for the purpose of *"connecting life and the gut microbiome,"* according to the official Noster motto. "Noster is built on technology developed at Nitto Pharmaceutical Industries, Ltd. for cultivating gut microorganisms," says Kohey Kitao, CEO of Noster. "Our work to date shows that the gut microbiome—or more specifically, gut microorganisms—have positive effects on human health. It's amazing to think that microbes are working inside us making drugs to cure diseases!" Noster is focused on developing therapeutic drugs to treat diseases by controlling and manipulating gut microorganisms and their metabolites, explains Kitao. "It's an exciting and rapidly changing area of research and innovation."

The three pillars

Noster is focusing on three types of clinical trials to treat disease:

- Direct oral administration of microbes in humans, using a unique gut microorganism library of more than 1,000 strains previously isolated by Noster researchers.
- Testing fatty-acid (lipid) metabolites manufactured using in-house technology to separate metabolites produced by gut microorganisms, Noster has developed a library of over 300 lipid metabolites and is collaborating with partners to elucidate the effects of lipid metabolites on human health for the treatment of chronic diseases.
- A project that attempts to control gut microorganisms using antibodies, particularly immunoglobulin A (IgA), the most common antibody type present in the human body, acting as the first line of defense against infections.

Treatment of chronic diseases: The HYA–diabetes connection

"Our activities using metabolites to treat chronic diseases include studying diabetes and intestinal tract inflammation," says Kitao. "Currently, diabetes is treated using drugs to control the blood glucose level, but this does not treat the underlying disease itself. We want to develop therapeutic drugs based on metabolites produced by gut microorganisms that will address the root causes of such chronic diseases." Diabetes is known to adversely affect the liver, for example, increasing the incidence of nonalcoholic fatty liver disease and leading to an elevated risk of liver cancer. Kitao has his sights set on developing drugs to prevent this "domino effect" of one disease leading to another.

Noster is collaborating with academia to develop lipid metabolite–based drugs using the functional fatty acid 10-hydroxy-*cis*-12-octadecenoic acid (HYA), which is secreted by gut microorganisms. Notably, Jun Ogawa and Shigenobu Kishino of Kyoto University reported that dietary fatty acids are metabolized by gut microbes, and that these metabolites, especially HYA, reside in the intestinal tract and are transferred to the host (*1*). Furthermore, Ikuo Kimura of Tokyo University of Agriculture and Technology revealed that HYA reduces insulin resistance in mouse models (*2*), enabling the body to respond more effectively to insulin and avoid dangerously high blood-sugar levels. Disease targets for HYA include type 2 diabetes, nonalcoholic steatohepatitis, and inflammation of the intestinal barrier (*3*).

In May 2020, together with researchers at Kobe University School of Medicine, Noster initiated a program to perform human clinical trials testing the efficacy of HYA for treating diabetes.

"We expect to start the trials in 2020," says Kitao. Diabetic patients will receive oral administration of HYA, and their insulin resistance will be closely monitored. "The trials will last for three months. The main results of interest will be whether HYA does indeed improve insulin resistance and also the dose necessary to see an effect."

Direct administration of gut microorganisms

Another important target is arteriosclerosis—the narrowing and hardening of arterial walls, which is especially prevalent in old age. Noster is collaborating with Tomoya Yamashita at the Kobe University School of Medicine, who has identified *Bacteroides vulgatus* and *Bacteroides dorei*—anaerobic, rod-shaped bacteria isolated from the human gut—as inhibiting arteriosclerosis, preventing coronary artery disease, and having anti-inflammatory effects on intestinal and vascular tissue (*4*).

"Following the successful verification of the potential of *B. vulgatus* and *B. dorei* for inhibiting arteriosclerosis in mouse models, we are continuing our collaboration with Dr. Yamashita on clinical trials testing direct oral administration of these gut microbes in patients," explains Kitao. "We are making full use of our innovative microdroplet technology developed in collaboration with researchers at Waseda University in Tokyo to cultivate these *Bacteroides* strains in 50-micrometer droplets" (*5*).

The importance of open science

Kitao stresses the need to form strong, long-term global partnerships to produce innovative therapeutic drugs based on the gut microbiome. "We are carrying out extensive clinical trials in Japan and want to share the results with pharmaceutical industries with a global outlook," says Kitao. "Also, modern drug discovery and the pharmaceutical industry in general must be multidisciplinary in order to achieve their goals. This is the basis for innovative, open science. For example, we are looking for collaborators to identify new targets for HYA and lipid metabolites. The targets may differ from those normally pursued in the pharmaceutical sector. So, we welcome opportunities to collaborate with national research centers and academia outside of Japan."

Microbiome Research X (MRX)

Noster recently launched the Microbiome Research X (MRX) information platform to share their latest findings with a global audience. "This unique platform not only highlights the latest research, news, and trends in the world of the microbiome, but also offers a detailed 'researcher profile map' of people and their areas of expertise in this rapidly evolving area of research," explains Kitao. Initially, MRX will cover predominantly gut microbiome activities in Japan, but there are plans to expand it to cover research by the broader international community. "We are confident that MRX is a valuable source of the latest information on research on the gut microbiome for newcomers as well as more established researchers," says Kitao.

MRX can be found at https://noster-mrx.net.

"[W]e welcome opportunities to collaborate with national research centers and academia outside of Japan."
—Kohey Kitao

PHOTO: COURTESY OF NOSTER

Noster fosters multidisciplinary collaborations

Noster's strength lies in the fact that its scientific staff can cultivate almost any anerobic bacteria in the laboratory. This is no easy feat, considering that such bacteria usually exist in environments where there is little or no oxygen. The success of Noster's microbe cultivation technology underscores their deep understanding of the biochemistry and physiology of microorganisms. Importantly, the company extracts metabolites directly from the microbes they cultivate, which has enabled them to amass a large library of over 300 naturally occurring, bioactive compounds.

"Noster has deep in-house expertise to identify, analyze, and characterize the unique properties of hundreds of gut microorganisms," says Kitao. "Our know-how enables us to isolate and study cultures of individual bacterial strains and extract high-purity metabolites. These are important factors for generating the kind of robust, reproducible research necessary to advance this field, and [they] enable Noster to attract collaborators around the world across many different themes related to the gut microbiome." Noster's highly optimized and standardized procedures for analyzing the gut microbiome make them an attractive partner. This expertise enables them to transfer their procedure to any laboratory, so that the results produced will be independent of individual users and their equipment.

The Noster & *Science* Microbiome Prize

Kitao acknowledges that gut microbiome research is an increasingly multidisciplinary and global endeavor. "The Noster & *Science* Microbiome Prize was established in partnership with the American Association for the Advancement of Science, publisher of the journal *Science*, to inspire young scientists working on the microbiome to make contributions that improve human health and provide solutions to chronic diseases. We look forward to announcing the first recipients of the prizes in July 2020!"

Information about the prize and instructions on how to enter can be found at https://www.sciencemag.org/prizes/noster-science-microbiome-prize#.

References

1. S. Kishino *et al.*, *Proc. Natl. Acad. Sci. U. S. A.* **110**, 17808–17813 (2013).
2. J. Miyamoto *et al.*, *Nat. Commun.* **10**, 4007 (2019).
3. J. Miyamoto *et al.*, *J. Biol. Chem.* **290**, 2902–2918 (2015).
4. N. Yoshida *et al.*, *Circulation* **138**, 2486–2498 (2018).
5. M. Hosokawa *et al.*, *Biosens. Bioelectron.* **67**, 379–385 (2015).

CONTENTS

10 JULY 2020 • VOLUME 369 • ISSUE 6500

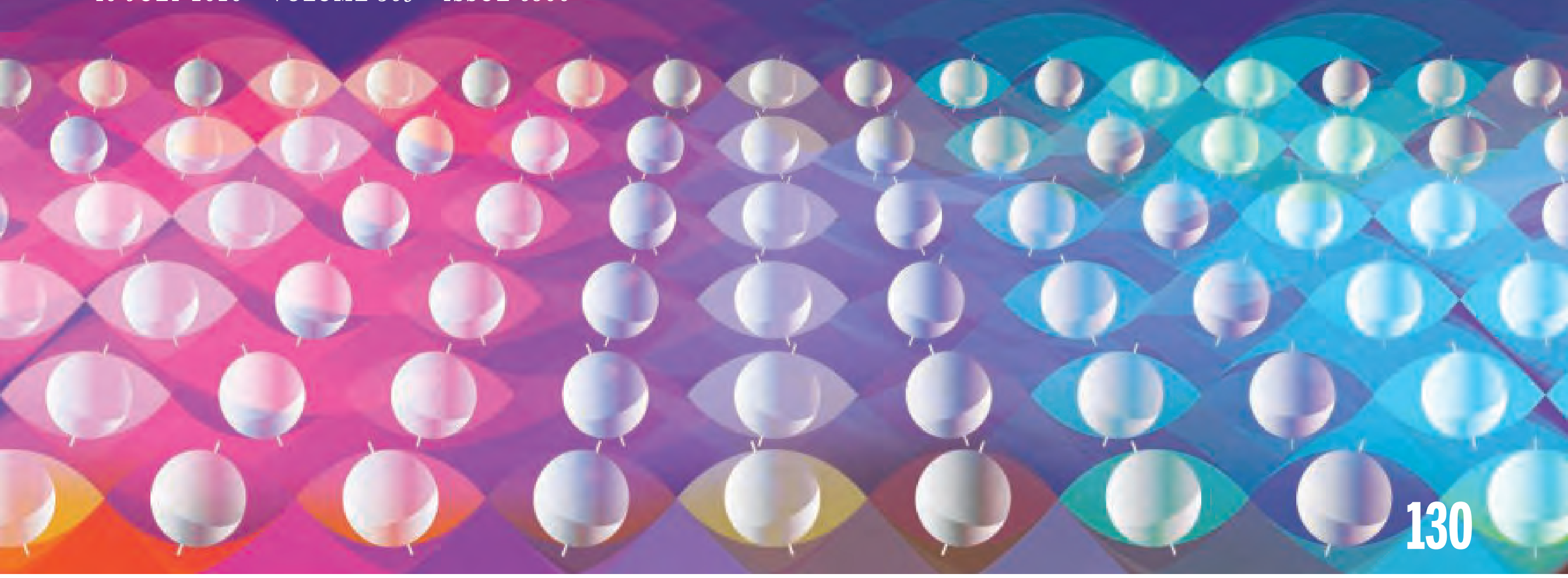

NEWS

IN BRIEF

122 News at a glance

IN DEPTH

124 U.K. megatrial outshines other drug studies
Efficient recruitment and simple design are key to Recovery trial's success
By K. Kupferschmidt
PODCAST

125 Can interferons stop COVID-19 before it takes hold?
Biology of infection supports early treatment with body's own viral defenses
By M. Wadman

127 UAE probe aims for Mars— and payoffs on Earth
Even before launch, the Hope satellite has boosted Emirati space science
By S. el-Showk

128 Polynesians, Native Americans met and mingled long ago
Islanders' DNA suggests contact before European arrival *By L. Wade*

129 New security law rattles Hong Kong universities
Researchers worry about academic freedom and city's ability to attract foreign talent
By D. Normile

FEATURES

130 No room for error
Developers of quantum computers face their true challenge: taming the noise that plagues the intertwined quantum bits *By A. Cho*

INSIGHTS

POLICY FORUM

134 How to build a more open justice system
Court records are unstructured and costly to access—here's how to fix it *By A. R. Pah et al.*

PERSPECTIVES

137 Climate change tweaks Arctic marine ecosystems
Nutrient input might enhance productivity in the Arctic Ocean of the future *By M. Babin*
REPORT p. 198

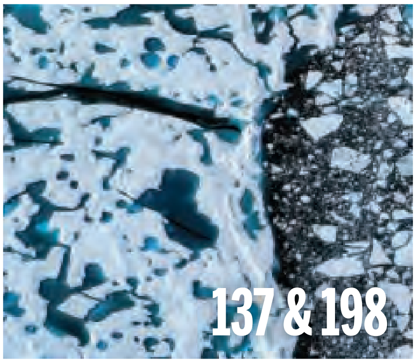

138 Fuel cells that operate at 300° to 500°C
High-conductivity electrolytes are needed for electrochemical systems *By M. Ni and Z. Shao*
REPORT p. 184

140 Reining in dissolved transition-metal ions
Approaches are needed for stabilizing transition metals in lithium-ion battery cathodes *By H. Yaghoobnejad Asl and A. Manthiram*

142 Bats navigate with cognitive maps
Tagging and tracking systems reveal the way-finding strategies of fruit bats *By M. B. Fenton*
REPORTS pp. 188 & 194

143 Exploring the source of human brain fluids
Human organoid cultures can be used to probe secretion and drug permeability into and out of the brain
By V. Silva-Vargas and F. Doetsch
RESEARCH ARTICLE p. 159

144 Exercising your mind
A circulating factor induced by exercise contributes to keeping the brain young in mice *By V. A. Ansere and W. M. Freeman*
RESEARCH ARTICLE p. 167

145 Rigorous wildlife disease surveillance
A decentralized model could address global health risks associated with wildlife exploitation *By M. Watsa and Wildlife Disease Surveillance Focus Group*

ILLUSTRATION: ANDY GILMORE; PHOTO: MARTIN FORTIER/UNIVERSITÉ LAVAL

BOOKS *ET AL.*

148 Paleoart comes into its own
A renaissance is occurring in the way we render extinct species *By I. Nieuwland*

149 Changing course
Navigational skills require nurturing, lest we lose our way *By L. Rosen*

LETTERS

150 Preparing for proactive dam removal decisions
By F. Vahedifard et al.

150 Unnecessary hesitancy on human vaccine tests
By N. Eyal

151 Response
By S. K. Shah et al.

PRIZE ESSAY

152 Poised for tissue repair
Skin microbes interact with the immune system to aid wound healing
By O. Harrison

RESEARCH

IN BRIEF

154 From *Science* and other journals

***Radotina*, one of the earliest jawed, toothed vertebrates, hiding in a nautiloid shell**

REVIEW

157 Lymphatic biology
Biological functions of lymphatic vessels
T. V. Petrova and G. Y. Koh
REVIEW SUMMARY; FOR FULL TEXT: DX.DOI.ORG/10.1126/SCIENCE.AAX4063

RESEARCH ARTICLES

158 Developmental biology
Contact area–dependent cell communication and the morphological invariance of ascidian embryogenesis *L. Guignard* et al.
RESEARCH ARTICLE SUMMARY; FOR FULL TEXT: DX.DOI.ORG/10.1126/SCIENCE.AAR5663

159 Organoids
Human CNS barrier-forming organoids with cerebrospinal fluid production
L. Pellegrini et al.
RESEARCH ARTICLE SUMMARY; FOR FULL TEXT: DX.DOI.ORG/10.1126/SCIENCE.AAZ5626
PERSPECTIVE p. 143

160 Coronavirus
Inferring change points in the spread of COVID-19 reveals the effectiveness of interventions *J. Dehning* et al.
RESEARCH ARTICLE SUMMARY; FOR FULL TEXT: DX.DOI.ORG/10.1126/SCIENCE.ABB9789
REPORT p. 208

161 Structural biology
Structure and selectivity engineering of the M_1 muscarinic receptor toxin complex *S. Maeda* et al.

167 Aging
Blood factors transfer beneficial effects of exercise on neurogenesis and cognition to the aged brain
A. M. Horowitz et al.
PERSPECTIVE p. 144; PODCAST

174 Quantum physics
Light-mediated strong coupling between a mechanical oscillator and atomic spins 1 meter apart *T. M. Karg* et al.

REPORTS

179 Topological matter
Observation and control of maximal Chern numbers in a chiral topological semimetal *N. B. M. Schröter* et al.

184 Fuel cells
Proton transport enabled by a field-induced metallic state in a semiconductor heterostructure
Y. Wu et al.
PERSPECTIVE p. 138

Cognitive maps

188 Cognitive map–based navigation in wild bats revealed by a new high-throughput tracking system *S. Toledo* et al.

194 The ontogeny of a mammalian cognitive map in the real world *L. Harten* et al.
PERSPECTIVE p. 142

198 Arctic productivity
Changes in phytoplankton concentration now drive increased Arctic Ocean primary production *K. M. Lewis* et al.
PERSPECTIVE p. 137

202 Immunodeficiencies
HEM1 deficiency disrupts mTORC2 and F-actin control in inherited immunodysregulatory disease
S. A. Cook et al.

208 Coronavirus
Estimating the burden of SARS-CoV-2 in France *H. Salje* et al.
RESEARCH ARTICLE p. 160

211 Paleontology
Marginal dentition and multiple dermal jawbones as the ancestral condition of jawed vertebrates *V. Vaškaninová* et al.

DEPARTMENTS

120 Editorial
Immigrants help make America great *By Sudip Parikh*

121 Editorial
Monumental patience
By H. Holden Thorp

218 Working Life
The day I left the lab
By Kelsey Hodge-Hanson

ON THE COVER

Monitoring large numbers of Egyptian fruit bats, like this one leaving its colony, and doing so as they mature into adults, suggests that bats navigate through their complex environment using a cognitive map. See pages 142, 188, and 194.
Photo: Ivan Kuzmin/Science Source

Science Careers 217

ILLUSTRATION: JAN SOVAK

SCIENCE (ISSN 0036-8075) is published weekly on Friday, except last week in December, by the American Association for the Advancement of Science, 1200 New York Avenue, NW, Washington, DC 20005. Periodicals mail postage (publication No. 484460) paid at Washington, DC, and additional mailing offices.

Domestic individual membership, including subscription (12 months): $165 ($74 allocated to subscription). Domestic institutional subscription (51 issues): $2148; Foreign postage extra: Air assist delivery: $98. First class, airmail, student, and emeritus rates on request. Canadian rates with GST available upon request, GST #125488122. Publications Mail Agreement Number 1069624. **Printed in the U.S.A.**

Change of address: Allow 4 weeks, giving old and new addresses and 8-digit account number. **Postmaster:** Send change of address to AAAS, P.O. Box 96178, Washington, DC 20090–6178. **Single-copy sales:** $15 each plus shipping and handling available from backissues.sciencemag.org; bulk rate on request. **Authorization to reproduce** material for internal or personal use under circumstances not falling within the fair use provisions of the Copyright Act can be obtained through the Copyright Clearance Center (CCC), www.copyright.com. The identification code for *Science* is 0036-8075. *Science* is indexed in the *Reader's Guide to Periodical Literature* and in several specialized indexes.

Immigrants help make America great

Sudip Parikh is the chief executive officer of the American Association for the Advancement of Science (AAAS) and executive publisher of the *Science* journals. sparikh@aaas.org

I am a scientist. I am an American. And I am the product of special expert visas and chain migration—among the many types of legal immigration into the United States. On 22 June, President Trump issued a proclamation that temporarily restricts many types of legal immigration into the country, including that of scientists and students. This will make America neither greater nor safer—rather, it could make America less so.

The administration claims that these restrictions are necessitated by the coronavirus disease 2019 (COVID-19) outbreak to prevent threats to American workers. This reasoning is flawed for science and engineering, where immigrants are critical to achieving advances and harnessing the resulting economic opportunity for all Americans.

For decades, the United States has inspired both immigrants and non-immigrants to make substantial contributions to science and technology that benefit everyone. Preventing highly skilled scientists and postdocs from entering the United States directly threatens this enterprise.

My uncle, a geologist, came to the United States in the 1960s to work at NASA. He then taught at Appalachian State University in North Carolina and later served as lead geochemist for the state of California. He sponsored my father to come to America in 1968. Leaving Mumbai, a city of millions, and arriving in Hickory, a town of thousands in North Carolina, my father came home to a place he had never been before. My parents worked in furniture factories and textile mills to put us though college and ensure we had opportunities. Today, my sister works at the U.S. Centers for Disease Control and Prevention, and I have the privilege of leading the American Association for the Advancement of Science (AAAS, the publisher of *Science*). We exist because of the Immigration and Nationality Act of 1965 and our parents' belief in the vision of the United States as a shining city on a hill. My family's story is repeated by thousands of American scientists.

These stories include uncertainty when an immigrant's status in America is in question. This uncertainty causes stress and the possibility that immigrants will leave and take their skills, talents, and humanity elsewhere. For the successful, these stories culminate with relief, celebration, and the pride of becoming a naturalized citizen. As President Reagan said, the United States is the one place in the world where "anybody from any corner of the world can come…to live and become an American." Naturalized citizens love the United States deeply because they chose to be American. They and other immigrants make huge contributions to science and engineering.

> **"…immigrants make huge contributions to science and engineering."**

According to the National Science Foundation, more than 50% of postdocs and 28% of science and engineering faculty in the United States are immigrants. Of the Nobel Prizes in chemistry, medicine, and physics awarded to Americans since 2000, 38% were awarded to immigrants to the United States. I don't know the number of prizes given to second-generation Americans but Steven Chu—current chair of the AAAS Board of Directors—is among them. The incredible achievements of the American scientific enterprise speak volumes about the vision and forethought of the American people who have worked to create a more perfect union.

Suspending legal immigration is self-defeating and breaks a model that is so successful that other nations are copying it. As Thomas Donohue, chief executive officer of the U.S. Chamber of Commerce, said regarding the administration's proclamation, "Putting up a 'not welcome' sign for engineers, executives, IT experts, doctors, nurses, and other workers won't help our country, it will hold us back. Restrictive changes to our nation's immigration system will push investment and economic activity abroad, slow growth, and reduce job creation."

To develop treatments and vaccines for COVID-19, cure cancers, go to Mars, understand the fundamental laws of the universe and human behavior, develop artificial intelligence, and build a better future, we need the brain power of the descendants of Native Americans, Pilgrims, Founding Mothers and Fathers, Enslaved People, Ellis Island arrivals, and immigrants from everywhere. The United States has thrived as a crossroads where people are joined together by ideas and contribute by choice to the freedom and opportunity provided by this wonderful, inspiring, and flawed country that is always striving to live up to its aspirations.

Scientists, look around your labs and offices. Think about your collaborations and friendships. We must ensure that this "temporary" restriction on legal immigration does not become permanent. Now is the time to speak up for your immigrant colleagues and for America.

–Sudip Parikh

10.1126/science.abd6868

PHOTO: ANDY DELGIUDICE

Monumental patience

Next week marks the 60th anniversary of Jane Goodall's arrival in what is now Tanzania's Gombe National Park to study wild chimpanzees.* Although her story is a familiar one to many scientists, it has taken on a new importance in this era when climate change, racism, and a rapidly spreading coronavirus ravage the globe. It is a story of genuine scientific curiosity, determination, and respect for nature and humanity—all the things we desperately need now.

I talked with Dr. Goodall, virtually, where she was spending her self-isolation in her childhood home in Bournemouth, England.† It is the familiar place where she spent her early years climbing trees and observing her dog, Rusty. She told me the well-known story of how she met paleoanthropologist Louis Leakey and convinced him that she should study wild animals in Africa. She was happy to tell the story one more time. "Some people get it wrong, even now," she said.

Leakey famously said that Goodall was a person of monumental patience. "There's definitely still lots of opportunity for the old way of watching and recording and being patient," she said. Goodall still insists that some observational work be done with handwritten note taking, but she also embraces the use of technology. "I believe that you cannot do everything digitally," she said. "We did graduate to using [tape] recorders, which of course made the transcription extremely laborious because when you are recording, you have caught far more than you could write." The important thing to Goodall was to get close and study the personalities and interactions among chimpanzee family members. She has been doing it for 60 years, saying "it yielded so much richness."

> "...Goodall's... is a story of genuine scientific curiosity, determination, and respect for nature and humanity..."

The science that started in Gombe back then has evolved, changing and developing as it grows. In partnership with the Jane Goodall Institute (founded in 1977), Crickette Sanz, professor of Anthropology at Washington University in St. Louis, has continued to build our understanding of chimpanzee tool use. Sanz told me that when her work began in the Republic of the Congo, Goodall traveled several days by plane, truck, and boat, and 20 km on foot to visit the research site and show her support. She says that "the world is yearning for [Goodall's] ideals of hope, compassion, and change."

And that is where Goodall devotes most of her time now. Although the science is still important—over 300 research papers have now emerged from groups working in Gombe—Goodall lights up when she talks about her new efforts to build respect and hope for the future of humanity and the natural world. The Lake Tanganyika Catchment Reforestation and Education (TACARE) program seeks to use satellite imaging, mobile, and other technologies to ensure that local communities develop their own land-use management solutions and are included as partners in the overall scientific and conservation efforts conducted there.

Another program she devotes most of her time to now, Roots & Shoots, reflects her faith in young people and the future. She still has many concerns about the world. "How do we move into a new green economy?" she wonders. "How do we alleviate poverty so people can make the right choices and stop destroying the environment? How do we realize that putting the short-term economic gain over and above protection of nature is going to be the end of our species as well as the end of most life as we know it?"

In an effort to answer these questions, she uses her platform, and her story, to inspire the younger generation, just as she has also inspired the established scientists of today. To Goodall, "every individual makes a difference," says Sanz, who sees Goodall as "a steward for nature, with equal concern for the smallest creatures to the largest remaining tracts of intact forest, and gifted in sharing all of its wonders. Through her global presence, she's also emphasized the connectedness of all people and our responsibility to each other. From what I have witnessed, both her compassion and her impact are truly limitless."

And so is Goodall's empathy. "When you're empathetic," she says, "you're watching something you don't understand and you get that 'aha' moment because you understand them, and then you have a platform as a scientist to find out if your 'aha' moment is actually correct. Without the empathy you'd never get there."

–H. Holden Thorp

H. Holden Thorp
Editor-in-Chief, *Science* journals.
hthorp@aaas.org; @hholdenthorp

PHOTO: CAMERON DAVIDSON

*See janegoodall.org/gombe60 and https://arcg.is/H04Db.
†See more of the conversation at https://blogs.sciencemag.org/editors-blog/.

10.1126/science.abd6799

NEWS

IN BRIEF

Edited by **Jeffrey Brainard**

A worker removes graffiti at the University of Cambridge aimed at statistician Ronald Fisher.

RACIAL JUSTICE

Tainted names are removed from places of honor

In recent days, scientific institutions and groups have changed the names of journals, prizes, and programs that honor researchers who held racist views. On 3 July, Cold Spring Harbor Laboratory announced it had removed the name of DNA co-discoverer James Watson from its School of Biological Sciences, a request made on 21 June by 133 Ph.D. students and alumni of the school. (They cited repeated, racially offensive statements by Watson.) Recent police killings of Black people and increased recognition of institutional racism have prompted many similar efforts. The University of Cambridge decided on 24 June to remove a stained-glass window named after leading 20th century biostatistician Ronald Fisher, a prominent supporter of eugenics. On 3 July, the board of the American Society of Ichthyologists and Herpetologists voted to change the name of its flagship journal, *Copeia*, named after Edward Cope, a 19th century scientist who described nonwhite people as "more ape-like." The journal's new name, *Ichthyology and Herpetology*, will debut with the first issue of 2021. Also on 3 July, the Entomological Society of America renamed its annual Linnaean Games, a student trivia competition named after Carl Linnaeus, the 18th century botanist who invented the system used worldwide to classify species but who also assigned negative traits to nonwhite populations. The competition's new title: the Entomology Games.

Self-citations sideline journals

PUBLISHING | Clarivate, the analytics firm that provides the Web of Science database of scientific publications, last week removed 33 journals from its annual report on journal impact factors because of excessive self-citations, which can artificially boost their score. Although critics question the importance of a journal's impact factor and the methodology for calculating the metric, it remains widely regarded as an indicator of quality. The 33 journals, many of which are produced by the largest publishers, were just a fraction of the more than 12,000 in the annual report. Among the journals excluded, self-citations made up between 26% and 71% of all citations in the 2-year period Clarivate examined. Clarivate said it would consider restoring the 33 journals to its annual *Journal Citations Reports* if self-citations decline. For now, the journals will continue to appear in the Web of Science database, but with no impact factor.

Emergency money for NIH, Energy

FUNDING | Spending panels in the U.S. House of Representatives this week proposed a way to skirt tight budget caps and award large increases to the National Institutes of Health (NIH) and the Department of Energy's (DOE's) national laboratories for the next fiscal year. The lawmakers want to give NIH a 13% hike, to $47 billion, by adding $5.5 billion—all but $500 million of it as emergency funding, which is exempt from the caps. Similarly, DOE labs would receive $6.2 billion in emergency funds, justified by the COVID-19 pandemic, for construction and upgrades, while the science office budget would rise by $50 million, to $7.05 billion in fiscal 2021. But lawmakers did not use the mechanism to supplement the budgets of the National Science Foundation, which would get a 3% increase, or science programs at NASA, which would be flat.

PHOTO: JOE GIDDENS/PA WIRE/AP IMAGES

Online students face visa woes

IMMIGRATION | Hundreds of thousands of foreign students attending U.S. universities are in an uproar over a proposed government policy that would force them to leave the country if all their fall courses are offered exclusively online. Many foreign students are studying science, including Ph.D. candidates who have completed coursework but hope to remain in the country to finish dissertations. Hybrid classes with online and in-person sessions are OK, the Department of Homeland Security said in a 6 July notice signaling changes in the status of international students. But the ban on online-only classes could force students already in the United States to exit the country or transfer to another institution that offers face-to-face instruction. Higher education officials labeled the new policy "mean-spirited" and accused the Trump administration of using the coronavirus pandemic to expand its campaign to limit immigration.

New satellite fears in astronomy

ASTRONOMY | One company's plan to launch a new constellation of communications satellites is worrying astronomers, who fear it will spoil the view for ground-based survey telescopes. The threat had faded when OneWeb filed for bankruptcy protection in March, but the U.K. government and the Indian cellphone operator Bharti Global last week pledged $1 billion to rescue it. Astronomers have been working with rival operator SpaceX to reduce the visibility of its constellation, already 540 strong; those measures have not yet been validated. But OneWeb's planned fleet of up to 42,000 satellites will be harder to miss because they will orbit at a higher altitude, 1200 kilometers, and so will be visible throughout the night.

Illegal gold mining in Peru and elsewhere has stripped Amazon forests.

PHOTO: JANINE COSTA/REUTERS

CONSERVATION

Gold mining batters forests

Amazon forests destroyed by gold mining fail to regrow when the miners move on, researchers report—and these mining operations are expanding. At some survey sites in Guyana, no young trees had sprouted 3 to 4 years after mining stopped, the team reported 29 June in the *Journal of Applied Ecology*. Surface mining for gold removes the topsoil, leaving behind scant nutrients for plants. A Guyanese law requires miners to replace the soil, but many don't comply. Across the Amazon, an estimated 130 square kilometers are lost to gold mining annually, about 1% of the total deforestation from agriculture, logging, and other activities across the Amazon. But regrowth after gold mining was lower than in other disturbed areas, the study found—and the global economic crisis caused by the COVID-19 pandemic has driven up the price of gold, encouraging more mining.

COVID-19

Dispatches from the pandemic

Shortage of AIDS drugs looms

The lockdowns to slow the COVID-19 pandemic have disrupted the production and supply of antiretroviral (ARV) treatments for HIV, threatening years of declines in AIDS infections and deaths, according to a report released on 6 July. A model by the World Health Organization (WHO) and Joint United Nations Programme on HIV/AIDS (UNAIDS) shows that a shortage of these drugs for 6 months could lead to 500,000 new AIDS-related deaths in sub-Saharan Africa alone. Globally, 38 million people are living with HIV, and of the 25.4 million receiving ARVs at the end of 2019, one-third live in countries with shortages, says a survey conducted by WHO in the wake of the modeling exercise. The UNAIDS report also notes that although HIV infection rates since 2010 have dropped by 23% globally, they have jumped by 72% in Eastern Europe and Central Asia in the same period. "Our progress towards ending AIDS as a public health threat by 2030 was already off track before the COVID-19 outbreak," the report states. "Now this crisis has the potential to blow us even further off course."

Gun sales and violence rise

U.S. firearm purchases and interpersonal gun violence have increased significantly during the coronavirus pandemic, a study has found. Researchers at the University of California, Davis, used recent data from the National Instant Criminal Background Check System to compare rates of gun purchases from March through May in the 48 contiguous states and the District of Columbia with those expected based on prior state-specific patterns and seasonal trends in purchasing since 2011. They estimate that 2.1 million more firearm purchases occurred nationally during these three months than expected from the historical data—a 64.3% increase. The researchers also used public reports to calculate the association between the purchases and intentional interpersonal firearm injuries and deaths during the same period. Based on statistical modeling of what would have been expected without the spike in gun purchases, they found 776 more injuries, a 7.8% jump, which the authors suggest may be due to pandemic-related stress. The findings appear in a preprint posted on the medRxiv server on 4 July.

IN DEPTH

A World Health Organization trial of COVID-19 treatments has been slow to recruit patients, such as this one in Spain.

COVID-19

U.K. megatrial outshines other drug studies

Efficient recruitment and simple design are key to Recovery trial's success

By **Kai Kupferschmidt**

On 29 June, University of Oxford clinical scientists Martin Landray and Peter Horby changed how physicians around the world consider treating COVID-19—for the third time in little more than 3 weeks. The principal investigators of a U.K. megatrial called Recovery, which has been testing existing drugs as therapies for the new disease, the pair had just finished reviewing data from 1596 patients who had received a combination of lopinavir and ritonavir, two antivirals known to curb HIV, and 3376 patients who had received only standard care. In a press release, they and their Recovery colleagues announced there had been no significant difference in the death rate between the two groups. "This could have worked. And it was a bust," says Eric Topol, director of the Scripps Research Translational Institute. "It was really important to clarify that."

Earlier in June, and again through press releases, Recovery (Randomised Evaluation of COVID-19 Therapy) delivered widely accepted verdicts on two other treatments. It revealed that dexamethasone, a cheap steroid, reduced deaths by one-third in patients on a ventilator and showed that hydroxychloroquine, the antimalarial drug controversially touted for COVID-19, did not benefit hospitalized patients. A run on dexamethasone ensued as physicians in the United Kingdom and elsewhere quickly made it part of their standard of care for the sickest patients, whereas many other studies of hydroxychloroquine now looked futile and were halted.

Large, randomized trials are the gold standard for testing a drug's efficacy. But they have been scarce so far in the COVID-19 pandemic. "Everybody has the first part about "randomized," but they omitted the "large" part, says Ana Maria Henao Restrepo, a medical officer at the World Health Organization's (WHO's) Emergencies Programme. "Every clinician, every researcher wants to help and then they end up having a trial with 300 or 400 patients that cannot come up with conclusive evidence."

Science's COVID-19 coverage is supported by the Pulitzer Center.

In a sea of small, single institution studies, Recovery, with 12,000 patients and hundreds of participating hospitals, stands out—and offers lessons for the few other megatrials, organized by WHO and other bodies, which have been slow off the mark. "The three Recovery trials are the best trials that have been performed to date," Topol says.

One reason Recovery has done so well is that it is backed by the United Kingdom's centralized National Health Service (NHS), involving 176 of its hospitals. In the United States, where the health care system is fragmented, the National Institutes of Health has only begun a few large trials so far and completed just one, a study of Gilead Sciences's antiviral compound remdesivir that showed COVID-19 patients given the drug recovered faster. The dearth of results from a country that has seen more cases of COVID-19 than any other is "surprising and a bit disappointing," says John-Arne Røttingen, who heads the steering committee of Solidarity, WHO's attempt to evaluate repurposed drugs as possible COVID-19 therapies.

In contrast, Recovery took advantage of the United Kingdom's own bungled public health response to the new virus, which has led to Europe's largest outbreak and the third most deaths in the world so far. "They have been able to recruit well, because they have had a lot of hospitalized patients," Røttingen says.

In a letter to all NHS hospitals, the United Kingdom's five most senior doctors urged health care workers to enroll patients in Recovery and two other important trials. "Use of treatments outside of a trial, where participation was possible, is a wasted opportunity to create information that will benefit others," the doctors, including Chris Whitty, chief medical officer for England, wrote. Because of that coordination, "One in every six COVID-19 patients that come into the U.K. hospitals go into the trial," Landray says.

PHOTO: PAU BARRENA/AFP/GETTY IMAGES

Organizers also kept Recovery simple, allowing any NHS hospital to participate. Inspired by trials of heart-attack treatments that his Oxford colleague Richard Peto and others did in the 1980s, Landray says they radically cut down on the data health care workers need to collect, with only a few questions asked at enrollment and at just one later point: when the patient dies, is discharged, or 28 days after enrollment. Clinical trials have become excessively cumbersome in recent years, Landray argues.

Solidarity has a similarly straightforward design, but its more international nature has proved a challenge. The trial, designed to test four treatments—hydroxychloroquine, lopinavir/ritonavir, interferon beta plus lopinavir/ritonavir, and remdesivir—was announced on 20 March and enrolled its first patient in Norway 1 week later. But rolling out the trial in dozens of countries has meant getting approval from dozens of regulatory agencies and ethics boards as well. "That has taken a surprisingly long time in many jurisdictions, including in Europe," Røttingen says, and recruitment in Europe slowed over time as the epidemic subsided. "When countries were ready to sort of start, the epidemic was under control in many ways," he notes.

"The three Recovery trials are the best trials that have been performed to date."

Eric Topol, Scripps Research Translational Institute

A European trial called Discovery, coordinated by the French research institute INSERM and meant to join with Solidarity in testing the same drugs, also fell short. The goal was to enroll 3200 patients across the continent. The study almost met its goal of 800 participants in France, but it barely managed to recruit patients elsewhere. Although France funded its part of the trial, it expected partner countries to pick up their own tabs. "One of the issues was that not all the countries had funding," says Yazdan Yazdanpanah, head of infectious diseases at INSERM.

Meanwhile dozens of small trials competed for patients in countries, most of them focusing on the same drugs, such as hydroxychloroquine. "I don't understand why everyone was looking at the same thing," Yazdanpanah says. "I think we can do better." Susanne Herold, an expert on pulmonary infections at the University of Giessen, agrees. "There needs to be more coordination both within countries and across borders," she says.

Another problem has been the widespread use of treatments outside of randomized trials. Landray notes that tens of thousands of COVID-19 patients in the United States have been given convalescent plasma, for instance, but not alongside a group receiving a placebo. "We'll know what happened to those patients, but we won't know whether they would have been better off actually, if they hadn't got the convalescent plasma." Convincing clinicians that therapies still need to be tested can be difficult, Henao Restrepo says. "Some are convinced they know which drugs work."

She still has high expectations for the Solidarity trial. "The preparatory work is paying off," she says. Its recruitment has picked up as more countries, many with surging cases such as Iran, have joined. So far, 39 countries are participating and 60 more signing up. "One of the advantages of such a global trial is that you can follow the pandemic as it evolves," Røttingen says.

With recruitment running at about 500 patients per week now, Solidarity's two remaining treatment arms—it stopped the hydroxychloroquine and the lopinavir/ritonavir ones as results emerged—are likely to yield answers soon, raising the question of what drugs to test afterward. More repurposed drugs are being discussed, but increasingly the attention is turning to monoclonal antibodies targeting the virus.

Henao Restrepo thinks the international nature of Solidarity makes its results more generalizable and likely to be accepted. Herold expects that the Discovery trial contribute as well. Started in part to supplement Solidarity, it collects not only basic mortality data, but also information on viral levels and blood parameters. Those data can indicate not just which drugs are effective, but also how they work and at what stage of the disease.

The Recovery trial continues, with its team scrambling to publish full results. Some researchers have criticized its practice of releasing important results as press releases; so far, it has given details for only one of the three headline findings, on dexamethasone, in a preprint posted 6 days after the release. The Recovery team is still collecting trial data on the antibiotic azithromycin, an antibody called tocilizumab, and the antibody-rich plasma collected from recovered patients.

Results on those therapies are likely months away, Landray says. But he cautions he has been wrong before. On the morning of 4 June, he had predicted the first results from Recovery would likely come in early July. A few hours later, the chairperson of the trial's data monitoring committee called him to say there was enough patient data to declare a verdict on hydroxychloroquine. ■

COVID-19

Can interferons stop COVID-19 before it takes hold?

Biology of infection supports early treatment with body's own viral defenses

By **Meredith Wadman**

On 30 April, Valerie McCarthy's test result confirmed that her grinding fatigue and pummeling headaches were caused by the new coronavirus. She wasn't hospitalized, but the very next day, a nurse at Stanford University Medical Center gave the 52-year-old marathon runner an injection that contained either a placebo or a natural virus fighter: interferon.

McCarthy was Patient 16 in a clinical trial that, it's hoped, will help fill a huge void in treatments for COVID-19: Doctors have no drugs that, given early, have been proven to prevent infection or help beat back the virus before it takes hold. So far, the two scientifically validated treatments for COVID-19—remdesivir and dexamethasone—have only been shown to work in hospitalized patients with serious illness.

But a small flurry of recent papers suggests the novel coronavirus does some of its deadly work by disabling interferons, powerful proteins that are the body's own frontline defenders against viral invasion. If so, synthetic interferons given before or soon after infection may tame the virus before it causes serious disease—a welcome possibility that additional recent studies support.

Several interferons were approved decades ago by the U.S. Food and Drug Administration, their immune-boosting powers deployed against diseases including cancer and hepatitis. And in an early, unrandomized preventive trial in a hospital in China's Hubei province, none of 2415 medical workers who took daily interferon nose drops got the virus, according to a medRxiv preprint.

The Stanford trial is one of dozens now trying interferons against COVID-19, including in people who aren't sick but might have been exposed to the virus. First results from a controlled trial at the Univer-

sity of Southampton are expected by August.

"Every study in every species has shown that if you induce interferons before [a] virus comes in, the virus loses," says Andreas Wack, an immunologist at the Francis Crick Institute. "The earlier you can give it, the better, and the best thing you can do is to give it before the virus is there."

Timing is crucial, adds Miriam Merad, an immunologist at the Icahn School of Medicine at Mount Sinai. "It's going to be important to know when to give these drugs." If given too late in the course of infection, interferons might pour fuel on the out-of-control inflammation that is a hallmark of severe COVID-19, she and others say. "Interferons are strong antivirals," Merad says. "But they also activate immune cells and can cause immunopathology."

Interferons are molecular messengers that launch an immediate, intense local response when a virus invades a cell. They trigger production of myriad proteins that attack the virus at every stage of invasion and replication, and they alert uninfected neighboring cells to prepare their own defenses. Interferons also help recruit immune cells to the site of infection and activate them when they arrive.

But SARS-CoV-2, the virus that causes COVID-19, disables this defense by blocking the powerful interferons that lead it, says Benjamin tenOever, a virologist at Mount Sinai. He and his colleagues studied SARS-CoV-2 infection in a range of models: human lung and bronchial cells, ferrets, lung tissue from deceased COVID-19 patients, and blood from living ones. In virtually every system, "interferon is badly suppressed," tenOever says. As it shuts down interferons, his team reported in *Cell* in May, the virus also ramps up production of chemokines, a different set of messenger molecules that summon distant immune cells and trigger inflammation.

Findings from a team led by immunologist Benjamin Terrier of the Cochin Hospital in Paris and published as a preprint on medRxiv, echo tenOever's. Terrier's team also looked at blood from 50 COVID-19 patients, finding strikingly depressed interferon activity and elevated chemokines in those whose disease became severe and critical—but not in those who ended up with mild or moderate disease. Terrier posits that local viral replication, unchecked by interferons, gins up tissue-damaging inflammation, as do armies of immune cells summoned from afar. The result is the out-of-control inflammatory response that ends many lives (*Science*, April 24, p. 356).

But not everyone is persuaded that the virus itself is responsible for missing-in-action interferons. Are low interferons "the cause or the consequence of severe disease?" asks Jean-Laurent Casanova, an infectious disease geneticist at the Rockefeller University. Since 2015, he has found three inherited mutations that profoundly inhibit the interferon response, raising the possibility that genetic predisposition plays a role in some cases of severe COVID-19.

And some data challenge the notion that interferons are suppressed at all. One report, published in *Cell Host & Microbe* by Jianwei Wang of Peking Union Medical College and colleagues last month, found strong expression of numerous interferon-stimulated genes (ISG's)—often used as a marker for interferon activity—in the lung fluid of eight COVID-19 patients. Similarly, in unpublished data, John Tsang, a systems immunologist at the U.S. National Institute of Allergy and Infectious Diseases, found robust ISG expression in immune cells in the blood of 35 severely ill COVID-19 patients.

Valerie McCarthy received an injection that contained either placebo or an interferon.

All the same, at least five studies since April have found that interferon treatment or pretreatment has a protective effect in cells and in mice infected with SARS-CoV-2. These studies parallel earlier ones that found beneficial effects of early interferon administration in mice infected with the new coronavirus' cousins, severe acute respiratory syndrome (SARS) and Middle East respiratory syndrome. The data support giving interferons as a treatment for COVID-19, especially early in infection, advocates say.

But plenty of caveats remain. For starters, when given as drugs, the powerful type I interferons can have awful side effects, as patients who have taken them for months on end for cancer and other diseases know. Side effects include flulike symptoms, headache, vomiting, and depression. But COVID-19 treatment does not require continuous dosing for months, and one trial in chronic hepatitis showed that a synthetic type III interferon had fewer side effects than a type I interferon. (Type I interferons have receptors on every cell in the body, but type III do not.)

McCarthy's trial was of a type III interferon. She was warned of "headaches and fatigue," but was not dissuaded. "I thought: 'I'm already tired … that's OK,'" she says.

Two papers published in *Science* last month suggested type III interferons might be harmful if given late in infection. In one paper, Wack's group reported that in mice, naturally occurring type III interferon disrupted the lung repair crucial to recovery from influenza; in the other, a team led by immunologist Ivan Zanoni of Boston Children's Hospital reported similar findings in mice—and also found type III interferons in the lung fluid of severely ill COVID-19 patients. "The take home message for the clinical people," says Zanoni, is: "If you want to give type III interferons as antivirals, give them early."

Eleanor Fish, an immunologist at the University of Toronto who is launching, with colleagues, two preventive interferon trials, says data already point to interferons' safety. She and colleagues published an uncontrolled study of 77 hospitalized patients in Wuhan, China, in *Frontiers in Immunology*. They reported that patients given a type I interferon (with or without an antiviral medicine) had lower levels of a key inflammatory biomarker than other patients—and also cleared the virus 7 days sooner. Similar promising findings emerged from uncontrolled studies that Fish published years ago, examining the effects of the drugs in patients hospitalized with SARS and Ebola. "This notion of [interferons being] harmful later, I just want to throw it out the window," Fish says.

Even as scientists debate the underlying biology, they are keenly aware that only controlled clinical trials will answer their questions. As for McCarthy, 8 weeks after first testing negative for the virus, she struggles to slowly run 3 kilometers. She still doesn't know whether she received placebo or an interferon. Like everyone else, she'll have to wait for the trial's results. ■

PHOTO: STEVE FISCH

The Hope satellite will orbit Mars in a way that enables it to see the planet's surface at all times of day.

PLANETARY SCIENCE

UAE probe aims for Mars—and payoffs on Earth

Even before launch, the Hope satellite has boosted Emirati space science

By **Sedeer el-Showk**

The United Arab Emirates (UAE), a small Persian Gulf nation, is on the cusp of a big breakthrough: joining the United States, the Soviet Union, Europe, and India in the elite club of nations that have successfully sent spacecraft to Mars. On 15 July, the Emirates Mars Mission (EMM)—also known as the Hope satellite—is set to launch on a Japanese rocket, arriving at the Red Planet in February 2021.

Planners hope the mission will boost UAE industry and science capacity while also delivering sorely needed data on the martian atmosphere. "One of the primary objectives of the mission from the start was to do science that is relevant to the international community," says Sarah Amiri, Hope's science lead.

Most of the six spacecraft now at Mars are in polar orbits that only offer views of the surface at fixed times of day. But Hope will be inserted into an inclined orbit that provides a view of any given point at a different time on each orbit. A camera and infrared spectrometer will collect data about dust, moisture, and ozone in the lower atmosphere, while an ultraviolet spectrometer will measure carbon monoxide, hydrogen, and oxygen in the upper atmosphere.

The data will fill in gaps in computer models of the martian atmosphere, says Francois Forget, a member of the Hope science team at the Laboratory of Dynamic Meteorology. Primed by observations, these global climate models (GCMs) rely on basic physical laws to make predictions about the weather and climate. Yet at Mars, "we observe some processes which we cannot represent using our universal equations," Forget says. For example, the models cannot reproduce how atmospheric dust is distributed or explain why some dust storms grow into global events that completely shroud the planet. Monitoring the atmosphere throughout the day may help solve these enigmas, Forget says.

Lori Neary, who models the martian atmosphere at the Royal Belgian Institute for Space Aeronomy and isn't involved with the mission, is also looking forward to its data. "The more instruments that are taking measurements of Mars, the better," she says. She hopes the data will help her team understand daily changes in ozone levels, which depend strongly on sunlight. Continuous EMM data will help calibrate model predictions for ozone levels throughout a martian day.

The mission has given equal weight to building capacity for space science research in the UAE. "This mission created expertise in the country in areas we never had expertise in before," says Amiri, who was a program engineer on the UAE's DubaiSat satellites before becoming EMM science lead and, later, UAE's minister of State for Advanced Science. Emirati aerospace firms enhanced their know-how by manufacturing many of Hope's precision components. Hope was tested in the nation's first double-story clean room, which will now be used for future projects, including university built drones and small cube satellites.

The mission has also spurred an interest in science at Emirati universities, which have launched five new undergraduate science programs and a graduate program in physics. At the University of Sharjah, the number of students in applied physics and astronomy has doubled since the start of the EMM.

A science apprenticeship program, built into the mission itself, has also helped build expertise. When the EMM was conceived in 2014, the UAE had only a handful of planetary scientists but plenty of trained engineers. The team realized "the best way was to retool engineers to think like scientists," Amiri recalls. The program matches Emirati engineers with scientists at partner institutes. For example, Hessa Al Matroushi, the EMM data management and analysis lead, originally trained as an image processing engineer, but shifted gears by apprenticing with scientists on NASA's MAVEN mission, which studies Mars's upper atmosphere. "The experience taught me how to be flexible, how to handle scientific data, filter it and analyze it," she says.

Many of the apprentices plan to continue as space scientists after the mission. "This is where we see our future," Al Matroushi says. ■

Sedeer el-Showk is a science journalist in Helsinki.

PHOTO: MOHAMMED BIN RASHID SPACE CENTRE

Polynesians on Nuku Hiva, an island in the North Marquesas, carry traces of Native American ancestry.

GENETICS

Polynesians, Native Americans met and mingled long ago

Islanders' DNA suggests contact before European arrival

By **Lizzie Wade**

By about 1200 C.E., Polynesians were masters of oceanic exploration, roaming 7000 kilometers across the Pacific Ocean in outrigger canoes. Guided by subtle changes of wind and waves, the paths of migrating birds, bursts of light from bioluminescent plankton, and the position of the stars, they reached and settled islands from New Zealand to Rapa Nui, or Easter Island, the closest Polynesian island to South America.

So it's natural to wonder: Did these world-class explorers make it the last 3800 kilometers to South America? A genomic study of more than 800 modern Polynesians and Native Americans suggests they did.

The work strengthens earlier evidence that somewhere—perhaps on the northern coast of South America—the two groups met and mixed well before the era of European colonialism. And it shakes up the most popular model of where Native American genes first took root in Polynesia, shifting the focus from Rapa Nui to islands farther west.

"This is an excellent, exciting study," says Lars Fehren-Schmitz, an anthropological geneticist at the University of California (UC), Santa Cruz. Expanding genomic research to islands beyond Rapa Nui "was what was missing from the whole picture."

Earlier hints of contact between the two regions included the sweet potato, which was domesticated in the Andes but grown and eaten all over Polynesia for hundreds of years before Europeans arrived. And a 2014 study of 27 modern people from Rapa Nui found they had Native American ancestry dating back to between 1300 C.E. and 1500 C.E.—at least 200 years before the first Europeans landed there in 1722 C.E. But a 2017 ancient DNA study, led by Fehren-Schmitz, found no sign of Native American ancestry in five people who lived on Rapa Nui before and after European contact.

Population geneticist Andrés Moreno-Estrada and anthropologist Karla Sandoval, both at Mexico's National Laboratory of Genomics for Biodiversity, traveled to Rapa Nui in 2014 and invited the community to participate in a study. They analyzed genome-wide data from 166 people from the island. Then they combined those data with genomic analyses of 188 Polynesian people from 16 other islands, whose genetic samples had been collected in the 1980s.

"It's an amazing data set," says Anna-Sapfo Malaspinas, a population geneticist at the University of Lausanne who led the 2014 work that found evidence for contact.

Moreno-Estrada, Sandoval, and their team found that people on many islands had both Polynesian and European ancestry, reflecting their colonial histories. But they were also able to detect a small amount of Native American ancestry in people from the eastern Polynesian islands of Palliser, the Marquesas, Mangareva, and Rapa Nui. The Native American sequences were short and nearly identical—seemingly a legacy of one long-ago meeting with a Native American group, rather than sustained contact over generations, Moreno-Estrada says.

Comparing those sequences with genomes from people from 15 Indigenous groups from the Pacific coast of Latin America, researchers found most similarity to the Zenu, an Indigenous group from Colombia, the team reports this week in *Nature*.

Analyses of the length of the Native American sequences show this ancestry appeared first on Fatu Hiva in the South Marquesas roughly 28 generations ago, which would date it to about 1150 C.E. That's about when the island was settled by Polynesians, raising the possibility the contact happened even earlier. The genetic legacy of that mixing was then carried by Polynesian voyagers as they settled other islands, including Rapa Nui.

Where exactly the first encounter took place, the team can't say. Modern Latin American fishermen lost at sea have been known to drift all the way to Polynesian islands. "It could have been one raft lost in the Pacific," Moreno-Estrada says.

But it's more likely that Polynesians traveled to the northern coast of South America, says Keolu Fox, a genome scientist at UC San Diego. Polynesian voyagers frequently traveled between islands and could have journeyed to South America and back, perhaps multiple times, Fox says. "In the process, these Polynesians bring back the sweet potato, and they also bring back a small fragment of Native American DNA" from relationships on the mainland. "The ocean is not a barrier" for Polynesians, he says.

Fehren-Schmitz and other researchers agree contact is likely, but stress that only ancient DNA can provide direct evidence of an encounter. But DNA degrades quickly in the tropics—and Polynesian communities that remember being disrespected by Western scientists in the past may be reluctant to grant permission for genetic studies of their ancestors, says Fox, who is Kānaka Maoli (Native Hawaiian). To move forward, he says, researchers need to deeply engage on an ongoing basis with descendant communities on many islands.

For now, "This study shows us a new path to follow," says Francisco Torres Hochstetter, an archaeologist at the Father Sebastian Englert Anthropological Museum in Hanga Roa on Rapa Nui. "It opens our minds." ■

CHINA

New security law rattles Hong Kong universities

Researchers worry about academic freedom and city's ability to attract foreign talent

By **Dennis Normile**

The new security law China imposed on Hong Kong last week has created deep uncertainty in the city's academic community. Some researchers worry it could limit academic freedom in Hong Kong—along with freedom of speech and the right to protest—and make it harder to attract scientific talent from abroad. "We don't know exactly how the law will be implemented, but just the perception and uncertainty that it creates will be a problem for the universities," says Sun Kwok, a Hong Kong–born astronomer who was dean of science at the University of Hong Kong (HKU) for 10 years.

But others expect the law's impact on Hong Kong's thriving academic research to be minimal. While its details need to be interpreted by the courts, "I believe that academic research grounded in scientific rigor and thorough analysis of evidence without bias should prevail," says Fanny Cheung, pro-vice-chancellor for research at the Chinese University of Hong Kong (CUHK).

The law is China's answer to the monthslong demonstrations that rocked Hong Kong starting in spring 2019. Triggered by a proposed bill that would have allowed extradition of Hong Kongers to the mainland, the protests eventually targeted a long list of grievances, including the lack of direct elections to choose Hong Kong's chief executive.

Although the law states that Hong Kong's tradition of free expression will be protected, many worry about its emphasis on protecting national security. The law gives authorities new powers to punish "secession, subversion, perpetration of terrorist activities, and collusion with a foreign country or with external entities to endanger security." Approved by China's National People's Congress and signed by President Xi Jinping on 30 June, the law took effect that same day. Within hours, Hong Kong authorities reportedly rounded up hundreds of protesters.

In a joint statement issued in early June, when the text of the law was not yet known, the heads of five of Hong Kong's eight public universities—Lingnan University, CUHK, the Education University of Hong Kong, Hong Kong Polytechnic University, and HKU—wrote that they "understand the need for national security legislation" but pledged, "Our universities will continue to stand fast in upholding the principles of academic freedom and institutional autonomy."

Many expect repercussions. The law "will play into the issue that we've had persuading people from North America who are not ethnically Chinese to think about coming to Hong Kong," says Matthew Evans, an ecologist and dean of science at HKU. The ban on "colluding" with foreign entities could discourage joint studies with foreign organizations disliked by Beijing in areas such as environmental and food safety research, says Chan King Ming, an environmental scientist at CUHK. Evans also worries about the U.S. decision, in response to the law, to impose the same restrictions on exports of sensitive technologies to Hong Kong as it does on China. Those restrictions might affect imports of laboratory equipment, he says.

Pro-democracy lawmaker Andrew Wan was among hundreds arrested in Hong Kong on 1 July during protests against a new security law.

PHOTO: ROY LIU/BLOOMBERG/GETTY IMAGES

Others fear more direct effects. The Chinese government tries to control the release of certain research results on the mainland, notes Peter Baehr, a professor of social theory at Lingnan University. In what Baehr calls a "draconian action," authorities shut down the lab of Zhang Yong-Zhen of Fudan University in Shanghai in January after his group published the first genome of the novel coronavirus without authorization. Baehr worries China may try to influence the dissemination of Hong Kong research results as well.

Bruce Lui, a lecturer in journalism at Hong Kong Baptist University, adds that the mainland's concept of national security extends to such areas as economics. That means Hong Kong scholars might have to tread softly if reporting, for example, inflation statistics embarrassing to the government. "Politics and state stability come first," Lui says.

There could also be shifts in university curricula. One article in the new law calls for Hong Kong to "promote national security education in schools and universities," though it does not say how. "There have been voices in certain political circles in Hong Kong that liberal education is to blame for the student unrest in 2019," Kwok says.

Some scholars are urging caution before pronouncing the death of the "one country, two systems" principle agreed on when sovereignty over Hong Kong was transferred from the United Kingdom to China in 1997. "I believe we need to wait before coming to that very serious and in my view tragic conclusion," says one Hong Kong-based foreign scientist who asked not to be identified because of the political sensitivities. He adds that the law's lack of detail is already leading to rampant speculation. As a result, "Anyone who is able to leave is probably considering it seriously," he says. But another senior academic says the few scholars who have already left were motivated not by the security law but "because of the social unrest."

Whatever happens next, Hong Kong's researchers shouldn't engage in self-censorship, Kellee Tsai, dean of humanities and social science at Hong Kong University of Science and Technology, wrote in a 2 July message to her faculty and staff. "There may well be non-obvious 'red lines' in Hong Kong's higher education sector that cannot be crossed without severe legal consequences," she said. "Let's not draw those lines ourselves." ■

FEATURES

NO ROOM FOR ERROR

Developers of quantum computers face their true challenge: taming the noise that plagues the intertwined quantum bits

By **Adrian Cho**

In October 2019, researchers at Google announced to great fanfare that their embryonic quantum computer had solved a problem that would overwhelm the best supercomputers. Some said the milestone, known as quantum supremacy, marked the dawn of the age of quantum computing (*Science*, 27 September 2019, p. 1364). However, Greg Kuperberg, a mathematician at the University of California, Davis, who specializes in quantum computing, wasn't so impressed. He had expected Google to aim for a goal that is less flashy but, he says, far more important.

Whether it's calculating your taxes or making Mario jump a canyon, your computer works its magic by manipulating long strings of bits that can be set to 0 or 1. In contrast, a quantum computer employs quantum bits, or qubits, that can be both 0 and 1 at the same time, the equivalent of you sitting at both ends of your couch at once. Embodied in ions, photons, or tiny superconducting circuits, such two-way

ILLUSTRATION: ANDY GILMORE

states give a quantum computer its power. But they're also fragile, and the slightest interaction with their surroundings can distort them. So scientists must learn to correct such errors, and Kuperberg had expected Google to take a key step toward that goal. "I consider it a more relevant benchmark," he says.

If some experts question the significance of Google's quantum supremacy experiment, all stress the importance of quantum error correction. "It is really the difference between a $100 million, 10,000-qubit quantum computer being a random noise generator or the most powerful computer in the world," says Chad Rigetti, a physicist and co-founder of Rigetti Computing. And all agree with Kuperberg on the first step: spreading the information ordinarily encoded in a single jittery qubit among many of them in a way that maintains the information even as noise rattles the underlying qubits. "You're trying to build a ship that remains the same ship, even as every plank in it rots and has to be replaced," explains Scott Aaronson, a computer scientist at the University of Texas, Austin.

The early leaders in quantum computing—Google, Rigetti, and IBM—have all trained their sights on that target. "That's very explicitly the next big milestone," says Hartmut Neven, who leads Google's Quantum Artificial Intelligence lab. Jay Gambetta, who leads IBM's quantum computing efforts, says, "In the next couple of years, you'll see a series of results that will come out from us to deal with error correction."

Physicists have begun to test their theoretical schemes in small experiments, but the challenge is grand. To demonstrate quantum supremacy, Google scientists had to wrangle 53 qubits. To encode the data in a single qubit with sufficient fidelity, they may need to master 1000 of them.

THE QUEST FOR QUANTUM computers took off in 1994 when Peter Shor, a mathematician at the Massachusetts Institute of Technology, showed that such a machine—then hypothetical—should be able to quickly factor huge numbers. Shor's algorithm represents the possible factorizations of a number as quantum waves that can slosh simultaneously through the computer's qubits, thanks to the qubits' two-way states. The waves interfere so that the wrong factorizations cancel one another and the right one pops out. A machine running Shor's algorithm could, among other things, crack the encryption systems that now secure internet communications, which rely on the fact that searching for the factors of a huge number overwhelms any ordinary computer.

However, Shor assumed each qubit would maintain its state so the quantum waves could slosh around as long as necessary. Real qubits are far less stable. Google, IBM, and Rigetti use qubits made of tiny resonating circuits of superconducting metal etched into microchips, which so far have proved easier to control and integrate into circuits than other types of qubits. Each circuit has two distinct energy states, which can denote 0 or 1. By plying a circuit with microwaves, researchers can ease it into either state or any combination of the two—say, 30% 0 and 70% 1. But those in-between states will fuzz out or "decohere" in a fraction of a second. Even before that happens, noise can jostle the state and alter it, potentially derailing a calculation.

Such noise nearly drowned out the signal in Google's quantum supremacy experiment. Researchers began by setting the 53 qubits to encode all possible outputs, which ranged from zero to 2^{53}. They implemented a set of randomly chosen interactions among the qubits that in repeated trials made some outputs more likely than others. Given the complexity of the interactions, a supercomputer would need thousands of years to calculate the pattern of outputs, the researchers said. So by measuring it, the quantum computer did something that no ordinary computer could match. But the pattern was barely distinguishable from the random flipping of qubits caused by noise. "Their demonstration is 99% noise and only 1% signal," Kuperberg says.

To realize their ultimate dreams, developers want qubits that are as reliable as the bits in an ordinary computer. "You want to have a qubit that stays coherent until you switch off the machine," Neven says.

Scientists' approach of spreading the information of one qubit—a "logical qubit"—among many physical ones traces its roots to the early days of ordinary computers in the 1950s. The bits of early computers consisted of vacuum tubes or mechanical relays, which were prone to flip unexpectedly. To overcome the problem, famed mathematician John von Neumann pioneered the field of error correction.

Von Neumann's approach relied on redundancy. Suppose a computer makes three copies of each bit. Then, even if one of the three flips, the majority of the bits will preserve the correct setting. The computer can find and fix the flipped bit by comparing the bits in pairs, in so-called parity checks. If the first and third bits match, but the first and second and second and third differ, then most likely, the second bit flipped, and the computer can flip it back. Greater redundancy means greater ability to correct errors. Ironically, the transistors, etched into microchips, that modern computers use to encode

Mapping a qubit

Whereas an ordinary bit must be either 0 or 1, a qubit can be in any combination of 0 and 1 at the same time. Those two parts of the state mesh in a way described by an abstract angle, or phase. So the qubit's state is like a point on a globe whose latitude reveals how much the qubit is 0 and how much it is 1, and whose longitude indicates the phase. Noise can jostle the qubit in two basic ways that knock the point around the globe.

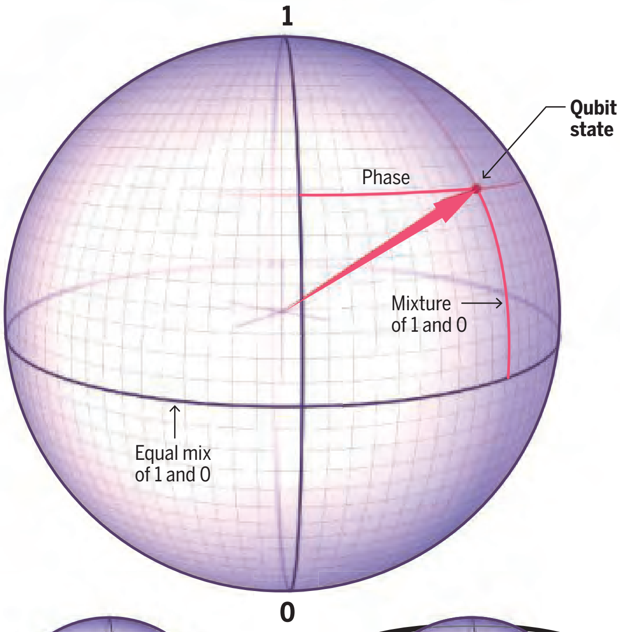

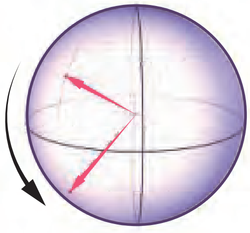

Bit-flip error
Exchanges 0 and 1, flipping the qubit in latitude

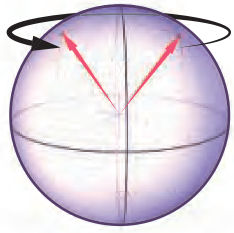

Phase-flip error
Pushes the qubit's state halfway around the sphere in longitude

GRAPHIC: C. BICKEL/SCIENCE

their bits are so reliable that error correction isn't much used.

But a quantum computer will depend on it, at least if it's made of superconducting qubits. (Qubits made of individual ions suffer less from noise, but are harder to integrate.) Unfortunately for developers, quantum mechanics itself makes their task much harder by depriving them of their simplest error-correcting tool, copying. In quantum mechanics, a no-cloning theorem says it's not possible to copy the state of one qubit onto another without altering the state of the first one. "This means that it's not possible to directly translate our classical error correction codes to quantum error correction codes," says Joschka Roffe, a theorist at the University of Sheffield.

Even worse, quantum mechanics requires researchers to find errors blindfolded. Although a qubit can have a state that is both 0 and 1 at the same time, according to quantum theory, experimenters can't measure that two-way state without collapsing it into either 0 or 1. Checking a state obliterates it. "The simplest [classical error] correction is that you look at all the bits to see what's gone wrong," Kuperberg says. "But if it's qubits then you have to find the error without looking."

An easy fix

In a conventional computer, a bit is a switch that can be set to either 0 or 1. To protect a bit, a computer can copy it. If noise then flips a copy, the machine can find the error by making parity measurements: comparing pairs of bits to see whether they're the same or different.

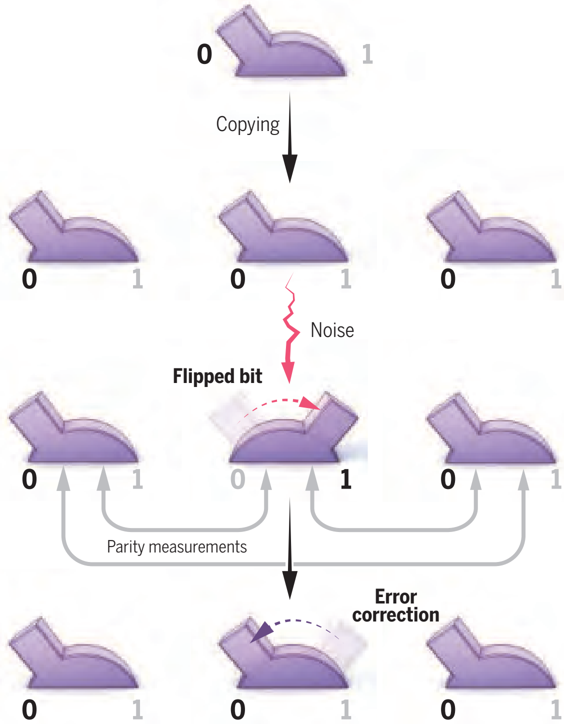

GRAPHIC: C. BICKEL/*SCIENCE*

Those hurdles may sound insurmountable, but quantum mechanics points to a potential solution. Researchers cannot copy a qubit's state, but they can extend it to other qubits using a mysterious quantum connection called entanglement.

How the entangling is done shows just how subtle quantum computing is. Prodded with microwaves, the original qubit interacts with another that must start in the 0 state through a "controlled not" (CNOT) operation. The CNOT will change the state of the second qubit if the state of the first is 1 and leave it unchanged if the first qubit is 0. However, the maneuver doesn't actually measure the first qubit and collapse its state. Instead, it maintains the both-ways state of the first qubit while both changing and not changing the second qubit at the same time. It leaves the two qubits in a state in which, simultaneously, they are both 0 and both 1.

If the original qubit is in, for example, a 30% 0 and 70% 1 state, physicists can link it to other qubits to make a chain of, say, three qubits that share an entangled state that's 30% all three are 0 and 70% all three are 1. That state is distinct from three copies of the original qubit. In fact, none of the three entangled qubits in the string possesses a well defined quantum state of its own. But now, the three qubits are completely correlated: If you measure the first one and it collapses to 1, then the other two must also instantly collapse to 1. If the first collapses to 0, the others must also. That correlation is the essence of entanglement.

With that bigger entangled state, scientists can now keep an eye out for errors. To do that, they entangle still other "ancillary" qubits with the chain of three, one with first and second qubits in the string and another with the second and third. They then use measurements on the ancillas to make the quantum mechanical equivalent of parity checks. For example, without breaking the entanglement, noise can flip any one of the three coding qubits so that its 0 and 1 parts get switched, changing the latent correlations among all three. If researchers set things up right, they can make "stabilizer" measurements on the ancillary qubits to probe those correlations.

Although measuring the ancillary qubits collapses their states, it leaves the coding qubits unperturbed. "These are specially designed parity measurements that don't collapse the information encoded in the logical state," Roffe says. For example, if the measurement shows the first ancilla is 0, it reveals only that the first and second coding qubits must be in the same state, but not which state that is. If the ancilla is 1, then the measurement reveals only that the coding qubits must be in opposite states. If researchers can find a flipped qubit more quickly than the qubits tend to fuzz out, they can use microwaves to flip it back to its original state and restore its coherence.

That's just the basic idea. The state of a qubit is more complex than just a combination of 0 and 1. It also depends on exactly how those two parts mesh, which, in turn, depends on an abstract angle called the phase. The phase can range from 0° to 360° and is key to the wavelike interference effects that give a quantum computer its power. Quantum mechanically, any error in a qubit's state can be thought of as some combination of a bit-flip error that swaps 0 and 1 and a phase flip that changes the phase by 180°.

To correct both types, researchers can expand into another dimension—literally. Whereas a string of three entangled qubits, with two ancillas woven between them, is the smallest array that can detect and correct a bit-flip error, a three-by-three grid of qubits, with eight interspersed ancillas, is the simplest one that can detect and correct both bit-flip and phase-flip errors. The logical qubit now resides in an entangled state of the nine qubits—be thankful you don't have to write it out mathematically! Stabilizer measurements along one dimension of the grid check for bit-flip errors, while slightly different stabilizer measurements along the other dimension check for phase-flip errors.

Schemes for pushing into two dimensions vary, depending on the geometric arrangement of the qubits and the details of the stabilizer measurements. Nevertheless, researchers' road to error correction is now clear: Encode a single logical qubit in a grid of physical qubits and show that the fidelity of the logical qubit gets better as the size of the grid increases.

Experimenters have already made a start. For example, in a *Nature Physics* study published on 8 June, Andreas Wallraff at ETH Zurich and colleagues demonstrated that they could detect—but not correct—errors in a logical qubit encoded in a square of four qubits with three ancillary qubits.

But experimenters face a daunting challenge. Manipulating individual qubits can introduce errors, and unless that error rate falls below a certain level, then

entangling more qubits with the original one only adds more noise to the system, says Maika Takita, a physicist at IBM. "To demonstrate anything you have to get below that threshold," she says. The ancillary qubits and other error-correction machinery add even more noise, and once those effects are included, the necessary error threshold plummets further. To make the scheme work, physicists must lower their error rate to less than 1%. "When I heard we achieved an 3% error rate, I thought that was great," Takita says. "Now, it needs to be much lower."

Error correction also requires twiddling with qubits repeatedly. That makes the process more demanding than quantum supremacy, which involved measuring all the qubits just once, says Marissa Giustina, a physicist with Google. Error correction "requires you to measure and measure and measure over and over again in a cycle, and that has to be done quickly and reliably," she says.

Although a handful of qubits would suffice to demonstrate the principle of quantum error correction, in practice physicists will have to control huge numbers of them. To run Shor's algorithm well enough to factor, say, a number 1000 bits long—roughly the size used in some internet encryption schemes—they'll need to maintain logical qubits with a part-in-1-billion error rate. That may require entangling a grid of 1000 physical qubits to safeguard a single logical qubit, researchers say, a prospect that will take generations of bigger and better quantum computing chips.

Ironically, overcoming that challenge would put developers back where they were 20 years ago, when they were just setting out to make pairs of physical qubits interact to perform the various logical operations, or "gates," needed for computation. Once scientists have begun to master error correction, they'll have to repeat nearly every development so far in quantum computing with the more robust but highly complex logical qubits. "People say that error correction is the next step in quantum computing; it's the next 25 steps," Giustina quips.

Retracing those steps won't be easy. It's not just that any logical gate currently involving two qubits will require thousands of them. Worse, another theorem from quantum mechanics states that, no matter what scheme researchers use, not all of the logical gates can be easily translated from individual physical qubits to diffuse logical ones.

Researchers think they can sidestep that problem if they can initialize all the qubits in their computer in particular "magic states" that, more or less, do half the work of the problematic gates. Unfortunately, still more qubits may be needed to produce those magic states. "If you want to perform something like Shor's algorithm, probably 90% of the qubits would have to be dedicated to preparing these magic states," Roffe says. So a full-fledged quantum computer, with 1000 logical qubits, might end up containing many millions of physical qubits.

Google has a plan to build just such a machine within 10 years. At first blush, that sounds preposterous. Superconducting qubits need to be cooled to near absolute zero, in a device called a cryostat that fills a small room. A million-qubit machine conjures visions of a thousand cryostats in a huge factory. But Google researchers think they can keep their device compact. "I don't want to tip my hand, but we believe we figured this out," Neven says.

Others are taking different tacks. Google's scheme would require 1000 physical qubits to encode a single logical qubit because its chip allows only neighboring qubits to interact. If more distant qubits can be made to interact, too, the number of physical qubits could be much smaller, Gambetta says. "If I can achieve that, then these ridiculously scary numbers for the overhead of error correction can come crashing down," he says. So IBM researchers are exploring a scheme with more distant interconnections among the qubits.

Nobody is willing to predict how long it will take researchers to master error correction. But it is time to turn to the problem in earnest, Rigetti says. "Thus far, substantially all the researchers who would identify themselves as error correction researchers are theorists," he says. "We have to make this an empirical field with real feedback on real data generated with real machines." Quantum supremacy is so 2019. In quantum computing, error correction is the next hot thing. ■

Quantum fixes are harder

The rules of quantum mechanics make it impossible to watch for errors by copying and measuring qubits (top). Instead, physicists want to spread the qubit's state to other qubits through "entanglement" (middle) and monitor those to detect errors; then nudge an errant bit back to the correct state (bottom).

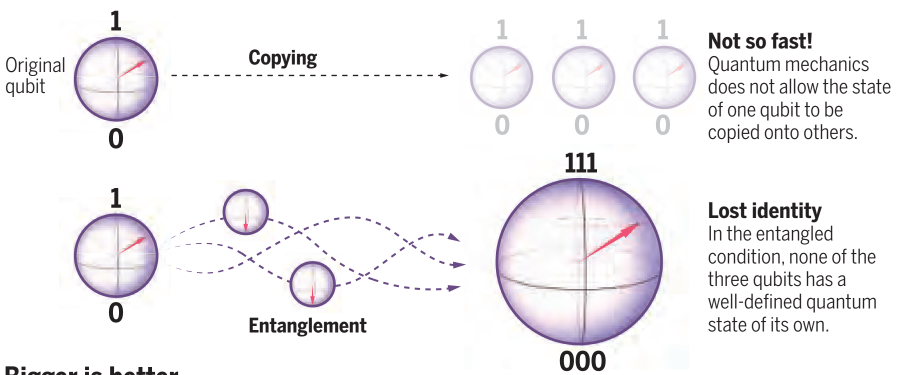

Bigger is better

Instead of trying to copy the state of a qubit, physicists can enlarge it by entangling the qubit with others, resulting in a single state that corresponds to the same point on a sphere.

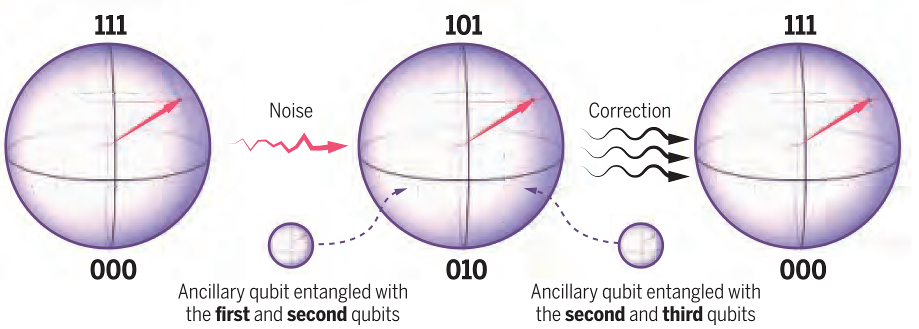

Gentle correctives

Now, if noise flips one of the qubits, physicists can detect the change without actually measuring the state. They entangle pairs of the main qubits with other ancillary qubits whose state can be measured and will be 0 if the correlation between a pair remains the same and 1 if the correlation is flipped. Microwaves can then unflip the qubit and restore the initial entangled state.

GRAPHIC: C. BICKEL/*SCIENCE*

INSIGHTS

POLICY FORUM

GRAPHIC: DAVIDE BONAZZI/SALZMANART

LEGAL RESEARCH

How to build a more open justice system

Court records are unstructured and costly to access—here's how to fix it

By **Adam R. Pah[1,2], David L. Schwartz[3], Sarath Sanga[3], Zachary D. Clopton[3], Peter DiCola[3], Rachel Davis Mersey[4,5], Charlotte S. Alexander[6], Kristian J. Hammond[7], Luís A. Nunes Amaral[2,7]**

Modern governments gather information across an extraordinary range of activities and use this information to direct policy. Whether a central bank monitoring inflation or a health agency monitoring disease, these entities typically publicly disclose the information gathered so that their actions can be reviewed and evaluated by others. But in many respects, the justice system is a glaring exception. In the United States, a range of technical and financial obstacles blocks large-scale access to public court records—all but foreclosing their use to direct policy. Yet a growing body of empirical legal research demonstrates that systematic analyses of court records could improve legal practice and the administration of justice. And although much of the legal community resists quantitative approaches to law, we believe that even the skeptics will be receptive to quantitative feedback—so long as it is straightforward, apolitical, and incontrovertible. We offer an example of this kind of feedback as well as a collaborative research agenda to dismantle access barriers to court records and enable the public to analyze them.

Although court records in the United States sit in the public domain, federal courts charge $0.10 per printed page to view any record online (*1*). Accessing a single case might cost $10 or more. Accessing all cases from a given year would cost millions of dollars (*2*). To be sure, the federal judiciary releases in-house studies that use federal court records, as well as a database of basic information

about each case, such as the subject matter (e.g., tort, contract, civil rights) and disposition (e.g., settled, transferred, jury verdict) (*3*). The federal judiciary has steadfastly refused, however, to make the underlying public court records freely accessible.

Selective access is not the approach taken by the rest of the U.S. federal government: Congressional records are freely available at congress.gov. Executive agencies' records are freely available at regulations.gov. It's hard to conceive of a compelling argument for selective access to judicial records that does not apply equally to selective access to congressional records or federal agencies. More to the point, it's hard to conceive of a reason why public records should not generally be accessible to the public.

There are some alternative sources for court records, but barriers to systematic analysis remain. Commercial legal services have directly purchased many court records, but they impose their own fees, prohibit bulk downloads, and thus foreclose systematic analysis even for subscribers. Individual judges and commercial services occasionally grant ad hoc fee reductions for research purposes, but these grants are rare, cumbersome to acquire, limited to subsets of the data, and always come with the condition that the underlying records are not disclosed to the public (*4*). An open alternative, *Free Law Project*, maintains a crowdsourced repository of free court records, but coverage remains too low to support systematic research.

DATA AND OPENNESS

The lack of access to court records seemingly undercuts any claim that the courts are truly "open" (*5*, *6*). It surely conflicts with researchers' conception of openness. Scientific practice is grounded on a commitment to sharing data and enabling others to replicate findings. But the law's conception of openness is different, a commitment to carrying out public acts in a public space. A scientist might restrict access to a lab and still claim that the research she conducts there is "open." Closed proceedings in a legal setting, on the other hand, are only tolerated in extraordinary circumstances.

Also in contrast to scientific practice, much of the legal profession resists quantitative or evidence-based approaches to improving legal practice and instead prefers to rely on personal experience and professional judgment (*7*). In a recent Supreme Court case challenging the constitutionality of partisan gerrymandering, Chief Justice John Roberts summarily dismissed empirical approaches to gerrymandering as "sociological gobbledygook" that any "intelligent man on the street" would denigrate as "a bunch of baloney" (*8*). Such skepticism is by no means confined to the United States. France, for example, has recently prohibited the publication of any statistical analysis of a judge's or clerk's decisions "with the object or effect of evaluating, analyzing, comparing or predicting their actual or supposed professional practices." Violators face up to 5 years in prison (*9*).

We believe that these differences help explain why the lack of large-scale access to data is not viewed as a priority—or even as a concern—by much of the legal community. The differences in priorities reflect not just commitments to different values but different conceptions of the same values. Yet, if court records are to be truly accessible and evaluable by the public, the legal and scientific communities must cooperate, and appreciate the values that the other holds dear.

EVALUATING ACCESS TO JUSTICE

Access to justice is a fundamental right and the foundation of any fair and legitimate justice system. But how can one quantify and empirically evaluate this concept? Consider court fees. For a litigant without means, court fees are a substantial barrier to the civil justice system. Anyone who files a lawsuit in federal court must pay a $400 filing fee, along with other costs related to litigation such as formal service of the complaint. Litigants in need can file an application to waive court fees, but there is no uniform standard to review these requests (*10*). Application forms differ by district. Most ask the applicant to list sources of income, assets, and cash on hand—and then leave the decision to the judge's discretion. Individual judges thus have considerable power over whether to grant or deny access to the justice system.

How do judges exercise this power? This is but one of the myriad questions that is difficult, and arguably impossible, to answer without easy access to structured court records. Even with free access to the data, the answer would be difficult to infer without being able to computationally analyze the text of the court records. In this case, the analysis is straightforward. When a party submits a fee waiver request, the case docket report adds a separate entry for that request, and the textual summary accompanying the entry typically includes some reference to whether the request was granted or denied. We analyzed these entries to compute the grant rate of each federal judge in 2016.

Average grant rates naturally differ among federal districts because cases are not randomly assigned to districts. However, once a case is filed in, say, San Francisco, it is then randomly assigned to one of the judges sitting in the federal district that includes San Francisco. Thus, if all judges reviewed fee waiver applications under the same standard, then grant rates should not systematically differ within districts.

We find, however, that they do (see the figure). At the 95% confidence level, nearly 40% of judges—instead of the expected 5%—approve fee waivers at a rate that statistically significantly differs from the average rate for all other judges in their same district. In one federal district, the waiver approval rate varies from less than 20% to more than 80%.

These findings were recently presented to a group of federal judges who are responsible for amending the rules in their local district. On learning of the inconsistent treatment of fee waiver requests, these judges expressed interest in using our data to improve the decision-making process (*11*). We count this as an early and encouraging validation of our claim that judges will be especially receptive to quantitative feedback that is straightforward, apolitical, and incontrovertible.

DISMANTLING BARRIERS

Going forward, we believe that the best way to provide the judiciary with quantitative feedback is to develop a forum where individuals can collaborate and build on each other's efforts. With this vision in mind, we propose a three-pronged collaborative research agenda to empower the public to access and analyze court records.

Make court records free

In theory, Congress could make federal records free by repealing the laws that authorize the judiciary to charge for access (*12*), or the Judicial Conference of the United States (the policy-making body of the federal judiciary) could stop charging fees. Both Congress and the courts have rejected calls to do so. A principal reason, it seems, is money. About 2% of the federal judiciary's budget comes from online record access fees ($145 million in fiscal year 2019). The judiciary is naturally unwilling to forgo this revenue without a commensurate increase from Congress, and Congress, for its part, is unwilling to increase funding. The stalemate persists because not enough judges, members of Congress, and people realize that this is an issue of legitimacy, not just an issue of money.

[1]Kellogg School of Management, Northwestern University, Evanston, IL, USA. [2]Northwestern Institute on Complex Systems, Northwestern University, Evanston, IL, USA. [3]Pritzker School of Law, Northwestern University, Evanston, IL, USA. [4]Medill School of Journalism, Northwestern University, Evanston, IL, USA. [5]Moody College of Communication, University of Texas, Austin, TX, USA. [6]Robinson College of Business, Georgia State University, Atlanta, GA, USA. [7]McCormick School of Engineering, Northwestern University, Evanston, IL, USA. Email: amaral@northwestern.edu

To break this impasse, we believe that organizations outside government should directly purchase and publicize court records. The most impactful first step is to make docket reports accessible. A docket report is essentially a lawsuit's table of contents. It lists the case title, presiding judge, subject matter of the suit, and information on the plaintiffs, defendants, and their attorneys. A docket report also gives the date that a document was filed, along with a summary of the document that can be analyzed to extract important features of a case. The data for the figure, for example, were constructed by parsing docket reports, not the underlying court records. Though docket reports represent only a fraction of all court records, acquiring them will be expensive. The docket reports used in the figure, which cover all cases filed in 2016, cost more than $100,000.

Inconsistency in judicial fee waiver decisions

Litigants filed 34,001 applications to waive court fees in U.S. federal courts in 2016. For visual simplification, we show only the 294 judges (out of 1742 total) who ruled on at least 35 applications. We would expect 5% of judges to differ from their within-district peers at 95% confidence. Instead, we find that nearly 40% of judges differ.

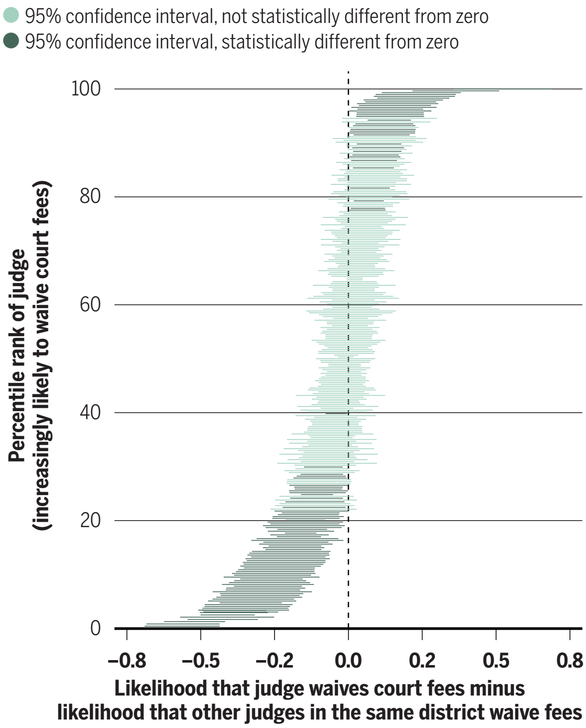

Link data in a knowledge network

Because court records are mostly unstructured text, researchers will need to dedicate extensive time and resources to organizing the data. Documents must be analyzed using natural language processing; entities must be disambiguated; and events, such as the filing of a fee waiver, must be classified using machine learning. The docket reports should also be linked to external metadata such as information on judges, litigants, and lawyers. By linking court records to outside data sources, individual users can conduct more powerful searches, such as for litigation against big tech firms or for suits currently pending against the federal government.

Although we already have solutions to many of the problems associated with organizing and classifying the data, for many more we will need additional research. For example, it is straightforward to link the presiding judge of each case to outside data on the judge's characteristics such as age, gender, and appointing president. By contrast, to assemble information about litigants and lawyers, researchers will need to make considerable progress on named-entity recognition techniques while protecting litigants' and third parties' privacy. We believe that an open and collaborative platform is the best way to make substantial and rapid progress on these challenges.

Empower the public

The ultimate goal must be to enable the public to directly evaluate and engage with the work of the courts. To this end, we should create applications that not only support scholars and researchers who may want to analyze the data but also enable members of the judiciary, entrepreneurs, journalists, potential litigants, and concerned citizens to learn more about the functioning of the courts. To support inquiries made by the public, we should develop applications that can process natural language queries such as "What are the most recent data privacy cases?" or "How often do police officers invoke qualified immunity?"

Funding the efforts we propose will be challenging because the cause does not slot nicely into standard philanthropic categories. To carry out our proposals, the academic community should partner with other stakeholders such as nongovernmental organizations, law firms, legal clinics, and other advocacy groups. Indeed, we believe that one of the main reasons why past calls for change failed is because they were not coordinated.

Opening up court records could lead to some flawed or misleading analyses, yet such problems apply to any setting with open data. No one can control what people do with congressional records, federal agency records, census data, etc. Nevertheless, these data are—and should remain—available to everyone. As in any discipline, standards and best practices eventually emerge, and there is already a thriving literature of empirical legal studies. Many scholars have engaged with these data, albeit on a smaller scale. Thus, for the most part, standards and best practices already exist (*13*).

We believe that the judiciary should be shielded from outside pressures so that it can decide cases according to the law, not the latest poll. But the judiciary also acts on behalf of the public. Its independence must therefore be balanced with commensurate transparency. Ultimately, the judiciary's principal asset is not its annual appropriation from Congress or the revenue generated by access fees, but the public trust. And the most effective way to cultivate this trust—to promote transparency, dismantle barriers to access (*14*, *15*), and build an open knowledge network—is to do it together. ■

REFERENCES AND NOTES

1. Public Access to Court Electronic Records (PACER), "PACER user manual for CM/ECF courts" (United States Courts, 2019).
2. United States Courts, Federal judicial caseload statistics 2018 (2018); www.uscourts.gov/statistics-reports/federal-judicial-caseload-statistics-2018.
3. W. Hubbard, *J. Empir. Leg. Stud*. **14**, 474 (2017).
4. J. B. Gelbach, *Yale Law J*. **121**, 2270 (2011).
5. A. Bronstad, "PACER fees harm judiciary's credibility, Posner says in class action brief," 25 January 2019; www.law.com/2019/01/25/pacer-fees-harm-judiciarys-credibility-posner-says-in-class-action-brief/.
6. L. Doggett, M. J. Mucchetti, *Tex. Law Rev*. **69**, 643 (1990).
7. H. F. Lynch *et al.*, *Science* **367**, 1078 (2020).
8. Gill v. Whitford, Transcript of oral argument at 38 and 40, no. 16-1161, 138 S. Ct. 1916 (2018).
9. J. Tashea, "France bans publishing of judicial analytics and prompts criminal penalty," *ABA Journal*, 7 June 2019; www.abajournal.com/news/article/france-bans-and-creates-criminal-penalty-for-judicial-analytics.
10. A. Hammond, *Yale Law J*. **128**, 1478 (2018).
11. Owing to the preliminary nature of discussions, the identities of courts and judges are not reported, but *Science* has confirmed this claim.
12. 28 U.S. Codes §§ 1913, 1914, 1926, 1930, 1932.
13. W. Baude *et al.*, *Univ. Chic. Law Rev*. **84**, 37 (2017).
14. A. Madison, "Team tapped to review PACER amid fee dispute (corrected)," *Bloomberg Law*, 9 January 2020; https://news.bloomberglaw.com/us-law-week/team-tapped-to-review-pacer-amid-fee-dispute.
15. A. Kragie, "Court transparency bill calls for live audio, free PACER," 2 March 2020; www.law360.com/articles/1249148.

ACKNOWLEDGMENTS

We thank K. Sanga for valuable feedback. This research was supported by a gift from John and Leslie McQuown and by the National Science Foundation Convergence Accelerator Program under grant no. 1937123. The data and code used for this article, along with full replication instructions and additional discussion of the analyses, are available at https://github.com/scales-okn/research-materials and at Zenodo (10.5281/zenodo.3905128).

10.1126/science.aba6914

GRAPHIC: X. LIU/*SCIENCE*

An aerial view of summer ice in the Canadian Beaufort Sea, adjacent to the Arctic Ocean. Here, climate change has greatly altered the icepack, making it less extensive, thinner, more dynamic, and covered with more melt ponds.

PHOTO: MARTIN FORTIER/UNIVERSITÉ LAVAL

ECOLOGY

Climate change tweaks Arctic marine ecosystems

Nutrient input might enhance productivity in the Arctic Ocean of the future

By **Marcel Babin**

Icepack reduction enhances exposure of the fairly dark Arctic Ocean (AO) to sunlight, thus promoting microalgae biomass buildup and productivity of the marine ecosystem. This seemingly reasonable assertion is a matter of lively debate centered on the function and fate of the Arctic marine ecosystem under climate change pressure. A second paradigm postulates that additional inputs of nitrogen, which is chronically low over large stretches of the AO, would be required to enable the algae to take full advantage of greater availability of light. On page 198 of this issue, Lewis *et al.* (*1*) confirm the latter notion with observations of recent biomass buildup at the AO surface that is likely driven by hydrodynamical processes that replenish essential nitrogen fuel.

The AO hosts a rich community of living organisms. From microbes to mammals, nearly all depend directly or indirectly on primary production (PP) of plant biomass by microscopic marine algae (phytoplankton). In this most polar of oceans, phytoplankton must cope with two extraordinary constraints: a roller coaster–like seasonal light cycle and a water column vertically organized into a “mille-feuille” structure. The underwater light regimen is controlled by the polar night and midnight Sun alternation as well as by sea ice, which acts as a blind on top of the AO before abruptly vanishing over most of the AO each summer. The AO vertical structure is characterized by a density gradient formed from massive inputs of lightweight fresh water from rivers and ice melts at the surface. The resulting stratification limits vertical exchanges of solutes and thus the replenishment, in the surface layer, of inorganic nutrients necessary to the growth of microalgae. This phenomenon

Takuvik International Research Laboratory, Université Laval and CNRS, Université Laval, Quebec City, QC G1V 0A6, Canada. Email: marcel.babin@takuvik.ulaval.ca

ultimately constrains the production of biomass at all levels of the food chain.

On the basis of a prior analysis of historical data, a recent study hypothesized that the annually cumulated PP in seasonally ice-free regions is determined primarily by the input of nutrients (essentially nitrate) brought to the surface through vertical mixing (*2*). Despite the increase in underwater light from shrinking sea ice, growing freshwater inputs more strongly stratify the AO. This likely will lower the nutrient supply and thus PP, unless other physical changes reverse this trend (*3*).

Ocean color can be detected from space and analyzed to estimate the concentration of chlorophyll *a* at the sea surface (a proxy for phytoplankton biomass) and the rate at which solar energy hits the AO surface. When the atmosphere is cloud free, these first-order determinants of PP, together with sea surface temperature, are monitored daily by several satellites over the entire world ocean. Such ocean color data have been available uninterruptedly since 1998.

From the late 2000s on, several studies based on ocean color data have reported a substantial increase in the annual PP of seasonally ice-free Arctic waters (*4*, *5*). Ecologists have ascribed this increase primarily to a decrease in the icepack during summer and early fall, combined with the lengthening of the ice-free season. As sea ice decreases, open waters are exposed to much more sunlight, which promotes photosynthesis and phytoplankton biomass production. It is unclear, however, how much of this increase results from new production that can be transferred to the food chain versus "useless" recycled production.

Lewis *et al.* used satellite observations of AO color to determine the response of annual PP to climate change during the past two decades, the longest Arctic PP time series available. The authors observed a progressive increase in PP that over time reached 57%, which far exceeds previous estimates. These findings confirmed the role of sea ice shrinking as a driver of PP, but only during the 1998 to 2008 period. Lewis *et al.* then showed that the increase in PP between 2009 and 2018 was driven primarily by an increase in chlorophyll *a* concentration, although the authors documented substantially different regional trends.

The standing stock of phytoplankton depends on the balance between gains from growth and losses from grazing by small animals. However, the stock also generally correlates with nutrient concentrations. A key conclusion that can be drawn from Lewis *et al.*'s study is that the budget of inorganic nutrients might be increasing rather than diminishing in specific AO sectors over the time periods studied. Nutrient input might intensify at the Pacific and Atlantic boundaries, whereas the reduction in sea ice cover might expose the AO to stronger atmospheric forcings that promote more vertical mixing.

Lewis *et al.* also found that PP did not change in several areas. Therefore, it remains unknown whether overall AO-wide PP will continue to increase if the amount of sea ice keeps shrinking. The rest of this story will stem from longer time series and a better grasp of the physical phenomena that control nutrient concentrations. Although satellite observations provide relatively long time series and a means for exploring the AO at a large scale, information from AO satellite images comes with limitations—for example, restriction to surface properties and low spatial and time resolution, especially for optical sensors in thick cloud cover. Furthermore, scales relevant to PP span millimeters to the ocean basin (spatial) and seconds to decades (time).

Satellites provide no observation under sea ice, where much occurs that is equally important to PP. Indeed, massive phytoplankton blooms were recently observed under sea ice and are thought to be more common than previously anticipated (*6*). The ongoing thinning of sea ice and increasing occurrence of melt ponds, which act as skylights at the ocean's surface in spring, might make blooms even more prevalent (*7*). Emerging approaches for capturing the various scales important to PP include autonomous sampling platforms with sensors for exploring the medium to large scales in ice-free and ice-covered waters.

Much remains to be discovered about the small scales, such as those relevant to microalgae living in the inner interstices of sea ice. To address current and future changes of PP in the AO and their effects on the marine trophic network, researchers require new devices to explore tiny components and an integrated observation system to capture and connect all relevant scales. ■

REFERENCES AND NOTES

1. K. M. Lewis, G. L. van Dijken, K. R. Arrigo, *Science* **369**, 198 (2020).
2. J. E. Tremblay et al., *Prog. Oceanogr.* **139**, 171 (2015).
3. W. K. W. Li, F. A. McLaughlin, C. Lovejoy, E. C. Carmack, *Science* **326**, 539 (2009).
4. K. R. Arrigo, G. L. van Dijken, *Prog. Oceanogr.* **136**, 60 (2015).
5. S. Bélanger, M. Babin, J.-É. Tremblay, *Biogeosciences* **10**, 4087 (2013).
6. K. R. Arrigo *et al.*, *Science* **336**, 1408 (2012).
7. K. E. Lowry, G. L. van Dijken, K. R. Arrigo, *Deep Sea Res. Part II Top. Stud. Oceanogr.* **105**, 105 (2014).

ACKNOWLEDGMENTS

M.B. thanks M. Lizotte, A. Randelhoff, J.-E. Tremblay, and M.-H. Forget for valuable editing and scientific comments.

10.1126/science.abd1231

ELECTROCHEMISTRY

Fuel cells that operate at 300° to 500°C

High-conductivity electrolytes are needed for electrochemical systems

By **Meng Ni**[1,2] *and* **Zongping Shao**[3,4]

Reducing the operating temperature of ceramic fuel cells (CFCs) from 800° to 1000°C to the 300°-to-500°C range would improve efficiency, sealing, durability, and cost while still maintaining favorable electrode reaction kinetics as compared with those of low-temperature fuel cells such as polymer electrolyte fuel cells. Developing stable electrolytes with a low ionic resistance and negligible electronic conductivity, however, is challenging. In principle, reducing the electrolyte thickness can reduce the resistance. Fabricating an ultrathin electrolyte requires advanced techniques that inevitably make mass production difficult and costly. Developing new high-conductivity electrolyte materials is another way to address this problem. On page 184 of this issue, Wu *et al.* (*1*) report a fuel cell with a distinct, high proton conductivity electrolyte.

Conventional CFCs have an oxygen-ion conducting electrolyte (OCFC) that usually operates at above 800°C to allow for fast oxygen-ion transport. Because the proton has a lower barrier for diffusion, protonic CFCs (PCFCs) are generally accepted to be more promising than conventional OCFCs for operation at reduced temperatures. In addition, because the fuel-diluting H_2O is produced in the cathode chamber of PCFCs, the expectation is for higher fuel utilization and higher theoretical performance. The authors' electrolyte consists of a Na_xCoO_2/CeO_2 composite, which shows a conductivity of 0.1 to 0.3 S cm^{-1} at 370° to 520°C. The authors believe that the proton

[1]Research Institute for Sustainable Urban Development and Research Institute for Smart Energy, Hong Kong Polytechnic University, Hong Kong SAR, China. [2]Department of Building and Real Estate, Hong Kong Polytechnic University, Hong Kong SAR, China. [3]State Key Laboratory of Materials-Oriented Chemical Engineering, College of Chemical Engineering, Nanjing Tech University, Nanjing, China. [4]WA School of Mines: Minerals, Energy, and Chemical Engineering, Curtin University, Perth, WA 6845, Australia. Email: meng.ni@polyu.edu.hk; shaozp@njtech.edu.cn

Three different proton diffusion mechanisms

Proton (H^+) transport through electrolytes is attractive for lower-temperature applications. The Grotthuss mechanism allows either an "excess" H^+ or a defect to diffuse through the hydrogen bond network of water molecules through the formation and cleavage of bonds. The vehicle mechanism allows H^+ to migrate bound to another element. An example is the formation of OH^- and an oxygen vacancy (V_o) that occurs in perovskite structured oxides. Wu *et al*. propose transport by a local electric field (LEF)–promoted diffusion mechanism in which H^+ migrates along the oxide interface. This requires an unbalanced charge distribution generated from oxygen and sodium vacancies (V_{Na}).

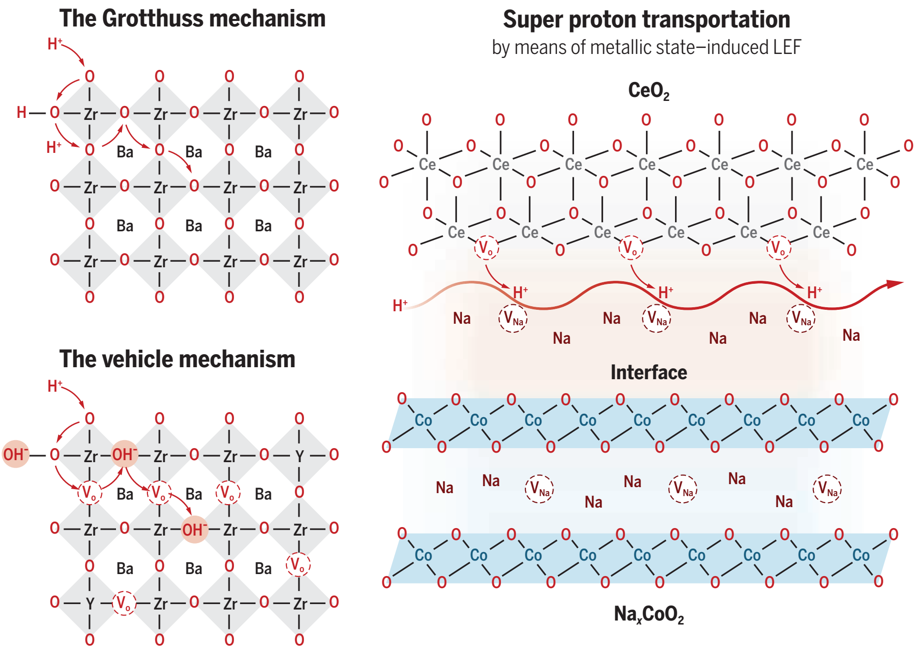

diffusion, which is different from the well-known Grotthuss and vehicle mechanisms (*2*, *3*), was confined to the Na_xCoO_2/CeO_2 heterostructure interface (see the figure). This was driven by an induced local electric field (LEF) within the interface region because of the unbalanced charge distribution between the Ce–O and Co–O layers. The authors demonstrated a cell with 400-µm electrolyte thickness that achieved peak power densities of 1000 and 830 mW cm^{-2} at furnace temperatures of 520° and 490°C. These values are substantially higher than the benchmark PCFC with a well-known thin-film $BaCe_{0.7}Zr_{0.1}Y_{0.1}Yb_{0.1}O_{3-\delta}$ electrolyte (455 mW cm^{-2} at 500°C) (*4*) and the OCFC (500 mW cm^{-2} at 550°C) (*5*).

Protonic conductors with high conductivity are also in demand for hydrogen production, electrochemical synthesis of ammonia, dehydrogenation or hydrogenation, hydrogen separation, and other applications. In the reversed operation, the PCFCs can function as protonic ceramic electrolyzer cells (PCECs) for hydrogen production through steam electrolysis (*6*). Compared with low-temperature (below 100°C) polymer-based electrolyzer cells that require a noble metal catalyst such as platinum and high electrical energy input, a nonprecious catalyst can be used for PCECs, with the required electrical energy input partially replaced by thermal energy. Thus, the reversible operation of PCFCs makes them a good candidate for storing excess renewable solar or wind power and effective for utilization of industrial waste heat.

"In the reversed operation, the PCFCs can function as protonic ceramic electrolyzer cells…for hydrogen production…"

Ammonia synthesis is a key industrial chemical process because ammonia is widely used in fertilizer and many other industries. Unlike the dominating Haber-Bosch process at a high pressure (~30 MPa) and with a low conversion (15%), protonic conductor–based electrochemical cells can synthesize ammonia at atmospheric pressure with a high hydrogen-to-ammonia conversion of 78% (*7*). Successful implementation of this technology requires protonic conductors with high conductivity and suitable catalysts with high selectivity toward ammonia synthesis.

The fuel cell properties reported by Wu *et al.* are inspiring because they offer a different strategy for the development of proton-conducting electrolyte materials. It is notable how the LEF can accelerate the hopping of the proton but not the electron. If such a mechanism is reliable, it may also be applied for the development of electrolytes with high oxygen-ion conductivity. Much more work is still needed to realize the practical application of the authors' device. The composite electrolytes were developed by means of dry pressing without high-temperature sintering, which may make the electrolytes porous. Direct oxidation of fuel by oxygen gas through the pores will reduce the overall fuel efficiency (*8*). The metastability of Na_xCoO_2 under a hydrogen atmosphere is another concern. The reduction of this compound will lead to the formation of metallic cobalt and NaO. The NaO could further react with water to form NaOH. This compound itself has a low melting point of 318°C, and molten NaOH can conduct OH^- at the fuel cell's operating temperature of 370° to 520°C.

The electrode that the authors developed is rich in cobalt and nickel oxides, and both of these compounds are widely used as electrodes in conventional alkaline fuel cells. Additional comprehensive studies will help illuminate the processes involved in the fuel cell operation. An evaluation of the long-term stability of the cell is important for determining whether there is a viable pathway to commercialization.

Different cathode and anode materials are needed for improving highly efficient PCFCs that operate in the 300° to 500°C range. For example, sulfur deposits and coke can build up on anode materials, so developing materials that are resistant to these processes will improve performance and durability. Water produced at the cathode side is especially harmful because it may impede the oxygen reduction over the cathode of PCFCs. Solving these sorts of problems should lead to the successful application of protonic conductors with high conductivities in PCFCs and other relevant electrochemical systems. ■

REFERENCES AND NOTES

1. Y. Wu *et al.*, *Science* **369**, 184 (2020).
2. H. Wang *et al.*, *J. Ind. Eng. Chem.* **60**, 297 (2018).
3. C. Zhou *et al.*, *J. Mater. Chem. A* **7**, 13265 (2019).
4. C. Duan *et al.*, *Science* **349**, 1321 (2015).
5. T. Suzuki *et al.*, *Science* **325**, 852 (2009).
6. L. Lei *et al.*, *Adv. Funct. Mater.* **29**, 1903805 (2019).
7. G. Marnellos, M. Stoukides, *Science* **282**, 98 (1998).
8. H. Xu *et al.*, *J. Power Sources* **440**, 227102 (2019).

ACKNOWLEDGMENTS

M.N. is thankful for the grants (project nos. PolyU 152214/17E and PolyU 152064/18E) from the Research Grant Council, University Grants Committee, Hong Kong SAR.

10.1126/science.abc9136

GRAPHIC: KELLIE HOLOSKI/*SCIENCE*

LITHIUM BATTERIES

Reining in dissolved transition-metal ions

Approaches are needed for stabilizing transition metals in lithium-ion battery cathodes

By **Hooman Yaghoobnejad Asl** *and* **Arumugam Manthiram**

With an increasing deployment of large-size lithium-ion batteries (LIBs) for applications beyond consumer electronics, critical questions surround their life span and safety. The LIB technology is based on oxide cathodes and graphite anodes developed in the 1980s (*1*). The current ~350 cycle-life warranty (based on 100,000 miles and 300-mile range per full charge) (*2*) provided by major electric vehicle manufacturers falls short of the 1000 cycle-life target sought by the U.S. Department of Energy (*3*). As a result, a major focus has been to understand the fundamental factors that cause the degradation of LIBs. Among them, dissolution of transition-metal (TM) ions from the cathode into the liquid electrolyte has been recognized as a leading cause. We discuss the causes of the dissolution of certain metal ions from the cathode into the electrolyte, including the possible role of electronic structure.

A typical commercial lithium-ion cell has a lithiated TM oxide (TMO) cathode (positive electrode), such as $Li(Ni_{1/3}Co_{1/3}Mn_{1/3})O_2$. These cathodes are variants of the very stable but expensive $LiCoO_2$ cathode in which some of the Co is replaced with less costly TMs. The challenge is that these replacement TM cations tend to dissolve into the liquid electrolyte and migrate and deposit on the graphite anode. Once there, they increase the solid-electrolyte interphase (SEI) layer thickness on graphite, trap cyclable lithium in the SEI, and raise the cell impedance, thereby limiting the cell cycle life (*4*, *5*). The thicker SEI on the graphite anode also promotes lithium dendrites, which can result in fire and safety hazards.

The problem of TM-ion dissolution is aggravated by the cathode chemistries that involve Jahn-Teller (J-T) distorted TM ions and can be attributed to trace amounts of hydrofluoric acid (HF) generated in the electrolyte. For example, metal dissolution is substantially higher for cathode compositions containing the J-T–active Mn^{3+} ions (*6*, *7*). This finding raises the issue of delineating the complex chemistry involving the H^+ acidic species, J-T distortion of TMOs, and the enhanced TM-ion dissolution observed.

The electronic structure of TM cations is modified by J-T distortion. Most of the TM cations in TMOs adopt an aggregation of six oxide ligands arranged symmetrically along the Cartesian axes, giving rise to an octahedral (O_h) coordination (see the first figure, left). The O_h ligand electric field separates the d orbitals of the TM cation into triply degenerate t_{2g} (d_{xy}, d_{xz}, and d_{yz}) and doubly degenerate e_g (d_{z^2} and $d_{x^2-y^2}$) sets. This arrangement is preferred for TM cations that have a cubically symmetric electron density that is achieved when the e_g orbital set is completely filled, half-filled, or empty (for example, $t_{2g}^3\,e_g^0$, $t_{2g}^3\,e_g^2$, and $t_{2g}^6\,e_g^0$).

However, for certain TM cations, including high-spin Mn^{3+}, high-spin Fe^{4+}, and low-spin Ni^{3+}, the electron density follows a noncubic distribution as a result of the single occupancy of the doubly degenerate e_g set (for example, e_g^1). This unfavorable state is relaxed according to the J-T theorem by an elongation of two axial TM–O bonds and a shrinkage of the other four equatorial ones, which reduces the TMO_6 symmetry from cubic to tetragonal (see the first figure, right). Note that the $Co^{3+/4+}$ (high-spin or low-spin) ions in the commonly used $LiCoO_2$ cathode (Co^{3+}: $t_{2g}^6\,e_g^0$; Co^{4+}: $t_{2g}^5\,e_g^0$) in LIBs avoid the problematic e_g^1 electronic state and resulting metal-ion dissolution and help account for their successful implementation in first-generation LIBs.

The J-T effect can vary in strength with a global, macroscopic distortion of the crystal structure, as is the case often with Mn^{3+}, or a local, microscopic distortion, as is usually observed with TMOs with Ni^{3+} and Fe^{4+}. In the local distortion case, the individual TM–O bond lengths may vary without affecting the average macroscopic structure, which leads to a dynamic lattice instability. The strength of J-T distortion also correlates inversely with the covalency of TM–O bonds, which increases in the order $Mn^{3+} < Ni^{3+} < Fe^{4+}$ because of an increase in the effective nuclear charge (Mn < Fe < Ni) combined with a higher formal charge on Fe^{4+}. Thus, the local J-T distortion in TMOs with dynamic lattice instability also makes them reactive enough toward acidic species and susceptible to TM-ion dissolution.

Understanding how J-T distortion, whether global or local, can cause TM-ion dissolution in acidic electrolytes can be addressed best through molecular orbital (MO) considerations. The axial-equatorial splitting of TM–O bonds alters the degree of overlap of the atomic orbitals of TM cations and O ligands. The e_g^1 electronic configuration (e.g., $d_{z^2}^1\,d_{x^2-y^2}^0$) allows the empty $d_{x^2-y^2}$ or-

Jahn-Teller (J-T) distortions

The ligand field in manganese oxides used in lithium-ion battery cathodes distorts the six equivalent metal-oxygen bonds (left) into two longer axial bonds and four shorter equatorial bonds (right). Charge is transferred from the metal cation to the axial oxygens, which become more basic.

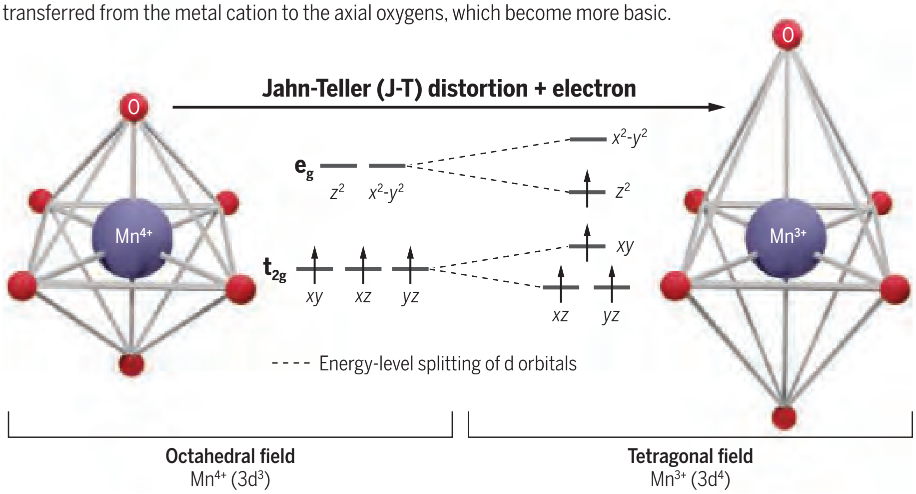

GRAPHIC: A. KITTERMAN/SCIENCE

Materials Science and Engineering Program and Texas Materials Institute, University of Texas at Austin, Austin, TX 78712, USA. Email: manth@austin.utexas.edu

bital to overlap strongly with the four filled 2p orbitals of the oxide ligand-group in the equatorial *x-y* plane, yielding four σ-bonding orbitals that are predominantly oxygen in character. However, the half-filled $d_{z^2}{}^1$ orbital, oriented along the *z* axis, overlaps weakly with the two filled 2p orbitals of the oxide ligand group along the same axis. This case leads to the formation of a low-energy axial σ-bonding orbital filled with oxide electrons and a high-energy axial σ-antibonding orbital half-filled with the d_{z^2} single electron.

The longer axial TM–O bonds with a weaker overlap are more ionic compared to the shorter, more covalent equatorial TM–O bonds, resulting in a higher negative charge on the axial oxygen atoms with a more basic character from a Lewis acid-base perspective. Thus, J-T distortion induces higher reactivity with acid and increased TM-ion dissolution in LIBs in two ways: It places an electron into the $d_{z^2}{}^1$ orbital, and the electron is delocalized over the TM and O atoms; and it enhances the Lewis-base strength of the axial oxygens compared to the equatorial oxygens.

Given this background, we can now address how the presence of acid leads to metal-ion dissolution in LIBs from TMOs with J-T ions. The hydrolysis of the $LiPF_6$ salt in the electrolytes of LIBs by residual moisture generates the strong Lewis acid HF, whose H^+ ions interact exclusively with the axial oxygens, which are the stronger Lewis bases, at the cathode-electrolyte interface (see the second figure, top). The acid-base interaction may lead to the formation of H_2O, through oxide protonation. However, this cannot happen independently, as the oxygens in the TMO have less negative charge compared to the oxygen in H_2O because of the higher covalency of TM–O bonds compared to the H–O bonds.

The formation of H_2O by the protonation of the TMO oxides requires a net electron transfer from the TMO to the axial oxide orbital. This charge transfer originates from the $d_{z^2}{}^1$ orbital of the TMO that contains the most reactive electron. Thus, protonation of the axial oxide ion and formation of H_2O are accompanied by a simultaneous metal-to-ligand electron transfer that leaves the TM with a higher oxidation state (see the second figure, bottom). These as-formed TM cations (Mn^{4+}, Fe^{5+}, and Ni^{4+}) are strong oxidizers that reduce back directly to the stable, J-T free state (Mn^{2+}, Fe^{3+}, and Ni^{2+}) through a two-electron reduction pathway by oxidizing electrolyte solvent molecules into CO_2 and other reactive protic species (*8*, *9*). These stable, lower-valence TM oxides and fluorides tend to readily dissolve into the electrolyte. In turn, the as-formed water molecule can further react with the $LiPF_6$ salt to generate more HF, creating a closed-loop cycle whose net effect is the destruction of the electrolyte salt and solvent, the cathode and the anode.

The problem of proton-induced oxidation of TMOs extends to various degrees to other TMOs beyond Mn^{3+} that contain J-T–active ions. For example, the oxidation of TM to higher states under protic environments has been observed in $LiMn^{3+}Mn^{4+}O_2$, $LiNi^{3+}O_2$, and $Na_4Fe^{4+}O_4$ (*10–12*), where Mn^{3+}, Ni^{3+}, and Fe^{4+} are J-T–active ions. Despite the fundamental reactivity of J-T–active ions, oxides containing Ni, Fe, and Mn offer the advantage of abundance and low cost compared to Co, which is beneficial to the mass production of batteries.

To reduce metal-ion dissolution, current research efforts are focused on two fronts. On an engineering level, surface coating of the electrodes by passive layers has been used to minimize direct electrode-electrolyte contact (*13*), but at the expense of increased cell resistance. On a chemistry level, the uneven electron density of the J-T–active TM ions has been diluted through ionic-doping and defect introduction strategies (*7*). For exmaple, the doping strategy can be executed by incorporating electrochemically inactive, J-T free Mn^{4+} in the $LiNi_{1-x-y}Co_xMn_yO_2$ series cathodes and a consequent reduction of an equivalent amount of Ni^{3+} to J-T free Ni^{2+} (*4*).

In parallel to the above cathode-level remedies, other cell-level measures can also be invoked to limit the extent of the acid-base reaction. For example, the electrolyte salt anion can be replaced with bis(trifluoromethane)sulfonimide [TFSI, $(CF_3SO_2)_2N^-$], in which the covalent C–F bonds are not prone to hydrolysis, unlike the highly polar P–F bonds as in the PF_6^- anion. Also, apart from the native moisture present, the anodic decomposition of electrolyte solvents on the cathode at the high applied charging potentials serves as a second source of protic species (*14*). Thus, limiting the charging potential, introduction of additives that can scavenge the H^+ byproduct, increasing the solvent-system anodic decomposition potential threshold, or decreasing the kinetics of such reactions may all be pursued to achieve the promise of long–cycle-life rechargeable batteries. ■

How electrolytes affect cathodes

The J-T distortion of Mn^{3+} cations makes it susceptible to dissolution from acid formed from the electrolyte attacking basic axial oxygens.

Acid generation

The hydrolysis of the $LiPF_6$ salt and generation of HF with the electrolyte solvent releases Mn^{2+} ions into the electrolyte.

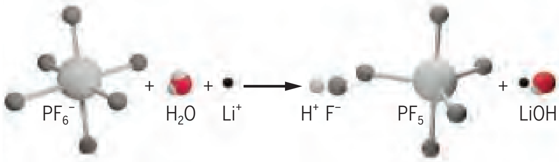

Ion dissolution

The partial structure of a J-T–active Mn^{3+} oxide at the solid surface, with the highest occupied molecular orbital with appreciable d_{z^2} character, is shown for one of the TMO_6 units superimposed.

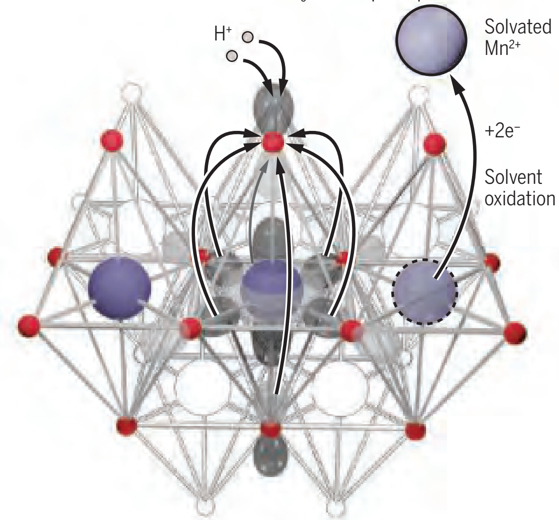

Nucleophilic attack by the axial oxide on two protons (H^+) in the electrolyte transfers electrons from the $d_{z^2}{}^1$ orbital of the manganese to oxygen. This process forms water and causes oxidation of the Mn^{3+} to Mn^{4+}.

GRAPHIC: A. KITTERMAN/*SCIENCE*

REFERENCES AND NOTES

1. A. Manthiram, *Nat. Commun*. **11**, 1550 (2020).
2. D. Sperling, A. Brown, Long Live Batteries (2018); www.forbes.com/sites/danielsper-ling/2018/08/30/long-live-batter-ies/#488060e4e98a.
3. Advanced Batteries 2016 Annual Progress Report (2017); www.energy.gov/sites/prod/files/2018/03/f49/FY2016_APR_Advanced_Batteries_R%26D_Part-1of5-opt.pdf.
4. J. Li, A. Manthiram, *Adv. Energy Mater*. **9**, 1902731 (2019).
5. C. Zhan *et al*., *Nat. Commun*. **4**, 2437 (2013).
6. D. H. Jang, *J. Electrochem. Soc*. **143**, 2204 (1996).
7. W. Choi, A. Manthiram, *J. Electrochem. Soc*. **153**, A1760 (2006).
8. L. Xing, O. Borodin, *Phys. Chem. Chem. Phys*. **14**, 12838 (2012).
9. A. Wuersig, W. Scheifele, P. Novák, *J. Electrochem. Soc*. **154**, A449 (2007).
10. J. C. Hunter, *J. Solid State Chem*. **39**, 142 (1981).
11. H. Arai, Y. Sakurai, *J. Power Sources* **81–82**, 401 (1999).
12. P. Novak *et al*., *Phys. Chem. Chem. Phys*. **20**, 30247 (2018).
13. K. T. Lee, S. Jeong, J. Cho, *Acc. Chem. Res*. **46**, 1161 (2013).
14. N. P. W. Pieczonka *et al*., *J. Phys. Chem. C* **117**, 15947 (2013).

ACKNOWLEDGMENTS

This work was supported by the Welch Foundation (grant F-1254).

10.1126/science.abc5454

ECOLOGY

Bats navigate with cognitive maps

Tagging and tracking systems reveal the way-finding strategies of fruit bats

By **M. Brock Fenton**

A cognitive map can allow an animal to navigate from its current position to an undetected goal. There is a long-standing, ongoing debate about which animals have and use cognitive maps (*1*–*3*). On pages 188 and 194 of this issue, Toledo *et al*. (*4*) and Harten *et al*. (*5*), respectively, show that Egyptian fruit bats (see the figure) use cognitive maps, as evidenced by taking previously unused shortcuts. These are movements between two known sites that are beyond detectable range of one another. Shortcuts are strong evidence of cognitive maps.

Toledo *et al*. used ATLAS, a new high-throughput tracking system, to document the travels and home ranges of 172 tagged Egyptian fruit bats over 3449 bat-nights across 4 years. Each tag weighed 4 g (<4% of the animal's body mass) and provided over 18 million localizations. The ATLAS system simultaneously tracked dozens of animals with high resolution and accuracy. Using direct observations and translocation experiments, Toledo *et al*. showed that to get to fruit trees, tagged bats repeatedly used goal-directed, long, straight flights rather than random searches. Tagged bats also commonly took shortcuts to go directly to fruit trees. The researchers used trajectory analyses and time-lag embedding to rule out nonmap strategies. Their analyses revealed that the tagged bats did not systematically follow known routes, nor did they directly sense cues such as landmarks or beacons. These animals relied on a cognitive map frame of reference for their current positions in relation to a goal that they had not yet detected. Some Egyptian fruit bats have home ranges of over 100 km^2, and earlier research revealed that tagged animals typically flew directly (in a straight line) to specific fruit trees within their home ranges (*6*). But, as Toledo *et al*. cautioned, they lack data about the early experience of the animals that they tracked.

Harten *et al*. addressed this shortcoming by establishing an in-house colony of Egyptian fruit bats on campus. By day, bats in the colony roosted on site and, at night, freely foraged in the surrounding area. The researchers collected data using continuous Global Positioning System tags (0.99 g, or 0.42 g) affixed to the bats. Tag readers in the roost and at nearby sites downloaded data about the bats' comings and goings and their specific routes. Harten *et al*. focused on data from the flights of 22 Egyptian fruit bat pups from their initial flights outdoors through the first months of their lives. These bats gradually increased the sizes of their home ranges, after 70 days reaching typical adult areas of 60 km^2. Over time, after feeding at local trees within their home ranges, young animals sometimes made exploratory flights that involved going well beyond their normal home ranges before returning to the roost.

Egyptian fruit bats (*Rousettus aegyptiacus*) range widely from South Africa north to Turkey, developing shortcuts to fruit trees where they feed.

Young bats also took shortcuts, identified by conservative criteria. To be considered a shortcut, at least 50% of the trajectory of a movement had to be original, and the destination at least 100 m from any other site the bat had previously visited. These stringent criteria reduced the numbers of recorded shortcuts.

Like other bats, Egyptian fruit bats are long-lived (often over 20 years in the wild), have low reproductive output (usually one young per litter), large neonate size (25% of mother's mass), and often roost in social groups (*7*, *8*). Adult masses range from 80 to 170 g, making them well suited for work involving relatively large tags. Advances in the capacity of tags, such as those used in either study, have greatly increased our knowledge of bats. Further embellishments involve tags that record video and audio from free-flying bats (*9*). In addition, proximity tags (*10*) provide new insight into social interactions of bats. Researchers have used active tags on bats for over 50 years, typically keeping tag size to <5% of bat body mass (*11*). Yet, most of the ~1400 species of bats weigh <50 g as adults, putting many, if not most, beyond the range of current tag technology (*12*). Documenting the home ranges of bats will prove central to their conservation, which might mean setting aside and protecting larger areas.

The hallmarks of these two groups of researchers include innovative use of tags, thorough and consistent analyses, and demanding criteria, as well as exhaustive long-term field work and strong collaborations. Their results convincingly show that Egyptian fruit bats navigate using cognitive maps. Together, both studies (*4*, *5*) advance our knowledge and understanding of cognitive maps and open the door to learning how widespread this cognitive behavior may be among animals. Further advances in tag technology will expand our knowledge of how bats learn their home ranges, from nursery colonies to hibernation sites. Such developments will put other findings in broader perspective such as bats' use of food resources with predictable distribution in space and time. Details about social organization and interactions also can further elucidate bats' roles as disease vectors (*13*, *14*). ■

Department of Biology, The University of Western Ontario, London, Ontario, Canada. Email: bfenton@uwo.ca

REFERENCES AND NOTES

1. E. C. Tolman, *Psych. Rev*. **55**, 189 (1948).
2. D. R. Griffin, Animal Minds (Univ. of Chicago Press, 1992).
3. M. Geva-Sagiv, *et al*., *Nat. Rev. Neurosci*. **16**, 94 (2015).
4. S. Toledo *et al*., *Science* **369**, 188 (2020).
5. L. Harten *et al*., *Science* **369**, 194 (2020).
6. A. Tsoar *et al*., *Proc. Natl. Acad. Sci. U.S.A*. **108**, E718 (2011).
7. G. Kwiecinski, T. Griffiths, *Mamm. Species* **611**, 1 (1999).
8. R. Cohen, Rousettus aegyptiacus , Animal Diversity Web. accessed 2 June 2020; https://animaldiversity.org/accounts/Rousettus_aegyptiacus/ (2011).
9. L. Stidsholt *et al*., *Methods Ecol. Evol*. **10**, 48 (2019).
10. S. P. Ripperger *et al*., *Curr. Biol*. **29**, 1 (2019).
11. H. D. J. N. Aldridge, R. M. Brigham. *J. Mammal*. **69**, 379 (1988).
12. M. B. Fenton, N. B. Simmons, *Bats: A World of Science and Mystery* (Univ. of Chicago Press, 2015).
13. K. M. Bakker *et al*. *Nat. Ecol. Evol*. **3**, 1697 (2020).
14. M. B. Fenton *et al*., *Nat. Ecol. Evol*. **4**, 517. (2020).

10.1126/science.abd1213

PHYSIOLOGY

Exploring the source of human brain fluids

Human organoid cultures can be used to probe secretion and drug permeability into and out of the brain

By **Violeta Silva-Vargas** *and* **Fiona Doetsch**

The cerebrospinal fluid (CSF) is an optically clear but molecularly complex liquid that flows within the brain ventricles. It cushions the brain and delivers nutrients and signaling molecules while removing others. The CSF is produced by the choroid plexus (ChP), an understudied epithelial barrier that regulates the entry of factors from the blood into CSF and is also highly secretory. As a central hub with multiple functions, the ChP is emerging as a key contributor to normal brain physiology and disease (*1*). A lack of tools has limited exploration of the ChP, especially in humans. On page 159 of this issue, Pellegrini *et al*. (*2*) establish human ChP organoids, three-dimensional multicellular in vitro structures. They form compartments filled with a CSF-like fluid and exhibit functional barrier and secretion properties, resembling those in vivo. They are a powerful tool to predict drug permeability and investigate ChP secretion and cell diversity.

The CSF is a complex and dynamic milieu whose composition changes at different stages of development, in adulthood and with aging, as well as in different physiological states (*1*, *3*, *4*). CSF composition even varies diurnally in adults. A variety of biologically active moieties—including signaling and growth factors, hormones, lipoproteins, neurotransmitters, extracellular matrix, and extracellular vesicles—are present in the CSF (*1*, *3*). The ChP is a key, though not exclusive, source and transport route of factors in the CSF. The ChP and CSF together form a highly tuned flowing milieu integrating the delivery of local and long-range factors that affect processes, including stem cell proliferation, during development and adulthood, as well as neural circuit plasticity and brain physiology (*1*, *3*, *5*–*8*).

Biozentrum, University of Basel, 4056 Basel, Switzerland.
Email: fiona.doetsch@unibas.ch

GRAPHIC: V. ALTOUNIAN/*SCIENCE*

The ChP is a highly vascularized structure anchored to the wall of the brain ventricle and floating in the CSF, with multiple key functions (*1*, *4*, *9*). It consists of a single outer epithelial cell layer surrounding an inner layer with fenestrated blood vessels, multiple stromal cell types, and surveilling immune cells (*1*). Cuboidal choroidal epithelial cells are highly polarized. Their apical side contains many villi and/or cilia and contacts the CSF. They are interconnected by tight junctions, forming the blood-CSF barrier, and tightly regulate access of factors from the blood into the CSF (see the figure). Choroidal epithelial cells are metabolically active and a key site for synthesis and modification of numerous polypeptides and detoxification of metabolites from the CSF. They are highly secretory, with large numbers of multivesicular bodies. Although epithelial cells are the major source of secreted factors in vivo, all ChP cell types can contribute to the CSF.

The multifunctional choroid plexus

A choroid plexus (ChP) is found in each brain ventricle and makes the cerebrospinal fluid (CSF). Chorodial epithelial cells are interconnected by tight junctions to form the blood-CSF barrier. Other ChP functions include secretion, detoxification, and immune surveillance.

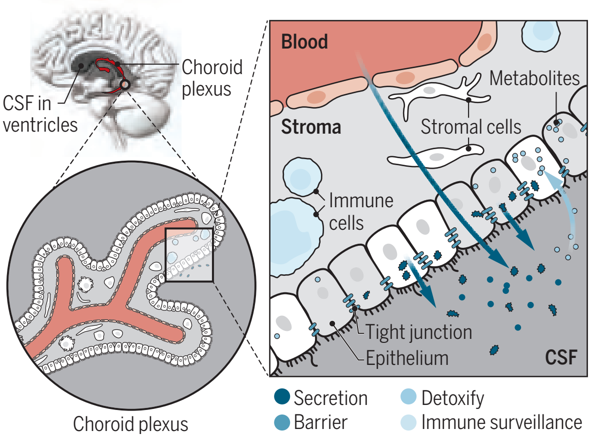

Two-dimensional cultures of primary and embryonic stem cell–derived choroidal epithelial cells have provided important insight into ChP function. Organoids are self-organizing, three-dimensional structures, which more completely capture tissue complexity (*10*). ChP tissue has previously been induced in brain organoids (*11*). Pellegrini *et al.* have developed a protocol for the robust generation of human ChP organoids from pluripotent embryonic stem cells that contain polarized epithelial cells, with tight junctions that develop barrier properties and secrete a clear liquid that resembles in vivo CSF into a self-contained compartment. A key issue for all organoid systems is which developmental stage they model and how mature the cells become. Single-cell RNA sequencing and characterization of the ChP organoids revealed progressively mature epithelial cells and increasing numbers of stromal cells in older organoids that resemble the cellular organization and molecular profiles of in vivo human ChP tissue. Likewise, proteomics of the CSF-like fluid over time showed that the organoid CSF composition underwent a progressive maturation to postnatal stages.

A major challenge in medicine is to deliver drugs to the brain, owing to the blood-CSF and blood-brain barriers. The blood-CSF barrier in the ChP is a highly regulated system, allowing the selective transport or passage of key macromolecules and small molecules (*9*). The human ChP organoids reported by Pellegrini *et al.* display barrier properties that predict drug permeability. Sampling the CSF-like fluid after exposing the organoids to different drugs in the medium revealed that the system recapitulates the (in)ability of known compounds, including antidepressants and chemotheraputic agents, to cross the barrier and showed the accumulation in organoid fluid of a preclinical drug that induced neurotoxicity in patients. Thus, ChP-CSF organoids may be a powerful screening platform for assessing and predicting blood-CSF drug permeability in humans.

Morphologically, light and dark epithelial cells have been described in vivo by electron microscopy (*12*). Single-cell RNA sequencing of human ChP organoids identified multiple epithelial cell subtypes with distinct molecular signatures: light and dark cells, which Pellegrini *et al.* show are enriched in ciliary versus mitochondrial genes, respectively, and an undescribed population of myoepithelial cells, which are contractile cells found in other secretory organs. These subtypes of epithelial cells showed differences in their secretory profiles. Future characterization of the stromal cells found in the organoids and the addition of other cell types such as immune cells

to ChP organoids will allow further dissection of different ChP compartments and their cross-talk. ChP organoids will thus be an attractive system to investigate the secretome of different choroidal cells and to identify human-specific and evolutionarily conserved signaling factors. The ChP is also an important contributor to disease. A further translational application will be the generation of ChP organoids from induced pluripotent stem cells from individual patients to investigate links between specific mutations and ChP dysfunction.

An exciting next step is to probe the functional implications of ChP epithelial cell hetereogeneity, and of other ChP cell types, including their in vivo distribution and whether there are regional differences between different brain ventricles, which differ in their secretomes (*3*). Choroidal epithelial cells may be specialized for different functions, given their many roles in vivo, and use different modes of secretion. The challenge now is to unravel how the functions of each choroidal cell type are regulated by different inputs to the ChP. Indeed, the ChP lies at the interface of blood and the central nervous system and is therefore singularly poised to sense and integrate signals from the periphery as well as the brain and to dynamically adapt its secretome in different physiological states of homeostasis and disease. It is an exciting time in the field to discover how this system is orchestrated and dynamically participates in brain function. ■

"A major challenge in medicine is to deliver drugs to the brain, owing to the blood-CSF and blood-brain barriers."

REFERENCES AND NOTES

1. J. F. Ghersi-Egea *et al.*, *Acta Neuropathol.* **135**, 337 (2018).
2. L. Pellegrini *et al.*, *Science* **369**, eaaz5626 (2020).
3. R. M. Fame, M. K. Lehtinen, *Dev. Cell* **52**, 261 (2020).
4. F. Marques *et al.*, *Neurobiol. Dis.* **107**, 32 (2017).
5. V. Silva-Vargas *et al.*, *Cell Stem Cell* **19**, 643 (2016).
6. M. K. Lehtinen *et al.*, *Neuron* **69**, 893 (2011).
7. K. Baruch *et al.*, *Science* **346**, 89 (2014).
8. J. Myung *et al.*, *Nat. Commun.* **9**, 1062 (2018).
9. N. R. Saunders, K. M. Dziegielewska, K. Møllgård, M. D. Habgood, *J. Physiol.* **596**, 5723 (2018).
10. T. Takebe, J. M. Wells, *Science* **364**, 956 (2019).
11. H. Sakaguchi *et al.*, *Nat. Commun.* **6**, 8896 (2015).
12. G. J. Dohrmann, P. C. Bucy, *J. Neurosurg.* **33**, 506 (1970).

ACKNOWLEDGMENTS

F.D. is supported by European Research Council (ERC) Advanced Grant NeuroStemCircuit, Swiss National Science Foundation Grant 31003A_163088, and the University of Basel. We thank D. Thaler for comments.

10.1126/science.abd0269

PHYSIOLOGY

Exercising your mind

A circulating factor induced by exercise contributes to keeping the brain young in mice

By **Victor A. Ansere**[1] *and* **Willard M. Freeman**[2,3,4]

Although the beneficial effects of exercise on the brain and cognition are generally accepted, the mechanisms by which physically active people remain mentally sharp later in life have been unclear. On page 167 of this issue, Horowitz *et al.* (*1*) demonstrate that the beneficial effects of exercise in mitigating brain aging can be conveyed from exercising mice to sedentary mice through plasma transfer. The authors also provide compelling evidence that the positive effects of exercise on brain aging are at least partially mediated through hepatic mechanisms and identify a promising target for further study.

The economic, social, and health consequences of the growing aged population are profound, thus necessitating interventions that promote healthy aging. Interventions to maintain health later into life, such as rapamycin (*2*) and caloric restriction (*3*), have been reported to improve memory and cognition in animal models but are challenging to translate to humans. Approaches such as heterochronic parabiosis (the surgical joining of young and aged animals resulting in plasma exchange) or heterochronic plasma transfer by infusion have gained considerable attention and also offer great promise in rejuvenating the aged hippocampus in mice (*4*). However, regular physical exercise is arguably the most consistently effective health-enhancing strategy to attenuate the age-related deterioration in brain structure and function in laboratory animals and humans (*5*). Using exercise to probe the mechanisms of brain aging could also identify new therapeutic avenues for the maintenance of brain health throughout life.

Horowitz *et al.* transferred plasma from regularly exercising adult or aged mice to aged sedentary mice. This increased the formation of new hippocampal neurons, increased the concentrations of neurotrophic factors, and improved cognition in behavioral tests of the sedentary mice. Potential circulating factors responsible for this effect were identified by a plasma proteomic screen. Among these, the authors found that the glycosylphosphatidylinositol-specific phospholipase D1 (GPLD1), a protein abundant in the liver, was induced by regular exercise in mice. Higher plasma GPLD1 concentrations were also observed in physically active older people (ages 66 to 78) compared to inactive older people. Furthermore, induction of GPLD1 specifically in the mouse liver through in vivo transfection was sufficient to recapitulate the rejuvenative effects of exercise in sedentary mice.

GPLD1 hydrolyzes the inositol phosphate linkage in glycosylphosphatidylinositol (GPI) that anchors proteins to membranes, releasing them into the circulation. Horowitz *et al.* found that this activity of GPLD1 was necessary for the improved cognition and increased hippocampal neurogenesis observed after GPLD1 induction in vivo. Intriguingly, neither liver nor circulating GPLD1 concentrations were found to decline with age, and GPLD1 did not appear to enter the brain from the circulation. This suggests that the beneficial effects of GPLD1 on the hippocampus may involve intermediary factors that are released by peripheral organs and are capable of entering the brain to act directly on the hippocampus (see the figure). This concept is supported by studies such as those that demonstrated the induction of muscle peroxisome proliferator–activated receptor–γ coactivator 1α (PGC-1α) by exercise, which ultimately results in increased circulating concentrations of irisin, a myokine that acts directly on the brain (*6*, *7*). Therefore, determining tissue-level targets of circulating GPLD1 as well as the resultant alterations in circulating factors that can cross the blood-brain barrier is crucial to understanding the direct mechanism of action on the brain. Horowitz *et al.* identified coagulation and complement signaling cascades as possible intermediary factors mediating the effects of GPLD1; however, additional investigation is required to fully understand their role.

These findings integrate with the myriad effects of exercise across organ systems that may mediate the positive effects on brain aging (*8*). After exercise, circulating myokines

[1]Department of Physiology, University of Oklahoma Health Sciences Center, Oklahoma City, OK, USA. [2]Genes and Human Disease Program, Oklahoma Medical Research Foundation, Oklahoma City, OK, USA. [3]Oklahoma City Veterans Affairs Medical Center, Oklahoma City, OK, USA. [4]Department of Biochemistry and Molecular Biology, University of Oklahoma Health Sciences Center, Oklahoma City, OK, USA. Email: bill-freeman@omrf.org

The combined benefits of exercise on the aged brain

Exercise may directly affect the brain or involve a myriad of tissues, including the liver, muscle, and adipose tissue. Horowitz *et al*. demonstrate that exercise-induced glycosylphosphatidylinositol-specific phospholipase D1 (GPLD1) from the liver mediates improved cognition in mice. GPLD1 hydrolyzes glycosylphosphatidylinositol (GPI) linkages that anchor proteins to membranes, releasing them into the circulation. Which proteins are released and how this connects with other exercise-induced factors is unknown.

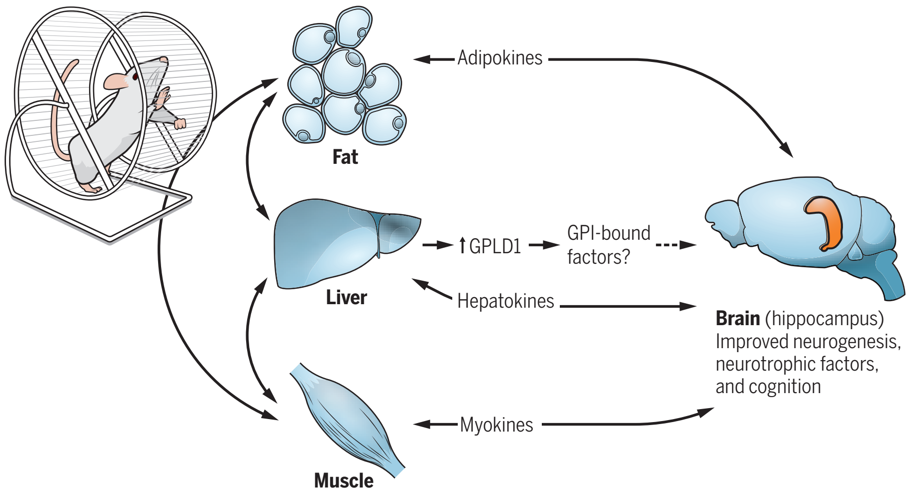

GRAPHIC: V. ALTOUNIAN/*SCIENCE*

from skeletal muscle (*9*), liver hepatokines (*10*), fat-derived adipokines (*11*), exosomes (a type of extracellular vesicle) (*12*), and metabolites are altered. These factors may work not only directly on the brain but also, as exemplified in the work of Horowitz *et al.*, through extensive tissue cross-talk. Because exercise has such complex effects, systems biology approaches will be necessary to unravel the intricacies of how exercise contributes to cognitive function (*13*).

Although hippocampal neurogenesis and behavioral outcomes were tested in mice by Horowitz *et al.*, the increase of GPLD1 also needs to be tested against other hallmarks of brain aging, including neuroinflammation, synapse pruning, and neurophysiological deficits that have also been shown to cause age-associated cognitive decline (*14*). Studies using GPLD1 in mouse models of neurodegenerative disorders such as Alzheimer's disease may also be warranted.

The observation that GPLD1 was increased in exercised mice as well as in physically active humans underlines the robustness of this finding and the potential for future translational studies. The ability to transfer the functional benefits of exercise through plasma adds to current interest in plasma rejuvenation as an intervention to delay or reverse aspects of the aging process. However, the safety and ethical concerns inherent in provision and access to plasma remain to be addressed. These findings also correspond to a prior report that showed the inverse—that the negative effects of age and peripheral muscle injury could be transferred between mice by plasma transfer (*15*). Generally, exercise is thought to prevent only age-associated changes, but an important insight from the study of Horowitz *et al.* is that exercise also has a rejuvenating effect. This emphasizes the importance of understanding how exercise has broad and advantageous effects on aging. Future studies will need to determine the intensity, duration, and frequency of exercise needed to engage these beneficial effects, particularly in humans. Whether these are acute effects of exercise or the result of chronic activity (the mice had running wheels for >40 days) is a central question to be answered. These findings, along with ongoing clinical studies, should help to provide the public with evidence-based knowledge to guide their own physical activity to promote healthy brain aging. ■

REFERENCES AND NOTES

1. A. M. Horowitz *et al.*, *Science* **369**, 167 (2020).
2. A. Richardson *et al.*, *Exp. Gerontol.* **68**, 51 (2015).
3. N. Pitsikas, S. Algeri, *Neurobiol. Aging* **13**, 369 (1992).
4. S. A. Villeda *et al.*, *Nat. Med.* **20**, 659 (2014).
5. C. H. Hillman *et al.*, *Nat. Rev. Neurosci.* **9**, 58 (2008).
6. M. V. Lourenco *et al.*, *Nat. Med.* **25**, 165 (2019).
7. P. Boström *et al.*, *Nature* **481**, 463 (2012).
8. C. Cooper *et al.*, *Cold Spring Harb. Perspect. Med.* **8**, a029736 (2018).
9. J. Delezie, C. Handschin, *Front. Neurol.* **9**, 698 (2018).
10. J. P. Thyfault, R. S. Rector, *Diabetes* **69**, 517 (2020).
11. S. W. Görgens *et al.*, *Prog. Mol. Biol. Transl. Sci.* **135**, 313 (2015).
12. M. Whitham *et al.*, *Cell Metab.* **27**, 237 (2018).
13. N. J. Hoffman, *Cold Spring Harb. Perspect. Med.* **7**, a029884 (2017).
14. M. P. Mattson, T. V. Arumugam, *Cell Metab.* **27**, 1176 (2018).
15. J. Rebo *et al.*, *Nat. Commun.* **7**, 13363 (2016).

ACKNOWLEDGMENTS

Supported by NIH grants R01AG05943, R21AG062894, and P30AG050911 and by a Veterans Administration grant I01BX003906.

10.1126/science.abc8830

VIEWPOINT: COVID-19

Rigorous wildlife disease surveillance

A decentralized model could address global health risks associated with wildlife exploitation

By **Mrinalini Watsa[1,2]** *and* **Wildlife Disease Surveillance Focus Group[3]**

Evidence suggests that zoonotic (animal origin) coronaviruses have caused three recent emerging infectious disease (EID) outbreaks: severe acute respiratory syndrome (SARS), Middle East respiratory syndrome (MERS), and the current coronavirus disease 2019 (COVID-19) pandemic. In the search for an intermediate host for SARS coronavirus 2 (SARS-CoV-2, which causes COVID-19), studies have identified SARS-CoV-2–like strains in bats (*1*) and pangolins (*2*), but these do not contain the same polybasic cleavage site that is present in SARS-CoV-2 (*3*). It is unknown what the intermediate host for this spillover event was because to date there are no international or national conventions on pathogen screening associated with animals, animal products, or their movements, and capacity for EID diagnostics is limited along much of the human-wildlife interface. EID risks associated with the wildlife trade remain the largest unmet challenge of current disease surveillance efforts.

Although viruses represent a fraction of ~1400 known human pathogens, they place a disproportionate burden on global health (*4*). Around 89% of the 180 recognized RNA viruses with the potential to harm humans are zoonotic. Coronaviruses are only the tip of the spillover iceberg: HIV came from nonhuman primates, Ebola came from bats, and H5N1 and H1N1 influenza strains came from birds and pigs, respectively. Indeed, 60% of EIDs are zoonotic in nature, and more than 70% of these have an origin in wildlife (*5*).

[1]Population Sustainability, San Diego Zoo Global, San Diego, USA. [2]Field Projects International, San Diego, USA. [3]Wildlife Disease Surveillance Focus Group authors and affliations are listed in the supplementary materials. Email: merkenswickwatsa@sandiegozoo.org

PHOTO: TOM LE LIEVRE/REDUX

Unchecked exploitation of wildlife—whether for sustenance or profit, legal or illegal—puts humans in direct contact with myriad unfamiliar species. Increased contact occurs in the global practice of bushmeat and game hunting and in wildlife farms, which often unsustainably and illegally supply wildlife for consumption or trade (*6*). Imported, hunted, and farmed wildlife then reach a common endpoint, wildlife markets. There, animals endure debilitating and immunocompromising conditions that promote disease transmission: packed cages, poor biosecurity, and unhygienic shedding of animal excreta (*7*). Direct human-wildlife contact, mixing of nonendemic wildlife species, and limited health and safety standards are all criteria for a zoonotic hotspot. Many wildlife markets around the world meet these criteria, yet disease surveillance in them is largely absent. More broadly, although the Convention on the International Trade in Endangered Species (CITES) regulates international wildlife trade on the basis of species' endangered status, only a few countries use strict veterinary import controls, and there are no global regulations on pathogen screening associated with the international trade in wildlife.

Pathogen biosurveillance and how humans interact with wildlife are at the crux of EID risk management and response. After bats were identified as likely reservoirs for a range of zoonotic events (such as Hendra, Nipah, SARS, MERS, and Ebola) (*8*), surveillance of a single cave in southwest China between 2011 and 2015 revealed 11 novel coronaviruses (*9*). From 2015 to 2017, of 1497 people tested in the surrounding Yunnan, Guangxi, and Guangdong districts, nine (0.6%) were positive for prior bat coronavirus antibodies, and 265 (17%) reported SARS- or influenza-type symptoms associated with contact with poultry, carnivores, rodents, shrews, or bats (*10*). These findings, formally reported in September 2019, provided a warning about the risk of zoonotic coronaviruses that was neither heard nor heeded. The COVID-19 pandemic is evidence that bridging the gap between research and response is critical to anticipating and mitigating future spillover events.

PREDICT, the intermittently federally funded offshoot of the 2009 United States Agency for International Development (USAID) Emerging Pandemic Threats program that partially financed the study of bat coronaviruses (*10*), screened 164,000 animals and humans and detected 949 novel viruses in zoonotic hotspots across 30 countries between 2009 and 2019. The Global Virome Project—a collaboration between experts in global health and pandemic prevention—aims to sequence all animal virus strains over a 10-year period, with a projected cost of $1.2 billion. Both projects share stakeholders, and although their missions are likely to adapt to a post–COVID-19 world, one of their stated goals includes strengthening existing laboratory capacities along the human-wildlife interface. But are there sufficient numbers of animal pathogen reference laboratories? According to the World Organisation for Animal Health (OIE) (*11*), there are 125 reference laboratories certified to screen for one or more target pathogens (and not for broad pathogen surveillance). Their global distribution does not reflect EID risks. Southeast Asia, Africa, and Central and South America carry the burden of EID risk, yet 78 (62%) of reference laboratories are in Europe and North America; only 33 (26%) are in Asia (14 in China and 8 in Japan), with 12 (34%) spread between 7 countries; 3 (~2%) are in Africa; 4 (~3%) are in Australia, and 8 (~6%) are in South America. Although this does not account for laboratory size or screening methods and capacity, it is evident that many regions with zoonotic hotspots lack testing facilities with the capability of conducting disease surveillance.

What can be done to mitigate future zoonotic EIDs? Centralized biosurveillance efforts produce results but are expensive, maintained by a select few countries, and subject to political whims, as evidenced by the 2019 shift in funding for PREDICT, a recent recall of U.S. National Institutes of Health (NIH) support for the EcoHealth Alliance, and the withdrawal of the United States from the World Health Organization (WHO). As such, they are not immediately scalable, nor do they stimulate widespread capacity. The international wildlife trade is a substantial global industry in need of greater oversight. Because ill-conceived restrictions would affect millions of people and likely drive these activities deeper underground, further impeding regulation (*12*), the first step is to establish a more cost-effective, decentralized disease surveillance system. It would empower local wildlife and public health professionals to test for diseases year round, at source, without criminalizing public participation in screening programs. Such screening was not technologically feasible after the emergence of the H1N1 influenza virus in 2009, but now, affordable modern technologies enable quick in situ biosample processing, whole-genome sequencing, metagenomics, and metabarcoding of pathogens. This would enable proactive, broad, routine wildlife pathogen screening in remote areas rather than reactive targeted testing.

Decentralized laboratories must be able to extract genomic material and conduct metagenomic sequencing and targeted pathogen testing if necessary. As demand increases, individual technologies have evolved to be smaller, simpler, and more affordable. Multiplex polymerase chain re-

Markets selling live animals, including wildlife such as this slow loris at the Borito Market in Jakarta, Indonesia, are hotspots for zoonotic spillover and should be monitored to better manage emerging infectious diseases.

action (PCR)–based viral enrichment protocols with portable DNA sequencers (such as MinION) have been deployed for in situ monitoring of Ebola virus, Zika virus, and now SARS-CoV-2 infections (*13*). Practical training in applying these laboratory solutions (such as miniature centrifuges, thermocyclers, and electrophoresis setups) is well documented, even in remote locations (*14*). However, most pathogen screening efforts that use such equipment have been in response to human disease outbreaks. These technologies could be used to regularly monitor entire pathogen families of increased global concern in animals and areas with increased risk of zoonotic spillover, including wildlife markets or farms and free-ranging high-risk taxa such as primates and bats (*15*). Local wildlife scientists and health care workers can be trained on how to safely use facilities with broadly accessible molecular equipment in local facilities with standard biosecurity practices to prevent risk of pathogen spillover into the community. Restricting such training and activities to relatively few specialized centers impedes broad surveillance efforts. Any animal surveillance program should integrate with testing programs for humans to capture early zoonotic pathogen circulation between human and nonhuman populations. Sources of zoonotic pathogens are frequently unclear and often not possible to determine after the early stages of a spillover event. Monitoring could remove much of this uncertainty, allowing molecular epidemiology to inform short- and long-term responses on both a local and global level.

To complement decentralized laboratories, a publicly accessible, centralized, curated system for monitoring pathogens must be established for three main reasons: (i) This would provide instant pathogen classifications based on comparative genomics, further cross-linked to reference data on prevalence by species and region. (ii) A centralized curated system could alert to EID indicators, including gains and losses of strains, pathogen-specific changes in host species numbers, rapid increases in mutation rates that may indicate pathogen spillover into a naive host, and pathogen detection in traded animals that do not occur in wild counterparts. (iii) For virus families that are poised to spillover into human populations, genomic sequence data can reveal diversity of key pathogen proteins in circulating strains (for example, the spike protein that mediates human cell entry of coronaviruses, and the RNA-dependent RNA polymerase that is important for viral replication). Such approaches assist in identifying broad-spectrum antivirals and vaccination targets as well as treatment-resistant pathogen variants that pose a risk of generating future EIDs.

An example of a disease-focused public database that could be expanded is the GISAID (global initiative on sharing all influenza data) EpiFlu repository, a global initiative developed for sharing influenza virus sequence data and currently also documenting SARS-CoV-2 sequences. It facilitates data access for registered users while securing data ownership by requiring that contributors be acknowledged in derivative research. Additionally, the database could include report-generating features such as those in the Zoological Information Management Software (ZIMS), used by more than 1000 Species360–accredited zoological institutions worldwide to upload biomedical data and compute reference ranges across multiple variables and species.

An internationally recognized standard for managing wildlife trade on the basis of known disease risks should be established. Currently, few countries consider disease risk as a factor in regulating wildlife imports and exports, and a disease status equivalent to CITES is lacking. Pathogen screening is also not required nor facilitated before, during, or after translocating wildlife products, leaving pathogen status to be declared by the shipper, who may not have the experience to make such determinations. Because a large number of animals naturally carry pathogens that could spillover to humans if improperly handled, the means to identify the species for which security standards should be enhanced, or for which trade and consumption should potentially be prohibited, is needed. An important caveat is that such classifications can stigmatize animals to their detriment and incite fear-based human behaviors that may threaten species conservation.

A decentralized network could improve feedback between those who screen samples and those who curate data to bolster the safety of wildlife and humans, a fundamentally "One Health" approach. This would increase localized knowledge of EID risks, provide earlier warnings and faster global responses to spillovers, and inform wildlife trade policy. This model is more robust to shifting political landscapes and funding and does not ignore the role of advanced regional research laboratories, which also provide vital targeted pathogen screening. Research laboratories can also provide samples for or generate high-quality host de novo reference genome assemblies and expand regional capacity for biobanking, including cell cultures, which will improve understanding of the co-evolutionary processes that underlie pathogen-host range and susceptibility. By giving more parties a stake in the effort, decentralization is more likely to succeed in garnering geographically representative participation that explicitly includes the most at-risk, underresourced regions. ■

REFERENCES AND NOTES

1. R. Lu *et al.*, *Lancet* **395**, 565 (2020).
2. X. Li *et al.*, *J. Med. Virol*. **6**, 6 (2020).
3. K. G. Andersen, A. Ram-baut, W. I. Lipkin, E. C. Holmes, R. F. Garry, *Nat. Med*. **26**, 450 (2020).
4. M. E. J. Woolhouse *et al.*, *Microbiol. Spectr*. **1**, 81 (2014).
5. K. E. Jones *et al.*, *Nature* **451**, 990 (2008).
6. L. Tensen, *Glob. Ecol. Conserv*. **6**, 286 (2016).
7. S. E. Baker *et al.*, *Bioscience* **63**, 928 (2013).
8. H.-J. Han *et al.*, *Virus Res*. **205**, 1 (2015).
9. B. Hu *et al.*, *PLOS Pathog*. **13**, e1006698 (2017).
10. H. Li *et al.*, *Biosaf. Health* **1**, 84 (2019).
11. OIE, List of Laboratories; www.oie.int/scientific-expertise/reference-laboratories/list-of-laboratories.
12. M. 't Sas-Rolfes, D. W. S. Challender, A. Hinsley, D. Veríssimo, E. J. Milner-Gulland, *Annu. Rev. Environ. Resour*. **44**, 201 (2019).
13. Oxford Nanopore Technologies, COVID-19: Community News; www.nanoporetech.com/about-us/news/covid19-community.
14. M. Watsa, G. A. Erkenswick, A. Pomerantz, S. Prost, *PLOS Biol*. **18**, e3000667 (2020).
15. C. K. Johnson *et al.*, *Proc. Biol. Sci*. **287**, 20192736 (2020).

SUPPLEMENTARY MATERIALS

science.sciencemag.org/content/369/6500/145/suppl/DC1

10.1126/science.abc0017

Artistic depictions of extinct species, like this Kulindadromeus, increasingly reflect scientific speculation.

IMAGE: MARK WITTON

PALEONTOLOGY

Paleoart comes into its own

A renaissance is occurring in the way we render extinct species

By **Ilja Nieuwland**

Paleontological art, or paleoart, is experiencing a veritable renaissance. Before the pandemic brought public events to a halt, the European mainland was set to witness no fewer than three exhibitions centered on this genre within the span of a year (*1–3*).

Esther van Gelder, guest curator of the *Dinomakers* exhibition at the Teylers Museum, attributes the mounting interest in paleoart to an increase in cross-disciplinary fertilization. "Firstly, we see a growing interest in general in hybrid genres that combine science (especially nature) and art," she says. "But the process of emancipation of paleoart has been going on for some time now, and the generation that got interested in paleontology through dramatic new images of dinosaurs in the eighties and early nineties is now starting to write books, make art, and curate exhibitions themselves."

Previously, reconstructions were rendered conservatively, depicting extinct creatures exclusively in postures and contexts that had been confirmed scientifically. But such renderings often ended up emphasizing the exceptionality of past life. By contrast, recent paleoart has increasingly come to underline the similarities between extinct and existing flora and fauna. What sets this new practice apart is its embrace of the "known unknowns" and its ability to recognize that more than one possibility may be worthy of consideration. The resulting art is simultaneously more fantastic and more scientifically probable than anything we have seen before.

Part of this transformation can be traced to a book published in 2012 called *All Yesterdays* (*4*). In it, the book's authors toy with the uncertainty inherent in paleontological reconstruction, emphasize how much knowledge could be gained by looking at contemporary nature, and even satirize some reconstruction practices. Paleontologist and paleoartist Mark Witton describes the book as "a game-changer for the current generation of paleoartists. It

The reviewer is at the Department of the History and Social Aspects of Science, Faculty of Science, Vrije Universiteit Amsterdam, 1081 HV Amsterdam, Netherlands. Email: i.j.j.nieuwland@vu.nl

both captured attitudes circulating about paleoart in the late 2000s and, [in] arguing for greater originality and bolder speculation in paleoartworks, set a clear course that inspired a lot of debate and discussion."

Whereas previous generations attempted to eliminate overt speculation about long-dead species, Witton, like many other contemporary practitioners, embraces it: "There are very few aspects of extinct animal anatomy that we can't say something intelligent about. A big new paper can spark a wave of new artwork and dissection among the paleoart community, and feedback and development of different interpretations can be rapid."

That newfound dynamism seems to have helped paleoart become more popular as an artistic genre. "Paleoart was not considered 'proper' art, unlike classic botanical and zoological painting," van Gelder explains. "But when Zoë Lescaze published her book *Paleoart* in 2017, with magnificent, high-quality reproductions, it became possible to convince my colleagues that we were dealing with a genre that possessed genuine artistic merit" (*5*).

Paleontologists use art not only to popularize their science but also to gain insights into their work that can be difficult to achieve using other means. "I'm definitely inspired by depictions of extinct animals that include 'real' behavior, in other words, not just roaring and eating, but grooming, display, and other natural things all animals get up to," notes University of Oxford paleontologist Elsa Panciroli. "It makes me wonder if those behaviors are likely—or even possible—and how I might scientifically approach finding out."

The genre still has some hurdles to tackle, including the fact that many museums lack budgets for commissioning paleoart. This has led to a constant recycling of older images, reinforcing the genre as both scientifically and artistically dated. But change is under way. "There's so much more discussion and interaction than there used to be. None of us really work in isolation anymore," says Witton. "Social media and the increase in online publishing have allowed people interested in paleoart—the artists themselves, their followers, paleontologists—to connect in ways we were unable to a decade or so ago." ■

REFERENCES AND NOTES

1. *Saurier – Die Erfindung der Urzeit* [Saurians – The Invention of Prehistoric Times], Stiftung Schloss Friedenstein Gotha, Gotha, Germany, 6 February 2021 to 22 August 2021.
2. *Paläo-Art. Von Jugenstil bis in die Moderne* [Paleo-Art. From Art Nouveau to Modernism], Paläontologisches Museum München, München, Germany, 5 September 2019 to 30 June 2020.
3. *Dinomakers*, Teylers Museum, Haarlem, Netherlands, 31 January 2020 to 23 August 2020.
4. J. Conway, C. M. Kosemen, D. Naish, *All Yesterdays: Unique and Speculative Views of Dinosaurs and Other Prehistoric Animals* (Irregular Books, 2012).
5. Z. Lescaze, *Paleoart: Visions of the Prehistoric Past* (Taschen, 2017).

10.1126/science.abd3642

NAVIGATION

Changing course

Navigational skills require nurturing, lest we lose our way

By **Lawrence Rosen**

The other day, I pulled into a gas station and swung around the pumps to reach my gas fill. After refueling, I turned back onto the road and drove some distance before realizing that I had turned the wrong way. Was I being inattentive, or do I just have a poor sense of direction? Or was this perhaps indicative of a larger problem? Have we replaced instinct with culture and, lacking local knowledge, had I lost my bearings? Or could it be that somewhere in my brain, there lurks a navigational capacity that has been dulled but could be revived? In his new book, *From Here to There*, Michael Bond guides readers through the neurological research and anecdotal tales that show how the brain supplies the equipment upon which our species has built its wayfinding skills.

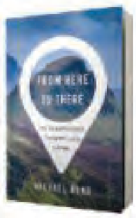

From Here to There
Michael Bond
Belknap Press, 2020. 304 pp.

Bond begins by accepting the fallacious characterization of contemporary hunter-gatherers as having "changed little" and thus being identical in their navigational habits to Paleolithic hominins. If, as he argues throughout the rest of the book, our ability to find our way is more learned than instinctual, his failure to attribute any history or cultural distinctiveness to such peoples starts us in the wrong direction.

Back on the right path, Bond reviews the science of wayfinding with graceful accounts of current research. Neuroscientists have demonstrated that there are distinct cells in the brains of rats that are activated to establish place, to mark position, to orient with reference to boundaries, and to capture a heads-up direction. Humans, however, tend to align themselves not so much with cardinal markers as with landmarks, giving prominence, at times, to a mental map that is built upon one's relation to particular sightings. Research has shown that the human brain's entorhinal cortex appears to feed this information to the hippocampus, although the author acknowledges that how these cells interact with one another remains mysterious.

The reviewer is the William Nelson Cromwell Professor Emeritus of Anthropology at Princeton University, Princeton, NJ, USA, and adjunct professor emeritus at Columbia Law School, Columbia University, New York, NY, USA. Email: lrosen@princeton.edu

Wayfinding places a premium on memory, and Bond cites many examples of the different personal and cultural modes through which such recall is inscribed. From the Australian aborigines who can find their way through seemingly featureless terrain to the Inuit who cross trackless oceans of ice, research indicates that these abilities come not simply from an innate capacity to organize space but by way of the learned process of noting our surroundings and taking advantage of our cognitive equipment. As one researcher put it, the hippocampus helps us navigate life, not just space.

Bond is especially good at confronting stereotypes. Studies, he writes, do show that men are marginally better at spatial navigation than women, but with proper encouragement and opportunity the differences evaporate. Similarly, he challenges the idea that some people are simply better endowed with wayfinding abilities than others, arguing instead that even orienteering champions, Polynesian seafarers, and phenomenal navigators excel primarily through trained attentiveness and experience. Not surprisingly, Bond cites approvingly the wayfarer's admonition that you should "trust your skills, not your instinct."

But what happens when those skills are severely attenuated? Bond rues the fact that British children rarely explore away from home anymore, thus muffling the biological ability to find their way. So, too, do the 80,000 men kept in solitary confinement in U.S. prisons often lose their sense of direction. Meanwhile sufferers of Alzheimer's disease, who also lose spatial control, may, like Bond's grandmother, express their confusion with the plaintive query "Am I here?" He describes the cases of lost individuals who make the mistake of racing to find a way out rather than staying put and awaiting rescue: As he notes, "no one gets smarter under stress."

Bond writes in an easygoing, chatty style, free of jargon and strained analogies. He concludes that, by setting aside our GPS devices, by redesigning parts of our cities and play areas, and sometimes just by letting ourselves get lost, we can indeed revivify our ability to find our way, to the benefit of our inner world no less than the outer one. ■

10.1126/science.abd1847

Rising flood waters advance on Midland, Michigan, after the breach of the Edenville and Sanford dams.

Edited by **Jennifer Sills**

Preparing for proactive dam removal decisions

On 18 May, the Edenville and Sanford dams, built in the 1920s to serve the people of Michigan, failed after a series of extreme rainfall events. More than 10,000 residents were evacuated, and flood waters inundated a major chemical complex, raising concerns of a widespread environmental catastrophe (*1*). These incidents, the latest in the long line of increasingly frequent (*2*) dam failures, highlight once again the importance of proactively addressing aging and problematic dams. To move forward, we need a scientific and legal framework in place to evaluate if and when dam removal is required and to ensure that adequate funds are devoted to implementing responsible decisions.

The United States has removed about 1700 dams (*3*), many of them since 2000, but our understanding of how these decisions are made and the effects on local ecosystems remains incomplete. Less than 10% of dam removal cases have been scientifically evaluated (*4*). Most post-dam removal studies are less than a decade old and do not adequately represent the diversity of dam types, watershed conditions, dam-removal methods, and the decision-making processes in the United States. To prepare for future decisions, scientists should document, share, and analyze the collected data and lessons from both past and ongoing dam removal missions.

We also lack information about the effects of dam removal on the environment. Records show that the local river and ecosystem do not fully revert to their pre-dam condition (*5*). Environmental impact assessments should inform all dam rehabilitation and removal decisions by considering a wide range of ecosystem evolution trajectories. Restoring the environment will require careful planning, close monitoring of the state of the ecosystem, sediment removal, and land use regulations.

Finally, we must identify and address socio-economic, technological, and regulatory barriers to judicious and timely dam maintenance, rehabilitation, and removal. Both of the Michigan dams were more than 90 years old and previously classified as "high hazard," as are a third of Michigan's 1059 dams and more than 15,600 dams across the United States (*6*). Because rehabilitating the nation's non-federal dams would cost more than $65 billion (*7*), unsafe dams continue to operate. To prevent future catastrophic events like the one in Michigan, we must clarify the importance of making funds available for rehabilitation and removal by raising awareness about the risks of problematic dams to human safety and environmental health.

Farshid Vahedifard[1]*, Kaveh Madani[2,3], Amir AghaKouchak[4], Sannith Kumar Thota[1]

[1]Department of Civil and Environmental Engineering, Mississippi State University, Mississippi State, MS 39762, USA. [2]The MacMillan Center for International and Area Studies, Yale University, New Haven, CT 06511, USA. [3]Department of Physical Geography, Stockholm University, Stockholm, SE-106 91, Sweden. [4]Department of Civil and Environmental Engineering, University of California, Irvine, CA 92697, USA.

*Corresponding author.
Email: farshid@cee.msstate.edu

REFERENCES AND NOTES

1. D. K. Li, "Chemical plant and hazardous waste sites in path of Michigan flooding," *NBC News* (2020).
2. National Performance of Dams Program, "Dam failures in the U.S., NPDP-01 V1" (Department of Civil & Environmental Engineering, Stanford University, 2018); https://npdp.stanford.edu/sites/default/files/reports/npdp_dam_failure_summary_compilation_v1_2018.pdf.
3. American Rivers, American Rivers Dam Removal Database, Version 7 (2020); https://doi.org/10.6084/m9.figshare.5234068.v7.
4. R. Bellmore *et al.*, *WIREs Wat.* **4**, e1164 (2017).
5. M. M. Foley *et al.*, *Wat. Resour. Res.* **53**, 5229 (2017).
6. A. Singhvi, T. Griggs, "Two dams that failed were rated 'high hazard.' A Third of Michigan's dams hold a similar risk," *The New York Times* (2020).
7. Association of State Dam Safety Officials, State Performance and Current Issues (2020); www.damsafety.org/state-performance.

10.1126/science.abc9953

Unnecessary hesitancy on human vaccine tests

In their Policy Forum "Ethics of controlled human infection to address COVID-19" (22 May, p. 832), S. K. Shah and colleagues provide an ethical framework to determine whether controlled human infection studies (CHIs) are justifiable for studying potential vaccines and treatments for severe acute respiratory syndrome coronavirus 2 (SARS-CoV-2), the virus that causes coronavirus disease 2019 (COVID-19). Some of the Policy Forum authors reportedly disagreed that "the social value of such CHIs is sufficient to justify the risks" at this time. Their reluctance is unfounded. The risks of a properly conducted CHI are low enough, and the social value of expedited SARS-CoV-2 vaccine development is high enough, that properly conducted CHIs with a fair chance at accelerating that development remain a legitimate strategy.

Shah *et al.* identify an ineliminable risk to participants: a 0.03% death rate among "healthy adults aged 20 to 29" infected with SARS-Cov-2. The source for this mortality rate (*1*) documents death among all infected 20- to 29-year-olds. In healthy people in this age range, death should be rarer. CHIs will only recruit healthy people. And, perhaps thanks to evolving COVID-19 treatment practices, the mortality rate is already lower in that age group than it was when the Policy Forum was published (*2*). Moreover, as shown in Shah *et al.*'s table S1, live kidney donation, a broadly accepted

practice, carries a similar mortality risk of <0.03%. An alternative suggestion cited by Shah *et al.* would limit risk to below a 1% death rate (*3*), but that threshold is far higher than their own estimate of 0.03%.

Further mitigating the overall risk, CHI participation could reduce participants' relative risk—i.e., their risk in the trial minus their risk if they decline to participate (*4*, *5*)—and improve their treatment access (*4*). Shah *et al.* agree that recruiting in "locations with high community spread of SARS-CoV-2 could be an acceptable way to reduce relative risks for participants" (*6*). CHIs should also guarantee participants critical care [which most young COVID-19 patients survive (*7*–*9*)] and any novel therapeutics. Those may be scarce in some locations with high community spread (*6*), even absent economic or racial injustices that might create ethical complications (*5*). These factors push overall risk further below limits.

Shah *et al.* question the social value of CHIs because of the necessary "coordination of stakeholders," but no trial guarantees coordinated delivery. Even a fairly moderate chance at substantially curbing colossal (*10*, *11*) mortality through an accelerated vaccine rollout would imbue CHIs with high expected social value.

Nir Eyal
Center for Population-Level Bioethics and Department of Philosophy, Rutgers University, New Brunswick, NJ 08901, USA, and Department of Health Behavior, Society and Policy, Rutgers School of Public Health, Piscataway, NJ 08854, USA. Email: nir.eyal@rutgers.edu

REFERENCES AND NOTES

1. R. Verity *et al.*, *Lancet Infect. Dis.* **20**, 669 (2020).
2. H. Salje *et al.*, *Science* 10.1126/science.abc3517 (2020).
3. D. B. Resnik, *Theor. Med. Bioeth*. **33**, 137 (2012).
4. R. Palacios, S. K. Shah, *Trials* **20**, 702 (2019).
5. N. Eyal, *Ethics Hum. Res.* 10.1002/eahr.500056 (2020).
6. N. Eyal, M. Lipsitch, P. G. Smith, *J. Infect. Dis*. **221**, 1752 (2020).
7. Intensive Care National Audit & Research Centre (ICNARC), "ICNARC report on COVID-19 in critical care 08 May 2020" (ICNARC, London, UK, 2020).
8. G. Grasselli *et al.*, *JAMA* **323**, 1574 (2020).
9. X. Yang *et al.*, *Lancet Respir. Med*. **8**, 475 (2020).
10. P. G. T. Walker *et al.*, "The global impact of COVID-19 and strategies for mitigation and suppression," (WHO Collaborating Centre for Infectious Disease Modelling, MRC Centre for Global Infectious Disease Analysis, Abdul Latif Jameel Institute for Disease and Emergency Analytics, Imperial College London, 2020).
11. T. Roberton *et al.*, *Lancet Infect. Dis*. **8**, E901 (2020).

COMPETING INTERESTS

N.E. is funded by National Institute of Allergy and Infectious Diseases grant R01 AI114617-01A1.

10.1126/science.abc8264

Response

Eyal contends that the expected social value of controlled human infection studies (CHIs) conducted in an effort to find vaccines and treatment for coronavirus disease 2019 (COVID-19) will be high enough to justify the risks to participants. We are concerned that Eyal and others (*1*) underestimate the uncertainties inherent in making such a determination. CHIs could take too long to be sufficiently valuable or may even hinder vaccine uptake and introduce risks that are not well understood. Because of these uncertainties, our Policy Forum supports laying the groundwork for CHIs but not deploying them to address COVID-19 until there is greater confidence that their value can justify the risks.

Whether severe acute respiratory syndrome coronavirus 2 (SARS-CoV-2) CHIs can be integrated into a highly dynamic vaccine development pipeline is an open question. It takes months to develop a challenge strain (*2*), even under a highly compressed schedule, and additional time to establish an appropriate challenge model. If SARS-CoV-2 transmission continues at a relatively high rate, other vaccine trials might speed ahead and produce efficacy data before CHIs could be launched (*3*). On the other hand, if field trials are not feasible because of declining transmission, SARS-CoV-2 CHIs could provide crucial efficacy data about candidate vaccines and would have much higher and clearer social value.

Potential implementation challenges also make the social value from SARS-CoV-2 CHIs highly uncertain. For example, if CHIs feed distrust among the public, they could exacerbate challenges in vaccine roll-out (*4*) and delay uptake of an effective vaccine. Given these uncertainties, it is difficult to determine whether there is a credible case that CHIs are likely to save substantial time in vaccine development. Although there are other possible reasons to conduct SARS-CoV-2 CHIs, as we have argued, such as identifying correlates of immune protection, whether they will have high social value is also currently uncertain.

It is difficult to predict whether risks to participants will be better understood or further reduced by the time CHIs could be implemented. For example, investigators might be able to identify with greater confidence individuals at substantial risk of severe and potentially long-term symptoms and exclude them from participation. If new evidence reveals that SARS-CoV-2 CHIs pose lower risks than those currently estimated, they would require less social value to justify. These major uncertainties as to whether, why, and how to conduct SARS-CoV-2 CHIs should not be disregarded in a rush to judgment.

We also disagree with Eyal's assessment that the overall risk from study participation is already lower than the limits proposed for research with consenting adults. Not enough is known about the risks of serious and chronic complications other than mortality. Given that current estimates of mortality risks—which remain contentious—are in the upper range of what might be acceptable, emerging risks of long-term, serious complications, including kidney damage and strokes (*5*, *6*), could push the risk estimates above acceptable limits. Even trials with low risks of severe outcomes can only be justified by a reasonable chance of sufficient benefit.

We maintain our stance of open-minded, cautious consideration of SARS-CoV-2 CHIs rather than unwavering advocacy. To be clear, continued debate and rapidly evolving evidence should not delay technical development (including challenge agent manufacture), stakeholder coordination efforts, and broader public engagement to determine, for example, whether such studies would be widely acceptable. The balance between social value and individual risk should be formally assessed as soon as feasible and reassessed if and when CHIs are ready to launch.

Seema K. Shah*, Franklin G. Miller, Thomas C. Darton, Devan Duenas, Claudia Emerson, Holly Fernandez Lynch, Euzebiusz Jamrozik, Nancy S. Jecker, Dorcas Kamuya, Melissa Kapulu, Jonathan Kimmelman, Douglas MacKay, Matthew J. Memoli, Sean C. Murphy, Ricardo Palacios, Thomas L. Richie, Meta Roestenberg, Abha Saxena, Katherine Saylor, Michael J. Selgelid, Vina Vaswani, Annette Rid
*Corresponding author. Email: seema.shah@northwestern.edu
The list of author affiliations is available at www.sciencemag.org/cgi/content/full/science.abc1076/DC1.

REFERENCES AND NOTES

1. S. A. Plotkin, A. Caplan, *Vaccine* **38**, 3987 (2020).
2. A. P. Catchpole *et al.*, *BMC Res. Notes* **11**, 620 (2018).
3. J. Cohen, *Science* **368**, 14 (2020).
4. E. Conis, M. McCoyd, J. E. Moravek, "What to expect when a coronavirus vaccine finally arrives: Sobering lessons from the history of the polio vaccine," *The New York Times* (2020).
5. A. A. Divani *et al.*, *J. Stroke Cerebrovasc. Dis*. **Aug. 29**, 104941 (2020).
6. A. B. Docherty *et al.*, *BMJ* **369**, m1985 (2020).

COMPETING INTERESTS

The opinions expressed in the article are the authors' and do not reflect the views of organizations with which the authors have affiliations, including the National Institutes of Health, the Department of Health and Human Services, or the United States government. The authors receive support from a Making a Difference Grant from the Greenwall Foundation (S.K.S., A.R., R.P., D.D.), the Wellcome Trust (S.K.S., E.J., D.K., M.K., R.P., M.J.S., V.V.), Brocher Foundation (S.K.S., A.R., R.P., D.D., T.C.D., H.F.L., E.J., N.S.J., D.K., J.K., D.M., S.C.M., T.L.R., M.R., A.S., M.J.S., V.V.), and NIH Clinical Center Department of Bioethics (A.R.).

10.1126/science.abc9380

PRIZE ESSAY

MICROBIOME

Poised for tissue repair

Skin microbes interact with the immune system to aid wound healing

By **Oliver Harrison**

The immune system acts as a formidable guardian of health, protecting and restoring tissue function during infectious and environmental challenges. To date, our understanding of host immunity stems from models of inflammation and infection with pathogenic microbes. However, the vast majority of microbial-immune encounters occur as a symbiotic relationship with the commensal microbiota, the trillions of microorganisms that inhabit our barrier tissues, including the gastrointestinal tract and skin. Indeed, far from being ignored by the host, commensal microbes promote the development, education, and function of the mammalian immune system (*1*). In return, immune responses to commensal microbes, particularly those mediated by the adaptive immune system, act to bolster epithelial fortifications for antimicrobial function, restraining systemic translocation of both commensal and pathogenic microbes (*2*).

A striking feature of immune responses to commensal microbes present at barrier surfaces is the uncoupling from inflammation and maintenance of tissue integrity at both the onset and effector phases of the response. This form of homeostatic immunity to commensal microbes raises several questions. In particular, to what extent do the conventional rules of adaptive immunity to pathogens apply to these noninvasive microbes? And, how do commensal-specific T cells sense and respond to environmental stresses during tissue injury?

As a postdoctoral fellow in Yasmine Belkaid's laboratory at the National Institutes of Health, I sought to address these questions, investigating the mechanisms by which commensal-specific T cell responses are mounted and their role in tissue homeostasis. Initial efforts to identify, track, and profile commensal-specific T cells led us to uncover three aspects of host immunity specifically engaged by commensal microbes resident at the skin surface: a nonclassical major histocompatibility complex (MHC) restriction, a hybrid differentiation profile, and a direct contribution to wound repair.

Center for Fundamental Immunology, Benaroya Research Institute, Seattle, WA, USA.
Email: oharrison@benaroyaresearch.org

NONCLASSICAL IMMUNITY TO COMMENSAL MICROBES

Despite the overwhelming quantity of proteins potentially produced by the microbiota, only a smattering of microbe-derived antigens and epitopes recognized by commensal-specific T cells have been identified, hampering mechanistic insight into the biology of these cells (*3*–*6*). For this reason, we began by exploring the antigen-specificity of commensal-specific T cells resident within the skin, using a model of neocolonization with the common human skin commensal *Staphylococcus epidermidis* (*7*).

A combination of in vitro screening and in silico epitope prediction revealed that commensal-specific CD8⁺ T cell responses were coordinated by the noncanonical MHC1b molecule, H2-M3, presenting *N*-formylmethionine (fMet)–containing peptides (*8*). These findings demonstrated that fMet peptides, a canonical class of bacterial antigens known to activate the innate immune system, also induced a tailored adaptive immune response to noninvasive bacteria. They also highlighted the distinct contribution of nonclassical MHC molecules to the cross-talk that occurs between microbiota and the immune system. Identification of H2-M3–binding fMet peptides facilitated the generation of peptide:MHC tetramers and T cell receptor (TCR)–transgenic mice, enabling the tracking and profiling of commensal-specific $CD8^+$ T cells within skin tissues during homeostasis and inflammation. Using these tools as complementary strategies to track commensal-specific $CD8^+$ T cells in vivo, we determined that these T cells display a tissue-resident memory profile, surviving locally as long-term sentinels of the skin barrier.

POISED IMMUNITY TO COMMENSAL MICROBES

To determine how commensal-specific $CD8^+$ T cells were educated by the local skin microenvironment, we assessed their cytokine production and effector potential. Commensal-specific $CD8^+$ T cells polarized toward an unusual hybrid state, highly distinct from those commonly invoked by pathogen infections. Specifically, $CD8^+$ T

Commensal-specific $CD8^+$ T cells harbor a poised type-2 transcriptome during homeostasis

Tissue injury licenses poised type-2 immunity, including translation of interleukin-13 (IL-13) protein by commensal-specific $CD8^+$ T cells, thereby promoting tissue repair.

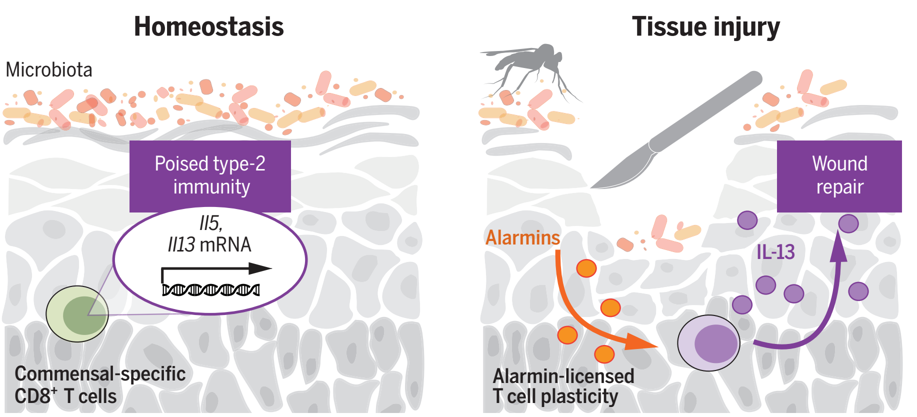

GRAPHIC: ADAPTED FROM O. J. HARRISON *ET AL.* (9) BY N. CARY/*SCIENCE*

cells coexpressed two normally mutually exclusive transcription factors, retinoic acid–related orphan receptor–γt (RORγt) and GATA-binding protein 3 (GATA-3), that are essential for type-17 immunity to fungi and type-2 immunity to parasites, respectively. We next investigated the impact of such coexpression by characterizing the epigenetic and transcriptional landscape of these cells.

Unexpectedly, we identified accessible chromatin and mRNA expression for type-2 immunity cytokines, *Il5* and *Il13*. By contrast, although competent for *Il5* and *Il13* mRNA expression, these cells did not subsequently translate either interleukin-5 (IL-5) or IL-13 proteins. Thus, in healthy skin tissue, commensal-specific T cells adopt a distinct differentiation profile, which we have termed "poised type-2 immunity" (*9*).

A mechanistic understanding of the post-transcriptional machinery that regulates this immune axis remains a focus of ongoing research. However, given the fundamental role of the skin as a protective barrier, we hypothesized that poised type-2 immunity might be influenced by environmental insults, including tissue injury. We determined that it could be unleashed through stimulation with local alarmins, factors released during skin inflammation, triggering rapid protein translation of type-2 cytokines by commensal-specific $CD8^+$ T cells locally within injured skin tissue. Thus, induction of type-2 cytokine mRNA expression and subsequent protein translation can be temporally decoupled in commensal-specific $CD8^+$ T cells, allowing for pleiotropic functions under homeostatic and inflammatory conditions.

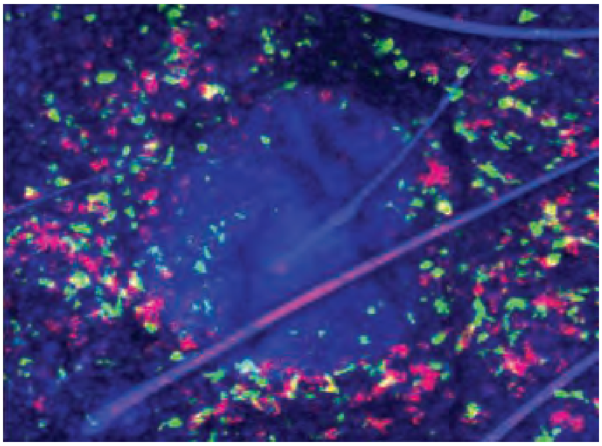

Confocal imaging of the T cell response to *S. epidermidis* colonization of the skin. Foxp3, green; DAPI, blue; CD8α, red.

COMMENSAL-SPECIFIC T CELL PLASTICITY AIDS TISSUE REPAIR

Given the anatomical proximity of commensal-specific $CD8^+$ T cells to the skin epithelium, and their remarkable functional plasticity upon exposure to inflammatory mediators, we sought to address the contribution of these skin-resident sentinels to tissue repair. Using wound bed re-epithelialization as a quantifiable hallmark of tissue repair, we observed that prior commensal colonization of the skin and associated recruitment of commensal-specific $CD8^+$ T cells accelerated wound repair (*8*). The ability of *S. epidermidis* colonization to accelerate this healing process was dependent on the capacity of commensal-specific $CD8^+$ T cells to produce IL-13 protein after tissue injury, formally linking MHC1b-restricted commensal-specific $CD8^+$ T cells, poised type-2 immunity, and tissue repair (see the figure) (*9*).

CO-OPTING LESSONS FROM COMMENSAL-SPECIFIC IMMUNITY TO UNDERSTAND DISEASE

By identifying a tissue checkpoint that is reliant on the plasticity of tissue-resident commensal-specific T cells, we extend our understanding of a fundamental but poorly understood form of immunity. Our findings highlight the exquisite specificity that underlies the interplay between commensal microbes and the immune system as a key element of tissue homeostasis and repair. We, like others, hypothesize that perturbations in this symbiotic relationship are likely triggering events for the onset and perpetuation of chronic inflammatory disorders of barrier tissues. Further understanding the contribution of commensal-specific immunity to tissue physiology may tailor future therapies toward critical immune-microbe interactions driving chronic inflammation and disease. ■

REFERENCES AND NOTES

1. Y. Belkaid, O. J. Harrison, *Immunity* **46**, 562 (2017).
2. K. Honda, D. R. Littman, *Nature* **535**, 75 (2016).
3. Y. Cong, T. Feng, K. Fuji-hashi, T. R. Schoeb, C. O. Elson, *Proc. Natl. Acad. Sci. U.S.A.* **106**, 19256 (2009).
4. Y. Yang *et al.*, *Nature* **510**, 152 (2014).
5. M. Xu *et al.*, *Nature* **554**, 373 (2018).
6. E. Ansaldo *et al.*, *Science* **364**, 1179 (2019).
7. S. Naik *et al.*, *Nature* **520**, 104 (2015).
8. J. L. Linehan *et al.*, *Cell* **172**, 784 (2018).
9. O. J. Harrison *et al.*, *Science* **363**, eaat6280 (2019).

ACKNOWLEDGMENTS

I am extremely grateful to my mentor, Y. Belkaid, with whom I am lucky to have trained and benefitted from her vision, drive, and mentorship for several years. I also thank the members of the Belkaid laboratory, past and present, and our collaborators for their generosity in advice and friendship.

10.1126/science.abc5618

GRAND PRIZE WINNER

Oliver Harrison

Oliver Harrison received an undergraduate degree from the University of Bath and a Ph.D from the University of Oxford. After completing his postdoctoral fellowship at the National Institutes of Health, Oliver started his laboratory in the Center for Fundamental Immunology at Benaroya Research Institute in 2019. His research investigates how T and B cell responses to commensal microbes promote barrier tissue integrity and repair and how this goes awry in disease.

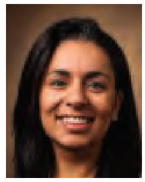

FINALIST

Mariana X. Byndloss

Mariana X. Byndloss received her D.V.M. and a Ph.D. from Universidade Federal de Minas Gerais in Brazil. After completing her postdoctoral fellowship at the University of California, Davis, Mariana started her laboratory in the Department of Pathology, Microbiology, and Immunology at Vanderbilt University Medical Center in 2018. Her research aims to understand how inflammation-mediated changes in gut epithelial metabolism lead to gut dysbiosis and increased risk of infectious gastroenteritis by *Salmonella typhimurium* and noncommunicable diseases, namely obesity-associated cardiovascular disease and colon cancer. **www.sciencemag.org/content/369/6500/153.1**

FINALIST

Chun-Jun (CJ) Guo

Chun-Jun (CJ) Guo received undergraduate degrees from Fudan University and a Ph.D. from the University of Southern California. After completing his postdoctoral fellowship at the University of California, San Francisco, and Stanford University in the Fischbach group, CJ started his laboratory in the Jill Roberts Institute for Research in Inflammatory Bowel Disease at Weill Cornell Medicine in 2018. His research uses CRISPR-based microbial genetics, state-of-the-art analytical chemistry, and healthy and diseased mouse models to mechanistically dissect how microbiome-derived genes, pathways, and metabolites affect host biology. **www.sciencemag.org/content/369/6500/153.2**

RESEARCH

IN *SCIENCE* JOURNALS

Edited by **Michael Funk**

PALEONTOLOGY

Teeth and jaws

The first vertebrates were jawless, much like a modern hagfish. There has been a lot of interest in how these forms transitioned to having jaws like most of their descendants, including humans. Much of our understanding of this process has focused on how the teeth are replaced relative to the jaw. Previous theories suggested that tooth growth that occurred lingually—or from inside out as in modern fishes—was a derived condition. Vaškaninová *et al*. vertebrates, suggesting that it may have been ancestral. —SNV

Science, this issue p. 211

Lingual (from inside out) tooth addition, observed in modern fishes such as this great white shark, has now also been observed in fossils of basal jawed vertebrates.

STRUCTURAL BIOLOGY

Engineering a toxin

Developing drugs that target a specific subtype in a G protein–coupled receptor (GPCR) family is a major challenge. Maeda *et al*. examined the basis of specificity of a snake venom toxin binding to muscarinic acetylcholine receptors (MAChRs), which mediate many functions of the central and parasympathetic nervous systems. They determined a structure that shows why the mamba venom toxin MT7 is specific for one receptor, M_1AChR, and also explains how it inhibits downstream signaling. Based on this structure, they engineered MT7 to be selective for another receptor, M_2AChR, instead of M_1ChR. The toxin may present a promising scaffold for developing specific GPCR modulators. —VV

Science, this issue p. 161

BIOCHEMISTRY

Conserved redox regulation of kinases

The effects of pathological oxidative stress are partially mediated through functional modification of various proteins. A pair of papers show that the oxidation of kinases at evolutionarily conserved cysteine residues regulates cell metabolism and mitosis. Shrestha *et al*. found that oxidation of the diabetes-associated metabolic kinase FN3K promoted its functional oligomerization and altered cellular redox status. Byrne *et al*. found that oxidation of mitotic kinases in human cells and yeast suppressed kinase catalytic activity and impaired cellular division in yeast. —LKF

Sci. Transl. Med. **12**, eaaz6313, eaax2713 (2020).

BIOENGINEERING

Beneficial bioartificial livers

Bioartificial livers are an attractive option as a bridge to transplant or to promote liver regeneration in cases of acute liver failure. Li *et al*. tested an extracorporeal bioartificial liver system composed of human liver progenitor-like cells cultured on macroporous scaffolds in a bioreactor that provides alternating air-liquid exposure. Three hours of treatment improved survival, reducing inflammation and promoting native liver regeneration in pigs with drug-induced acute liver failure. These results suggest that extracorporeal, cell-based bioartificial livers may be a promising treatment for acute liver failure. —CC

Sci. Transl. Med. **12**, eaba5146 (2020).

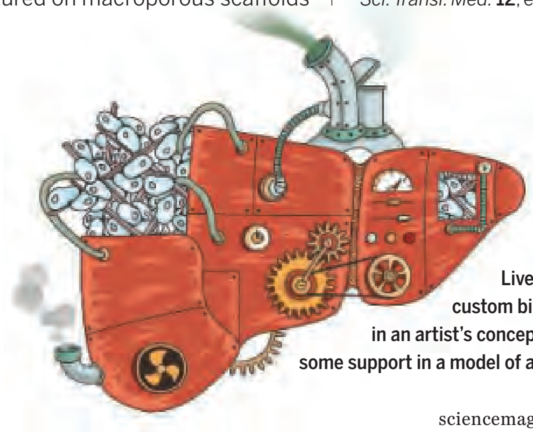

Liver cells grown in a custom bioreactor, as seen in an artist's conception, can provide some support in a model of acute liver failure.

IMMUNODEFICIENCIES

An inherited disorder makes WAVEs

The WAVE regulatory complex (WRC) is a multiunit complex that regulates actin cytoskeleton formation. Although other actin-regulatory proteins modulate human immune responses, the precise role for the WRC has not yet been established. Cook *et al*. studied five patients from four unrelated families who harbor missense variants of the gene encoding the WRC component HEM1. These patients presented with recurrent infections and poor antibody responses, along with enhanced allergic and autoimmune disorders. HEM1 was found to be required for the regulation of cortical actin and granule release in T cells and also interacted with a key metabolic signaling complex contributing to the disease phenotype. By linking these interactions to immune function, this work suggests potential targets for future immunotherapies. —STS

Science, this issue p. 202

QUANTUM PHYSICS

Strongly coupled at distance

The development of hybrid quantum systems provides a flexibility that allows for various components to be coupled together, thereby expanding the opportunity to build quantum sensors and devices that can be designed for specific purposes. Key to doing so is being able to strongly couple the different components. Most developments to date have relied on the components being in close proximity, which can hamper design flexibility. Karg *et al*. used a laser to induce strong coupling between a cloud of atoms and an optomechanical membrane. With the components separated by 1 meter, this approach demonstrates a methodology of coupling quantum systems and easing up restrictions on spatial proximity. —ISO

Science, this issue p. 173

ARCTIC PRODUCTIVITY

Food for thought

Phytoplankton abundances in the Arctic Ocean have been increasing over recent decades as the region has warmed and sea ice has disappeared. The presumptive causes of this increase were expanding open water area and a longer growing season—at least until now. Lewis *et al*. show that although these factors may have driven the productivity trends before, over the past decade, phytoplankton primary production rose by more than half because of increased phytoplankton concentrations (see the Perspective by Babin). This finding means that there has been an influx of new nutrients into the region, suggesting that the Arctic Ocean could become more productive and export additional carbon in the future. —HJS

Science, this issue p. 198; see also p. 137

AGING

Plasma transfers exercise benefit in mice

Exercise has a broad range of beneficial healthful effects. Horowitz *et al*. tested whether the beneficial effects of exercise on neurogenesis in the brain and improved cognition in aged mice could be transferred in plasma (blood without its cellular components) from one mouse to another (see the Perspective by Ansere and Freeman). Indeed, aged mice that received plasma from young or old mice that had exercised showed beneficial effects in their brains without hitting the treadmill. The authors identified glycosylphosphatidylinositol-specific phospholipase D1 as a factor in plasma that might, in part, mediate this favorable effect. —LBR

Science, this issue p. 167; see also p. 144

IN OTHER JOURNALS

Edited by **Caroline Ash** *and* **Jesse Smith**

PLANT BIOLOGY

Getting to the root of a problem

Plants are rooted to a spot; they cannot migrate away from sources of damage, except potentially by growth. If a plant's roots are damaged, then the plant has to restore them. Hoermayer *et al.* examined restorative root growth in the model plant *Arabidopsis thaliana*. They used single-cell tracing and live-cell imaging to visualize the processes by which roots perceive a wound and then coordinate their regrowth response. After laser wounding, collapsed damaged cells triggered the release of the plant growth hormone auxin next to the wound site. This in turn regulated cell expansion and restorative division as the root cells divided to fill in the wound in response to changes in turgor pressure. Interfering with auxin signaling leads to overproliferation and the formation of tumorous growths on the repaired roots. —SMH

Proc. Natl. Acad. Sci. U.S.A. **117**, 15322 (2020).

The model plant *Arabidopsis thaliana* is used to show how plant roots respond to and repair wounding.

PHOTO: CUSTOM LIFE SCIENCE IMAGES/ALAMY STOCK PHOTO

EPIDEMIOLOGY

Early warning signs

Modeling an emerging infectious disease is an inexact science. At an early stage of an epidemic, we only have sparse data, little knowledge of the mechanisms driving emergence, and an urgent need to devise control measures that will be effective. Using epidemiological incidence reports, Brett and Rohani have developed a detection algorithm for disease (re)emergence that is agnostic to the mechanisms involved. This supervised statistical learning algorithm was

Although macaques have the auditory anatomy for speech and making music, they do not speak because they lack control in the upper vocal tract.

NEUROSCIENCE

Monkeying with the piano

The anatomical organization of auditory cortical pathways in nonhuman primates (NHPs) shows remarkable similarities with humans. So why don't NHPs have a more speech-like communication system? Archakov *et al*. trained macaques to perform an auditory-motor task using a purpose-built piano. Mapping brain activity by functional magnetic resonance imaging showed that sound sequences activated the auditory midbrain and cortex. More importantly, sound sequences that had been learned by self-production also activated motor cortex and basal ganglia. This shows that monkeys can form auditory-motor links and that this is not the reason why they do not speak. Instead, the origin of speech in humans may have required the evolution of a command apparatus that controls the upper vocal tract. —PRS

Proc. Natl. Acad. Sci. U.S.A. **117**, 15242 (2020).

trained on data collected for mumps outbreaks in England and resurgent pertussis in the United States. The algorithm successfully anticipated reemergence of mumps 4 years in advance, which would have given plenty of time for mitigation efforts to be implemented. The algorithm also performed well for vector-borne diseases, including dengue in Puerto Rico, and predicted the rapid emergence of plague in Madagascar. The success of this approach stems from the common statistical properties of incidence data across disease emergence contexts and has obvious application for monitoring waves of severe acute respiratory syndrome coronavirus 2 (SARS-CoV-2) reemergence. —CA

PLOS BIOL. **18**, e3000697 (2020).

PHYSIOLOGY

DNA repair in the placenta

The human developmental disorder called Cornelia de Lange syndrome (CdLS) is caused by mutations that impair the function of cohesin, a protein complex that is important for genome organization and DNA repair. Singh *et al*. examined placentation in mouse models of CdLS and found evidence of persistent DNA damage, exit from the cell cycle (senescence), and inflammatory cytokine production. This identifies DNA damage responses as an important facet of placenta homeostasis that can affect embryo health. Further studies are needed to determine whether DNA damage responses in the placenta affect embryo development more broadly. —GKA

Dev. Cell 10.1016/j.devcel.2020.05.025 (2020).

EDUCATION

Getting active to increase equity

Attrition and underrepresentation in science, technology, engineering, and math (STEM) go hand in hand. Part of this relationship is due to underrepresented students experiencing achievement gaps, especially in "gateway" courses. Theobald *et al*. investigated whether underrepresented students in active-learning classrooms experience narrower achievement gaps than underrepresented students in a traditional lecture course. The research team collected data on exam scores and failure rates for ~54,000 students in both traditional lecturing and active-learning STEM courses taught by the same instructor. On average, active learning reduced achievement gaps in exam scores and passing rates and offered disproportionate benefits for underrepresented groups. These results provide more support for replacing traditional lecturing with active learning, which now has the added benefit of being a strategy for increasing equity in higher education. —MMc

Proc. Natl. Acad. Sci. U.S.A. **117**, 6476 (2020).

BIOMOLECULAR IMAGING

Holding protein pairs in place

Superresolution fluorescence imaging can determine where protein interactions occur in cells. However, this method can suffer from false positives because the detection of protein proximity is a function of optical resolution. Clowsley *et al*. ensured that the detected signals come from a particular pair of interacting proteins by using the DNA-PAINT (point accumulation imaging in nanoscale topography) method. In this method, proteins bind to two different antibodies that in turn are bound to DNA constructs. DNA-imaging strands are active only if the two constructs are close enough to enable DNA dimerization. This was used to image cardiac proteins in isolated cardiomyocytes with nanoscale resolution. —PDS

J. Am. Chem. Soc. 10.1021/jacs.9b03418 (2020).

PSYCHOLOGY

Greater variability, greater punishment

Prior research has linked unpredictability in outcomes to a heightened sense of vulnerability. It has also been found that feelings of vulnerability can generate more severe forms of morality. Building on these lines of research, Ding *et al*. investigated whether exposing people to greater variability in outcomes may lead to harsher moral judgment. Participants who saw graphs presenting more extreme data or who rolled dice that were manipulated to yield more extreme scores were more likely to support harsher punishment and to engage in more punitive behaviors in economic games. These findings have implications for how individuals may cope with increasingly unpredictable and variable environments. —TSR

J. Pers. Soc. Psychol. **118**, 1101 (2020).

PHOTO: REINHARD DIRSCHERL/ALAMY STOCK PHOTO

REVIEW SUMMARY

LYMPHATIC BIOLOGY

Biological functions of lymphatic vessels

Tatiana V. Petrova* and Gou Youngo Koh*

BACKGROUND: Blood and lymphatic vessel networks form two arms of the vertebrate cardiovascular system that play complementary roles in body homeostasis maintenance and multiple diseases. Lymphatic vessels are lined with lymphatic endothelial cells (LECs), which represent a distinct endothelial cell lineage characterized by a specific transcriptional and metabolic program. The general functions of lymphatic vessels in fluid transport and immunosurveillance are well recognized, as is their specialization into capillaries, serving as an entrance point of interstitial components and immune cells and collecting vessels that deliver lymph to lymph nodes (LNs) and blood circulation. It is becoming increasingly clear that adult lymphatic vessels, exposed to different organ-specific environments, acquire distinct characteristics and in turn execute multiple tissue-specific functions.

ADVANCES: This Review provides an overview of the recent advances in our understanding of new functions of adult mammalian lymphatic vessels, such as immunomodulation, contribution to neurodegenerative and neuroinflammatory diseases, and response to anticancer therapies. LN LECs have been shown to archive antigens and directly regulate immune cell properties, including immune cell survival and positioning within the LN. Rediscovery of meningeal lymphatic vessels has uprooted the dogma of brain immune privilege, and these vessels now emerge as key regulators of neuroinflammation and neurodegeneration. Intestinal lacteals display distinct cellular characteristics that make them especially suitable for dietary fat uptake and designate them as promising targets for the treatment of obesity. Tumor lymphatics have long been recognized as conduits for metastatic cell dissemination; however, recent data show that lymphatic vessels have multiple additional functions, such as forming metastatic cancer cell niches but also controlling productive response to antitumor immune therapies. Last, discovery of vascular beds with hybrid blood and lymphatic characteristics, such as the Schlemm's canal in the eye and the kidney ascending vasa recta, underscores the degree and potential of endothelial cell plasticity.

OUTLOOK: Molecular characteristics of organ-specific vascular beds and understanding their organotypic functions are among the current fundamental questions of vascular biology. Emerging evidence points to the major contribution of lymphatic vessels, a vascular system generally associated only with tissue-drainage functions. High-resolution analyses of endothelial heterogeneity and organotypic lymphatic vessel architecture, in addition to deciphering the molecular codes that LECs use for communication with other cell types, are necessary to fully understand the role of lymphatics in organ physiology and pathology. Integration of such knowledge with research from other fields, such as immunology and bioengineering, will uncover new possibilities for promoting tissue regeneration and developing new therapies for cancer, obesity, neuroinflammation, and neurodegeneration. ■

ON OUR WEBSITE

Read the full article at https://dx.doi.org/10.1126/science.aax4063

The list of author affiliations is available in the full article online.
*Corresponding author. Email: tatiana.petrova@unil.ch (T.V.P.); gykoh@kaist.ac.kr (G.Y.K.)
Cite this article as T. V. Petrova, G. Y. Koh, *Science* **369**, eaax4063 (2020). DOI: 10.1126/science.aax4063

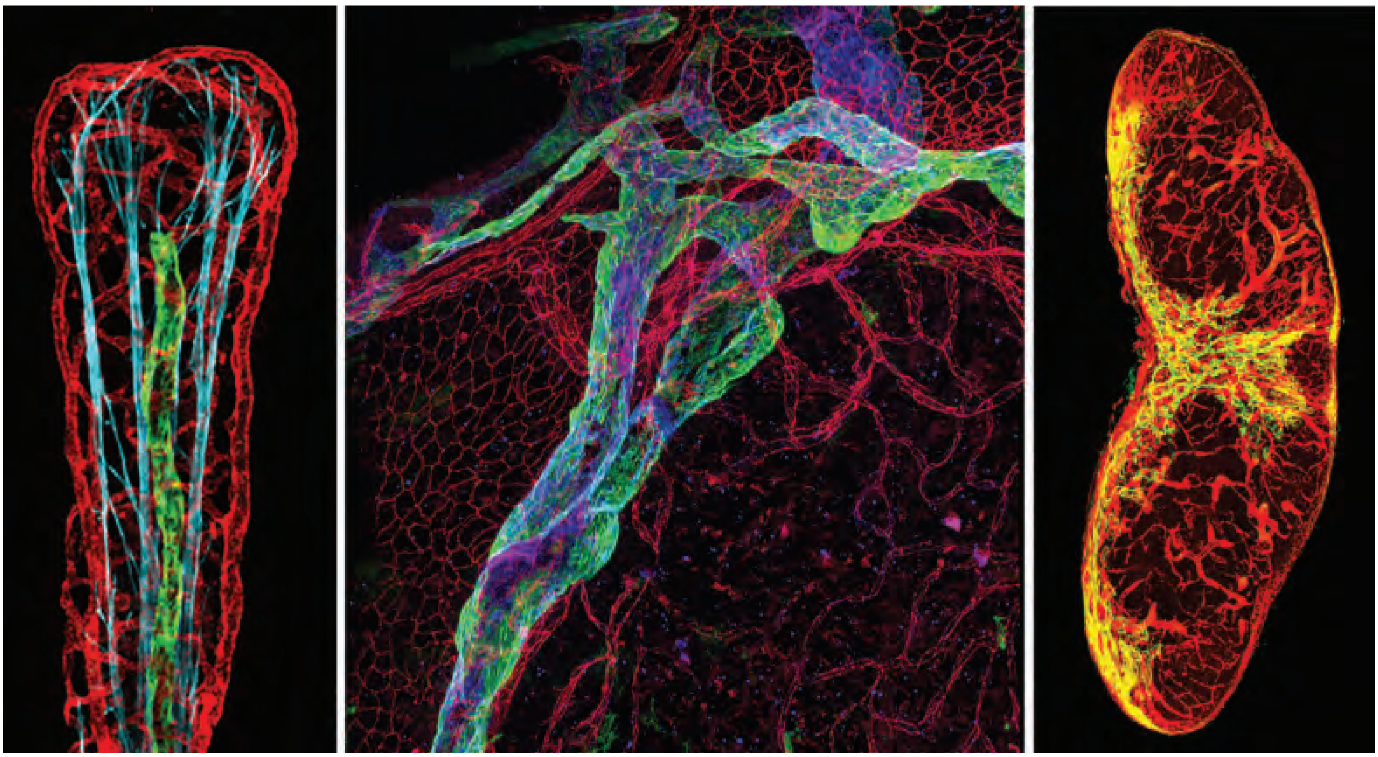

Organ-specific lymphatic vessels in small intestine, meninges, and LN. (Left) Small intestine. Shown are LYVE-1$^+$ (green) lacteal, CD31$^+$(red) capillary plexus, and α-smooth actin$^+$ (blue) longitudinal smooth muscle cells. (Middle) Meninges. Shown are LYVE-1$^+$ (green) and VEGFR3$^+$ (blue) lymphatic vessels and CD31$^+$ (red) blood vessels. (Right) LN. Shown are LYVE-1$^+$ (green) lymphatic vessels and CD31$^+$(red) blood vessels, including high endothelial venules.

IMAGES: J. BERNIER-LATMANI AND H. CHO

RESEARCH ARTICLE SUMMARY

DEVELOPMENTAL BIOLOGY

Contact area–dependent cell communication and the morphological invariance of ascidian embryogenesis

Léo Guignard*, Ulla-Maj Fiúza*, Bruno Leggio, Julien Laussu, Emmanuel Faure, Gaël Michelin, Kilian Biasuz, Lars Hufnagel†, Grégoire Malandain†‡, Christophe Godin†‡, Patrick Lemaire†‡

INTRODUCTION: Within each animal species, embryonic development is highly reproducible, ensuring the faithful production of a complex organism with precisely arranged and shaped organs. In most animal embryos, reproducibility is found at the tissue scale, the behaviors of individual cells being stochastic beyond the first cell divisions. Ascidians, a group of marine invertebrate chordates, show an extreme form of embryonic reproducibility: Homologous cells can be found across individual embryos, and early embryonic cell lineages are considered invariant. Embryonic geometries are even conserved between species, which diverged 400 million years ago and have very dissimilar genomes. Because of their evolutionary conservation of early embryonic development and ability to buffer genetic divergence, ascidians constitute attractive model systems to study the mechanisms driving cellular reproducibility.

RATIONALE: To quantify embryonic reproducibility in the ascidian *Phallusia mammillata*, we first built a high-resolution atlas of embryonic cell lineages, cell shapes, and cell interactions. We imaged 10 live embryos every 2 min up to the end of the neurula stages using multiview light-sheet microscopy. To systematically measure the developmental variability of a range of temporal and spatial cellular features, we developed a robust and scalable adaptive segmentation and tracking of embryonic cells procedure (ASTEC) compatible with high-throughput multiview light-sheet imaging datasets. We related these features to cell fate specification, which in ascidians is mainly controlled by differential sister cell inductions. Inspired by previous work indicating that the area of contact to signaling cells controls ascidian neural induction, we integrated our geometric description with a signaling gene expression atlas. This integration allowed us to test, through computational and experimental approaches, the hypothesis that contact area–dependent cell communication imposes constraints on embryonic geometries.

RESULTS: We found that, up to the neurula stages, *Phallusia* embryos develop without cell growth, programmed cell death, or cell neighbor exchanges. Beyond cell position, cell cycle duration, and cell lineages, we observed a high reproducibility of cell arrangements: 75% of cells shared at least 80% of their neighbors in all 10 embryos studied. Furthermore, the areas of contact between homologous cells varied by less than 20% across embryos. Mechanistically, we uncovered a tight link between the control of cell arrangements and asymmetric cell divisions, which give rise to sister cells of distinct fates. We then combined computational and experimental approaches to reveal that areas of cell contact between signaling and responding cells have sufficient encoding potential to explain all known early embryonic inductions, without the need to invoke gradients of ligand concentration. Finally, using geometrical perturbations of embryonic development we demonstrated that precise areas of cell-cell contact were important for mesendodermal and neural fate specification.

CONCLUSION: Our work establishes the highly reproducible ascidian embryo as a framework to bridge cell behaviors, morphogenesis, and the underlying regulatory program. The ASTEC pipeline allows systematic automated whole-cell segmentation and tracking across whole embryos in high-throughput light-sheet datasets. Second, we establish the geometric control of embryonic inductions as an alternative to classical morphogen gradients and suggest that the range of cell signaling events sets the scale at which embryonic reproducibility is observed. Finally, our study suggests that the high level of reproducibility of ascidian embryonic geometries may paradoxically lift constraints on the evolution of ascidian genomes, thereby contributing to rapid molecular evolution. ■

ON OUR WEBSITE

Read the full article at https://dx.doi.org/10.1126/science.aar5663

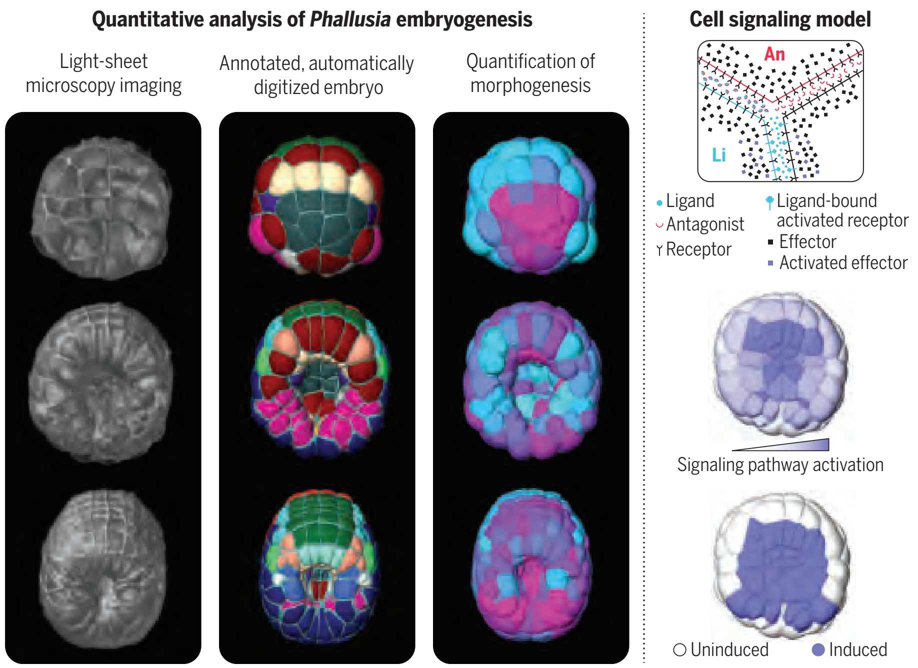

Reconstruction and modeling of *Phallusia* embryogenesis. (Left) Quantitative analysis of *Phallusia* embryogenesis. We combined live light-sheet imaging of cell membranes (left images) with automated cell segmentation and tracking with color-coded cell fates (center images) to extract quantitative cell morphological properties (right images, color-coded by cell compactness). From top to bottom: embryo at the 64-cell, mid-gastrula, and late gastrula stages. (Right) Cell signaling model. We first made simplifying assumptions concerning the distribution and diffusion of signaling pathway components (top) and then integrated cell contact geometry with gene expression profiles to predict pathway activation levels in single cells (center) and binarized induction status (bottom).

The list of author affiliations is available in the full article online.
*These authors contributed equally to this work.
†Corresponding author. Email: hufnagel@embl.de (L.H.); gregoire.malandain@inria.fr (G.Ma.); christophe.godin@inria.fr (C.G.); patrick.lemaire@crbm.cnrs.fr (P.L.)
‡These authors contributed equally to this work.
Cite this article as L. Guignard *et al.*, *Science* 369, eaar5663 (2020). DOI: 10.1126/science.aar5663

RESEARCH ARTICLE SUMMARY

ORGANOIDS

Human CNS barrier-forming organoids with cerebrospinal fluid production

Laura Pellegrini, Claudia Bonfio, Jessica Chadwick, Farida Begum, Mark Skehel, Madeline A. Lancaster*

INTRODUCTION: The choroid plexus is a secretory epithelial tissue of the central nervous system (CNS) responsible for cerebrospinal fluid (CSF) production and functions as a barrier that regulates entry of compounds and nutrients into the brain. The CSF plays key roles in the delivery of nutrients to the brain, circulation of instructive signaling molecules, and clearance of toxic by-products such as protein aggregates.

RATIONALE: Current understanding of the choroid plexus and CSF has primarily come from animal models or CSF collected from human volunteers. These have yielded insight into general CSF composition, but the specific cellular and tissue sources of various secreted proteins have remained elusive. There is also limited understanding of the development of the choroid plexus in humans and of the relative changes in CSF composition over time. All of these deficiencies in our understanding come from a lack of experimental access to the human choroid plexus. Although several previous studies have successfully generated cells with a choroid plexus identity from human pluripotent stem cells, none have been able to recapitulate the morphology, maturation, and function of the choroid plexus, and currently, no in vitro model exists for authentic human CSF. Knowledge of the processes that regulate choroid plexus development and CSF composition could provide better strategies to manipulate and therapeutically target this vital brain tissue.

RESULTS: To study the development and function of the human choroid plexus, we developed a pluripotent stem cell–derived organoid model. Choroid plexus organoids recapitulate key morphological and functional features of human choroid plexus. First, organoids form a tight barrier that selectively regulates the entry of small molecules such as dopamine. We demonstrate that organoids can qualitatively and quantitatively predict the permeability of new drugs, and we take advantage of this system to reveal a potential toxic accumulation of BIA 10-2474, a drug that caused severe neurotoxicity only in humans and not in animal models tested. Second, choroid plexus organoids secrete a CSF-like fluid containing proteins and known biomarkers within self-contained compartments. We examine changes in secretion of CSF proteins over time and identify distinct cell types within the epithelium that contribute to dynamic changes in CSF composition. We find that these cell types can be traced to rather obscure descriptions in the literature of "dark" and "light" cells, and we demonstrate that these cells exhibit opposing features related to mitochondria and cilia. We also uncover a previously unidentified cell type in the choroid plexus: myoepithelial cells. These interacting subpopulations exhibit distinct secretory roles in CSF production and reveal previously uncharacterized human-specific secreted proteins that may play important roles in human brain development.

CONCLUSION: Human choroid plexus organoids provide an easily tractable system to study the key functions of this organ: CSF secretion and selective transport into the CNS. As such, they can predict CNS permeability of new compounds to aid in the development of neurologically relevant therapeutics. They also provide a source of more authentic CSF and can be used to understand development of this key organ in brain development and homeostasis. ■

ON OUR WEBSITE

Read the full article at https://dx.doi.org/10.1126/science.aaz5626

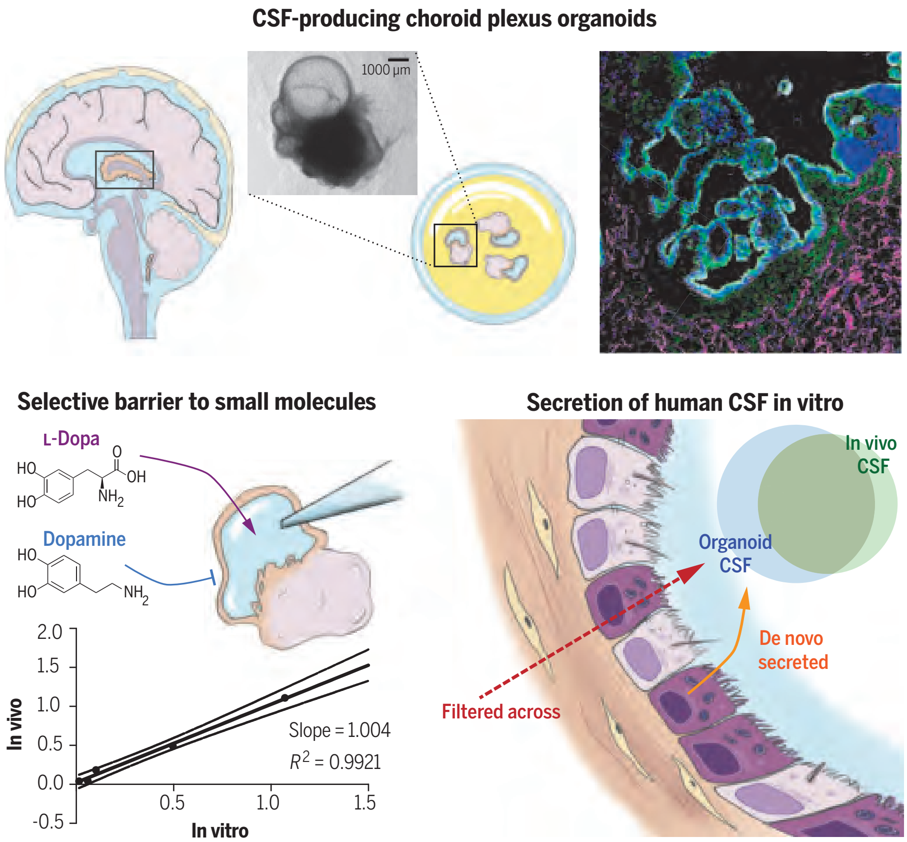

CSF-producing choroid plexus organoids predict CNS permeability of drugs. Choroid plexus organoids develop highly intricate folded tissue morphology (section stained for choroid plexus markers shown at top right) similar to choroid plexus tissue in vivo (top left) and, later, self-contained fluid-filled compartments containing a CSF-like fluid (top middle) that is separate from media. (Bottom left) Choroid plexus organoids accurately predict the permeability of small molecules such as dopamine and levodopa (L-dopa) and quantitatively predict the permeability of a range of therapeutic molecules. The graph shows the correlation between permeability in vivo and in vitro for the drugs tested. R^2, coefficient of determination. (Bottom right) Single-cell RNA sequencing reveals newly identified epithelial subtypes (colored dark and light) that participate in filtration and specialized secretion of CSF proteins. The Venn diagram shows overlap between proteins detected in CSF in vivo and in the organoid.

MRC Laboratory of Molecular Biology, Francis Crick Avenue, Cambridge CB2 0QH, UK.
*Corresponding author. Email: mlancast@mrc-lmb.cam.ac.uk
Cite this article as L. Pellegrini *et al.*, *Science* 369, eaaz5626 (2020). DOI: 10.1126/science.aaz5626

RESEARCH ARTICLE SUMMARY

CORONAVIRUS

Inferring change points in the spread of COVID-19 reveals the effectiveness of interventions

Jonas Dehning*, Johannes Zierenberg*, F. Paul Spitzner*, Michael Wibral, Joao Pinheiro Neto, Michael Wilczek*, Viola Priesemann*†

INTRODUCTION: When faced with the outbreak of a novel epidemic such as coronavirus disease 2019 (COVID-19), rapid response measures are required by individuals, as well as by society as a whole, to mitigate the spread of the virus. During this initial, time-critical period, neither the central epidemiological parameters nor the effectiveness of interventions such as cancellation of public events, school closings, or social distancing is known.

RATIONALE: As one of the key epidemiological parameters, we inferred the spreading rate λ from confirmed SARS-CoV-2 infections using the example of Germany. We apply Bayesian inference based on Markov chain Monte Carlo sampling to a class of compartmental models [susceptible-infected-recovered (SIR)]. Our analysis characterizes the temporal change of the spreading rate and allows us to identify potential change points. Furthermore, it enables short-term forecast scenarios that assume various degrees of social distancing. A detailed description is provided in the accompanying paper, and the models, inference, and forecasts are available on GitHub (https://github.com/Priesemann-Group/covid19_inference_forecast). Although we apply the model to Germany, our approach can be readily adapted to other countries or regions.

RESULTS: In Germany, interventions to contain the COVID-19 outbreak were implemented in three steps over 3 weeks: (i) Around 9 March 2020, large public events such as soccer matches were canceled; (ii) around 16 March 2020, schools, childcare facilities, and many stores were closed; and (iii) on 23 March 2020, a far-reaching contact ban (*Kontaktsperre*) was imposed by government authorities; this included the prohibition of even small public gatherings as well as the closing of restaurants and all nonessential stores.

From the observed case numbers of COVID-19, we can quantify the impact of these measures on the disease spread using change point analysis. Essentially, we find that at each change point the spreading rate λ decreased by ~40%. At the first change point, assumed around 9 March 2020, λ decreased from 0.43 to 0.25, with 95% credible intervals (CIs) of [0.35, 0.51] and [0.20, 0.30], respectively. At the second change point, assumed around 16 March 2020, λ decreased to 0.15 (CI [0.12, 0.20]). Both changes in λ slowed the spread of the virus but still implied exponential growth (see red and orange traces in the figure).

To contain the disease spread, i.e., to turn exponential growth into a decline of new cases, the spreading rate has to be smaller than the recovery rate μ = 0.13 (CI [0.09, 0.18]). This critical transition was reached with the third change point, which resulted in λ = 0.09 (CI [0.06, 0.13]; see blue trace in the figure), assumed around 23 March 2020.

From the peak position of daily new cases, one could conclude that the transition from growth to decline was already reached at the end of March. However, the observed transient decline can be explained by a short-term effect that originates from a sudden change in the spreading rate (see Fig. 2C in the main text).

As long as interventions and the concurrent individual behavior frequently change the spreading rate, reliable short- and long-term forecasts are very difficult. As the figure shows, the three example scenarios (representing the effects up to the first, second, and third change point) quickly diverge from each other and, consequently, span a considerable range of future case numbers.

ON OUR WEBSITE

Read the full article at https://dx.doi.org/10.1126/science.abb9789

Inference and subsequent forecasts are further complicated by the delay of ~2 weeks between an intervention and the first useful estimates of the new λ (which are derived from the reported case numbers). Because of this delay, any uncertainty in the magnitude of social distancing in the previous 2 weeks can have a major impact on the case numbers in the subsequent 2 weeks. Beyond 2 weeks, the case numbers depend on our future behavior, for which we must make explicit assumptions. In sum, future interventions (such as lifting restrictions) should be implemented cautiously to respect the delayed visibility of their effects.

CONCLUSION: We developed a Bayesian framework for the spread of COVID-19 to infer central epidemiological parameters and the timing and magnitude of intervention effects. With such an approach, the effects of interventions can be assessed in a timely manner. Future interventions and lifting of restrictions can be modeled as additional change points, enabling short-term forecasts for case numbers. In general, our approach may help to infer the efficiency of measures taken in other countries and inform policy-makers about tightening, loosening, and selecting appropriate measures for containment of COVID-19. ■

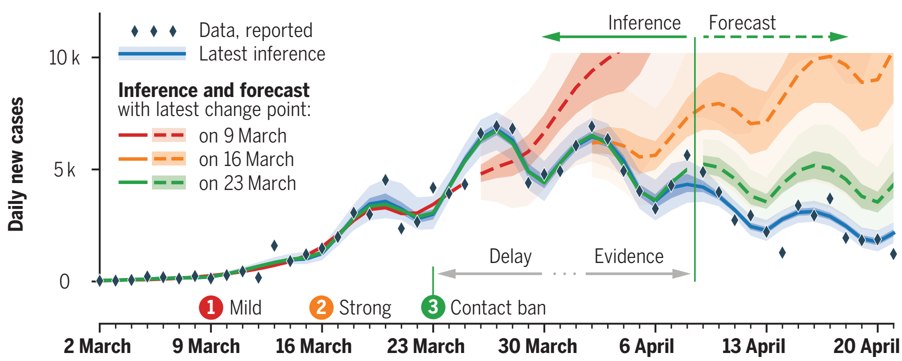

Bayesian inference of SIR model parameters from daily new cases of COVID-19 enables us to assess the impact of interventions. In Germany, three interventions (mild social distancing, strong social distancing, and contact ban) were enacted consecutively (circles). Colored lines depict the inferred models that include the impact of one, two, or three interventions (red, orange, or green, respectively, with individual data cutoff) or all available data until 21 April 2020 (blue). Forecasts (dashed lines) show how case numbers would have developed without the effects of the subsequent change points. Note the delay between intervention and first possible inference of parameters caused by the reporting delay and the necessary accumulation of evidence (gray arrows). Shaded areas indicate 50% and 95% Bayesian credible intervals.

The list of author affiliations is available in the full article online.
*These authors contributed equally to this work.
†Corresponding author. Email: viola.priesemann@ds.mpg.de

Cite this article as J. Dehning *et al.*, *Science* 369, eabb9789 (2020). DOI: 10.1126/science.abb9789

RESEARCH ARTICLES

STRUCTURAL BIOLOGY

Structure and selectivity engineering of the M_1 muscarinic receptor toxin complex

Shoji Maeda[1]*, Jun Xu[2], Francois Marie N. Kadji[3], Mary J. Clark[4], Jiawei Zhao[5], Naotaka Tsutsumi[1,6,7], Junken Aoki[3], Roger K. Sunahara[4], Asuka Inoue[3], K. Christopher Garcia[1,6,7], Brian K. Kobilka[1,2]*

Muscarinic toxins (MTs) are natural toxins produced by mamba snakes that primarily bind to muscarinic acetylcholine receptors (MAChRs) and modulate their function. Despite their similar primary and tertiary structures, MTs show distinct binding selectivity toward different MAChRs. The molecular details of how MTs distinguish MAChRs are not well understood. Here, we present the crystal structure of M_1AChR in complex with MT7, a subtype-selective anti-M_1AChR snake venom toxin. The structure reveals the molecular basis of the extreme subtype specificity of MT7 for M_1AChR and the mechanism by which it regulates receptor function. Through in vitro engineering of MT7 finger regions that was guided by the structure, we have converted the selectivity from M_1AChR toward M_2AChR, suggesting that the three-finger fold is a promising scaffold for developing G protein–coupled receptor modulators.

Selective targeting of a specific subtype of a G protein–coupled receptor (GPCR) among its family members is a major challenge in developing receptor-specific drugs with minimal undesired effects (*1*). Efforts to design compounds with strict specificity toward target GPCRs are often hampered by high conservation of the orthosteric binding site. Allosteric binding sites, on the other hand, share less homology between family members and thus have been targeted as alternative sites for drug discovery (*2*, *3*). Muscarinic toxins (MTs) are small protein toxins consisting of 65 to 66 amino acid residues derived from the venoms of African mambas. They belong to a large superfamily, the three-finger toxin (3FT) family (*4*–*6*). Despite their high similarity in the sequence and structure, 3FTs exhibit distinct interaction profiles against the five muscarinic acetylcholine receptor (MAChR) subtypes (M_1AChR to M_5AChR) (*7*–*11*). Among the subtypes, MT7 has the highest specificity toward M_1AChR over other muscarinic receptors, with a difference in affinity of more than five orders of magnitude (*12*–*16*). Studies have shown that MT7 binds M_1AChR at subnanomolar affinity with a very slow dissociation rate (*17*), inhibits agonist-mediated guanosine 5′-*O*-(3′-thiotriphosphate) (GTP-γ-S) binding and downstream signaling (*16*, *18*–*20*), and decreases the dissociation rate of orthosteric antagonists {[^{3}H]*N*-methylscopolamine ([^{3}H]NMS) or [^{3}H]pirenzepine} (*20*). Thus, MT7 is a potent negative allosteric modulator (NAM) for M_1AChR activation and a positive allosteric modulator (PAM) for antagonist binding. Because of its extremely high specificity toward M_1AChR, MT7 has attracted research interest into understanding the structural basis for its mode of action. Here, we present the crystal structure of the M_1AChR-MT7 complex bound to the orthosteric antagonist. The structure reveals the molecular mechanism of the allosteric regulation by MT7 as well as the specific interactions that dictate subtype selectivity. On the basis of this structural information, we engineered MT7 in vitro to redirect its selectivity, yielding a modulator specific for M_2AChR. More broadly, this work shows the utility of the 3FT fold for solving the difficult problem of generating specific high-affinity binding proteins to GPCR extracellular loops.

Preparation and structure determination of the M_1AChR-MT7 complex

The M_1AChR-MT7 complex was formed by using recombinantly expressed M_1AChR from Sf9 insect cells and MT7 from Hi5 insect cells as described in the supplementary materials (fig. S1A). Although we were able to form a stable complex between M_1AChR bound to the antagonist atropine and MT7 (fig. S1B), our initial attempts to crystallize this complex in lipidic cubic phase (LCP), a widely used method for crystallizing GPCRs, were unsuccessful, yielding crystals made of M_1AChR alone. It has been shown that low–molecular weight polyethylene glycols (PEGs), reagents commonly used as precipitants in LCP crystallography, can occupy the extracellular vestibule of M_4AChR (*21*). We determined that low–molecular weight PEGs could compete with MT7 for binding to M_1AChR (fig. S1, C and D), supporting the notion that MT7 is displaced by the PEG molecules during crystallogenesis. Through the screening of alternative precipitant reagents, we finally succeeded in obtaining crystals of the M_1AChR-MT7 complex by using the hanging drop vapor diffusion method in a condition with no PEG, and the structure was determined at 2.55-Å resolution (fig. S2 and table S1).

Interactions between M_1AChR and MT7

The structure shows that the extracellular vestibule is occupied, with finger loop 2 blocking access to the orthosteric site (Fig. 1A and fig. S3), and this explains the reported slow dissociation of [^{3}H]NMS from the orthosteric site when bound to MT7 (*18*). Comparison of MT7 alone and MT7 in complex with M_1AChR showed that finger loops 1 and 3 undergo large structural rearrangements upon binding to M_1AChR, facilitating extensive interactions with the receptor, while finger loop 2 is mostly unchanged (*22*) (fig. S4). The large displacement of finger loops 1 and 3 is consistent with molecular dynamics simulations on another snake-derived 3FT, toxin α from *Naja nigricollis* (*23*), which revealed finger loops 1 and 3 to be highly dynamic. The flexibility of finger loops 1 and 3 may explain why some 3FTs can bind to multiple targets (*24*). In agreement with previous studies, the interactions between M_1AChR and MT7 occur predominantly with extracellular loop 2 (ECL2) of M_1AChR (Fig. 1B) (*25*–*27*). Finger loop 1 of MT7 forms extensive hydrophobic interactions with residues in transmembrane helix 4 (TM4) and ECL2 (Fig. 1B, red rectangle). Because these hydrophobic residues are conserved in finger loop 1 of other MT members and in TM4 and ECL2 of other muscarinic receptor subtypes (Fig. 1B and fig. S5), these interactions are not likely to contribute to MT7 subtype selectivity. Finger loop 2 forms the most extensive interactions with ECL2 and TM7, largely consisting of polar contacts. Residues in finger loops 2 and 3 form specific interactions with M_1AChR residues E170 and L174 in ECL2 and E397$^{7.32}$ and E401$^{7.36}$ at the top of TM7 [superscripts correspond to Ballesteros-Weinstein numbering (*28*)] (Fig. 1B, yellow and cyan rectangles). Sequence alignment of MAChRs shows that E170, L174, E397$^{7.32}$, and E401$^{7.36}$ are not conserved in other MAChRs, suggesting that these M_1AChR-specific interactions likely dictate the subtype selectivity of MT7 (Fig. 1B). This conclusion is supported by studies where substitution of these residues of M_1AChR into the equivalent positions in M_3AChR or M_5AChR yields receptors that bind MT7 (*25*, *26*, *29*). Not surprisingly, these

[1]Department of Molecular and Cellular Physiology, Stanford University School of Medicine, Stanford, CA 94305, USA. [2]Beijing Advanced Innovation Center for Structural Biology, School of Life Science, Tsinghua University, Beijing, China. [3]Graduate School of Pharmaceutical Science, Tohoku University, Sendai, Japan. [4]Department of Pharmacology, University of California San Diego School of Medicine, La Jolla, CA 92093, USA. [5]Tsinghua-Peking Joint Center for Life Sciences, School of Life Sciences, Tsinghua University, Beijing, China. [6]Department of Structural Biology, Stanford University School of Medicine, Stanford, CA 94305, USA. [7]Howard Hughes Medical Institute, Stanford University School of Medicine, Stanford, CA 94305, USA.
***Corresponding author. Email: shojim@stanford.edu (S.M.); kobilka@stanford.edu (B.K.K.)**

subtype-specific residues engaged in MT7 binding also form part of the binding pocket of M_1AChR-selective small-molecule allosteric modulators (*30*–*32*).

Structural changes in M_1AChR stabilized by MT7

When superposing M_1AChR-MT7 bound to atropine and toxin-free M_1AChR bound to tiotropium, engagement of MT7 stabilizes a 3- to 4-Å outward movement of TM6, ECL3, and TM7 due to the insertion of finger loop 2 into the extracellular vestibule (Fig. 2A). The outward displacement of TM7 is stabilized by a polar network involving $E401^{7.36}$ and $Y82^{2.61}$ in M_1AChR and R34 from the tip of finger loop 2 (Figs. 1B and 2B). This tyrosine residue, together with $Y85^{2.64}$, which is located one helical turn above $Y82^{2.61}$, has been reported to be one of the key elements for the binding of allosteric compounds (*31*, *33*). In addition, Y51 and R52 in finger loop 3 form polar interactions with $E397^{7.31}$ (Fig. 2B). These interactions position P33 in finger loop 2 to interact with the backbone and side chains of $W400^{7.35}$ and $E401^{7.36}$ of TM7, displacing it outward. The outward movement of $W400^{7.35}$ at the top of TM7 in turn stabilizes the outward displacement of TM6 through interactions with $M384^{6.54}$ (Fig. 2B and fig. S6). A tryptophan residue at position 7.35 ($W^{7.35}$) has been identified as a critical residue for the binding of small-molecule allosteric modulators in M_1AChR (*30*–*32*) and M_2AChR (*34*). These residues in the active MAChRs undergo inward displacement, and $W^{7.35}$ forms an aromatic stacking interaction with a PAM, LY2119620, in M_2AChR (*35*, *36*). Therefore, $W^{7.35}$ plays a role in both the positive and negative allosteric modulation of MAChRs by stabilizing the extracellular side of TM6 either inward or outward, respectively (Fig. 2B and fig. S6). We recently reported the active-state structure of M_1AChR in complex with the G protein G_{11} (*36*). In this structure, there is a 5.7-Å inward movement at the extracellular end of TM6 (at the α carbon of F390) relative to the inactive-state M_1AChR, which is accompanied by an outward movement of the cytoplasmic side of TM6 (Fig. 2C). In contrast, the outward movement of the extracellular end of TM6 in the M_1AChR-MT7 structure is associated with a small inward movement of the cytoplasmic end of TM6 (Fig. 2, B and C). The allosteric coupling of the extracellular and intracellular ends of TM6 can be explained by a rigid body movement which pivots around $W378^{6.48}$, the "rotamer toggle switch" (*37*) (Fig. 2C). As a result of the inward displacement of the cytoplasmic end of TM6 in the M_1AChR-MT7 complex, $R123^{3.50}$ in the DRY motif forms polar interactions with $N60^{2.39}$ from TM2 and the backbone carbonyl of $A363^{6.33}$ from TM6 (Fig. 2B). These interactions enhance the tight interhelical packing and lock the receptor in the inactive state. The extracellular end of TM5 is displaced slightly inward in the M_1AChR-MT7 complex compared with its position in the tiotropium-bound state (Fig. 2A). Unlike displacements of TM6 and TM7 helices that are stabilized by MT7, the displacement of TM5 could be attributed to the different sizes of the orthosteric antagonists. Atropine has a single phenyl group that faces TM3 and TM4, whereas tiotropium has two ring systems (2-thienyl groups), with the second ring facing TM5 (fig. S7). The lack of the second ring in atropine likely allows the slight inward displacement of TM5 relative to the position in the tiotropium-bound state. Indeed, the superposition of the tiotropium into the orthosteric binding site of the atropine-bound state makes a steric clash with $T192^{5.42}$ (fig. S7).

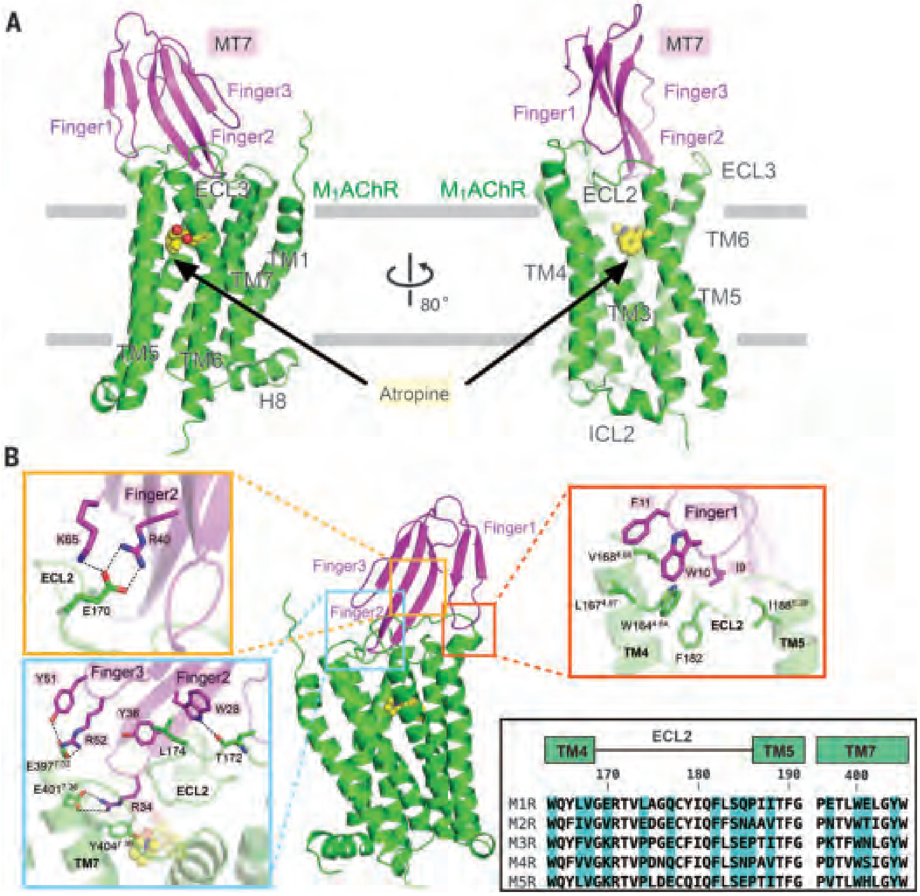

Fig. 1. Structure of the M_1AChR-MT7 complex. (**A**) Side view of the overall structure of M_1AChR-MT7. For clarity, T4L fused to M_1AChR was removed from the structure. MT7 and M_1AChR are colored magenta and green, respectively. The orthosteric antagonist atropine is colored yellow. Finger loops 1 to 3 of MT7 and ECLs and TM helices of M_1AChR are labeled. (**B**) Detailed interactions between finger loops of MT7 and M_1AChR. Interactions with finger loop 1 (red rectangle) and finger loops 2 and 3 (cyan and orange rectangles) are featured in enlarged views. Side chains making interactions are depicted as sticks. Sequence alignments of TM4-ECL2-TM5 and ECL3-TM7 from the five MAChR subtypes are shown in the bottom box. Residue numbers and TM helices of M_1AChR are represented above the alignment. Amino acid residues interacting with MT7 in M_1AChR are highlighted in blue. Single-letter abbreviations for the amino acid residues are as follows: A, Ala; C, Cys; D, Asp; E, Glu; F, Phe; G, Gly; H, His; I, Ile; K, Lys; L, Leu; M, Met; N, Asn; P, Pro; Q, Gln; R, Arg; S, Ser; T, Thr; V, Val; W, Trp; and Y, Tyr.

Redirecting the subtype selectivity of MT7 from M_1AChR to M_2AChR

With its small size and high stability, the 3FT fold has been utilized as an alternative scaffold to generate protein binders (*38*, *39*). Therefore, we designed a phage display library using MT7 as a template scaffold to explore whether we could redirect the specificity to other muscarinic receptor subtypes through structure-guided engineering. On the basis of the residues of MT7 in contact with M_1AChR in the crystal structure, we selected residues from each finger loop to be randomized (fig. S8). For the target molecule, we used M_2AChR in the presence of the antagonist atropine. After four rounds of phage panning, we identified clone 24, which binds subtype selectively toward M_2AChR over

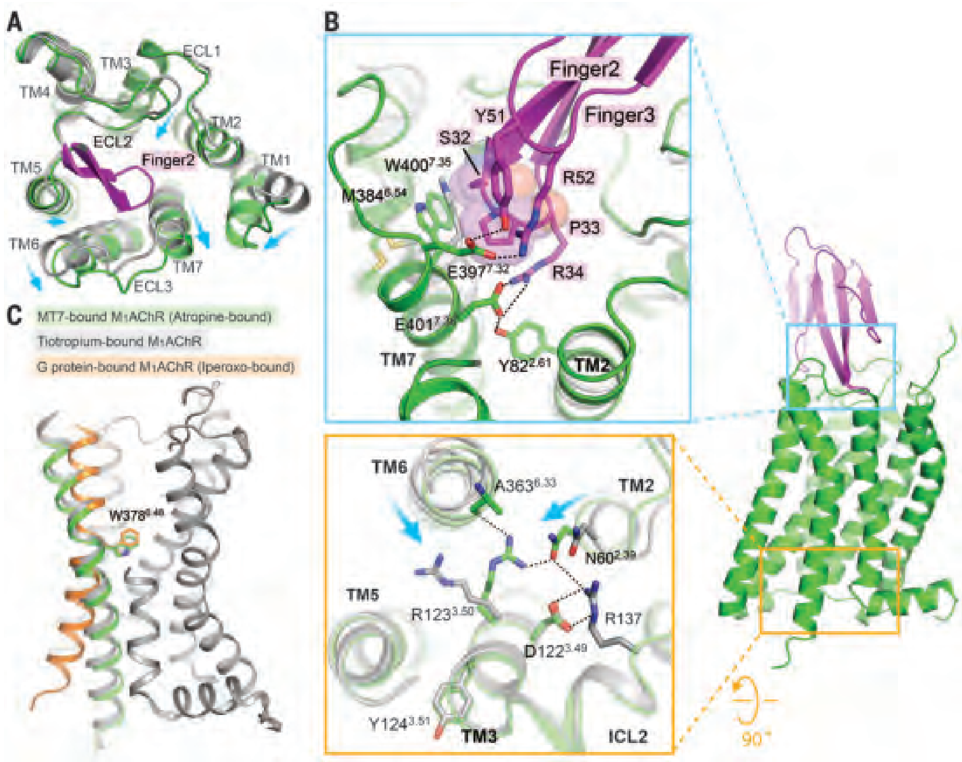

Fig. 2. Conformational changes in M_1AChR stabilized by MT7 binding. (**A**) Superposition of tiotropium-bound M_1AChR (gray; PDB ID 5CXV) and atropine-bound M_1AChR-MT7 complex (green) from the extracellular view. Part of finger loop 2 that interacts with TM7 is shown (magenta). Conformational changes are shown with arrows. (**B**) (Top) Insertion of finger loop 2 stabilizes conformational changes at the extracellular side of TM2, TM6, and TM7. Note that P33 from MT7, represented as spheres, stabilizes W400 outward. (Bottom) Differences in the organization of the DRY motif in the M_1AChR-MT7 complex compared with that of tiotropium-bound M_1AChR. Displacements of TM helices 2 and 6 are shown with arrows. (**C**) Conformational change of TM6 between different states of M_1AChR, with W378 serving as a pivotal position: M_1AChR from the M_1AChR-MT7 complex (green); M_1AChR from the tiotropium-bound inactive state (gray; PDB ID 5CXV), and M_1AChR from the M_1AChR-G_{11} complex (orange; PDB ID 6OIJ).

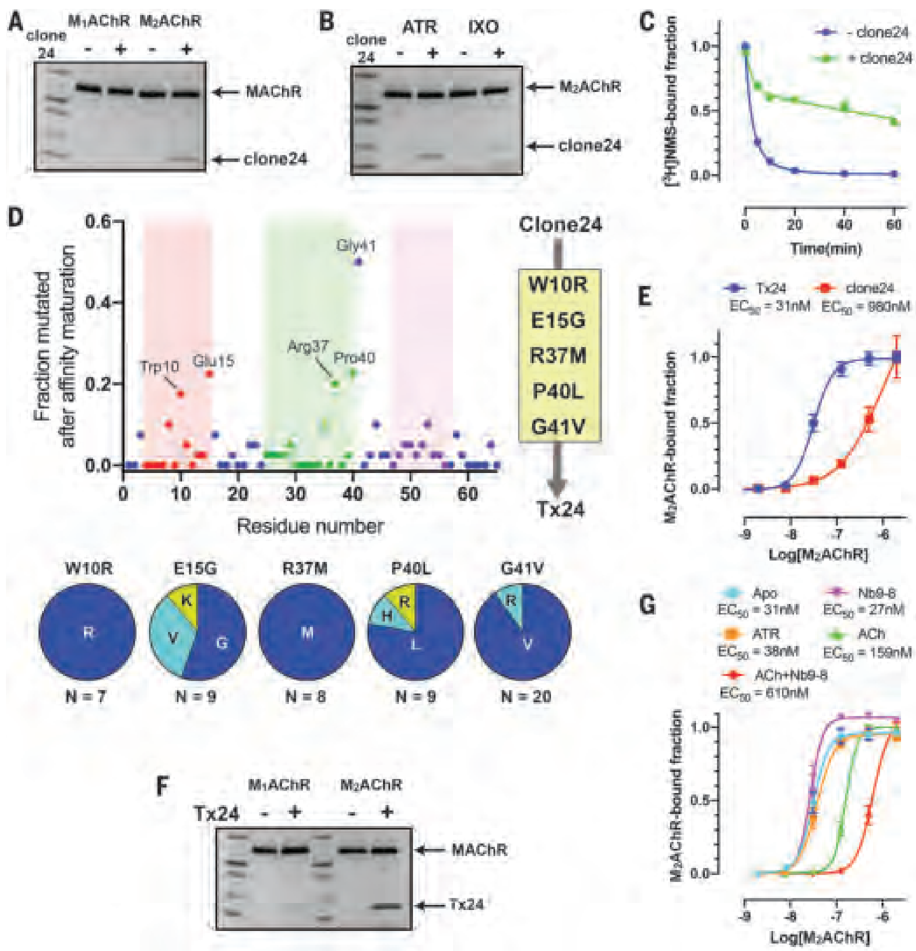

Fig. 3. Identification and affinity maturation of a subtype-selective M_2AChR allosteric modulator through in vitro selection. (**A**) Pull-down assay showing that clone 24 binds subtype selectively to M_2AChR over M_1AChR. The experiment was carried out in the presence of 10 μM atropine. (**B**) Pull-down assay showing the conformation preference of clone 24 toward the atropine (ATR)–bound state over the iperoxo (IXO)–bound state of M_2AChR. (**C**) Comparison of the dissociation kinetics of the orthosteric antagonist [^{3}H]NMS from M_2AChR in the clone 24–bound and apo state. Data represent means ± SEM of three experiments performed in triplicate. (**D**) Sequence analysis of 50 randomly selected clones after the second FACS enrichment. The finger loop regions 1, 2, and 3 are colored red, green, and purple, respectively. The five most frequent mutations (W10R, E15G, R37M, P40L, and G41V) were combined into clone 24 to generate Tx24. (**E**) Comparison of the affinities of clone 24 and Tx24 to M_2AChR using on-yeast affinity measurement in the presence of 10 μM atropine. Data represent means ± SEM of three independent experiments. (**F**) Pull-down assay of Tx24 using M_1AChR or M_2AChR in the presence of 10 μM atropine. Tx24 prefers M_2AChR over M_1AChR. (**G**) Comparison of the affinity of Tx24 for M_2AChR bound to different ligands alone or in combination with a G protein mimetic nanobody using on-yeast affinity measurement. Symbols and error bars represent means and SEM of three independent experiments.

M_1AChR and has conformational selectivity toward the inactive state (Fig. 3, A and B). Moreover, it confers a slow dissociation of the antagonist [^{3}H]NMS from the orthosteric binding pocket (Fig. 3C), suggesting that it binds allosterically to the extracellular vestibule. A substoichiometric amount of clone 24 in the pull-down assay suggested a weak affinity of the engineered toxin for M_2AChR. We therefore performed affinity maturation by introducing random mutations throughout the toxin coding region and selection using yeast surface display to obtain a high-affinity variant (fig. S9). High-affinity binders were enriched using progressively lower concentrations of M_2AChR bound with atropine during selections. After two rounds of magnetic-activated cell sorting, we further performed fluorescence-activated cell sorting (FACS) to select high-affinity clones. By combining the consensus mutations from randomly selected sequences of the affinity-maturated clones, we created a high-affinity variant, Tx24 (Fig. 3D). Tx24 gained a 30-fold enhancement in affinity for M_2AChR over clone 24 (Fig. 3E) and retained the same subtype and conformation selectivity as the original clone 24 (Fig. 3, F and G). Figure S10 shows the sequence alignments for MT7, clone 24, and Tx24.

Functional characterization of Tx24 on M_2AChR and other GPCRs

We subsequently investigated the pharmacological properties of Tx24. In the radioligand dissociation assay, Tx24 substantially decreased the dissociation rate of [^{3}H]NMS from M_2AChR, in accordance with the properties of the original clone 24 (Fig. 4). In contrast, Tx24 showed little or no impact on the dissociation rate of antagonists from other MAChR family members or from the β_2-adrenergic receptor (β_2AR) (Fig. 4A and fig. S11A), confirming the high subtype specificity of Tx24. A small (1.8-fold) decrease in the dissociation rate of [^{3}H]NMS in M_1AChR is likely caused by the residual binding between Tx24 and M_1AChR that was observed in the pull-down assay. However, this effect was much smaller than that for M_2AChR, for which a >700-fold decrease in off-rate was observed in the presence of Tx24 (fig. S11A). Moreover, the affinity of [^{3}H]NMS for M_2AChR became substantially higher in the presence of Tx24 (Fig. 4B), whereas enhancement of [^{3}H]NMS binding was barely detectable in M_1AChR and absent in M_4AChR, confirming the specificity of Tx24 for M_2AChR (fig. S11B). The median effective concentration of Tx24 for this effect on M_2AChR is in good agreement with the on-yeast affinity measurement (Fig. 3E and fig. S11B). Apart from the substantial influence on the behavior of antagonists, Tx24 has a slight negative allosteric effect on the potency of ACh, suggesting that it is a weak NAM for agonists (Fig. 4C). Next, we investigated the effect of Tx24 on G protein activation using the NanoBiT system (*40*). In the NanoBiT system, MAChR-dependent cognate G protein activation is monitored through the decrease of the luminescence signal due to the heterotrimer dissociation (fig. S12A). Tx24 on its own showed no agonistic or antagonistic activity (fig. S12A). When these results were taken together, Tx24 enhanced the inhibition by the antagonist atropine and this enhancement was specific for M_2AChR (Fig. 5A and table S2). In contrast, we observed no impact on G protein activation from other MAChRs or from the μ-opioid receptor or β_2AR (Fig. 5A and fig. S12). These results further validate the M_2AChR subtype selectivity of Tx24 in a cellular signaling context.

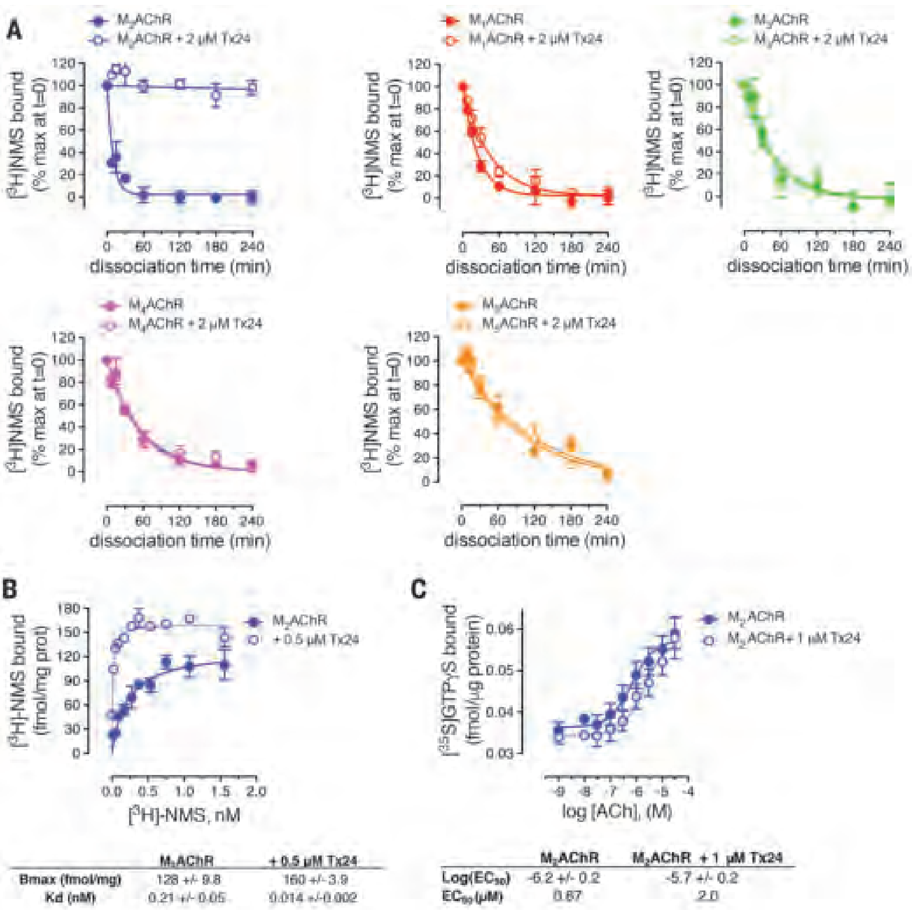

Fig. 4. Pharmacological impact of Tx24 for the dissociation of the orthosteric antagonist. (**A**) Comparison of the [^{3}H]NMS dissociation kinetics from M_2AChR (blue), M_1AChR (red), M_3AChR (magenta), M_4AChR (green), or M_5AChR (orange) in the absence (filled symbols, solid line), or presence (empty symbol, solid line) of 2 μM Tx24. Shown are the combined results from four assays performed in duplicate. (**B**) Saturation binding of [^{3}H]NMS to M_2AChR in the absence (filled symbol, solid line) or presence (empty symbol, dotted line) of 0.5 μM Tx24 after 24-hour incubation. Shown are the combined results from four assays performed in duplicate. (**C**) ACh-stimulated [^{35}S]GTP-γ-S binding at M_2AChR expressed in CHO cells in the absence (filled symbol, solid line) or presence (empty symbol, dotted line) of 1 μM Tx24. Symbols and error bars represent means and SEM of the combined results from three or four assays performed in duplicate.

Probe-dependent positive allosteric modulation of Tx24

Probe dependency of the allosteric modulator in M_2AChR has been reported with a PAM molecule for agonists that implicates a complex interaction between orthosteric and allosteric binding sites (*41*). To determine the probe dependency of Tx24, we assessed three orthosteric antagonist compounds: atropine, NMS, and tiotropium. Although Tx24 enhanced the inhibition of M_2AChR activity by atropine or NMS, it had no impact on the inhibition by tiotropium (Fig. 5B and table S3), indicating that Tx24 is a probe-selective PAM for atropine and NMS. Recent structural dynamics analysis by nuclear magnetic resonance (NMR) spectroscopy revealed distinct conformations of M_2AChR for NMS- and tiotropium-bound states (*42*). Atropine and NMS share a similar structure with a single ring system, whereas

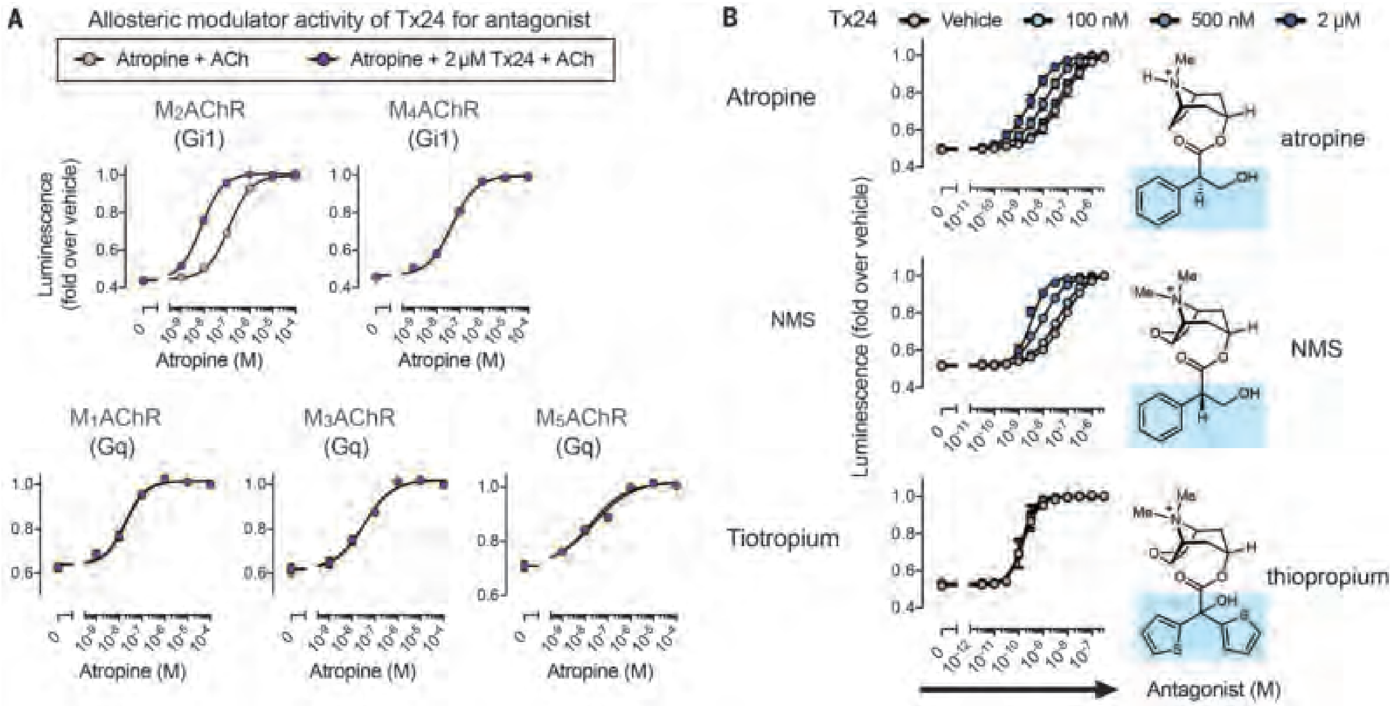

Fig. 5. Tx24 is a probe-selective PAM for antagonists. (**A**) Allosteric modulator activity of Tx24 toward antagonist atropine. The cells expressing the NanoBiT–G protein and the test GPCR were treated with titrated atropine followed by addition of Tx24 or vehicle. Luminescent signals were measured before and after ligand stimulation (10 μM ACh). (**B**) HEK293 cells transiently expressing the NanoBiT-G_{i1} protein and M_2AChR were loaded with coelenterazine and pretreated with titrated antagonist (atropine, NMS, or tiotropium), followed by addition of Tx24 (100 nM, 500 nM, or 2 μM). Luminescent signals were measured before and after ACh treatment (10 μM). Changes in luminescent signals were normalized to those with vehicle treatment. The chemical structure of each antagonist compound is placed next to the respective curve, with the aromatic head group highlighted in blue. Symbols and error bars represent means and SEM of three to five independent experiments, each performed in duplicate (see tables S2 and S3 for statistics).

tiotropium has two rings (Fig. 5B). The preferential allosteric effects of Tx24 for these smaller antagonists are likely due to the fact that it was developed against atropine-bound M_2AChR. Consistent with this notion, Tx24 has a higher affinity for M_2AChR bound to NMS than for M_2AChR bound to tiotropium (fig. S13).

Effect of Tx24 binding on conformation of M_2AChR

To assess the allosteric structural changes resulting from Tx24, we labeled T386$^{6.34}$ at the cytoplasmic end of TM6 with monobromobimane (mBBr) and introduced a tryptophan mutation at S210$^{5.62}$, which upon activation of the receptor quenched the fluorescence emitted from mBBr on TM6 (fig. S14). Compared with the apo state, the ACh-activated state had a significantly lower fluorescence intensity, which was further decreased in the presence of an intracellular G protein–mimetic nanobody, Nb9-8, whereas there was only a small decrease in fluorescence in the atropine-bound or Tx24-bound state (Fig. 6A). There was little change in the fluorescence intensity in the presence of both atropine and Tx24 regardless of the order of addition. When the receptor was first incubated with ACh, the addition of Tx24 resulted in only a small increase in fluorescence. However, when the receptor was first incubated with Tx24, the addition of ACh did not reduce the fluorescence. These results are consistent with the observation that Tx24 binds with lower affinity to ACh-bound M_2AChR (Fig. 3G) and, therefore, cannot stabilize an inactive conformation in TM6. Notably, the receptor remains in the active conformation in the presence of Nb9-8 regardless of the presence of Tx24 or the order of addition of these components.

The structural impact of Tx24 on M_2AChR conformation and dynamics was further investigated by solution NMR spectroscopy using methionine residues as conformational probes (*42*). The labeled methionines are well-positioned to detect conformational changes in the extracellular vestibule (M406$^{6.54}$), the orthosteric binding pocket (M77$^{2.58}$), the transduction core (M112$^{3.41}$), the junction of ICL2 and TM4 (M143$^{4.45}$), and the cytoplasmic ends of TM5 and TM6 (M202$^{5.54}$) (fig. S15). On the basis of the structure of M_1AChR-MT7, we would not expect Tx24 to directly interact with any of the methionine probes. Binding of Tx24 caused chemical shift perturbations of M77$^{2.58}$, M202$^{5.54}$, and M406$^{6.54}$ in the heteronuclear single-quantum coherence (HSQC) spectra among the five labeled methionines (Fig. 6, B to E). M77$^{2.58}$ underwent substantial changes in chemical shift and peak pattern upon binding to Tx24 compared with the apo or atropine-bound state, suggesting distinct local conformations and dynamics stabilized by Tx24. Co-incubation with atropine had no further influence on the M77$^{2.58}$ peak, which indicated that the conformation of the extracellular side of TM2 is mostly dominated by Tx24. Y80$^{2.61}$ and Y83$^{2.64}$, both located above M77$^{2.58}$, play pivotal roles in the allosteric transmission of structural changes in the extracellular vestibule to the orthosteric pocket (*31*, *33*). It is possible that Tx24 triggers a conformational change around Y80$^{2.61}$ in M_2AChR that is similar to the change we observed around the analogous Y82$^{2.61}$ residue in the M_1AChR-MT7 complex (Fig. 2B), and this conformational change is reported by M77$^{2.58}$ in the HSQC spectra. Although the M202$^{5.54}$ and M406$^{6.54}$ peak profiles showed little change from apo state to atropine-bound state, their positions shifted markedly upon binding with Tx24 (Fig. 6F). M406$^{6.54}$ is located in close contact with W422$^{7.35}$, which faces the extracellular vestibule in the inactive state (Fig. 6G). Given the

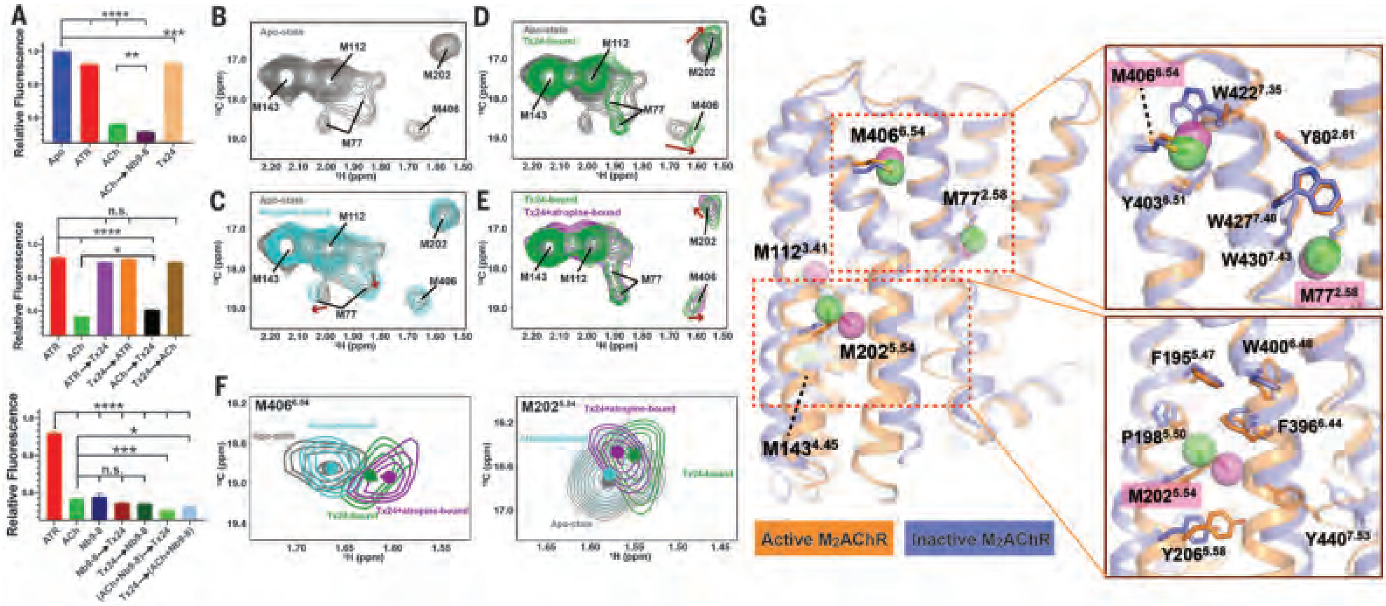

Fig. 6. Structural impact of Tx24 on M$_2$AChR conformation dynamics. (**A**) Comparison of the fluorescence intensity of the mBBr-labeled M$_2$AChR in various conditions. Receptor was first incubated with the compound or protein listed first and then further incubated with the second molecule(s) before fluorescence spectra were obtained. Fluorescence peak intensities at 461 nm are plotted. Data represent at least three independent measurements. *P < 0.05; **P < 0.005; ***P < 0.001; ****P < 0.0001; n.s., not significant (one-way analysis of variance). (**B** to **E**) Structural impact of Tx24 on the HSQC spectra of the apo state, atropine-bound state, Tx24-bound state, and Tx24+atropine–bound state of M$_2$AChRmini$_\Delta$5M. (**F**) Overlay of spectra for M406$^{6.54}$ and M202$^{5.54}$ in different conditions from panels (B) to (E): apo state (gray), atropine-bound (cyan), Tx24-bound (green), Tx24+atropine–bound (magenta). The centers of the resonances are indicated with dots. (**G**) Distribution of methionine probes with the structural comparison between inactive (blue; PDB ID 3UON) and active M$_2$AChR (orange; PDB ID 4MQS). Side-chain interactions surrounding M406, M77, and M202 are detailed in the right panels.

size of Tx24, it is likely that it interacts with W422$^{7.35}$ and provides M406$^{6.54}$ with a different microenvironment in the apo state and the atropine-bound state. Unlike M77$^{2.58}$ and M406$^{6.54}$, M202$^{5.54}$ is located at the TM5-TM6 interface on the intracellular side of the receptor and away from the putative Tx24 binding pocket (Fig. 6G). The spectral changes observed in M202$^{5.54}$ indicate that the extracellular conformational change induced by Tx24 propagates to the intracellular region and allosterically stabilizes a distinct intracellular conformation of the TM5-TM6 interface from the apo or atropine-bound state. Both M202$^{5.54}$ and M406$^{6.54}$ peaks further shift when co-incubated with atropine (Fig. 6F), indicating a cooperative action between Tx24 and atropine, as evident from the pharmacological response (Fig. 5G).

Discussion

Natural organisms such as plants, bacteria, fungi, and animals have developed various molecules for their survival: for self-defense against predators and for capturing prey. These molecules have been a rich source of drugs and tool compounds for a diverse range of targets, including GPCRs (*43*). Whereas small molecules dominate the pharmacopeia for GPCRs, there is growing interest in peptides and small proteins because of their potential to be highly selective. The structure of M$_1$AChR -MT7 reveals the molecular basis for its strict subtype selectivity and also how the conformational changes of M$_1$AChR upon MT7 binding lead to inactivation of the receptor. The ability to redirect its MAChR subtype preference through in vitro protein evolution demonstrates the promise of the 3FT fold as an alternative scaffold for generating protein-based modulators.

REFERENCES AND NOTES

1. S.-M. Lee, J. M. Booe, A. A. Pioszak, *Eur. J. Pharmacol.* **763**, 196–205 (2015).
2. A. Christopoulos, *Mol. Pharmacol.* **86**, 463–478 (2014).
3. C. J. Langmead, A. Christopoulos, *Curr. Opin. Cell Biol.* **27**, 94–101 (2014).
4. P. Kessler, P. Marchot, M. Silva, D. Servent, *J. Neurochem.* **142** (suppl. 2), 7–18 (2017).
5. I. Ségalas *et al.*, *Biochemistry* **34**, 1248–1260 (1995).
6. J. S. Liang *et al.*, *Toxicon* **34**, 1257–1267 (1996).
7. K. N. Bradley, *Pharmacol. Ther.* **85**, 87–109 (2000).
8. E. Karlsson, M. Jolkkonen, E. Mulugeta, P. Onali, A. Adem, *Biochimie* **82**, 793–806 (2000).
9. D. Jerusalinsky *et al.*, *Toxicon* **38**, 747–761 (2000).
10. D. Servent *et al.*, *Toxicon* **58**, 455–463 (2011).
11. D. Servent, C. Fruchart-Gaillard, *J. Neurochem.* **109**, 1193–1202 (2009).
12. S. I. Max, J. S. Liang, L. T. Potter, *J. Neurosci.* **13**, 4293–4300 (1993).
13. S. I. Max, J. S. Liang, L. T. Potter, *Mol. Pharmacol.* **44**, 1171–1175 (1993).
14. S. I. Max, J. S. Liang, H. H. Valentine, L. T. Potter, *J. Pharmacol. Exp. Ther.* **267**, 480–485 (1993).
15. J. M. Carsi, L. T. Potter, *Life Sci.* **68**, 2541–2547 (2001).
16. J. Näsman, M. Jolkkonen, S. Ammoun, E. Karlsson, K. E. O. Åkerman, *Biochem. Biophys. Res. Commun.* **271**, 435–439 (2000).
17. J. L. Krajewski, I. M. Dickerson, L. T. Potter, *Mol. Pharmacol.* **60**, 725–731 (2001).
18. M. C. Olianas *et al.*, *Br. J. Pharmacol.* **131**, 447–452 (2000).
19. K. N. Bradley, E. G. Rowan, A. L. Harvey, *Toxicon* **41**, 207–215 (2003).
20. M. C. Olianas, A. Adem, E. Karlsson, P. Onali, *Eur. J. Pharmacol.* **487**, 65–72 (2004).
21. D. M. Thal *et al.*, *Nature* **531**, 335–340 (2016).
22. C. Fruchart-Gaillard *et al.*, *Mol. Pharmacol.* **74**, 1554–1563 (2008).
23. B. Gilquin *et al.*, *Protein Sci.* **12**, 266–277 (2003).
24. G. Blanchet *et al.*, *Biochimie* **103**, 109–117 (2014).
25. A. Kukkonen, M. Peräkylä, K. E. O. Åkerman, J. Näsman, *J. Biol. Chem.* **279**, 50923–50929 (2004).
26. S. Rondinelli, K. Näreoja, J. Näsman, *Toxins* **3**, 1393–1404 (2011).
27. C. Marquer *et al.*, *J. Biol. Chem.* **286**, 31661–31675 (2011).
28. J. A. Ballesteros, H. Weinstein, in *Receptor Molecular Biology*, vol. 25 of *Methods in Neurosciences*, S. C. Sealfon, Ed. (Academic Press, 1995), pp. 366–428.
29. J. Xu *et al.*, *J. Mol. Recognit.* **28**, 239–252 (2015).
30. A. Abdul-Ridha *et al.*, *J. Biol. Chem.* **289**, 6067–6079 (2014).
31. A. Abdul-Ridha *et al.*, *J. Biol. Chem.* **289**, 33701–33711 (2014).
32. L. Ma *et al.*, *Proc. Natl. Acad. Sci. U.S.A.* **106**, 15950–15955 (2009).
33. S. A. Hollingsworth *et al.*, *Nat. Commun.* **10**, 3289 (2019).
34. R. O. Dror *et al.*, *Nature* **503**, 295–299 (2013).
35. A. C. Kruse *et al.*, *Nature* **504**, 101–106 (2013).
36. S. Maeda, Q. Qu, M. J. Robertson, G. Skiniotis, B. K. Kobilka, *Science* **364**, 552–557 (2019).
37. I. Visiers, J. A. Ballesteros, H. Weinstein, *Methods Enzymol.* **343**, 329–371 (2002).
38. M. Naimuddin *et al.*, *Mol. Brain* **4**, 2 (2011).
39. W. Cai *et al.*, *J. Recept. Signal Transduct.* **34**, 154–161 (2014).
40. A. Inoue *et al.*, *Cell* **177**, 1933–1947.e25 (2019).
41. C. Valant, C. C. Felder, P. M. Sexton, A. Christopoulos, *Mol. Pharmacol.* **81**, 41–52 (2012).
42. J. Xu *et al.*, *Mol. Cell* **75**, 53–65.e7 (2019).
43. E. Muratspahić, M. Freissmuth, C. W. Gruber, *Trends Pharmacol. Sci.* **40**, 309–326 (2019).

ACKNOWLEDGMENTS

We thank N. Fastman and D. Hilger for help with phage display experiments and C. Glassman for help with yeast surface display

experiments. We thank staff at Advanced Photon Source GM/CA beamlines for technical assistance and support for data collection. We thank K. Jude for technical advice in the crystal structure analysis; K. Sato, S. Nakano, and A. Inoue at Tohoku University for assistance in plasmid preparation and cell-based GPCR assays; and X. Niu and H. Li for help with NMR data collection. NMR data were collected at the Beijing NMR Center and the NMR facility of the National Center for Protein Sciences at Peking University. **Funding:** The work was supported by NIH grant R01GM083118 for R.K.S. B.K.K. was funded by R01NS028471. K.C.G. was funded by NIH R01AI125320, Mathers Foundation, and Howard Hughes Medical Institute. A.I. was funded by the PRIME 18gm5910013 and the LEAP 18gm0010004 from the Japan Agency for Medical Research and Development (AMED) and the Japan Society for the Promotion of Science (JSPS) KAKENHI 17K08264. J.A. was funded by the LEAP 18gm0010004 from AMED. B.K.K. is a Chan Zuckerberg Biohub investigator. **Author contributions:** S.M. conceived the project and carried out crystallography, protein engineering, and biochemical characterization of the engineered toxin. N.T. and K.C.G. supported yeast surface display experiments. F.M.N.K. and A.I. performed cellular signaling assays and analysis supported by J.A. J.X. performed NMR measurements and analysis. J.Z. established the M_2AChR bimane reporter construct. S.M. and J.X. performed bimane fluorescence assays and initial radioligand binding assays. M.J.C. and R.K.S. performed comprehensive radioligand binding assays. B.K.K. supervised the project. S.M. and B.K.K. wrote the manuscript with input from A.I., K.C.G., J.X., J.Z., R.K.S., and N.T. **Competing interests:** B.K.K. is a cofounder of and consultant for ConfometRx. **Data and materials availability:** The atomic coordinates of M_1AChR-MT7 have been deposited in the RCSB Protein Data Bank (PDB) with the identifier 6WJC. Materials for these engineered toxins are available from the corresponding authors upon request. Expression plasmids for the NanoBiT-G-protein dissociation assay are available from A.I. under a material transfer agreement with Tohoku University.

SUPPLEMENTARY MATERIALS

science.sciencemag.org/content/369/6500/161/suppl/DC1
Materials and Methods
Figs. S1 to S15
Tables S1 to S3
References (*44*–*53*)

19 October 2019; accepted 21 April 2020
10.1126/science.aax2517

AGING

Blood factors transfer beneficial effects of exercise on neurogenesis and cognition to the aged brain

Alana M. Horowitz[1,2]*, Xuelai Fan[1]*, Gregor Bieri[1], Lucas K. Smith[1,2], Cesar I. Sanchez-Diaz[1], Adam B. Schroer[1], Geraldine Gontier[1], Kaitlin B. Casaletto[3,4], Joel H. Kramer[3,4], Katherine E. Williams[5], Saul A. Villeda[1,2,6,7]†

Reversing brain aging may be possible through systemic interventions such as exercise. We found that administration of circulating blood factors in plasma from exercised aged mice transferred the effects of exercise on adult neurogenesis and cognition to sedentary aged mice. Plasma concentrations of glycosylphosphatidylinositol (GPI)–specific phospholipase D1 (Gpld1), a GPI-degrading enzyme derived from liver, were found to increase after exercise and to correlate with improved cognitive function in aged mice, and concentrations of Gpld1 in blood were increased in active, healthy elderly humans. Increasing systemic concentrations of Gpld1 in aged mice ameliorated age-related regenerative and cognitive impairments by altering signaling cascades downstream of GPI-anchored substrate cleavage. We thus identify a liver-to-brain axis by which blood factors can transfer the benefits of exercise in old age.

The ability to reverse or delay the effects of aging on the brain through systemic interventions such as exercise could help to mitigate vulnerability to age-related neurodegenerative diseases (*1*–*3*). Despite the evident benefit of exercise, its application is hindered in the elderly, as physical frailty or poor health can decrease a person's ability or willingness to exercise (*4*). Thus, it is critical to identify accessible therapeutic approaches that may confer the benefits of exercise.

In animal models, exercise reverses age-related declines in adult neurogenesis and cognitive function in the aged hippocampus (*5*–*8*), a brain region sensitive to the detrimental effects of aging (*9*). Similarly, transfer of blood from young animals, either by heterochronic parabiosis (in which young and old circulatory systems are joined) or by administration of young blood plasma, improves regenerative capacity and cognition in aged mice (*10*–*15*). Given parallels between the effects of exercise and young blood, we tested whether exercise-induced circulating blood factors could confer the beneficial effects of exercise on regenerative and cognitive function in the aged brain. We found that systemic administration of blood plasma derived from mice that exercised ameliorates age-related impairments in adult neurogenesis and cognitive function in the aged hippocampus. Furthermore, we identify glycosylphosphatidylinositol (GPI)–specific phospholipase D1 (Gpld1) as a liver-derived, exercise-induced circulating blood factor sufficient to improve function in the hippocampus of aged mice.

[1]Department of Anatomy, University of California, San Francisco, CA, USA. [2]Biomedical Sciences Graduate Program, University of California, San Francisco, CA, USA. [3]Department of Neurology, University of California, San Francisco, CA, USA. [4]Memory and Aging Center, University of California, San Francisco, CA, USA. [5]Sandler-Moore Mass Spectrometry Core Facility, University of California, San Francisco, CA, USA. [6]Department of Physical Therapy and Rehabilitation Science, San Francisco, CA, USA. [7]Eli and Edythe Broad Center for Regeneration Medicine and Stem Cell Research, San Francisco, CA, USA.
*These authors contributed equally to this work.
†Corresponding author. Email: saul.villeda@ucsf.edu

Systemic blood plasma administration transfers the benefits of exercise to the aged hippocampus

We characterized the effect of direct exercise on the aged hippocampus. As a control, we assessed age-related cellular and cognitive impairments in the hippocampus of aged (18 months) relative to young (3 months) mice (fig. S1, A to G). Subsequently, an independent cohort of aged mice was given continuous access to a running wheel for 6 weeks, while age-matched sedentary control mice were provided nesting material (fig. S2A). Direct exercise resulted in increased adult neurogenesis (fig. S2B), increased expression of brain-derived neurotrophic factor (BDNF) (fig. S2C), and improved hippocampal-dependent learning and memory (fig. S2, D to H) in aged mice (*5*, *16*).

We tested whether these effects of exercise on the aged hippocampus could be transferred through administration of exercise-induced circulating blood factors. After exercise, blood was collected and plasma was isolated from exercised and sedentary aged mice and pooled by group. An independent cohort of naïve aged mice was then intravenously injected with plasma from exercised or sedentary aged mice eight times over 3 weeks (Fig. 1A). We analyzed adult neurogenesis by immunohistochemical analysis. Although no difference in the number of neural stem cells expressing Sox2 (sex-determining region Y box 2) and glial fibrillary acidic protein (GFAP) was observed (Fig. 1B), we detected an increase in the number of newly born neurons containing doublecortin (Dcx) in the dentate gyrus region of the hippocampus in aged animals that were administered plasma from exercised mice (Fig. 1B). We assessed neuronal differentiation and survival by 5-bromo-2-deoxyuridine (BrdU) incorporation. Mature differentiated neurons express both BrdU and the neuronal marker NeuN. Naïve aged mice that were administered plasma from exercised mice showed an increase in the number of mature neurons expressing both BrdU and NeuN in the dentate gyrus (Fig. 1B). We examined the expression of BDNF by Western blot and observed an increase in hippocampal expression in naïve aged mice that were administered plasma from exercised mice (Fig. 1C). Together, these data indicate that systemic administration of plasma from exercised aged animals can transfer the beneficial effect of exercise on regenerative capacity in the aged hippocampus.

To assess the potential of plasma from exercised mice to rescue age-related impairments in hippocampal-dependent learning and memory, we used the radial-arm water maze (RAWM) and contextual fear conditioning paradigms (Fig. 1A). In the training phase of the RAWM paradigm, all mice showed similar spatial learning capacity (Fig. 1D). When naïve aged mice were administered plasma from aged mice that exercised, they demonstrated improved learning and memory for the platform location during the testing phase of the task relative to animals treated with plasma from sedentary aged mice (Fig. 1, D and E). During fear conditioning training, all mice exhibited similar baseline freezing regardless of treatment (Fig. 1F). However, aged mice receiving plasma from exercised aged mice demonstrated increased freezing in contextual (Fig. 1G), but not cued (Fig. 1H), memory testing. These data indicate that exercise-induced circulating blood factors in plasma can ameliorate impairments in hippocampal-dependent learning and memory in aged mice.

Exercise enhances regenerative capacity in young (*17*–*19*) and aged (*5*–*8*) animals. Correspondingly, we investigated whether the beneficial effects of exercise observed in mice at younger ages could also be transferred to aged mice through circulating blood factors. We administered plasma derived from exercised or sedentary mature (6 to 7 months) mice to aged mice. As a control, we examined the effect of direct exercise on the hippocampus of mature mice (fig. S3A). Exercise promoted neurogenic and cognitive enhancements in the hippocampus of mature mice (fig. S3, B to H). Next, we collected blood and isolated plasma from exercised and sedentary mature mice and pooled the plasma by group. Naïve aged mice were intravenously injected with the plasma (fig. S4A). To account for any potential benefit of blood from mature animals, we administered saline to an additional aged control group. No significant changes were observed between aged mice that were administered plasma from sedentary mature mice or were given saline. However, administration of plasma from exercised mature mice resulted in increased adult neurogenesis relative to controls (fig. S4B). Thus, exercise-induced circulating blood

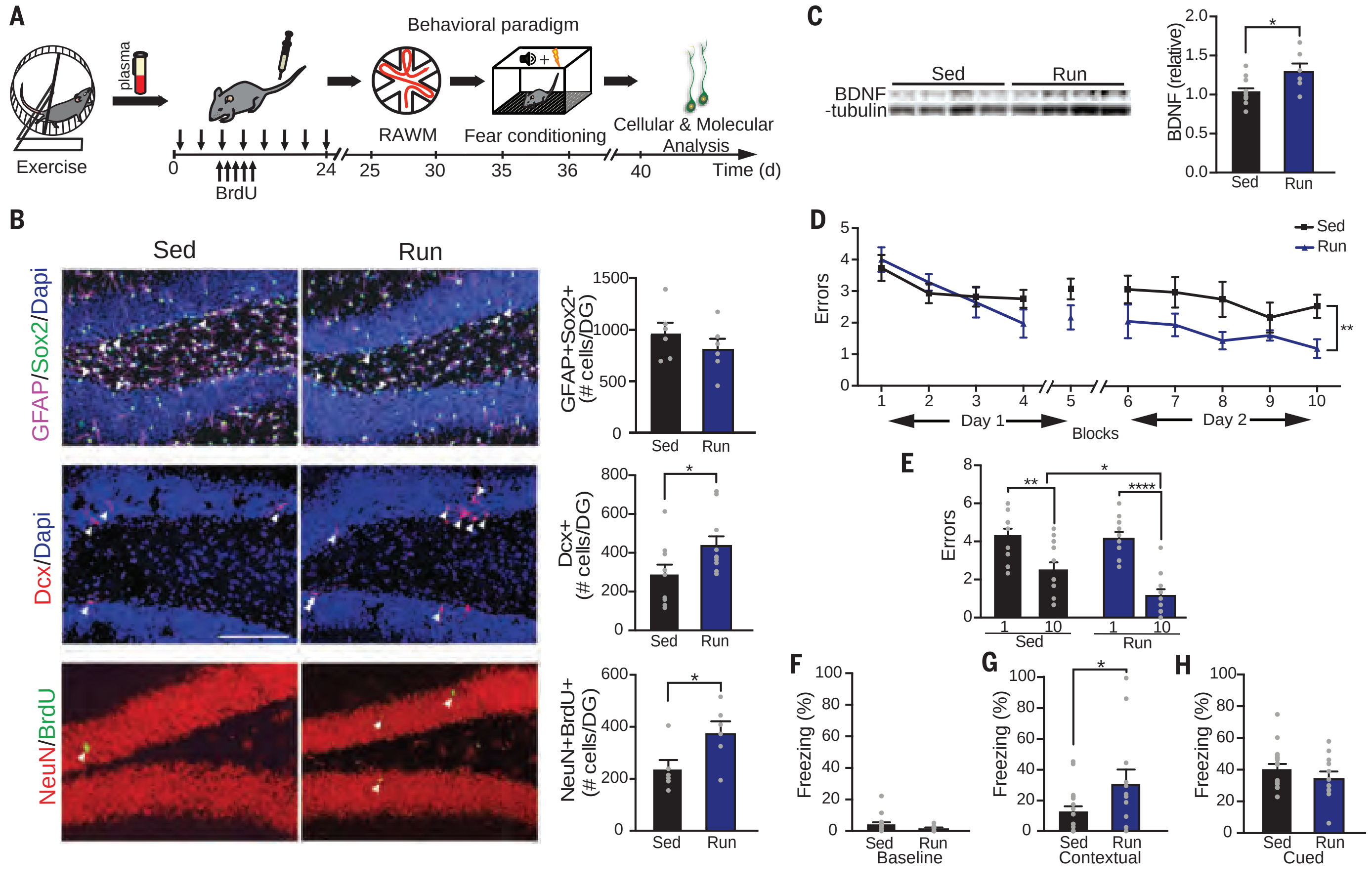

Fig. 1. Systemic administration of exercise-induced circulatory blood factors ameliorates impaired neurogenesis and cognition in the aged hippocampus. (**A**) Plasma was collected from exercised or sedentary aged (18 months) mice and administered to sedentary aged mice 8 times over 24 days (100 μl per intravenous injection). Schematic illustrates chronological order of plasma administration from exercised aged mice and cognitive testing. (**B**) Representative microscopic fields and quantification of GFAP/Sox2 double-positive, Dcx-positive, and NeuN/BrdU double-positive cells in the dentate gyrus (DG) of the hippocampus of naïve aged mice administered plasma from sedentary (Sed) or exercised (Run) aged mice (*n* = 10 or 11 per group; arrowheads point to individual cells; scale bar, 100 μm). Dapi, 4′,6-diamidino-2-phenylindole. (**C**) Western blot and quantification of BDNF in the hippocampus of naïve aged mice administered plasma from sedentary or exercised aged mice (*n* = 6 to 10 per group). Quantification is normalized to β-tubulin. (**D** and **E**) Spatial learning and memory were assessed by RAWM as the number of entry errors committed during the training and testing phases. Overall learning and memory were analyzed between block 1 and block 10 (1 block = 3 trials; *n* = 12 to 15 per group). (**F** to **H**) Associative fear memory was assessed using contextual (G) and cued (H) fear conditioning as percent time spent freezing 24 hours after training. Baseline freezing (F) was assessed as the percentage of time spent freezing prior to fear conditioning (*n* = 12 to 19 per group). Data are means ± SEM; *$P < 0.05$, **$P < 0.01$, ****$P < 0.0001$ [*t* test in (B), (C), (F), (G), and (H); repeated-measures analysis of variance (ANOVA) with Bonferroni post hoc test in (D); ANOVA with Tukey post hoc test in (E)].

factors across ages can confer the benefits of exercise on the aged hippocampus.

Gpld1 ameliorates age-related regenerative and cognitive decline in mice

Given that plasma from both aged and mature exercised mice alleviated age-related impairments in the hippocampus of naïve aged mice, we sought to identify individual circulating blood factors that mediated these effects. We used isobaric tagging together with liquid chromatography–tandem mass spectrometry to measure relative amounts of soluble proteins in the plasma from exercised or sedentary aged and mature mice (table S1). The abundance of 30 factors increased after exercise in aged mice (Fig. 2A and fig. S5A), and 33 factors increased after exercise in mature mice (Fig. 2A and fig. S5B). According to the Tabula Muris compendium of single-cell transcriptome data from mice (*20*) and the protein atlas (*21*), 63% and 67% of exercise-induced factors in aged and mature mice, respectively, are predominantly expressed in the liver. The abundance of 12 factors—Gpld1, Bche (cholinesterase), Napsa (napsin A), Pon1 (serum paraoxonase 1), Gpx3 (glutathione peroxidase 3), Mbl2 (mannose binding protein C), Ica (inhibitor of carbonic anhydrase), Itih2 (inter–α-trypsin inhibitor heavy chain H2), Pltp (phospholipid transfer protein), Ca2 (carbonic anhydrase 2), Serpina1a (α1-antitrypsin 1-1), and Serpina1d (α1-antitrypsin 1-4)—was increased in plasma from exercised aged and mature animals (Fig. 2A). Functional enrichment analysis of these factors using STRING, a search tool for the retrieval of interacting genes and proteins, identified largely metabolic processes, in which Gpld1 and Pon1 were overrepresented (Fig. 2B). We elected to investigate Gpld1, a GPI-degrading enzyme (*22*) not previously linked to aging, neurogenesis, or cognition.

We confirmed that concentrations of Gpld1 increased in plasma of individual aged (Fig. 2C) and mature (Fig. 2D) exercised mice relative to those in plasma from sedentary age-matched controls. In exercised and sedentary aged mice, we observed a significant correlation between increased Gpld1 concentrations in plasma and improved cognitive performance in the RAWM and contextual fear conditioning behavioral tests (Fig. 2, E and F). Furthermore, we detected an increase in Gpld1 in plasma from active, healthy elderly human individuals relative to their sedentary counterparts (Fig. 2G). These data identify Gpld1 as an exercise-induced circulating blood factor in aged mice and humans with potential relevance to cognitive function in mice.

To identify the potential source of exercise-induced systemic Gpld1, we characterized Gpld1 mRNA expression in mouse liver, lung, fat, spleen, skin, kidney, heart, muscle, cortex, hippocampus, and cerebellum (Fig. 3A). We detected the highest Gpld1 expression in the liver (Fig. 3A), consistent with previous reports identifying the liver as the primary source of circulating Gpld1 (*23*). We examined whether Gpld1 mRNA expression changed in the liver as a function of aging, exercise, or plasma administration. No changes in Gpld1 expression were detected during aging or after plasma administration (fig. S6, A and B). Gpld1 expression was increased in the liver of exercised aged mice relative to that in sedentary animals (Fig. 3B). As a control, we evaluated Gpld1 expression in muscle and hippocampus and observed no changes under any condition (fig. S6, C to I). We also observed no change in circulating levels of Gpld1 in plasma with age (fig. S6J). These data are consistent with a role of Gpld1 as a liver-derived, exercise-induced circulating factor in aged mice.

To test the effect of Gpld1 on the aged hippocampus, we used hydrodynamic tail vein injection (HDTVI)–mediated in vivo transfection to overexpress Gpld1 in the liver. Aged mice were injected with expression constructs encoding either Gpld1 or green fluorescent protein (GFP) control, and analysis was done in a time frame consistent with our previous plasma administration experiments (Fig. 3C). Increased Gpld1 mRNA expression in the liver and increased Gpld1 plasma concentrations were confirmed after HDTVI in aged mice (Fig. 3, D and E). By immunohistochemistry and Western blot analysis, we detected an increase in adult neurogenesis (Fig. 3F) and

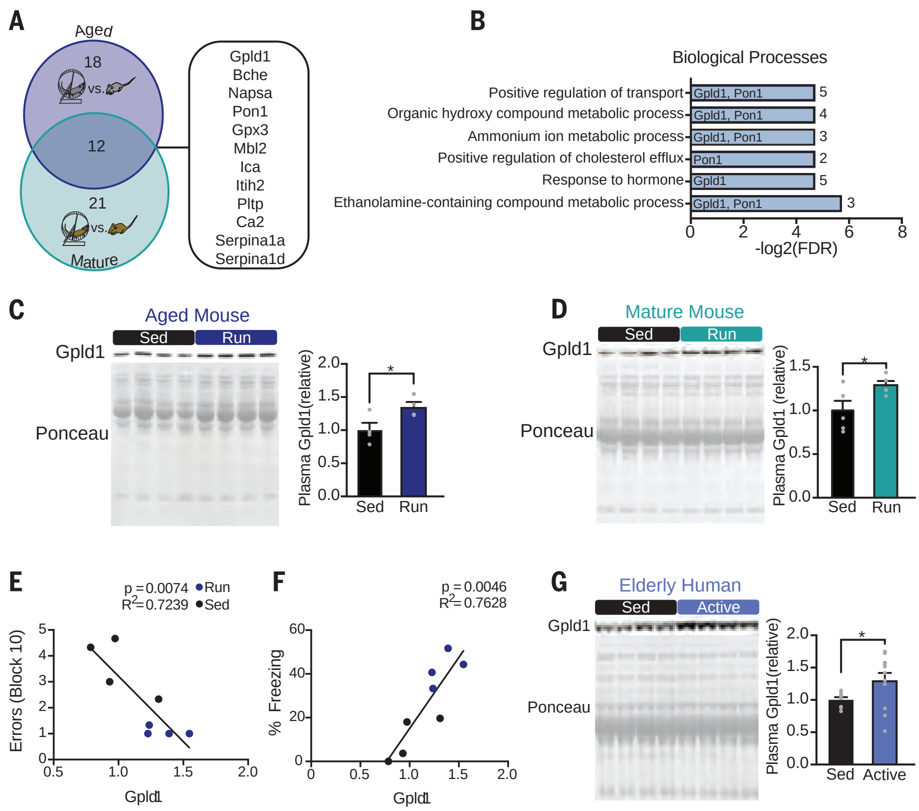

Fig. 2. Exercise increases systemic levels of Gpld1 in mature and aged mice and healthy elderly humans. (**A**) Venn diagram of results from proteomic screens of aged (18 months) and mature (7 months) exercised mice. Numbers of proteins whose concentrations increase with exercise in aged and mature mice are shown in the blue and teal regions, respectively. Proteins common to both groups are listed at the right. (**B**) Enrichment analysis of the 12 proteins up-regulated by exercise in mature and aged mice. Gpld1 and Pon1 are listed next to the processes in which they are implicated. Numerals at far right are numbers of proteins represented in each process. (**C** and **D**) Western blots with corresponding Ponceau S stains and quantification of Gpld1 in equal volumes of blood plasma from individual aged (C) and mature (D) sedentary and exercised mice (n = 4 or 5 per group). (**E** and **F**) Correlation between plasma Gpld1 levels in exercised and sedentary aged mice and number of errors committed during the final block of RAWM (E) or time spent freezing in contextual fear conditioning (F). (**G**) Western blot and quantification of Gpld1 in equal volumes of blood plasma from individual sedentary (<7100 steps per day) and active (>7100 steps per day) healthy elderly humans (aged 66 to 78 years; n = 8 to 12 per group). Data are means ± SEM; $*P < 0.05$ [t test in (C), (D), and (G); linear regression in (E) and (F)].

expression of BDNF (Fig. 3G) in the hippocampus of aged mice overexpressing Gpld1 in liver. To assess the effect of Gpld1 overexpression on hippocampal-dependent learning and memory, we used RAWM, forced alternation (Y maze), and novel object recognition (NOR) tests (Fig. 3C). Aged animals overexpressing Gpld1 committed significantly fewer errors in locating the target platform during the RAWM training and testing phases (Fig. 3, H and I) relative to controls. During Y maze and NOR testing, aged mice overexpressing Gpld1 spent significantly more time in the novel arm (Fig. 3J) and with the novel object (Fig. 3K). We also tested whether increasing Pon1, the other liver-derived circulating factor overrepresented in our exercise proteomic functional enrichment analysis (Fig. 2B), ameliorated age-related impairments in hippocampal-dependent cognitive function. Aged mice were given HDTVI with expression constructs encoding either Pon1 or GFP control (fig. S7, A and B); however, no cognitive improvements were observed in a time frame consistent with Gpld1 experiments (fig. S7, C to F). Together, these data indicate that selectively increasing liver-derived systemic concentrations of Gpld1 is sufficient to improve adult neurogenesis and cognitive function in the aged hippocampus.

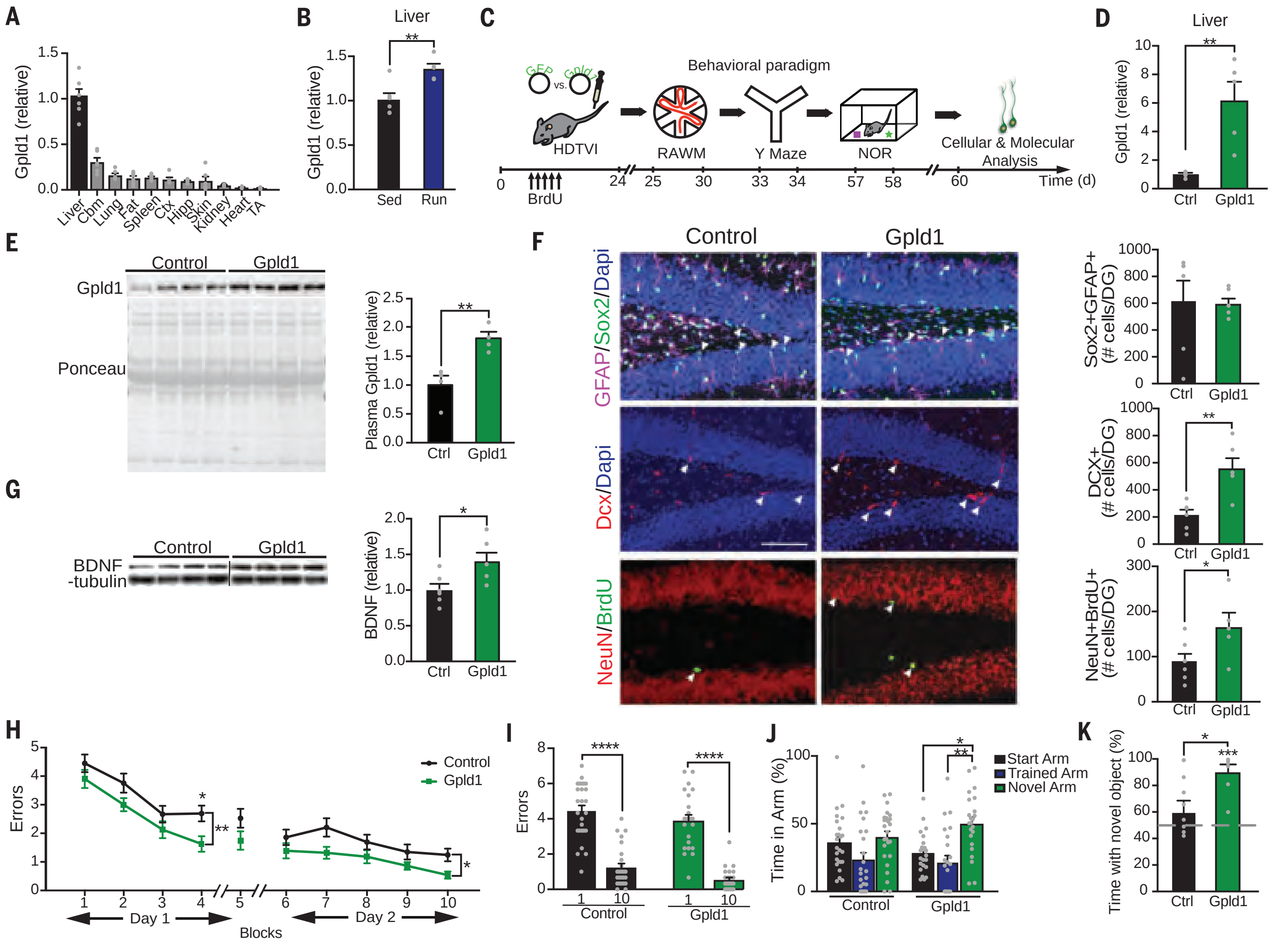

Fig. 3. Increased systemic GPLD1 ameliorates impaired neurogenesis and cognition in the aged hippocampus. (**A** and **B**) Quantitative reverse transcription polymerase chain reaction (qRT-PCR) of Gpld1 across tissues in sedentary aged mice (A) and in liver of exercised and sedentary aged mice (B). Gene expression is measured relative to Gapdh (n = 5 or 6 per group). Abbreviations: Cbm, cerebellum; Ctx, cortex; Hipp, hippocampus; TA, tibialis anterior muscle. (**C**) Aged (18 months) mice were given HDTVI of expression constructs encoding either Gpld1 or GFP control. Schematic illustrates chronological order of HDTVI, cognitive testing, and cellular and molecular analysis. (**D**) qRT-PCR of Gpld1 in liver of aged mice expressing Gpld1 or GFP control. Gene expression is measured relative to Gapdh (n = 5 per group). (**E**) Western blot with corresponding Ponceau S stain and quantification of Gpld1 in equal volumes of blood plasma from individual aged mice expressing Gpld1 or GFP control (n = 4 per group). (**F**) Representative microscopic fields and quantification of GFAP/Sox2 double-positive, Dcx-positive, and NeuN/BrdU double-positive cells in the DG of the hippocampus of aged mice expressing Gpld1 or GFP control (n = 6 per group; arrowheads point to individual cells; scale bar, 100 μm). (**G**) Western blot and quantification of BDNF in the hippocampus of aged mice expressing Gpld1 or GFP control (n = 6 per group). Quantification is normalized to β-tubulin. (**H** and **I**) Spatial learning and memory were assessed by RAWM as number of entry errors committed during the training and testing phases. Overall learning and memory was analyzed between block 1 and block 10 (1 block = 3 trials; n = 26 per group). (**J**) Spatial working memory was assessed by YMaze as time spent in the start, trained, and novel arms during the testing phase (n = 23 to 25 per group). (**K**) Object recognition memory was assessed by NOR as time spent exploring a novel object 24 hours after training (n = 8 to 12 per group). Data are means ± SEM; *P < 0.05, **P < 0.01, ***P < 0.001, ****P < 0.0001 [t test in (B), (D), (E), (F), (G), and (K); repeated-measures ANOVA with Bonferroni post hoc test in (H); ANOVA with Tukey post hoc test in (I) and (J); one-sample t test versus 50% in (K)].

Coagulation and complement signaling cascades are altered in response to Gpld1

We sought to delineate central versus peripheral mechanisms of action of liver-derived Gpld1. To evaluate the potential of Gpld1 to cross the blood-brain barrier, we generated expression constructs encoding a high-affinity nanoluciferase binary technology (HiBiT)–tagged version of Gpld1 (fig. S8A). HiBiT is a small peptide with high affinity to large BiT (LgBiT), with which it forms a complex that produces a luminescent signal (*24*), allowing for sensitive and quantitative detection of tagged proteins. Aged mice were given HDTVI with expression constructs encoding HiBiT Gpld1, which we detected in plasma (fig. S8B). We characterized HiBiT activity in mice in plasma, liver, cortex, hippocampus, and cerebellum (fig. S8, B and C). Luminescent signal was detected in plasma and liver (fig. S8, B and C). However, the signal detected in the brain (fig. S8C) was several orders of magnitude lower than that in plasma. Thus, liver-derived systemic Gpld1 appears not to readily enter the brain.

In its canonical role, Gpld1 hydrolyzes GPI anchors that have acylated inositol, releasing membrane-bound GPI-anchored proteins from the cell surface (*25*–*28*). Although the physiological role of Gpld1 is not fully understood, cleavage of its substrates regulates signaling cascades important in biological processes such as differentiation and inflammation (*27*, *29*). Therefore, we measured relative amounts of soluble proteins in the plasma of aged mice given HDTVI with expression constructs encoding Gpld1 or GFP control by label-free mass spectrometry (table S2). We surveyed the top 20 up- and down-regulated proteins (Fig. 4A) for known signaling cascades associated with Gpld1 substrates (*27*) and detected changes in the urokinase-type plasminogen activator receptor (uPAR) signaling pathway. uPAR is a Gpld1 GPI-anchored substrate whose proteolytic function regulates the plasminogen (Plg) activation system involved in coagulation. Nonproteolytic function of uPAR regulates extracellular matrix proteins through interactions with vitronectin (Vtn) (*29*, *30*). On Western blots, we observed decreased amounts of both Plg and Vtn in plasma of aged animals with increased systemic Gpld1 relative to those from control animals (Fig. 4, B and C). We surveyed our previous exercise proteomic analysis (table S1) for proteins that decrease in plasma of aged mice after exercise and also identified Plg (Fig. 4D). We compared functional enrichment analysis using STRING of factors identified to decrease in aged plasma after either

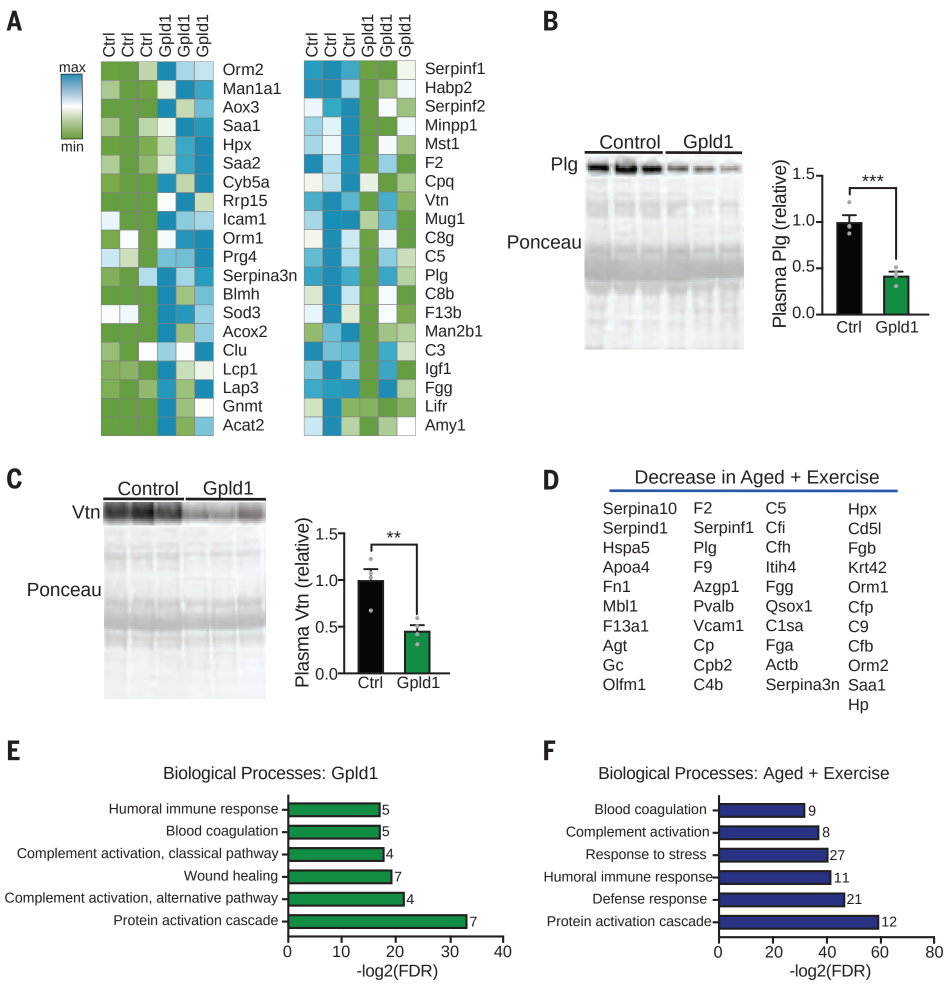

Fig. 4. Increased systemic Gpld1 alters signaling cascades downstream of GPI-anchored substrate cleavage in the aging systemic milieu. (**A**) Heat maps of top 20 proteins up- and down-regulated in blood plasma of aged mice after Gpld1 HDTVI relative to GFP HDTVI control, identified by mass spectrometry. (**B** and **C**) Western blot with corresponding Ponceau S stain and quantification of plasminogen [Plg; (B)] and vitronectin [Vtn; (C)] in equal volumes of blood plasma from individual aged mice 24 hours after HDTVI of Gpld1 or GFP control (n = 4 per group). (**D**) List of 41 proteins down-regulated in blood plasma from aged mice after exercise. (**E** and **F**) Enrichment analysis of plasma proteins down-regulated with Gpld1 HDTVI (E) or exercise (F) in aged mice, as identified by mass spectrometry. The number of proteins represented in each process is listed to the right of each bar. Data are means ± SEM; $^{**}P < 0.01$, $^{***}P < 0.001$ [t test in (B) and (C)].

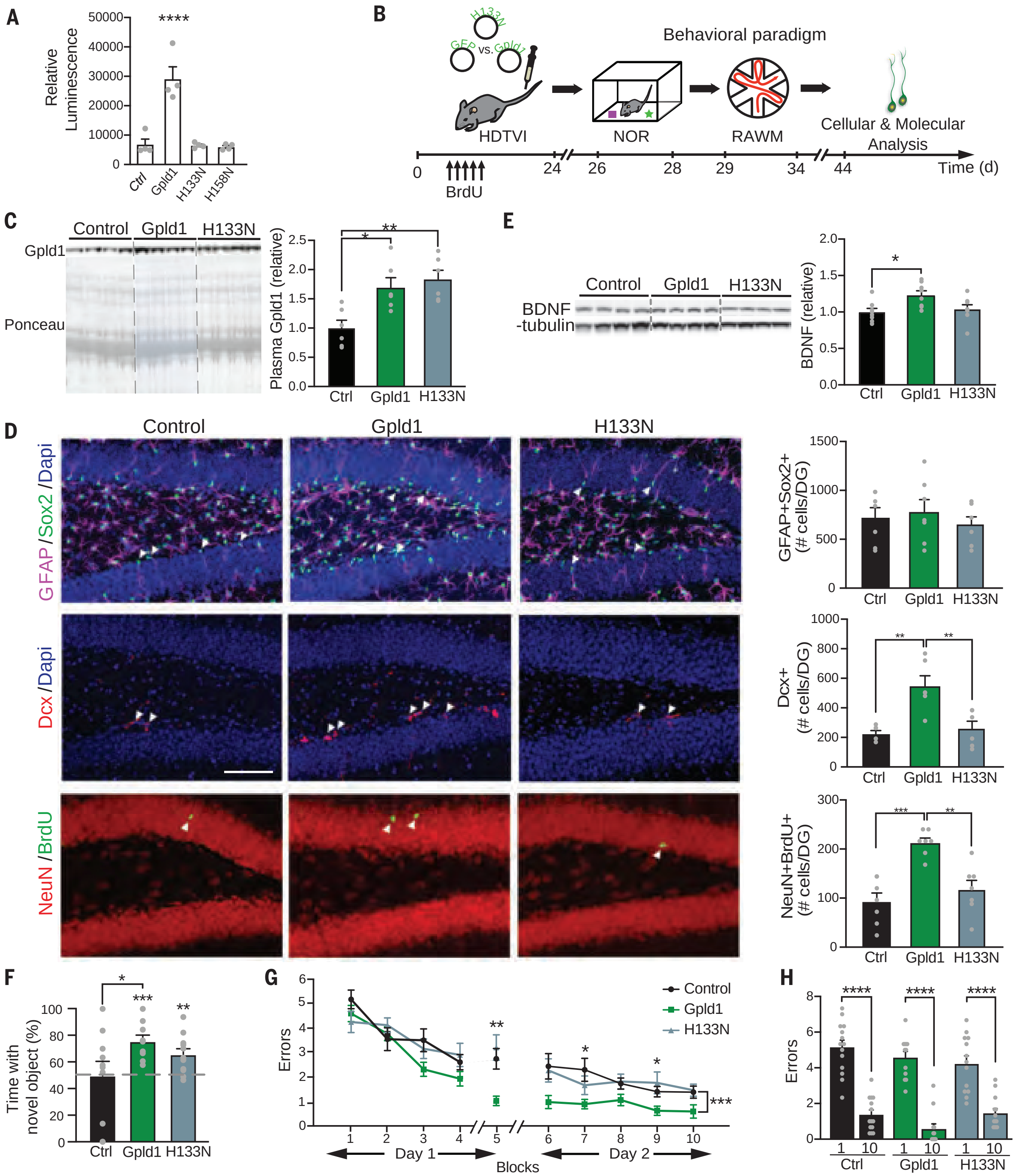

Fig. 5. GPI-anchored substrate cleavage is associated with restorative effects of Gpld1 on the aged hippocampus. (**A**) Luminescence-based quantification of alkaline phosphatase activity in cell culture supernatant 48 hours after transfection with ubiquitin-lox-stop-lox-PLAP (GPI-anchored alkaline phosphatase) and EF1a-Cre, in combination with GFP, Gpld1, H133N-Gpld1, or H158N-Gpld1 (n = 3 samples per group). (**B**) Aged (18 months) mice were given HDTVI of expression constructs encoding Gpld1, catalytically inactive H133N-Gpld1, or GFP control. Schematic illustrates chronological order of HDTVI, cognitive testing, and cellular and molecular analysis. (**C**) Western blot with corresponding Ponceau S stain and quantification of Gpld1 in equal volumes of blood plasma from individual aged mice expressing Gpld1, Gpld1-H133N, or GFP control (n = 6 per group). (**D**) Representative microscopic fields and quantification of GFAP/Sox2 double-positive, Dcx-positive, and NeuN/BrdU double-positive cells in the DG of the hippocampus of aged mice expressing Gpld1, Gpld1-H133N, or GFP control (n = 7 per group; arrowheads point to individual cells; scale bar, 100 μm). (**E**) Western blot and quantification of BDNF in the hippocampus of aged mice expressing Gpld1, Gpld1-H133N, or GFP control (n = 8 per group). Quantification is normalized to β-tubulin. (**F**) Object recognition memory was assessed by NOR as time spent exploring a novel object 24 hours after training (n = 9 to 11 per group). (**G** and **H**) Spatial learning and memory were assessed by RAWM as number of entry errors committed during the training and testing phases. Overall learning and memory were analyzed between block 1 and block 10 (1 block = 3 trials; n = 12 to 14 per group). Data are means ± SEM; *P < 0.05, **P < 0.01, ***P < 0.001, ****P < 0.0001 [repeated-measures ANOVA with Bonferroni post hoc test in (G); ANOVA with Tukey post hoc test in (C), (F), (G), and (H); one-sample t test versus 50% in (F)].

Gpld1 overexpression (Fig. 4A) or exercise (Fig. 4D). Consistent with changes in the uPAR signaling pathway, we identified biological processes involved in coagulation as well as the complement system under both conditions (Fig. 4, E and F). Of the factors surveyed after increased systemic Gpld1 and exercise, we identified 80% and 71%, respectively, to be predominantly expressed in the liver according to Tabula Muris (*20*) and the protein atlas (*21*). Together, systemic changes in signaling cascades downstream of GPI-anchored substrate cleavage correlate with beneficial effects of Gpld1 and exercise.

GPI-anchored substrate cleavage is necessary for the effects of Gpld1 on the aged hippocampus

We tested whether the enzymatic activity of liver-derived systemic Gpld1, and presumed subsequent GPI-anchored substrate cleavage, directly mediates its effects on adult neurogenesis and cognitive function in the aged hippocampus. The catalytic activity of Gpld1 is dependent on His^{133} and His^{158}, and mutations at either site abrogate enzymatic activity (*31*). We generated expression constructs encoding Gpld1 with site-directed His → Asn mutations, and abrogation of GPI-anchored substrate cleavage was validated in vitro (Fig. 5A). Aged mice were injected with expression constructs encoding Gpld1, catalytically inactive His^{133} → Asn (H133N) Gpld1, or GFP control (Fig. 5B), and plasma concentrations were measured (Fig. 5C). We observed increased adult neurogenesis (Fig. 5D), increased BDNF expression (Fig. 5E), and cognitive improvements in the RAWM and NOR tasks (Fig. 5, F to H) in aged mice with increased expression of Gpld1. However, no differences were observed in aged mice with increased expression of catalytically inactive H133N Gpld1 (Fig. 5, D to H). These data indicate that the enzymatic activity of liver-derived systemic Gpld1 is necessary for its effects on the aged hippocampus, and are consistent with signaling cascades activated after GPI-anchored substrate cleavage as possible molecular mediators of these beneficial effects.

Discussion

Cumulatively, our data show that beneficial effects of exercise on the aged brain can be transferred through administration of blood components. We identified the liver-derived factor Gpld1 as one such factor, and we suspect that signaling cascades activated by GPI-anchored substrate cleavage activity may also participate. Our results identify a liver-to-brain axis by which circulating blood factors confer the beneficial effects of exercise in old age.

Adult neurogenesis in humans remains controversial (*32*). Nonetheless, adult neurogenesis is reported in the human hippocampus through the ninth decade of life, with age-related decline exacerbated in Alzheimer's disease (AD) patients (*33*) and correlating with cognitive dysfunction (*34*). In the context of dementia-related neurodegenerative diseases, exercise is correlated with reduced risk for cognitive decline in the elderly, improves cognition in populations at risk for AD, and is associated with better neurobehavioral outcomes even in autosomal dominant AD (*35–37*). Exercise ameliorates impairments in learning and memory in animal models of AD (*38*, *39*) by increasing adult neurogenesis and abundance of BDNF in the aged hippocampus (*39*)—benefits that we found to be transferred with injected plasma.

Our data identify decreased uPAR signaling, and associated changes in the coagulation and complement system cascades, as potential pro-aging molecular targets. The effects of liver-derived Gpld1 and exercise are likely the result of changes in multiple signaling cascades. However, a prominent role is emerging for the coagulation and complement pathways in aging. Changes in the coagulation pathway have been identified as part of the senescence-associated secretory phenotype (SASP) (*40*), and blood-derived complement C1q promotes age-related regenerative decline in peripheral tissues (*41*). The benefits of targeting members of the coagulation pathway modulated by Gpld1 have been reported in the context of neurodegeneration (*42*). Genetic mouse models deficient for Plg were protected from demyelination and paralysis in a mouse model of multiple sclerosis (*43*). Moreover, targeting blood-derived Plg through oligonucleotide technologies decreased amyloid β plaque deposition and neuropathology in a mouse model of AD (*42*). Given that transfer of young blood simultaneously elicits central (*3*, *9*) and peripheral (*44–46*) enhancements in regenerative capacity in aged mice, our data raise the possibility that the beneficial effects of exercise could be promoted broadly across tissues through circulating blood factors.

REFERENCES AND NOTES

1. K. I. Erickson *et al*., *Proc. Natl. Acad. Sci. U.S.A.* **108**, 3017–3022 (2011).
2. A. Maass *et al*., *Mol. Psychiatry* **20**, 585–593 (2015).
3. A. M. Horowitz, S. A. Villeda, *F1000 Res.* **6**, 1291 (2017).
4. R. E. Rhodes *et al*., *Sports Med.* **28**, 397–411 (1999).
5. H. van Praag, T. Shubert, C. Zhao, F. H. Gage, *J. Neurosci.* **25**, 8680–8685 (2005).
6. A. Kumar, A. Rani, O. Tchigranova, W.-H. Lee, T. C. Foster, *Neurobiol. Aging* **33**, 828.e1–828.e17 (2012).
7. R. B. Speisman, A. Kumar, A. Rani, T. C. Foster, B. K. Ormerod, *Brain Behav. Immun.* **28**, 25–43 (2013).
8. I. Soto *et al*., *PLOS Biol.* **13**, e1002279 (2015).
9. X. Fan, E. G. Wheatley, S. A. Villeda, *Annu. Rev. Neurosci.* **40**, 251–272 (2017).
10. S. A. Villeda *et al*., *Nature* **477**, 90–94 (2011).
11. S. A. Villeda *et al*., *Nat. Med.* **20**, 659–663 (2014).
12. L. Katsimpardi *et al*., *Science* **344**, 630–634 (2014).
13. J. M. Castellano *et al*., *Nature* **544**, 488–492 (2017).
14. L. Khrimian *et al*., *J. Exp. Med.* **214**, 2859–2873 (2017).
15. G. Gontier *et al*., *Cell Rep.* **22**, 1974–1981 (2018).
16. C.-W. Wu *et al*., *J. Appl. Physiol.* **105**, 1585–1594 (2008).
17. H. van Praag, B. R. Christie, T. J. Sejnowski, F. H. Gage, *Proc. Natl. Acad. Sci. U.S.A.* **96**, 13427–13431 (1999).
18. S. Lugert *et al*., *Cell Stem Cell* **6**, 445–456 (2010).
19. D. J. Creer, C. Romberg, L. M. Saksida, H. van Praag, T. J. Bussey, *Proc. Natl. Acad. Sci. U.S.A.* **107**, 2367–2372 (2010).
20. Tabula Muris Consortium, *Nature* **562**, 367–372 (2018).
21. M. Uhlén *et al*., *Science* **347**, 1260419 (2015).
22. B. J. Scallon *et al*., *Science* **252**, 446–448 (1991).
23. G. A. Maguire, A. Gossner, *Ann. Clin. Biochem.* **32**, 74–78 (1995).
24. M. K. Schwinn *et al*., *ACS Chem. Biol.* **13**, 467–474 (2018).
25. M. A. Davitz *et al*., *Science* **238**, 81–84 (1987).
26. C. N. Metz *et al*., *EMBO J.* **13**, 1741–1751 (1994).
27. Y. Fujihara, M. Ikawa, *J. Lipid Res.* **57**, 538–545 (2016).
28. M. G. Low, A. R. S. Prasad, *Proc. Natl. Acad. Sci. U.S.A.* **85**, 980–984 (1988).
29. M. Del Rosso *et al*., *Curr. Pharm. Des.* **17**, 1924–1943 (2011).
30. F. Blasi, N. Sidenius, *FEBS Lett.* **584**, 1923–1930 (2010).
31. N. S. Raikwar, R. F. Bowen, M. A. Deeg, *Biochem. J.* **391**, 285–289 (2005).
32. S. F. Sorrells *et al*., *Nature* **555**, 377–381 (2018).
33. E. P. Moreno-Jiménez *et al*., *Nat. Med.* **25**, 554–560 (2019).
34. M. K. Tobin *et al*., *Cell Stem Cell* **24**, 974–982.e3 (2019).
35. N. T. Lautenschlager *et al*., *JAMA* **300**, 1027–1037 (2008).
36. Y. E. Geda *et al*., *Arch. Neurol.* **67**, 80–86 (2010).
37. S. Müller *et al*., *Alzheimers Dement.* **14**, 1427–1437 (2018).
38. K. A. Intlekofer, C. W. Cotman, *Neurobiol. Dis.* **57**, 47–55 (2013).
39. S. H. Choi *et al*., *Science* **361**, eaan8821 (2018).
40. C. D. Wiley *et al*., *Cell Rep.* **28**, 3329–3337.e5 (2019).
41. A. T. Naito *et al*., *Cell* **149**, 1298–1313 (2012).
42. S. K. Baker *et al*., *Proc. Natl. Acad. Sci. U.S.A.* **115**, E9687–E9696 (2018).
43. M. A. Shaw *et al*., *J. Neurosci.* **37**, 3776–3788 (2017).
44. I. M. Conboy *et al*., *Nature* **433**, 760–764 (2005).
45. M. Sinha *et al*., *Science* **344**, 649–652 (2014).
46. G. S. Baht *et al*., *Nat. Commun.* **6**, 7131 (2015).

ACKNOWLEDGMENTS

We thank A. Brack and J. Sneddon for critically reading the manuscript. **Funding:** Supported by Hillblom Foundation predoctoral (A.M.H.) and postdoctoral (K.B.C.) fellowships, an Irene Diamond AFAR postdoctoral fellowship (G.G.), a National Institute on Aging (NIA) Ruth L. Kirschstein NRSA fellowship (AG064823, A.B.S.), NIA [AG058752 (K.B.C.), AG023501 (J.H.K.), AG053382 (S.A.V.), AG067740 (S.A.V.)], and a gift from M. and L. Benioff (S.A.V.). **Author contributions:** A.M.H., X.F., and S.A.V. developed the concept and designed experiments; A.M.H. and X.F. collected and analyzed data; A.M.H. performed plasma administration and Gpld1 studies; X.F. performed plasma administration studies; G.B. assisted with Gpld1 studies; L.K.S. assisted with biochemical analysis. C.I.S.-D., A.B.S., and G.G. assisted with molecular and cognitive analysis; K.B.C. and J.H.K. provided human samples; K.E.W. performed mass spectrometry analysis; A.M.H. and S.A.V. wrote the manuscript; and S.A.V. supervised all aspects of this project. All authors had the opportunity to discuss results and comment on the manuscript. **Competing interests:** The authors declare no conflict of interest. A.M.H., X.F., and S.A.V. are named as inventors on a patent application arising from this work. **Data and materials availability:** All data needed to understand and assess the conclusions of this study are included in the text, figures, and supplementary materials.

SUPPLEMENTARY MATERIALS

science.sciencemag.org/content/369/6500/167/suppl/DC1
Materials and Methods
Figs. S1 to S8
Tables S1 to S3
References (*47–58*)

3 December 2018; resubmitted 15 October 2019
Accepted 15 May 2020
10.1126/science.aaw2622

QUANTUM PHYSICS

Light-mediated strong coupling between a mechanical oscillator and atomic spins 1 meter apart

Thomas M. Karg[1], Baptiste Gouraud[1]*, Chun Tat Ngai[1], Gian-Luca Schmid[1], Klemens Hammerer[2], Philipp Treutlein[1]†

Engineering strong interactions between quantum systems is essential for many phenomena of quantum physics and technology. Typically, strong coupling relies on short-range forces or on placing the systems in high-quality electromagnetic resonators, which restricts the range of the coupling to small distances. We used a free-space laser beam to strongly couple a collective atomic spin and a micromechanical membrane over a distance of 1 meter in a room-temperature environment. The coupling is highly tunable and allows the observation of normal-mode splitting, coherent energy exchange oscillations, two-mode thermal noise squeezing, and dissipative coupling. Our approach to engineering coherent long-distance interactions with light makes it possible to couple very different systems in a modular way, opening up a range of opportunities for quantum control and coherent feedback networks.

Many of the recent breakthroughs in quantum science and technology rely on engineering strong, controllable interactions between quantum systems. In particular, Hamiltonian interactions that generate reversible, bidirectional coupling play an important role in creating and manipulating nonclassical states in quantum metrology (*1*), simulation (*2*), and information processing (*3*). For systems in close proximity, strong Hamiltonian coupling is routinely achieved; prominent examples include atom-photon coupling in cavity quantum electrodynamics (*4*) and coupling of trapped ions (*5*) or solid-state spins (*6*) via short-range electrostatic or magnetic forces. At macroscopic distances, however, the observation of strong Hamiltonian coupling is hampered by a severe drop in the interaction strength. Moreover, as the distance increases, it becomes increasingly difficult to prevent information leakage from the systems to the environment, which renders the interaction dissipative (*7*). Overcoming these challenges would make Hamiltonian interactions available for reconfigurable long-distance coupling in quantum networks (*4*) and hybrid quantum systems (*8*, *9*), which so far depend mostly on measurement-based or dissipative interactions.

A promising strategy to reach this goal uses one-dimensional waveguides or free-space laser beams over which quantum systems can couple via the exchange of photons. Such cascaded quantum systems (*10*) have attracted interest in the context of chiral quantum optics (*11*, *12*) and waveguide quantum electrodynamics (*13*).

[1]Department of Physics and Swiss Nanoscience Institute, University of Basel, 4056 Basel, Switzerland. [2]Institute for Theoretical Physics and Institute for Gravitational Physics (Albert Einstein Institute), Leibniz Universität Hannover, 30167 Hannover, Germany.
*Present address: iXblue, 34 rue de la Croix de Fer, 78105 Saint-Germain-en-Laye, France.
†Corresponding author. Email: philipp.treutlein@unibas.ch

A fundamental challenge in this approach is that the same photons that generate the coupling eventually leak out, thus allowing the systems to decohere at an equal rate. For this reason, light-mediated coupling is mainly seen today as a means for unidirectional state transfer (*14*–*16*) or entanglement generation by collective measurement (*17*–*19*) or dissipation (*20*). Decoherence by photon loss can be suppressed if the waveguide is terminated by mirrors to form a high-quality resonator, which has enabled coherent coupling of superconducting qubits (*21*, *22*), atoms (*23*), or atomic mechanical oscillators (*24*) in mesoscopic setups. However, stability constraints and bandwidth limitations make it difficult to extend resonator-based approaches to larger distances. Despite recent advances with coupled cavity arrays (*25*, *26*), strong bidirectional Hamiltonian coupling mediated by light over a truly macroscopic distance remains a challenge.

To realize long-distance Hamiltonian interactions, we pursued an alternative approach that relies on connecting two systems by a laser beam in a loop geometry (*27*, *28*). The systems can exchange photons through the loop, thereby realizing a bidirectional interaction. Moreover, the loop leads to an interference of quantum noise introduced by the light field. For any system that couples to the light twice and with opposite phase, quantum noise interferes destructively and associated decoherence is suppressed. At the same time, information about that system is erased from the output field. In this way, the coupled systems can effectively be closed to the environment, even though the light field mediates strong interactions between them. Because the coupling is mediated by light, it allows systems of different physical nature to be connected over macroscopic distances. Furthermore, by manipulating the light field between the systems, one can reconfigure the interaction without having to modify the quantum systems themselves. These features will be useful for quantum networking (*4*).

We used this scheme to couple a collective atomic spin and a micromechanical membrane held in separate vacuum chambers, thereby realizing a hybrid atom-optomechanical system (*8*). First experiments with such setups have recently demonstrated sympathetic cooling (*29*, *30*), quantum back-action evading measurement (*31*), and entanglement (*32*). Here, we realize strong Hamiltonian coupling and demonstrate the versatility of light-mediated interactions: We engineer beamsplitter and parametric-gain Hamiltonians and switch from Hamiltonian to dissipative coupling by applying a phase shift to the light field between the systems. This high level of control in a modular setup gives access to a unique toolbox for designing hybrid quantum systems (*9*) and coherent feedback loops for advanced quantum control strategies (*33*).

Description of the coupling scheme

In the experimental setup (Fig. 1A) (*34*), the atomic ensemble consists of $N = 10^7$ laser-cooled ^{87}Rb atoms in an optical dipole trap. The atoms form a collective spin $\mathbf{F} = \sum_{i=1}^{N} \mathbf{f}^{(i)}$, where $\mathbf{f}^{(i)}$ is the $f = 2$ ground-state spin vector of atom *i*. Optical pumping polarizes $\mathbf{F}$ along an external magnetic field $\mathbf{B}_0$ in the x-direction such that the spin acquires a macroscopic orientation $\bar{F}_x = -fN$. The small-amplitude dynamics of the transverse spin components F_y, F_z are well approximated by a harmonic oscillator (*35*) with position $X_s = F_z/\sqrt{|\bar{F}_x|}$ and momentum $P_s = F_y/\sqrt{|\bar{F}_x|}$. It oscillates at the Larmor frequency $\Omega_s \propto B_0$, which is tuned by the magnetic field strength. A feature of the spin system is that it can realize such an oscillator with either positive or negative effective mass (*31*, *36*). This is achieved by reversing the orientation of $\mathbf{F}$ with respect to $\mathbf{B}_0$, which reverses the sense of rotation of the oscillator in the X_s, P_s plane (Fig. 1B). This feature allows us to realize different Hamiltonian dynamics with the spin coupled to the membrane.

The spin interacts with the coupling laser beam through an off-resonant Faraday interaction (*35*) $H_s = 2\hbar\sqrt{\Gamma_s/\bar{S}_x}X_sS_z$, which couples X_s to the polarization state of the light, described by the Stokes vector $\mathbf{S}$. Initially, the laser is linearly polarized along x with $\bar{S}_x = \Phi_L/2$, where Φ_L is the photon flux. The strength of the atom-light coupling depends on the spin measurement rate $\Gamma_s \propto d_0\Phi_L/\Delta_a^2$, which is proportional to the optical depth $d_0 \approx 300$ of the atomic ensemble (*34*). Choosing a large laser-atom detuning $\Delta_a = -2\pi \times 80$ GHz suppresses spontaneous photon scattering while maintaining a sizable coupling.

The mechanical oscillator is the (2, 2) square-drum mode of a silicon nitride membrane at a vibrational frequency of $\Omega_m = 2\pi \times 1.957$ MHz with a quality factor of 1.3×10^6 (*37*). It is placed

in a short single-sided optical cavity to enhance the optomechanical interaction while maintaining a large cavity bandwidth for fast and efficient coupling to the external light field. Radiation pressure couples the membrane displacement X_m to the amplitude fluctuations X_L of the light entering the cavity on resonance, with Hamiltonian $H_m = 2\hbar\sqrt{\Gamma_m}X_m X_L$ (*38*). Here, we define the optomechanical measurement rate $\Gamma_m = (4g_0/\kappa)^2\Phi_m$ that depends on the vacuum optomechanical coupling constant g_0, cavity linewidth κ, and photon flux Φ_m entering the cavity (*34*). In the present setup, the optomechanical cavity is mounted in a room-temperature vacuum chamber, making thermal noise the dominant noise source of the experiment.

The light field mediates a bidirectional coupling between the spin and the membrane. A spin displacement X_s is mapped by H_s to a polarization rotation $S_y = 2\sqrt{\Gamma_s \bar{S}_x}X_s$ of the light. A polarization interferometer (Fig. 1A) converts this to an amplitude modulation $X_L \approx S_y/\sqrt{\bar{S}_x}$ at the optomechanical cavity, resulting in a force $\dot{P}_m = -4\sqrt{\Gamma_m\Gamma_s}X_s$ on the membrane. Conversely, a membrane displacement X_m is turned by H_m into a phase modulation $P_L = -2\sqrt{\Gamma_m}X_m$ of the cavity output field. The interferometer converts this to a polarization rotation $S_z \approx \sqrt{\bar{S}_x}P_L$, resulting in a force $\dot{P}_s = 4\sqrt{\Gamma_s\Gamma_m}X_m$ on the spin. A small angle between the laser beams in the two atom-light interactions prevents light from going once more to the membrane. Consequently, the cascaded setup promotes a bidirectional spin-membrane coupling. A fully quantum mechanical treatment (*34*) confirms this picture and predicts a spin-membrane coupling strength $g = (\eta^2 + \eta^4)\sqrt{\Gamma_s\Gamma_m}$, accounting for an effective optical power transmission $\eta^2 \approx 0.8$ between the systems.

The light-mediated interaction can be thought of as a feedback loop that transmits a spin excitation to the membrane, whose response then acts back on the spin, and vice versa (Fig. 1B). After one round trip, the initial signal has acquired a phase ϕ, the loop phase. The discussion above refers to a vanishing loop phase $\phi = 0$ and shows that the forces $\dot{P}_m = -2gX_s$ and $\dot{P}_s = +2gX_m$ differ in their relative sign. Such a coupling is nonconservative and cannot arise from a Hamiltonian interaction. With full access to the laser beams, we can tune the loop phase by inserting a half-wave plate in the path from the membrane back to the atoms, which rotates the Stokes vector by an angle $\phi = \pi$ about S_x. This inverts both S_y and S_z, which respectively carry the spin and membrane signals, thus switching the dynamics to a fully Hamiltonian force, $\dot{P}_m = -2gX_s$ and $\dot{P}_s = -2gX_m$.

All these phenomena are unified in a rigorous quantum mechanical theory (*28*) of the cascaded light-mediated coupling, which also correctly describes the dynamics for an arbitrary loop phase. It allows us to describe the effective dynamics of

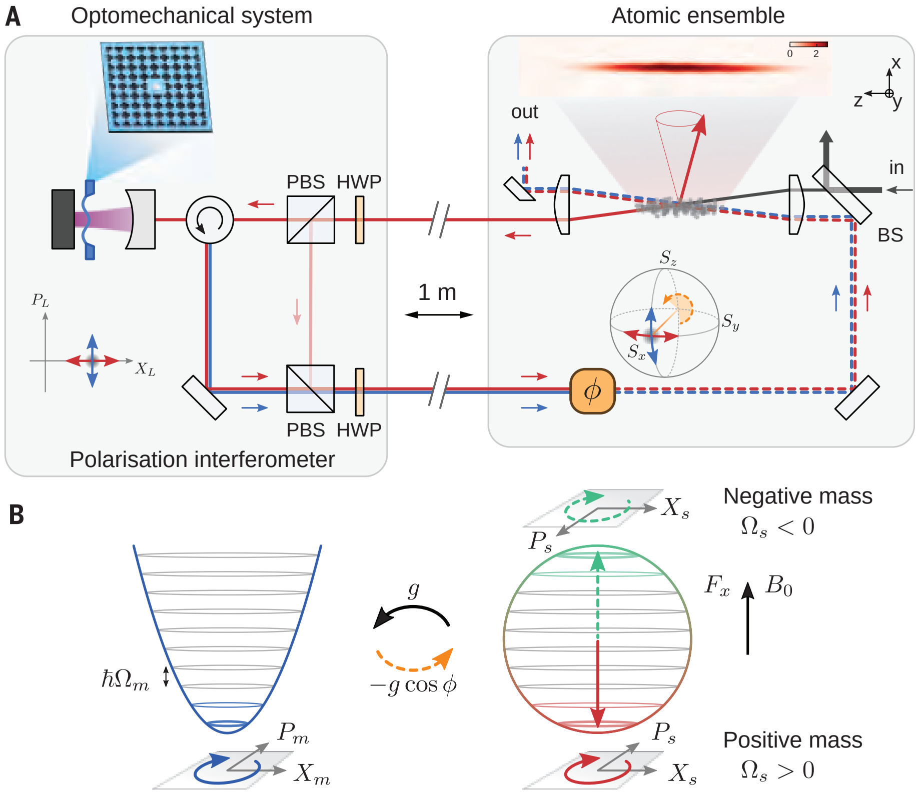

Fig. 1. Schematic setup for long-distance Hamiltonian coupling. (**A**) Cascaded coupling of an atomic spin ensemble (right) and a micromechanical membrane (left) by a free-space laser beam. The pictures show the silicon nitride membrane embedded in a silicon chip with phononic crystal structure and a side-view absorption image of the atomic cloud (color scale indicates optical density). The laser beam first carries information from the atoms to the membrane and then loops back to the atoms such that it mediates a bidirectional interaction. A polarization interferometer (PBS, polarizing beamsplitter; HWP, half-wave plate) maps between the Stokes vector **S** (defining the polarization state of light at the atoms) and field quadratures X_L, P_L (relevant for the optomechanical interaction). The loop phase ϕ is controlled by a rotation of **S** by an angle ϕ in the optical path from the membrane to the atoms. (**B**) Effective interaction. The membrane vibration mode (harmonic oscillator) is coupled to the collective spin of the atoms (represented on a sphere). If the mean spin is oriented along an external magnetic field B_0 to either the south or north pole of the sphere, its small-amplitude dynamics can be mapped onto a harmonic oscillator with positive or negative mass, respectively. The relative phase of the spin-to-membrane coupling constant g and the membrane-to-spin coupling constant $-g\cos\phi$ defines whether the effective dynamics are Hamiltonian ($\phi = \pi$) or dissipative ($\phi = 0$).

the coupled spin-membrane system with density operator ρ by a Markovian master equation,

$$\dot{\rho} = \frac{1}{i\hbar}[H_0 + H_{\text{eff}}, \rho] - \frac{1}{2}(J^\dagger J\rho + \rho J^\dagger J) + J\rho J^\dagger \quad (1)$$

Here, we neglect optical loss and light propagation delay between the systems for brevity. The dynamics consist of a unitary part with free harmonic oscillator Hamiltonian $H_0 = \sum_{i=s,m}\hbar\Omega_i(X_i^2 + P_i^2)/2$ and effective interaction Hamiltonian $H_{\text{eff}} = (1-\cos\phi)\hbar g X_s X_m + 2\sin(\phi)\hbar\Gamma_s X_s^2$, and a dissipative part with collective jump operator $J = \sqrt{2\Gamma_m}X_m + i[1 + \exp(i\phi)]\sqrt{2\Gamma_s}X_s$. Next to the coherent spin-membrane coupling, H_{eff} also includes a spin self-interaction that vanishes for the specific cases $\phi = 0, \pi$ considered here. The jump operator contains a constant membrane term and a spin term that is modulated by ϕ as a result of interference of the two spin-light interactions. From the dependence of H_{eff} and J on ϕ, it is clear that $\phi = 0$ corresponds to vanishing Hamiltonian coupling and maximum dissipative coupling. Accordingly, we refer to $\phi = 0$ as the dissipative regime. On the other hand, $\phi = \pi$ maximizes the coherent spin-membrane coupling in H_{eff} and at the same time leads to destructive interference of the spin term in J; thus, we call $\phi = \pi$ the Hamiltonian regime. We experimentally explored both regimes, each with the atomic spin realizing either a positive- or negative-mass oscillator. This gives rise to a whole range of different dynamics in a single system, which can be harnessed for different purposes in quantum technology.

Results

Normal-mode splitting

We first investigate the light-mediated coupling in the Hamiltonian regime ($\phi = \pi$) and with the spin realizing a positive-mass oscillator. At a magnetic field of B_0 = 2.81 G, the spin is tuned into resonance with the membrane ($\Omega_s = \Omega_m$). In this configuration, the resonant terms in H_{eff} realize a beamsplitter interaction $H_{\mathrm{BS}} = \hbar g(b_s^\dagger b_m + b_m^\dagger b_s)$, which generates state swaps between the two systems. Here $b_s = (X_s + iP_s)/\sqrt{2}$ and $b_m = (X_m + iP_m)/\sqrt{2}$ are annihilation operators of the spin and mechanical modes, respectively.

We perform spectroscopy of the coupled system using independent drive and detection channels for the spin and the membrane. The membrane vibrations are recorded by balanced homodyne detection using an auxiliary laser beam coupled to the cavity in orthogonal polarization. This beam is amplitude-modulated to drive the membrane. The spin precession is detected by splitting off a small portion of the coupling beam on the path from spin to membrane. A radio-frequency magnetic coil drives the spin. We measure the amplitude and phase response of either system using a lock-in amplifier that demodulates the detector signal at the drive frequency (*34*). After spin-state initialization, we simultaneously switch on coupling and drive and start recording. The drive frequency is kept fixed during each experimental run and stepped between consecutive runs.

Figure 2, A and B, shows the membrane's response in amplitude and phase, respectively. With the coupling beam off, it exhibits a Lorentzian resonance of linewidth $\gamma_m = 2\pi \times$ 0.3 kHz, broader than the intrinsic linewidth as a result of optomechanical damping by the red-detuned cavity field (*38*). For the uncoupled spin oscillator (Fig. 2, C and D) with cavity off-resonant, we also measure a Lorentzian response of linewidth $\gamma_s = 2\pi \times 4$ kHz, broadened by the coupling beam. When we turn on the coupling to the spin, the membrane resonance splits into two hybrid spin-mechanical normal modes. This signals strong coupling (*39*, *40*), where light-mediated coupling dominates over local damping. Fitting the well-resolved splitting yields $2g = 2\pi \times 6.1$ kHz, which exceeds the average linewidth $(\gamma_s + \gamma_m)/2 = 2\pi \times 2$ kHz and agrees with the expectation based on an independent calibration of the systems (*34*). A characteristic feature of the long-distance coupling is a finite delay τ between the systems. It causes a linewidth asymmetry of the two normal modes when $\Omega_s = \Omega_m$, which we observe in Fig. 2. The fits yield a value of τ = 15 ns, consistent with the propagation delay of the light between the systems and the cavity response time.

We also observe normal-mode splitting in measurements of the spin (Fig. 2, C and D). Here, the combination of the broader spin linewidth and the much narrower membrane resonance results in a larger dip between the two normal modes and a larger phase shift, in analogy to optomechanically induced transparency (*38*).

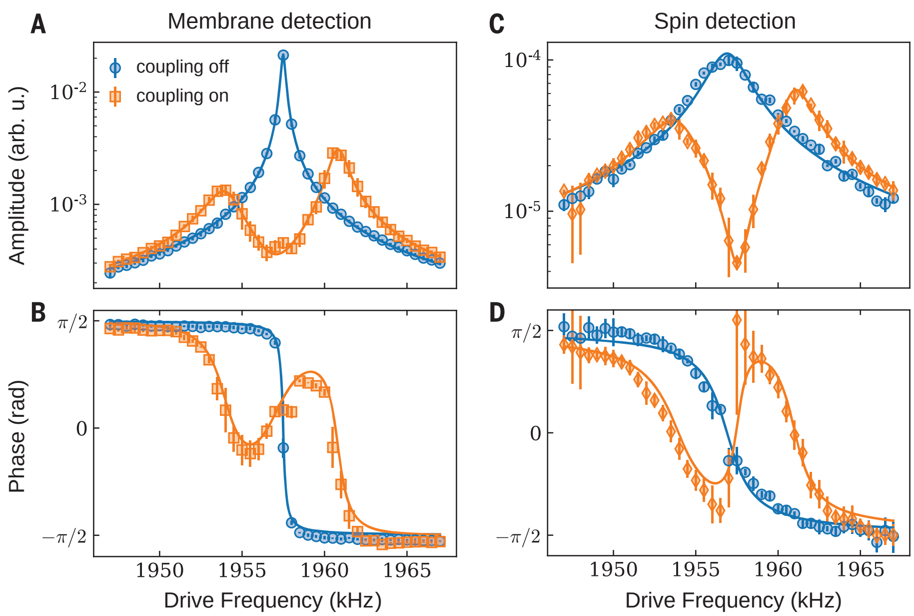

Fig. 2. Observation of strong spin-membrane coupling. (**A** to **D**) Spectroscopy of the membrane [(A) and (B)] and the spin [(C) and (D)], both revealing a normal-mode splitting if the coupling beam is on and the oscillators are resonant ($\Omega_s = \Omega_m$). For comparison we show the uncoupled responses of the membrane with coupling beam off [(A) and (B)] and of the spin with cavity off-resonant [(C) and (D)]. Lines are fits to the data with a coupled-mode model (*34*). Error bars denote SD of three independent measurements.

Energy exchange oscillations

Having observed the spectroscopic signature of strong coupling, we now use it for swapping spin and mechanical excitations in a pulsed experiment. We start by coherently exciting the membrane to ~2×10^6 phonons, a factor of 100 above its mean equilibrium energy, by applying an amplitude modulation pulse to the auxiliary cavity beam (Fig. 3A). At the same time, the spin is prepared in its ground state with $\Omega_s = \Omega_m$. The coupling beam is switched on at time t = 0 μs and the displacements $X_s(t)$ and $X_m(t)$ of the spin and membrane are continuously monitored via the independent detection. From the measured mean square displacements, we determine the excitation number of each system (*34*). Figure 3C shows the excitation numbers as a function of the interaction time. The data show coherent and reversible energy exchange oscillations from the membrane to the spin and back with an oscillation period of $T \approx 150$ μs, in accordance with the value π/g extracted from the observed normal-mode splitting. Damping limits the maximum energy transfer efficiency at time $T/2$ to about 40%.

The same experiment is repeated but with the initial drive pulse applied to the spin (Fig. 3, B and D). Here, we observe another set of exchange oscillations with the same periodicity, swapping an initial spin excitation of $n_s \approx 3 \times 10^5$ to the membrane and back. After the coherent dynamics have decayed, the systems equilibrate in a thermal state of ~3×10^3 phonons, lower than the effective optomechanical bath of 1.5×10^4 phonons, demonstrating sympathetic cooling (*29*) of the membrane by the spin. The observed sympathetic cooling strength agrees with simulations using the experimentally determined parameters.

Parametric-gain dynamics

So far we have explored Hamiltonian coupling of the membrane to a spin oscillator with positive effective mass, where the resonant interaction is of the beamsplitter type. If instead we reverse the magnetic field to B_0 = −2.81 G but keep the spin pumping direction the same, the collective spin is prepared in its highest-energy state with $\bar{F}_x = +Nf$. In this case, any excitation reduces the energy such that the spin oscillator has a negative effective mass (*17*) and $\Omega_s = -\Omega_m$ (Fig. 1B). The resonant term of H_{eff} is now the parametric-gain interaction (*38*) $H_{\mathrm{PG}} = \hbar g(b_s b_m + b_s^\dagger b_m^\dagger)$, which generates correlations between the two systems.

We investigate the dynamics generated by H_{PG} with the membrane driven by thermal noise. To quantify the development of spin-mechanical correlations, we determine slowly varying quadratures $\tilde{X}'_{s,m}$ and $\tilde{P}'_{s,m}$ of both systems as the cosine and sine components of the demodulated detector signals, respectively (*34*). Adjusting the demodulator phase allows us to find the basis with the strongest correlations. Figure 4A shows histograms of the measured spin-mechanical correlations after

an interaction time of t = 100 µs. In each subplot, the dashed ellipse corresponds to the Gaussian 1σ contour of the measured histogram at t = 0 µs, and the solid ellipse is the contour at t = 100 µs. Relative to the uncorrelated initial state, the histograms show strong amplification along the axes $\tilde{X}_+ = (\tilde{X}'_s + \tilde{X}'_m)/\sqrt{2}$ and $\tilde{P}_- = (\tilde{P}'_s - \tilde{P}'_m)/\sqrt{2}$, and a small amount of thermal noise squeezing along $\tilde{X}_- = (\tilde{X}'_s - \tilde{X}'_m)/\sqrt{2}$ and $\tilde{P}_+ = (\tilde{P}'_s + \tilde{P}'_m)/\sqrt{2}$. The quadrature pairs $\tilde{X}'_s, \tilde{P}'_m$ and $\tilde{P}'_s, \tilde{X}'_m$ remain uncorrelated.

In the time evolution of the combined variances $\tilde{X}_\pm$ and $\tilde{P}_\pm$ (Fig. 4B), at t = 0 all variances start from the same value, indicating an uncorrelated state. As time evolves, the variances of $\tilde{X}_+$ and $\tilde{P}_-$ grow exponentially, demonstrating the dynamical instability in this configuration, while $\tilde{X}_-$ and $\tilde{P}_+$ are squeezed and reach a minimum at t = 80 µs before they grow again. The exponential growth rate of 2π × 4.5 kHz is consistent with the value of $2g - (\gamma_m + \gamma_s)/2$ extracted from the normal-mode splitting. For comparison, we also show simulated variances for the experimental parameters, which are given by the lines in Fig. 4B (*34*). The solid lines show that good agreement between data and simulation is found when accounting for a spin detector noise floor of 6×10^3. The dashed lines correspond to perfect detection and show thermal noise squeezing by 5.5 dB. Realizing the parametric-gain interaction by light-mediated coupling represents an important step toward the generation of spin-mechanical entanglement by two-mode squeezing across macroscopic distances. Such entanglement is useful for metrology beyond the standard quantum limit (*1*).

Control of the loop phase

Equipped with control over both the loop phase and the effective mass of the spin oscillator, we can access four different regimes of the spin-membrane coupling: two Hamiltonian configurations with $\phi = \pi$ and $\Omega_s = \pm\Omega_m$, and the two corresponding dissipative configurations where we set $\phi = 0$ by omitting the half-wave plate in the optical path from membrane to atoms (*34*). Although the dynamics in these configurations are fundamentally different and have different quantum noise properties, we obtain simple equations of motion for the expectation values,

$$\ddot{X}_m + \gamma_m \dot{X}_m + \Omega_m^2 X_m = -g\Omega_m X_s(t-\tau) \quad (2)$$

$$\ddot{X}_s + \gamma_s \dot{X}_s + \Omega_s^2 X_s = +g\Omega_s \cos(\phi) X_m(t-\tau) \quad (3)$$

with the damped harmonic oscillations on the left and the delayed coupling terms on the right. These are derived from Heisenberg-Langevin equations of the full system (*34*) and reproduce the dynamics of the master equation in the limit $\tau \to 0$. Two distinct regimes can be identified. If $\Omega_s \cos\phi < 0$, we expect stable dynamics equivalent to a beamsplitter interaction. In the opposite case where $\Omega_s \cos\phi > 0$, the dynamics are equivalent to a parametric-gain interaction and are unstable. A simultaneous sign reversal of Ω_s and a π-shift of ϕ should leave the dynamics invariant.

To probe the dynamics in these configurations, we record thermal noise spectra of the membrane while the spin Larmor frequency is tuned across the mechanical resonance Ω_m = 2π × 1.957 MHz. The Hamiltonian configuration with positive-mass spin oscillator is depicted in Fig. 5A, showing an avoided crossing at $\Omega_s = \Omega_m$ with frequency splitting $2g$ = 2π × 5.9 kHz, as in Fig. 2. The dashed lines are the calculated normal-mode frequencies (*34*). The enhancement of the mechanical noise power

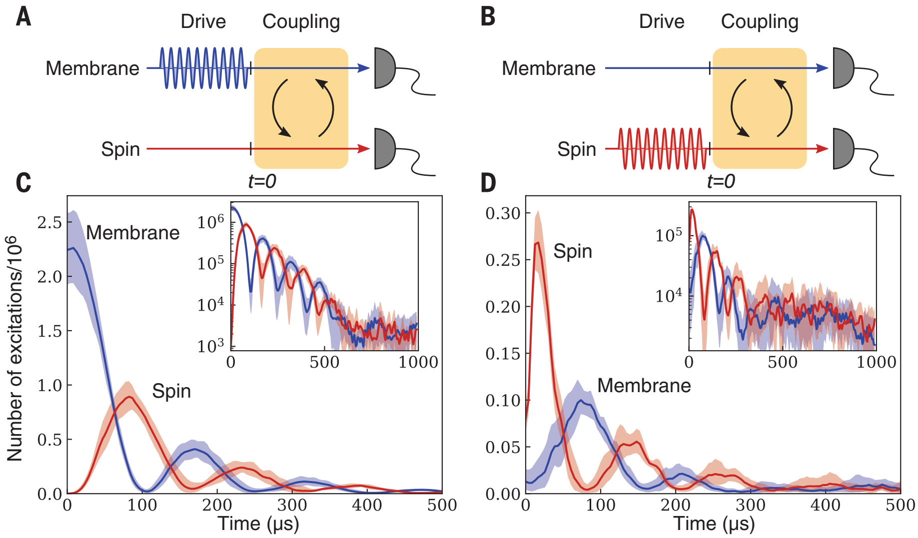

Fig. 3. Time-domain exchange oscillations showing coherent energy transfer between spin and membrane. (**A**) Pulse sequence for excitation of the membrane by radiation-pressure modulation via the auxiliary laser beam. (**B**) Pulse sequence for spin excitation with an external radio-frequency magnetic field. (**C**) Oscillations in the excitation numbers of membrane and spin as a function of the interaction time, measured using the pulse sequence in (A). (**D**) Data obtained with the pulse sequence in (B) and weaker drive strength than in (C). Here, the finite rise time of the spin signal at t = 0 corresponds to the turn-on of the coupling beam, which is also used for spin detection. Insets in (C) and (D) show the same data on a log scale. Lines and shaded areas denote means ± SD of five measurements.

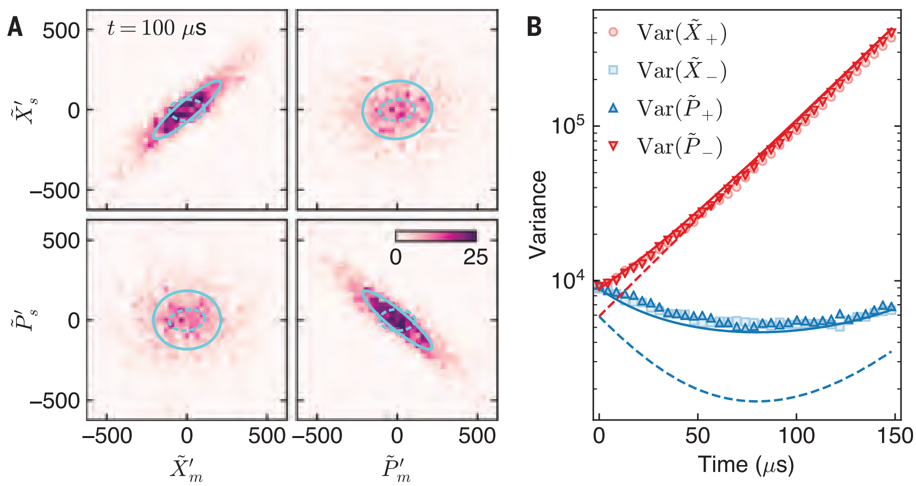

Fig. 4. Dynamics of the parametric-gain interaction with thermal noise averaged over 2000 realizations. (**A**) Phase-space histograms showing correlations between the rotated spin and membrane quadratures after 100 µs of interaction time. Solid ellipses enclose regions of 1 SD at t = 100 µs; dashed ellipses enclose regions of 1 SD at t = 0 µs. (**B**) Variances of the combined quadratures $\tilde{X}_\pm$ and $\tilde{P}_\pm$ as a function of interaction time. An exponential increase is observed for quadratures $\tilde{X}_+$ and $\tilde{P}_-$, whereas noise reduction is measured for $\tilde{X}_-$ and $\tilde{P}_+$. The solid lines are a simulation of the corresponding variances, including a spin detector noise floor of 6×10^3; the dashed lines assume noise-free detection.

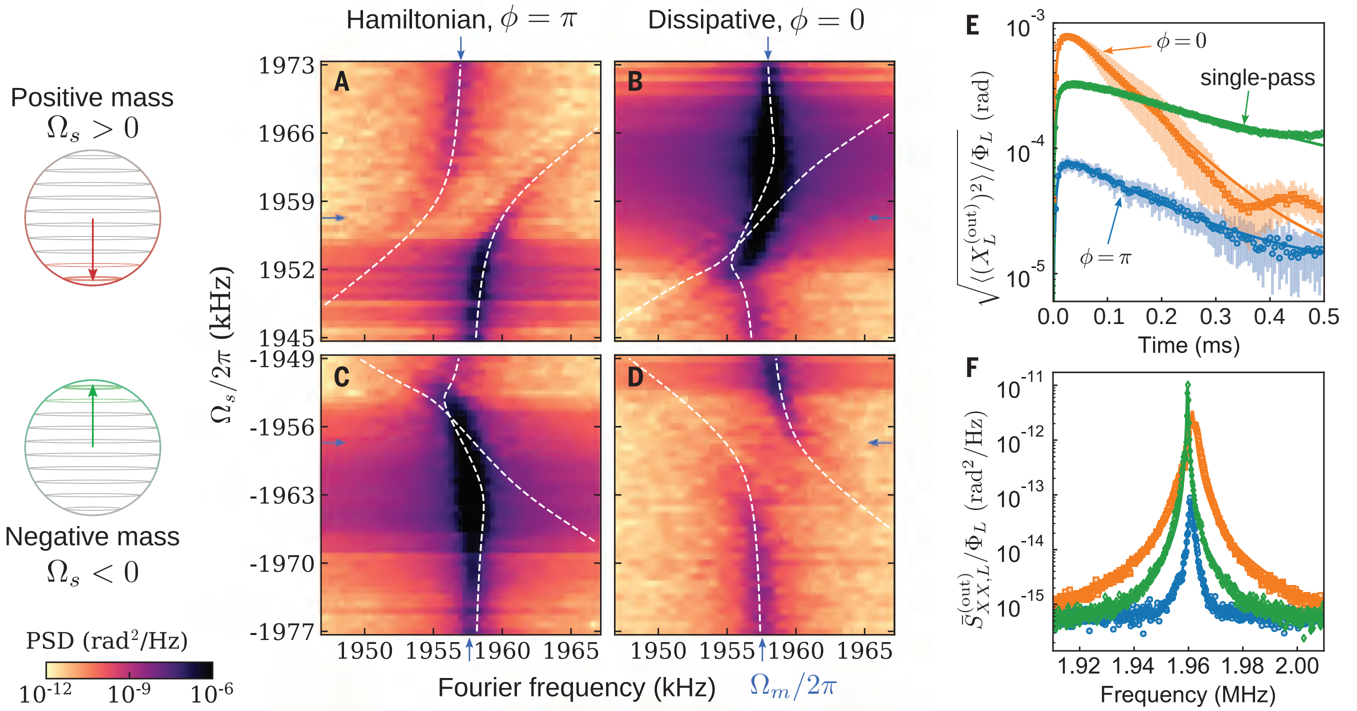

Fig. 5. Control of the loop phase. (**A** to **D**) Density plots of the membrane's thermal noise spectra in four different regimes, with membrane Fourier frequency on the horizontal axis (Ω_m indicated by blue arrows) and spin frequency Ω_s (controlled by magnetic field) on the vertical axis. Dashed white lines are the calculated normal-mode frequencies. (A) Hamiltonian coupling with a positive-mass spin oscillator (beamsplitter interaction): An avoided crossing is observed. (B) Dissipative coupling with a positive-mass spin oscillator: Level attraction and unstable dynamics at the exceptional point. (C) Hamiltonian coupling with a negative-mass spin oscillator (parametric gain interaction): Unstable dynamics and an exceptional point. (D) Dissipative coupling with a negative-mass spin oscillator: An avoided crossing is observed. (**E**) Atomic spin signal (RMS amplitude) on the output light after pulsed excitation: Constructive interference of the two atom-light interactions is observed for $\phi = 0$, and destructive interference of the interactions is observed for $\phi = \pi$. Data for a single-pass interaction are also shown for comparison. The membrane is decoupled by detuning the cavity. Error bars denote SD of 25 repetitions. (**F**) Frequency-domain power spectra corresponding to the data of (E).

for $\Omega_s < \Omega_m$, as compared to increased damping for $\Omega_s > \Omega_m$, is again a consequence of the finite optical propagation delay τ modifying the damping (*34*).

Switching to the dissipative regime with $\phi = 0$ renders the system unstable because of positive feedback of the coupled oscillations (Fig. 5B). Instead of an avoided crossing, the normal modes are now attracted and cross near $\Omega_s = 2\pi \times 1.953$ MHz, forming one strongly amplified and one strongly damped mode. The former leads to exponential growth of correlated spin-mechanical motion, finally resulting in limit-cycle oscillations that dominate the power spectrum. This results in a breakdown of the coupled oscillator model, such that the observed spectral peak shifts toward the unperturbed mechanical resonance. Still, the data are in good agreement with the theoretical model.

In Fig. 5, C and D, we repeat the experiments of Fig. 5, A and B, with a negative-mass spin oscillator. The data show that Hamiltonian coupling with a negative-mass spin oscillator produces spectra similar to those produced by dissipative coupling with a positive-mass spin oscillator. In these configurations, the coupled system features an exceptional point (*41*) where the normal modes become degenerate (*42*) and define the squeezed and antisqueezed quadratures. Conversely, dissipative coupling together with an inverted spin (Fig. 5D) shows an avoided crossing with parameters similar to those in the Hamiltonian case (Fig. 5A). This equivalence at the level of the expectation values is expected to break down once quantum noise of the light becomes relevant. As a result of interference in the loop, quantum back-action on the spin is suppressed in the Hamiltonian coupling configuration but is enhanced in the dissipative configuration.

A necessary condition for quantum back-action cancellation is destructive interference of the spin signal in the output field (*34*). Figure 5, E and F, shows homodyne measurements of coherent spin precession on the coupling beam output quadrature $X_L^{(\mathrm{out})}$ in the time and frequency domains, respectively. Toggling the loop phase between $\phi = 0$ and $\phi = \pi$, we observe a large interference contrast (>10) in the root-mean-squared (RMS) spin signal, showing that a spin measurement made by light in the first pass can be erased in the second pass. Optical loss of $1 - \eta^4 \approx 0.35$ inside the loop allows some information to leak out to the environment and brings in uncorrelated noise, limiting the achievable back-action suppression. Full interference in the output is still observed because the carrier and signal fields are subject to the same losses. Because this principle of quantum back-action interference is fully general, it could also be harnessed for other optical or microwave photonic networks (*4*, *27*).

Conclusion

The observed normal-mode splitting and coherent energy exchange oscillations establish strong spin-membrane coupling, where the coupling strength g exceeds the damping rates of both systems (*39*). To achieve quantum-coherent coupling (*40*), g must also exceed all thermal and quantum back-action decoherence rates. This will make it possible to swap nonclassical states between the systems or to generate remote entanglement by two-mode squeezing. Thermal noise on the mechanical oscillator is the major source of decoherence in our room-temperature setup. We expect that modest cryogenic cooling of the optomechanical system to 4 K together with an improved mechanical quality factor of $>10^7$ (*43*) will enable quantum-limited operation (*34*). The built-in suppression of quantum back-

action in the Hamiltonian configuration is a crucial feature of our coupling scheme. Interference of the two spin-light interactions reduces the spin's quantum back-action rate to $\gamma_{s,\mathrm{ba}} = (1 - \eta^4)\Gamma_s$, whereas it is $\gamma_{m,\mathrm{ba}} = \eta^2\Gamma_m$ for the membrane. Assuming thermal noise to be negligible, the quantum cooperativity $C = 2g/(\gamma_{s,\mathrm{ba}} + \gamma_{m,\mathrm{ba}})$ can be optimized for a given one-way transmission η^2. We find an upper bound $C \leq \eta(1+\eta^2)/\sqrt{1-\eta^4}$, reaching 2.7 for our current setup. The bound is achieved for an optimal choice of measurement rates $\Gamma_s/\Gamma_m = \eta^2/(1 - \eta^4)$, balancing the back-action on both systems. Further improvement is possible with a double-loop coupling scheme that also suppresses quantum back-action on the membrane (*28*). In this case, $C = \eta/(1 - \eta^2)$ at $\Gamma_s = \eta^2\Gamma_m$ is inversely proportional to optical loss, scaling more favorably at high transmission so that $C \approx 10$ can be reached for $\eta^2 = 0.9$.

Our results demonstrate a comprehensive and versatile toolbox for generating coherent long-distance interactions with light and open up a range of exciting opportunities for quantum information processing, simulation, and metrology. The coupling scheme constitutes a coherent feedback network (*33*) that allows quantum systems to directly exchange, process, and feed back information without the use of classical channels. The ability to create coherent Hamiltonian links between separate and physically distinct systems in a reconfigurable way substantially extends the available toolbox not only for hybrid spin-mechanical interfaces (*9*, *31*) but for quantum networks (*4*) in general. It facilitates the faithful processing of quantum information and the generation of entanglement between spatially separated quantum processors across a room-temperature environment.

REFERENCES AND NOTES

1. L. Pezzè, A. Smerzi, M. K. Oberthaler, R. Schmied, P. Treutlein, *Rev. Mod. Phys.* **90**, 035005 (2018).
2. C. Gross, I. Bloch, *Science* **357**, 995–1001 (2017).
3. T. D. Ladd *et al*., *Nature* **464**, 45–53 (2010).
4. H. J. Kimble, *Nature* **453**, 1023–1030 (2008).
5. R. Blatt, D. Wineland, *Nature* **453**, 1008–1015 (2008).
6. R. Hanson, D. D. Awschalom, *Nature* **453**, 1043–1049 (2008).
7. L. F. Buchmann, D. M. Stamper-Kurn, *Ann. Phys.* **527**, 156–161 (2015).
8. P. Treutlein, C. Genes, K. Hammerer, M. Poggio, P. Rabl, in *Cavity Optomechanics: Nano- and Micromechanical Resonators Interacting with Light*, M. Aspelmeyer, T. J. Kippenberg, F. Marquardt, Eds. (Springer, 2014), pp. 327–351.
9. G. Kurizki *et al*., *Proc. Natl. Acad. Sci. U.S.A.* **112**, 3866–3873 (2015).
10. C. Gardiner, P. Zoller, *Quantum Noise: A Handbook of Markovian and Non-Markovian Quantum Stochastic Methods with Applications to Quantum Optics* (Springer, 2004).
11. P. Lodahl *et al*., *Nature* **541**, 473–480 (2017).
12. D. E. Chang, J. S. Douglas, A. González-Tudela, C.-L. Hung, H. J. Kimble, *Rev. Mod. Phys.* **90**, 031002 (2018).
13. K. Lalumière *et al*., *Phys. Rev. A* **88**, 043806 (2013).
14. S. Ritter *et al*., *Nature* **484**, 195–200 (2012).
15. P. Campagne-Ibarcq *et al*., *Phys. Rev. Lett.* **120**, 200501 (2018).
16. P. Kurpiers *et al*., *Nature* **558**, 264–267 (2018).
17. B. Julsgaard, A. Kozhekin, E. S. Polzik, *Nature* **413**, 400–403 (2001).
18. J. Hofmann *et al*., *Science* **337**, 72–75 (2012).
19. R. Riedinger *et al*., *Nature* **556**, 473–477 (2018).
20. H. Krauter *et al*., *Phys. Rev. Lett.* **107**, 080503 (2011).
21. J. Majer *et al*., *Nature* **449**, 443–447 (2007).
22. M. Mirhosseini *et al*., *Nature* **569**, 692–697 (2019).
23. K. Baumann, C. Guerlin, F. Brennecke, T. Esslinger, *Nature* **464**, 1301–1306 (2010).
24. N. Spethmann, J. Kohler, S. Schreppler, L. Buchmann, D. M. Stamper-Kurn, *Nat. Phys.* **12**, 27–31 (2015).
25. S. Kato *et al*., *Nat. Commun.* **10**, 1160 (2019).
26. N. Leung *et al*., *Npj Quantum Inf.* **5**, 18 (2019).
27. A. F. Kockum, G. Johansson, F. Nori, *Phys. Rev. Lett.* **120**, 140404 (2018).
28. T. M. Karg, B. Gouraud, P. Treutlein, K. Hammerer, *Phys. Rev. A* **99**, 063829 (2019).
29. A. Jöckel *et al*., *Nat. Nanotechnol.* **10**, 55–59 (2015).
30. P. Christoph *et al*., *New J. Phys.* **20**, 093020 (2018).
31. C. B. Møller *et al*., *Nature* **547**, 191–195 (2017).
32. R. A. Thomas *et al*., arXiv 2003.11310 [quant-ph] (25 March 2020).
33. J. Zhang, Y. Liu, R.-B. Wu, K. Jacobs, F. Nori, *Phys. Rep.* **679**, 1–60 (2017).
34. See supplementary materials.
35. K. Hammerer, A. S. Sørensen, E. S. Polzik, *Rev. Mod. Phys.* **82**, 1041–1093 (2010).
36. E. S. Polzik, K. Hammerer, *Ann. Phys.* **527**, A15–A20 (2015).
37. J. D. Thompson *et al*., *Nature* **452**, 72–75 (2008).
38. M. Aspelmeyer, T. J. Kippenberg, F. Marquardt, *Rev. Mod. Phys.* **86**, 1391–1452 (2014).
39. S. Gröblacher, K. Hammerer, M. R. Vanner, M. Aspelmeyer, *Nature* **460**, 724–727 (2009).
40. E. Verhagen, S. Deléglise, S. Weis, A. Schliesser, T. J. Kippenberg, *Nature* **482**, 63–67 (2012).
41. H. Xu, D. Mason, L. Jiang, J. G. E. Harris, *Nature* **537**, 80–83 (2016).
42. N. R. Bernier, L. D. Tóth, A. K. Feofanov, T. J. Kippenberg, *Phys. Rev. A* **98**, 023841 (2018).
43. Y. Tsaturyan, A. Barg, E. S. Polzik, A. Schliesser, *Nat. Nanotechnol.* **12**, 776–783 (2017).
44. T. M. Karg *et al*., Zenodo doi:10.5281/zenodo.3779295 (2020).

ACKNOWLEDGMENTS

We thank G. Buser for setting up the dipole trap and M. Ernzer for discussions. **Funding:** Supported by the project "Modular mechanical-atomic quantum systems" (MODULAR) of the European Research Council (ERC) and by the Swiss Nanoscience Institute (SNI). K.H. acknowledges support through the cluster of excellence "Quantum Frontiers" and from DFG through CRC 1227 DQ-mat, projects A06. **Author contributions:** T.M.K., B.G., K.H., and P.T. conceived the experiment; T.M.K. and B.G. developed the theory, with input from K.H. and P.T.; T.M.K., B.G., C.T.N., and G.-L.S. built the experimental setup; T.M.K. took and analyzed the data, discussing with P.T.; T.M.K., P.T., and K.H. wrote the manuscript with input from other authors; and K.H. and P.T. supervised the project. **Competing interests:** The authors declare no competing interests. **Data and materials availability:** All data needed to evaluate the conclusions in the paper are present in the figures of the paper. The data can be accessed at (*44*).

SUPPLEMENTARY MATERIALS

science.sciencemag.org/content/369/6500/174/suppl/DC1
Supplementary Text
Figs. S1 to S4
Table S1
References (*45*–*56*)

27 January 2020; accepted 28 April 2020
Published online 7 May 2020
10.1126/science.abb0328

REPORTS

TOPOLOGICAL MATTER

Observation and control of maximal Chern numbers in a chiral topological semimetal

Niels B. M. Schröter[1]*, Samuel Stolz[2,3], Kaustuv Manna[4], Fernando de Juan[5,6], Maia G. Vergniory[5,6], Jonas A. Krieger[1,7,8], Ding Pei[9], Thorsten Schmitt[1], Pavel Dudin[10]†, Timur K. Kim[10], Cephise Cacho[10], Barry Bradlyn[11], Horst Borrmann[4], Marcus Schmidt[4], Roland Widmer[2], Vladimir N. Strocov[1], Claudia Felser[4]*

Topological semimetals feature protected nodal band degeneracies characterized by a topological invariant known as the Chern number (*C*). Nodal band crossings with linear dispersion are expected to have at most $|C| = 4$, which sets an upper limit to the magnitude of many topological phenomena in these materials. Here, we show that the chiral crystal palladium gallium (PdGa) displays multifold band crossings, which are connected by exactly four surface Fermi arcs, thus proving that they carry the maximal Chern number magnitude of 4. By comparing two enantiomers, we observe a reversal of their Fermi-arc velocities, which demonstrates that the handedness of chiral crystals can be used to control the sign of their Chern numbers.

Topological invariants are mathematical objects that can be used to classify Hamiltonians and have found widespread applications in physics, chemistry, and materials science. One of the best known topological invariants in condensed matter physics is the Chern number, which can be defined as the flux of Berry curvature through a closed two-dimensional surface. If this surface is taken to be the whole Brillouin zone, the Chern number classifies insulators in two dimensions, as first used in the context of the quantum Hall effect by Thouless and co-workers (*1*, *2*) in the 1980s. More recently, Chern numbers have also been used to classify topological nodal semimetals (*3*), where point-like energy degeneracies in their bulk electronic structure act as sources and sinks of quantized Berry flux through any local isoenergy surface enclosing the node. For the simplest case of a linear touching of two bands, which can occur in any noncentrosymmetric or

magnetic material and is called a Weyl point, the magnitude of the Chern number C is limited to $|C| = 1$. However, there is nothing preventing more complicated nodal crossings from having larger Chern numbers; this has important consequences, because the magnitude of many of the exotic phenomena predicted for topological semimetals is directly proportional to their Chern number. Examples include the number of topological Fermi-arc surface states (*3*, *4*), the number of chiral Landau levels influencing magnetotransport phenomena related to the chiral anomaly (*5*, *6*), the magnitude of the quantized rate of photocurrents in the quantized circular photogalvanic effect (*7*–*9*), and many more (*10*–*12*). Owing to the importance of the Chern number magnitude for these phenomena, it is natural to ask whether there is an upper limit for this topological invariant and whether there are real materials in which this limit can be reached.

It has recently been predicted that in chiral crystals, which possess neither mirror nor inversion symmetries, more complex band crossings can be pinned at high-symmetry lines or points that feature larger Chern numbers than Weyl semimetals. For example, twofold crossings with quadratic or cubic dispersion are predicted to host $|C| = 2$ or $|C| = 3$ (*13*, *14*). In materials with negligible spin-orbit coupling (SOC), threefold and fourfold crossings can be found with $|C| = 2$ per spin, whereas the combination of nonsymmorphic symmetries and substantial SOC gives rise to protected fourfold and sixfold degeneracies with Chern numbers up to a maximal magnitude of 4. The symmetry classification is exhaustive (*8*, *15*–*18*) and predicts that $|C| = 4$ only occurs thanks to SOC and is the highest possible Chern number achievable for a multifold node in nonmagnetic chiral topological semimetals. For linear band crossings in magnetic materials, the maximal Chern number is also 4 (*19*).

The family of chiral semimetals in space group 198—including RhSi, CoSi, AlPt, and PdBiSb—is expected to display these type of maximal $|C| = 4$ crossings, realized as a fourfold spin $S = 3/2$ crossing at the Γ point (known as the Rarita–Schwinger fermion) and a sixfold $S = 1$ crossing at the R point of the Brillouin zone, respectively. Despite several recent angle-resolved photoelectron spectroscopy (ARPES) experiments on all these candidates (*20*–*24*), the absolute magnitude of the Chern number, measured by counting the number of Fermi arcs, has not yet been observed for two reasons. The first is that SOC in some of these materials is low and spin-split Fermi arcs

[1]Swiss Light Source, Paul Scherrer Institute, CH-5232 Villigen PSI, Switzerland. [2]EMPA, Swiss Federal Laboratories for Materials Science and Technology, 8600 Dübendorf, Switzerland. [3]Institute of Condensed Matter Physics, Station 3, EPFL, 1015 Lausanne, Switzerland. [4]Max Planck Institute for Chemical Physics of Solids, Dresden D-01187, Germany. [5]Donostia International Physics Center, 20018 Donostia-San Sebastian, Spain. [6]IKERBASQUE, Basque Foundation for Science, Maria Diaz de Haro 3, 48013 Bilbao, Spain. [7]Laboratory for Muon Spin Spectroscopy, Paul Scherrer Institute, CH-5232 Villigen PSI, Switzerland. [8]Laboratorium für Festkörperphysik, ETH Zurich, CH-8093 Zurich, Switzerland. [9]Clarendon Laboratory, Department of Physics, University of Oxford, Oxford OX1 3PU, UK. [10]Diamond Light Source, Didcot OX11 0DE, UK. [11]Department of Physics and Institute for Condensed Matter Theory, University of Illinois at Urbana-Champaign, Urbana, IL 61801-3080, USA.
***Corresponding author. Email: niels.schroeter@psi.ch (N.B.M.S.); claudia.felser@cpfs.mpg.de (C.F.)** †Present address: Synchrotron Soleil, 91192 Gif-sur-Yvette, France.

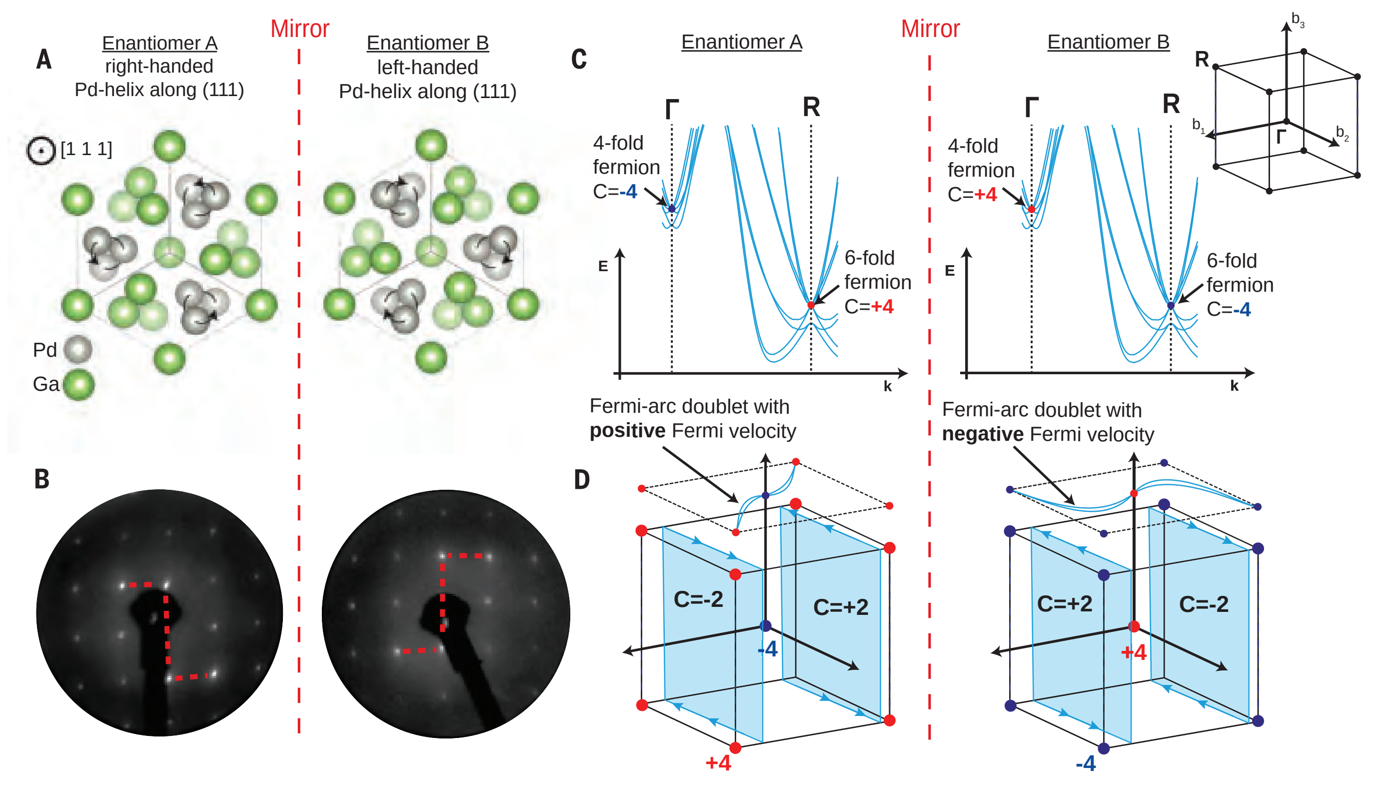

Fig. 1. Structural and electronic chirality in the two enantiomers of PdGa. (**A**) Illustration of the crystal structure of two enantiomers of PdGa with opposite handedness. (**B**) LEED patterns for two samples with opposite chirality, measured with an electron energy of E_{kin} = 95 eV. The S-shaped intensity distribution of the diffraction spots (highlighted by red dashed lines as guides for the eye) reflects the handedness of the crystal structure. (**C**) Ab initio calculations of the band structure in PdGa, showing fourfold and sixfold band crossings at the Γ and R points. The Chern numbers associated with the crossings are of magnitude 4 and flip their sign on a mirror operation. This reverses the direction of Berry flux that is flowing from the crossing with positive Chern number (red circles) toward the crossing with negative Chern number (blue circles). The inset shows the cubic Brillouin zone with high-symmetry points Γ at the zone center and R at the zone corner. (**D**) Illustration of bulk boundary correspondence for PdGa and related chiral topological semimetals. Blue-shaded slices indicate two-dimensional quantum Hall phase with Chern numbers of magnitude 2. Dashed black lines indicate the edges of the surface Brillouin zone, and solid blue lines and black arrows indicate the Fermi-arc surface states that are connecting the projections of R and Γ points.

cannot be resolved, effectively leading to only two observable arcs. Most photoemission studies to date (*20*–*22*) classify these nodes as having $|C| = 2$, whereas recent all-optical measurements (*25*) find a Chern number close to 4. The second reason is the difficulty in preparing clean and flat surfaces by cleaving or sputtering and annealing, which has resulted in rough or nonstoichiometric surfaces for all previously examined candidates, causing band broadening that can wash out signatures of spin-split bands caused by SOC. In this work, we overcome

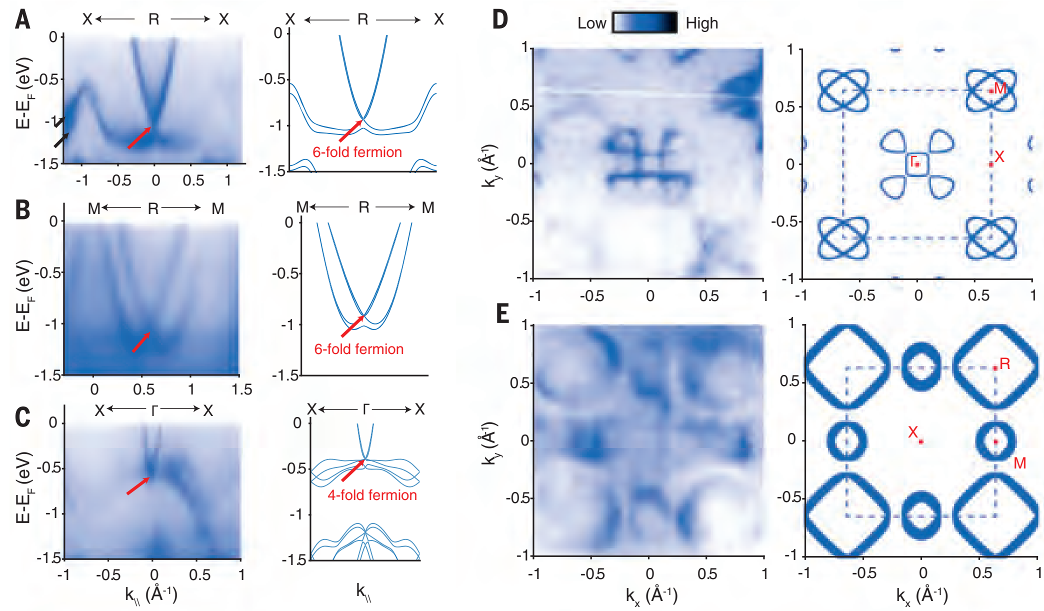

Fig. 2. Electronic characterization of the bulk electronic structure of PdGa measured on the (100) surface of enantiomer A. (**A** to **C**) Comparison between ARPES spectra (left) and ab initio calculations (right) along high-symmetry lines that pass through the Γ and R points. Multifold fermions are indicated by red arrows, and spin-orbit splitting is indicated by black arrows. Spectra were measured at *hν* = 550, 552, and 620 eV in (A) to (C), respectively, all with linear-vertical polarization (LV). E-E$_F$, the binding energy with respect to the Fermi-level; k$_{||}$, the in-plane wave vector. (**D** to **E**) Comparison between experimental Fermi surfaces (left) and ab initio calculations (right). (D) shows the Fermi surface in the high-symmetry plane that contains the G point (measured with *hν* = 620 eV, LV polarization), whereas (E) contains the plane that includes the R point (measured with *hν* = 540 eV, LV polarization). The blue dashed lines indicate the boundary of the bulk Brillouin zone. Ab initio calculations include k_z broadening of 0.1 Å^{-1}.

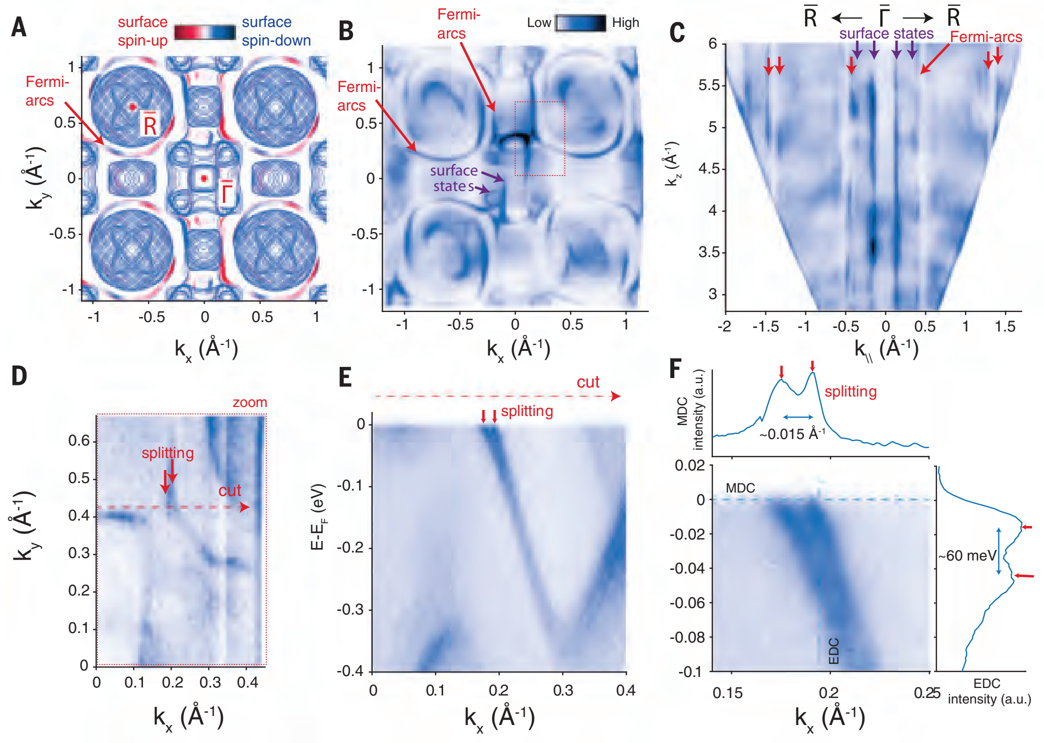

Fig. 3. Surface electronic structure of the (100) surface of enantiomer A. (**A**) Ab initio slab calculation of the Fermi surface in the (100) plane (i.e., k_x versus k_y plane) showing surface Fermi arcs (indicated by a red arrows), superimposed by projected bulk band structure calculation (solid blue lines). (**B**) Experimental Fermi surface measured with *hν* = 60 eV and linear-horizontal (LH) polarization. Red arrows indicate Fermi arcs, whereas purple arrows indicate additional surface states that overlap with the projected bulk states at $\bar{\Gamma}$. (**C**) Experimental Fermi surface perpendicular to the sample surface (i.e., k_y versus k_z plane), showing that the Fermi arcs and surface states (indicated by red and purple arrows, respectively) show negligible dispersion along the k_z direction. Conversion from photon energy was performed within free-electron final state approximation with inner potential of V_0 = 12 eV. (**D**) Magnified Fermi surface measured in the region of the red dashed rectangle shown in (B) with *hν* = 30 eV and LH polarization. Red arrows indicate spin splitting of Fermi arcs. (**E**) Band dispersion measured along the path in momentum space indicated by the red dashed arrow shown in (D) that is crossing the Fermi arcs, and red arrows indicate their spin splitting. (**F**) Magnified version of (E). Insets show the momentum distribution curve (MDC) and energy distribution curve (EDC) along the dashed blue lines. a.u., arbitrary units.

these obstacles by investigating a different chiral topological semimetal candidate PdGa from space group 198; this material has substantial SOC and can be prepared with flat, clean, and well-ordered surfaces by polishing and subsequent sputtering and annealing in ultrahigh vacuum (*26–28*). Using ARPES and ab initio calculations, we can clearly resolve the presence of multifold crossings in the bulk electronic structure of PdGa, as well as four topological Fermi arcs on its surface, thus observing an experimental realization of the maximal Chern number $|C| = 4$. Interestingly, PdGa is known as an important catalyst—for instance, for the semihydrogenation of acetylene (*29*)—and shows potential for enantioselective catalytic reactions of chiral molecules (*30*). Because the Fermi arcs are mostly derived from d orbitals of Pd that are well known to be important for catalysis (*31*), they enlarge the reservoir of catalytically active charge carriers at the sample surface where chemical reactions take place. Additionally, the topological protection of nonzero Chern numbers could suppress passivation of the Fermi arcs, e.g., by hydrogenation (*32*).

The PdGa samples used in this study crystallize in the cubic space group 198 with a lattice constant of a = 4.896 Å. The chiral motif in their structure is the helical arrangement of Pd and Ga atoms along the (111) direction (Fig. 1A). On a mirror operation, these helices reverse their handedness, which can be used to distinguish the two enantiomers of PdGa. We grew two enantiopure specimens of PdGa with opposite chirality through a self-flux method with a chiral seed crystal and used x-ray diffraction and the Flack method to determine the structural chirality of our samples, indicating almost ideal homochirality. More information about the refinements can be found in (*33*). The chirality of the crystal structure close to the surface can also be observed from the intensity distribution of low-energy electron diffraction (LEED) patterns of the (100) surface (*28*) at an electron energy of E_{kin} = 95 eV (Fig. 1B). As can be expected, the S-shaped intensity distribution is mirrored when comparing the two enantiomers. The crystals used for the ARPES and LEED studies were prepared by the same sputter-annealing recipe, which is well known to produce clean and stoichiometric surfaces of PdGa (*26*). In Fig. 1C, we display the results of an ab initio bulk band structure calculation, which shows fourfold and sixfold band crossings at the Γ and R high-symmetry points, respectively. Such band crossings in space group 198 were predicted to carry a Chern number of magnitude 4, with opposite signs at the Γ and R points (*15–18*). Because the Berry curvature is a pseudovector, a mirror operation will reverse the sign of the Chern numbers associated with the nodes at the high-symmetry points. Such a mirror operation also leads to a reversal of the propagation direction of the Fermi arcs (Fig. 1D). The multifold fermions at the Γ and R points act as sources (positive Chern number) or sinks (negative Chern number) of Berry curvature. One can imagine integrating the Berry flux passing through a two-dimensional slice that is dividing the Brillouin zone between the Γ and R points (blue shaded planes in Fig. 1D). Because of time-reversal symmetry, the Chern number of the slice is equivalent to half of the Chern number associated with the multifold fermions at Γ and R, and the sign of their Chern number depends on the direction of

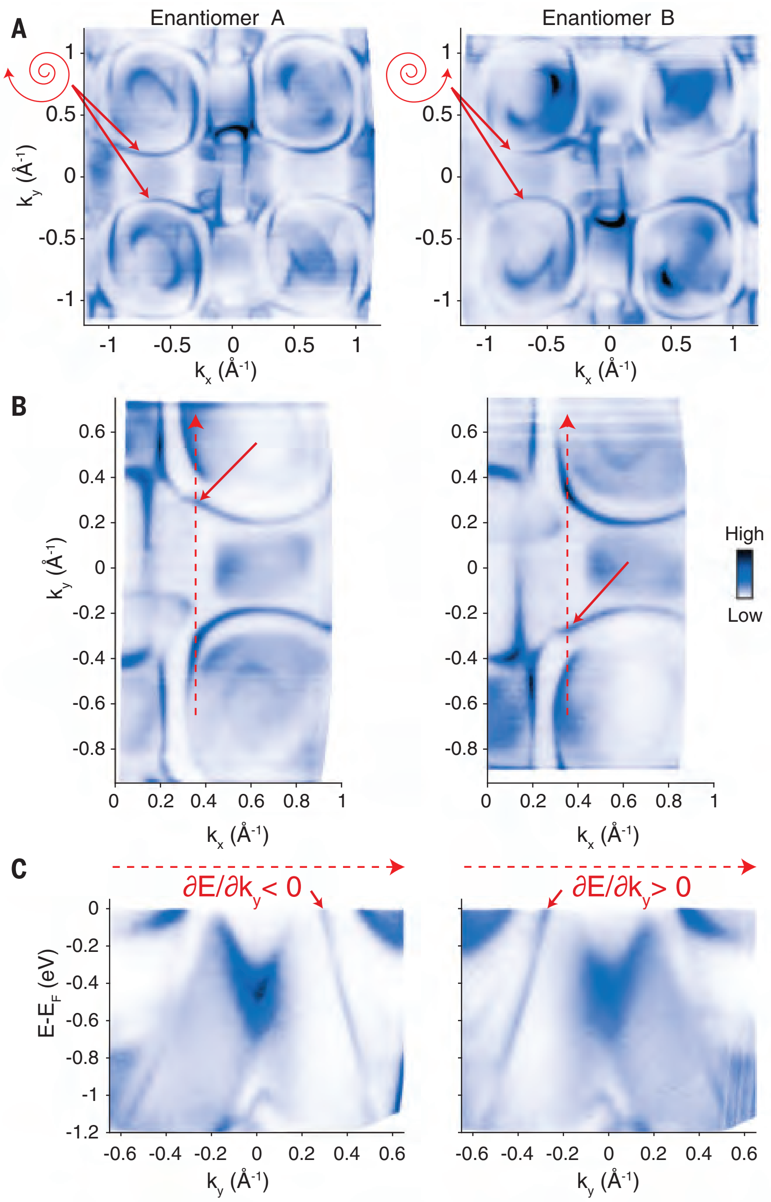

Fig. 4. Comparison of the surface electronic structure of the (100) surface of enantiomer A and enantiomer B. (**A**) Comparison of the Fermi-surfaces for enantiomer A (left) and enantiomer B (right), measured with photon energy $h\nu$ = 60 eV and LH polarization. Red arrows indicate Fermi arcs that reverse the direction along which they are dispersing around the $\bar{R}$ pocket under a mirror operation. (**B**) Comparison of magnified Fermi surfaces measured with photon energy $h\nu$ = 30 eV and LH polarization. The red dashed line indicates the momentum path shown in (C). Red solid arrows indicate Fermi arcs that are crossing the projected bulk band gap that separates the projected bulk pockets at $\bar{\Gamma}$ and $\bar{R}$. (**C**) Band dispersion along the path indicated by the red dashed line in (B). Red arrows indicate the Fermi arcs that are crossing the projected bulk band gap. One can see that the component of the Fermi velocity along the k_y direction switches sign between the two enantiomers.

Berry flux. If we imagine this slice to be a two-dimensional quantum Hall phase, then the number of edge states of the slice is directly related to its Chern number magnitude, whereas their direction depends on its Chern number sign. The observation of a Fermi-arc doublet that is connecting the Γ and R points is, therefore, an unambiguous signature of a Chern number with magnitude 4, and the observation of the reversal of the Fermi-arc velocity is an unambiguous signature of a change in the Chern number sign associated with the multifold fermions.

We performed bulk-sensitive soft x-ray ARPES measurements on the (100) surface of our PdGa samples to investigate their bulk electronic structure (Fig. 2). We find that multifold crossings predicted at the R and Γ points are indeed present (see Fig. 2, A to C), and that our ab initio calculations are in good qualitative agreement with the observed band dispersions. This agreement can also be observed from the Fermi surfaces for different high-symmetry planes displayed in Fig. 2, D and E. Further analysis of the spin-orbit splitting of the bulk bands can be found in (*33*).

After establishing the existence of multifold band crossings in PdGa, we now investigate the topological character of these crossings using surface-sensitive ARPES of the (100) surface of enantiomer A at low photon energies ($h\nu$ < 150 eV, where h is Planck's constant and ν is the photon's frequency), as well as ab initio slab calculations. By comparing the calculated and experimental Fermi surfaces in Fig. 3, A and B, we can identify the existence of Fermi-arc surface states (indicated by red arrows). They thread through the projected bulk band gap (white areas indicated by blue lines in Fig. 3A) and connect the projected bulk band pockets centered at $\bar{\Gamma}$ and $\bar{R}$. By performing photon energy–dependent ARPES along the $\bar{R}-\bar{\Gamma}-\bar{R}$ direction, we confirm experimentally that these Fermi arcs are indeed surface states without noticeable dispersion along the k_z direction (perpendicular to the sample surface), as can be seen from Fig. 3C. Interestingly, we also find additional surface states that overlap with the projected bulk pocket at $\bar{\Gamma}$ (indicated by purple arrows). Owing to the sizable SOC in PdGa and high resolution of our ARPES data, we are furthermore able to resolve a spin splitting in the surface Fermi arcs (see Fig. 3, D to F, and the calculation in Fig. 3A for comparison). We can therefore conclude that four Fermi arcs are connecting the projections of the multifold fermions located at the $\bar{\Gamma}$ and $\bar{R}$ points, which constitutes an experimental confirmation of their maximal Chern number of magnitude 4. We find that the SOC splitting of the Fermi arcs close to the Fermi level is ~0.015 Å^{-1} and ~60 meV. Because these multifold crossings are a generic feature of many chiral topological semimetals, we expect that our finding will also hold for other compounds from the same material family.

Next, we investigate how the maximal Chern number in PdGa can be controlled by tuning the handedness of its crystal structure. When comparing the Fermi surfaces for enantiomers A and B (Fig. 4A), we see that the Fermi arcs wind around the bulk pocket at $\bar{R}$ in opposite directions. By comparing the band dispersion of the Fermi arcs between the two enantiomers along a line cut (Fig. 4C), we can see that the Fermi velocity of the edge states is indeed reversed, which implies that the Chern number signs are reversed between the two enantiomers. [Dispersions along a different direction can be found in (*33*).] This observation shows that the sign of the Chern numbers in topological semimetals can be controlled by deliberately choosing a sample with a specific handedness for experiments. We expect that this finding will serve as a control parameter in experiments that investigate the response of topological semimetals to external perturbations, such as all-optical measurement of the quantized circular photogalvanic effect (*25*). Here, a comparison of the nonlinear response between two enantiomers should give the same magnitude of the mesa-like plateau region in the photocurrent spectrum, albeit with a reversed sign. We furthermore expect eight counterpropagaing topological edge modes at a domain wall between enantiomers in PdGa, given that the Chern numbers for positive and negative momenta change by 4 (*33*). The coupling of multifold fermions with opposite Chern number at this boundary could realize an interface Fermi surface that is qualitatively different from the boundary to the vacuum and thereby enable distinct topological and correlated phenomena.

REFERENCES AND NOTES

1. D. J. Thouless, M. Kohmoto, M. P. Nightingale, M. Den Nijs, *Phys. Rev. Lett.* **49**, 405–408 (1982).
2. M. Kohmoto, *Ann. Phys.* **160**, 343–354 (1985).
3. X. Wan, A. M. Turner, A. Vishwanath, S. Y. Savrasov, *Phys. Rev. B* **83**, 205101 (2011).
4. A. A. Burkov, M. D. Hook, L. Balents, *Phys. Rev. B* **84**, 235126 (2011).
5. D. T. Son, B. Z. Spivak, *Phys. Rev. B* **88**, 104412 (2013).
6. A. A. Burkov, *J. Phys. Condens. Matter* **27**, 113201 (2015).
7. F. de Juan, A. G. Grushin, T. Morimoto, J. E. Moore, *Nat. Commun.* **8**, 15995 (2017).
8. F. Flicker *et al*., *Phys. Rev. B* **98**, 155145 (2018).
9. F. de Juan *et al*., *Phys. Rev. Res.* **2**, 012017 (2020).
10. P. Hosur, X. Qi, *C. R. Phys.* **14**, 857–870 (2013).
11. N. P. Armitage, E. J. Mele, A. Vishwanath, *Rev. Mod. Phys.* **90**, 015001 (2018).
12. G. Chang *et al*., *Phys. Rev. Lett.* **124**, 166404 (2020).
13. C. Fang, M. J. Gilbert, X. Dai, B. A. Bernevig, *Phys. Rev. Lett.* **108**, 266802 (2012).
14. S. S. Tsirkin, I. Souza, D. Vanderbilt, *Phys. Rev. B* **96**, 045102 (2017).
15. B. Bradlyn *et al*., *Science* **353**, aaf5037 (2016).
16. G. Chang *et al*., *Phys. Rev. Lett.* **119**, 206401 (2017).
17. P. Tang, Q. Zhou, S.-C. Zhang, *Phys. Rev. Lett.* **119**, 206402 (2017).
18. G. Chang *et al*., *Nat. Mater.* **17**, 978–985 (2018).
19. J. Cano, B. Bradlyn, M. G. Vergniory, *APL Mater.* **7**, 101125 (2019).
20. D. Takane *et al*., *Phys. Rev. Lett.* **122**, 076402 (2019).
21. D. S. Sanchez *et al*., *Nature* **567**, 500–505 (2019).
22. Z. Rao *et al*., *Nature* **567**, 496–499 (2019).
23. N. B. M. Schröter *et al*., *Nat. Phys.* **15**, 759–765 (2019).
24. B. Q. Lv *et al*., *Phys. Rev. B* **99**, 241104 (2019).
25. D. Rees *et al*., arXiv1902.03230 [cond-mat.mes-hall] (8 February 2019).
26. D. Rosenthal *et al*., *Langmuir* **28**, 6848–6856 (2012).
27. J. Prinz *et al*., *Angew. Chem. Int. Ed.* **51**, 9339–9343 (2012).
28. J. Prinz, thesis, EPFL PP–Lausanne (2014).
29. J. Osswald *et al*., *J. Catal.* **258**, 219–227 (2008).
30. J. Prinz, O. Gröning, H. Brune, R. Widmer, *Angew. Chem.* **127**, 3974–3978 (2015).
31. B. Hammer, J. K. Nørskov, in *Advances in Catalysis*, B. Gates, H. Knoezinger, Eds. (Elsevier, 2000), vol. 45, pp. 71–129.
32. Q. Yang *et al*., *Adv. Mater.* **32**, e1908518 (2020).
33. See supplementary materials.
34. N. B. Schröter, APRES data linked to the publication of N.B.M. Schröter et al., Science aaz3480 (2020), PSI Public Data Repository (2020); http://dx.doi.org/10.16907/d4df1e49-6a62-40b5-b343-a8be757521f2.

ACKNOWLEDGMENTS

We would like to thank L. Nue, A. Pfister, and L. Rotach for excellent technical support. We acknowledge the Paul Scherrer Institut, Villigen, Switzerland, for provision of synchrotron radiation beam time at beamline ADRESS of the SLS. We also acknowledge the Diamond Light Source for time on Beamline I05 under proposals SI24703 and SI20617. N.B.M.S. would like to thank A. G. Grushin for valuable discussions and D. Schöpplein for inspiration at early stages of the project. M.S. would like to thank S. Scharsach for the differential thermal analysis and differential scanning calorimetry measurements. **Funding:** K.M. and C.F. acknowledge financial support from the European Research Council (ERC) Advanced Grant nos. 291472 "Idea Heusler" and 742068 "TOP-MAT", and Deutsche Forschungsgemeinschaft (project ID 258499086 and FE 633/30-1). N.B.M.S. was supported by Microsoft. M.G.V. acknowledges support from DFG INCIEN2019-000356 from Gipuzkoako Foru Aldundia. S.S. and R.W. acknowledge funding from the Swiss National Science Foundation under SNSF project number 159690. D.P. acknowledges support from the Chinese Scholarship Council. J.A.K. acknowledges support from the Swiss National Science Foundation (SNF-grant no. 200021_165910). **Author contributions:** N.B.M.S. conceived and coordinated the project, and performed the ARPES experiments and data analysis with support from S.S., J.A.K., D.P., and V.N.S. K.M. grew and characterized the samples with support from H.B. and M.S. M.G.V. performed the ab initio calculations. F.d.J. and B.B. provided theoretical support. V.N.S., T.S., P.D., T.K.K., and C.C. maintained the ARPES endstations and provided experimental support. N.B.M.S. wrote the paper with support from F.d.J. and input from other co-authors. R.W., V.N.S., and C.F. supervised parts of the project. **Competing interests:** The authors declare no competing interests. **Data and materials availability:** The data presented in this work are available on the PSI Public Data Repository (*34*).

SUPPLEMENTARY MATERIALS

science.sciencemag.org/content/369/6500/179/suppl/DC1
Materials and Methods
Supplementary Text
Figs. S1 to S4
Table S1
References (*35–50*)

2 September 2019; accepted 7 May 2020
10.1126/science.aaz3480

FUEL CELLS

Proton transport enabled by a field-induced metallic state in a semiconductor heterostructure

Y. Wu[1]*, B. Zhu[1,2]*†, M. Huang[3]*, L. Liu[1], Q. Shi[1], M. Akbar[3], C. Chen[4], J. Wei[5], J. F. Li[5], L. R. Zheng[6], J. S. Kim[7], H. B. Song[1]†

Tuning a semiconductor to function as a fast proton conductor is an emerging strategy in the rapidly developing field of proton ceramic fuel cells (PCFCs). The key challenge for PCFC researchers is to formulate the proton-conducting electrolyte with conductivity above 0.1 siemens per centimeter at low temperatures (300 to 600°C). Here we present a methodology to design an enhanced proton conductor by means of a Na_xCoO_2/CeO_2 semiconductor heterostructure, in which a field-induced metallic state at the interface accelerates proton transport. We developed a PCFC with an ionic conductivity of 0.30 siemens per centimeter and a power output of 1 watt per square centimeter at 520°C. Through our semiconductor heterostructure approach, our results provide insight into the proton transport mechanism, which may also improve ionic transport in other energy applications.

The key challenge for research with new-generation proton ceramic fuel cells (PCFCs) is to fabricate electrolytes with high proton conductivity (*1*–*3*). Goodenough proposed the development of oxide ion conductors based on the structural design for solid oxide fuel cells (SOFCs) (*4*). In this approach, oxide ion conductors are designed by doping such that host cations are replaced with those of lower valence to create oxygen vacancies for O^{2-} conductivity (e.g., Y^{3+} or Sm^{3+} replaces Zr^{4+} or Ce^{4+} in zirconia or ceria fluorite structures). However, the structural doping has not yet brought out alternatives to the conventional yttrium-stabilized zirconia electrolyte. The report of a functional triple-charge–conducting $BaCo_{0.4}Fe_{0.4}Zr_{0.1}Y_{0.1}O_{3-\delta}$ cathode has prompted exploration of a strategy to make PCFCs competitive with SOFCs (*5*), but the conductivities of proton ceramic electrolytes (*6*–*8*) are still far below the desired value of 0.1 S cm^{-1}. Our target is to develop functional conductors with proton conductivity of >0.1 S cm^{-1} at 500°C to meet the need for advanced PCFCs. Interfacial ionic transport properties in semiconductor heterostructures and local electric field (LEF) effects have notable advantages in terms of accessibility and tunability for creating extended functionalities (*9*, *10*). Here, we introduce p-type Na_xCoO_2 (NCO) materials (table S1) to construct a semiconductor heterostructure system with n-type CeO_2 (Fig. 1A). The LEF is built to form proton transport channels at the NCO surface to effectively modulate charge transport properties and confine fast ionic mobility to the NCO/CeO_2 heterostructure interfaces. This methodology is in marked contrast to the traditional approach of doping crystal structures.

To elucidate the origin of the emergent electronic state in the NCO/CeO_2 heterostructure, we performed first-principles calculations based on density functional theory for three systems: bulk NCO and CeO_2 (fig. S1), surfaces of the NCO and CeO_2, and an interface of the NCO/CeO_2 (Fig. 1B). The partial density of states (fig. S2) revealed that the interface across a CoO_2 layer of NCO and a Ce–O layer of CeO_2 causes band bending, with the d-orbital electrons dipping below the Fermi level, thereby forming the metallic state. Further, the ionic migration energy (ε) enhances our understanding of the optimal paths of proton transport. Although protons may be transported through the lattice of CeO_2 or layered-structure NCO, ε_i (i = 1 and 2 for CeO_2 and NCO, respectively) is high because of the structural bonding energy. By contrast, the H···NCO bonding interaction

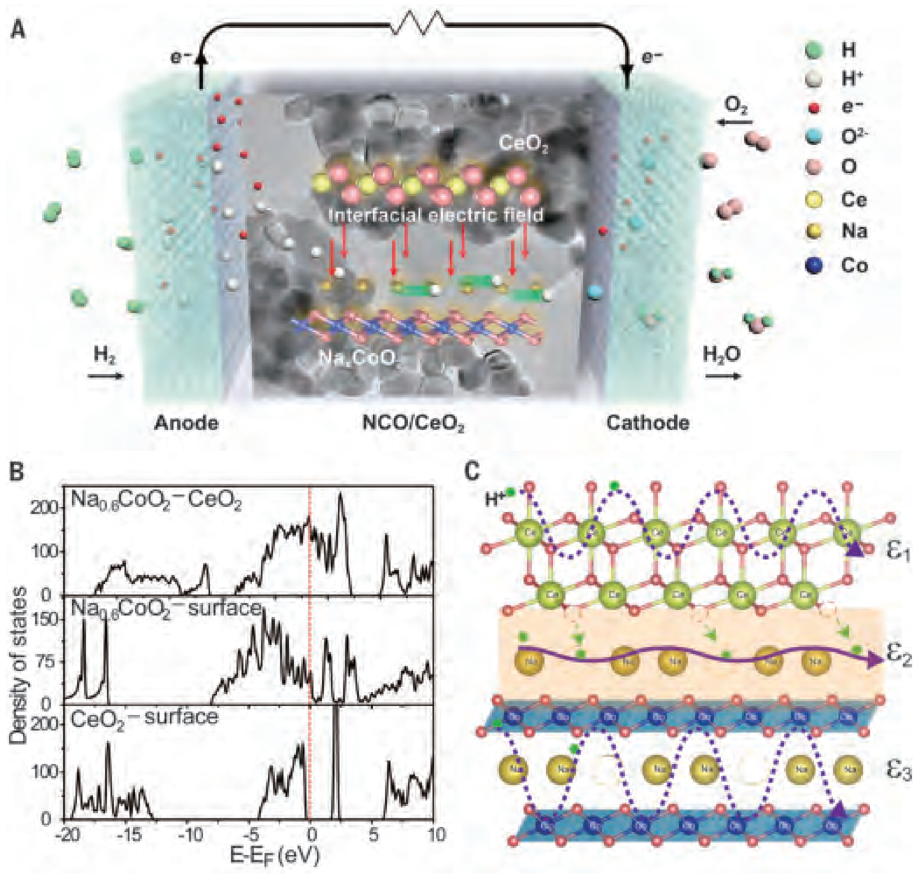

Fig. 1. Design of the NCO/CeO_2 heterostructure functionalities for fast proton migration. (**A**) Schematic of the NCO/CeO_2 fuel cell and its operation mechanism (a LEF built at the NCO/CeO_2 interface from the CeO_2 side to the NCO side confines protons along the NCO surface). (**B**) Total density of states of the surfaces of CeO_2 and NCO and the Na_xCO_2/CeO_2 interface (x = 0.60). (**C**) CeO_2 lattice with (111) plane, interface of the NCO/CeO_2 heterostructure, and NCO layer with (001) plane, with proton migration activation energies ε_1, ε_2, and ε_3, respectively.

[1]Engineering Research Center of Nano-Geo Materials of Ministry of Education, Faculty of Materials Science and Chemistry, China University of Geosciences, Wuhan, 430074, China. [2]Energy Storage Joint Research Center, Southeast University School of Energy and Environment, Southeast University, Nanjing, 210096, China. [3]Key Laboratory of Ferro and Piezoelectric Materials and Devices of Hubei Province, Faculty of Physics and Electronic Sciences, Hubei University, Wuhan, 430062, China. [4]Huazhong University of Science and Technology, Wuhan, 430074, China. [5]College of Chemistry and Chemical Engineering, Xiamen University, Xiamen, 361005, China. [6]Institute of High Energy Physics, Chinese Academy of Sciences, Beijing, 100049, China. [7]Department of Aeronautical and Automotive Engineering, Loughborough University, Loughborough LE11 3TU, UK.
*These authors contributed equally to this work.
†Corresponding author. Email: binzhu@kth.se (B.Z.); songhb@cug.edu.cn (H.B.S.)

could provide a highly conductive path in terms of out-of-plane doping control of the in-plane electronic charge (*11*). The diffusion barriers are 3.17 eV (ε_1) for proton migration in CeO_2, 3.89 eV (ε_2) in $Na_{0.6}CoO_2$, and 0.15 eV (ε_3) at the interface. The proton barrier energy at the interface is reduced by a factor of >20 compared with those of bulk CeO_2 and NCO. The interface between NCO and CeO_2 can provide a weak bonding interaction, thus building a proton transport highway with much lower migration energy (Fig. 1C).

The heterostructure exhibits a spherical CeO_2 cluster epitaxially grown at NCO, forming a uniform sphere-cluster–by–layer morphology with a top CeO_2 cluster and an NCO nanosheet (Fig. 2A). The high-resolution image in Fig. 2B demonstrates that the (111) plane of cubic CeO_2 has good contact with the (001) planes of the NCO nanosheets. The crystal structure and component have also been characterized (fig. S3). The oxygen K-edge spectra (Fig. 2C) in different local chemical environments of NCO/CeO_2 display an additional peak localized at 539 eV and associated with the interface region. This additional peak results from the distinctive electronic structure caused by the aggregation of oxygen in the interface region (*12*). Kelvin probe force microscopy (KPFM) is used to characterize the interface properties of CeO_2 and NCO (*13*–*15*). The topographic spatial map and the corresponding surface potentials of NCO/CeO_2 (Fig. 2, D and E) reveal notable changes between interfaces. In an illustrative line scan crossing the interface of NCO and CeO_2 (Fig. 2F), the surface potential difference between NCO and CeO_2 is ~15 mV, demonstrating the existence of a LEF at the NCO/CeO_2 interface, which is also verified by the NCO/CeO_2 heterostructure film device (Fig. 2G) with a clear rectifying effect.

We then performed chemical and structural characterizations of the NCO/CeO_2 hydrogenation process. Hydrogenation occurs only in the NCO structure, with H···OCo bond formation (peak at 1071 cm^{-1}) confirmed by in situ Raman measurement (Fig. 2H and fig. S4). In contrast, no change was observed in the CeO_2 structure (Fig. 2I). Ex situ x-ray absorption near-edge structure (XANES) measurements of the Co K-edge and Ce L_3-edge from pristine and tested NCO/CeO_2 samples are shown in fig. S5, confirming that hydrogenation takes place only during the in situ process.

The results of the designed NCO/CeO_2 heterostructure demonstrated in a PCFC device are presented in Fig. 3. The pristine NCO is an electron conductor (*16*, *17*) and does not show any performance in a fuel cell device (Fig. 3A). Owing to the existence of oxygen vacancies (fig. S6), pure CeO_2 electrolyte exhibits 300 mW cm^{-2} of power output at 520°C. After formation of the NCO/CeO_2 heterostructure interfaces, the device reaches 1000 mW cm^{-2} at 520°C, corresponding to an open-circuit

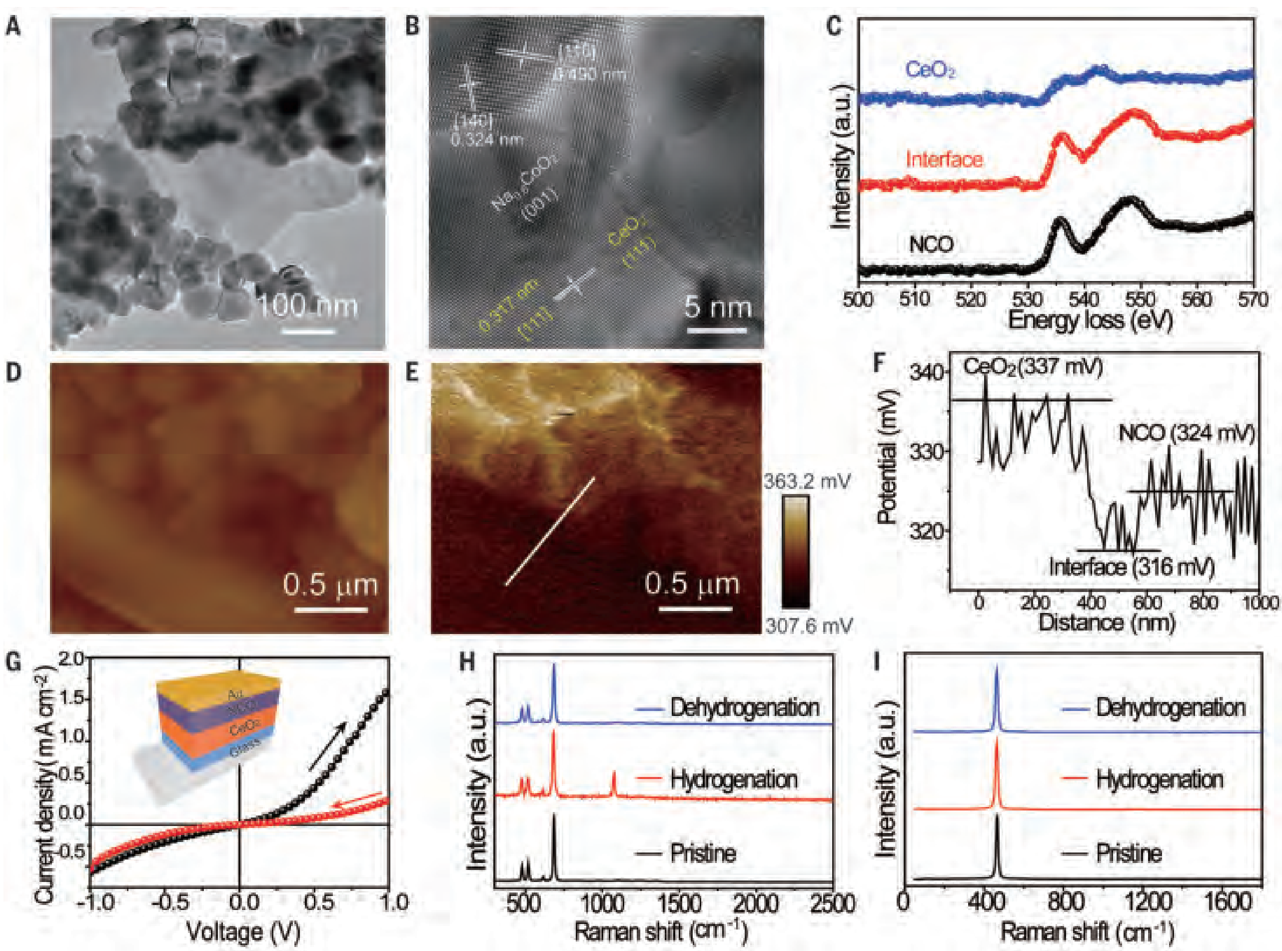

Fig. 2. Characterizations of NCO/CeO_2. (**A**) Transmission electron microscopy (TEM) image. (**B**) High-resolution TEM image. (**C**) Oxygen K-edge spectra in different local chemical environments. a.u., arbitrary units. (**D**) Atomic force microscopy image and (**E**) scanning KPFM image of NCO/CeO_2. The scanning area is 2.5 µm by 2.5 µm. (**F**) Contact potential difference along the white line in (E). (**G**) *I-V* curve of the NCO/CeO_2 heterostructure deposited on an ITO (indium tin oxide)/glass substrate with Au electrodes. (**H** and **I**) In situ and ex situ Raman spectra of NCO (H) and CeO_2 (I) under air and H_2 atmospheres.

voltage (OCV) of 1.07 V (Fig. 3B), with good reproducibility (fig. S7). Such enhancement of the power output is attributed to the synergic effects of the LEF at the interface and the metallic state of the NCO surface, which accelerated proton transport through the interface of NCO and CeO_2. The NCO/CeO_2 device can even run at 370°C and maintains a power density output above 100 mW cm^{-2} (Fig. 3B). The high OCV (e.g., 1.07 V at 520°C) is in agreement with the Nernst theoretical potential, indicating that the ionic transference number is near unity and the electron conduction has been suppressed (*18*, *19*). We have also investigated fuel cells that consist of different Na_xCoO_2 composite samples with varied Na content (x = 0.47, 0.55, and 0.71) that support the existence of the metallic state (fig. S8). These cells demonstrated a power density output of >550 mW cm^{-2} at 520°C (fig. S9), thus further supporting the electrolytic function of the NCO/CeO_2 heterostructure.

The Nyquist plot of the $Na_{0.6}CoO_2$/CeO_2 (2/8) cell under an OCV condition measured at 490°C is shown in Fig. 3C. The total ohmic area-specific resistance of this cell is particularly low (0.26 ohm·cm^2) for a NCO/CeO_2 thickness of 400 μm, which is comparable to the target value (0.15 ohm·cm^2) for a 15-μm-thick electrolyte used for high-performance PCFCs. The Nyquist plot is modeled by an equivalent circuit with an ohm resistor (R_o) and serial elements, each consisting of a resistor (R_i, i = 1, 2), and a constant phase element (CPE_i, i = 1, 2), as summarized in table S2. The two semicircles (Fig. 3C) originate from the electrode polarization resistances. The corresponding ionic conductivity of NCO/CeO_2 measured in the fuel cell condition is presented in Fig. 3D, in comparison with several other oxygen ion– and proton-conducting electrolyte materials (*20*–*22*). NCO/CeO_2 exhibits the highest ionic conductivity (0.30 S cm^{-1} at 520°C and 0.24 S cm^{-1} at 500°C), as well as the lowest activation energy (0.27 eV).

Proton conduction in NCO/CeO_2 was further verified with two experimental approaches. In the first, we constructed a fuel cell device with a proton-conducting $BaZr_{0.8}Y_{0.2}O_{3-\delta}$ (BZY) filter (fig. S10), where the NCO/CeO_2 was sandwiched between two BZY ion-filter layers, allowing only protons to pass through and enabling determination of proton transport property (*23*). The device with BZY filters achieved a power output of 890 mW cm^{-2} at 520°C (Fig. 3E), which is very close to the power output (1000 mW cm^{-2}) of the NCO/CeO_2 fuel cell. The difference can be attributed to the ohmic losses caused by two additional BZY layers with limited proton conductivity, which was substantially lower than that of the NCO/CeO_2 (Fig. 3D). Additional contact interfaces between BZY and NCO/CeO_2 also contributed to polarization loss. This result verifies proton-dominating conduction in the NCO/CeO_2 heterostructure. In another experiment, we measured the proton conduction isotopic effect, in which conductivities of NCO/CeO_2 were measured in a 5% H_2/95% Ar mixture and a 5% D_2/95% Ar mixture at various temperatures. The associated conductivities are substantially increased for 5% H_2 relative to 5% D_2, exhibiting a clear H/D isotope effect (Fig. 3F). This finding provides further evidence of proton conduction in the designed material (*24*).

Whereas the best-performing proton-conducting $BaZr_{0.4}Ce_{0.4}Y_{0.1}Yb_{0.1}O_3$ thin-film electrolyte fuel cell has a power output of 500 mW cm^{-2} at 500°C, the NCO/CeO_2 device has outputs of 800 mW cm^{-2} at 500°C and 1000 mW cm^{-2} at 520°C (Fig. 3B). In addition, NCO/CeO_2 as an electrolyte in different molar ratios also generates substantial outputs (fig. S11). The NCO/CeO_2 heterostructure has demonstrated promising advantages for PCFCs (*25*, *26*). The durability of the NCO/CeO_2 device was tested under 100 mA cm^{-2} during a

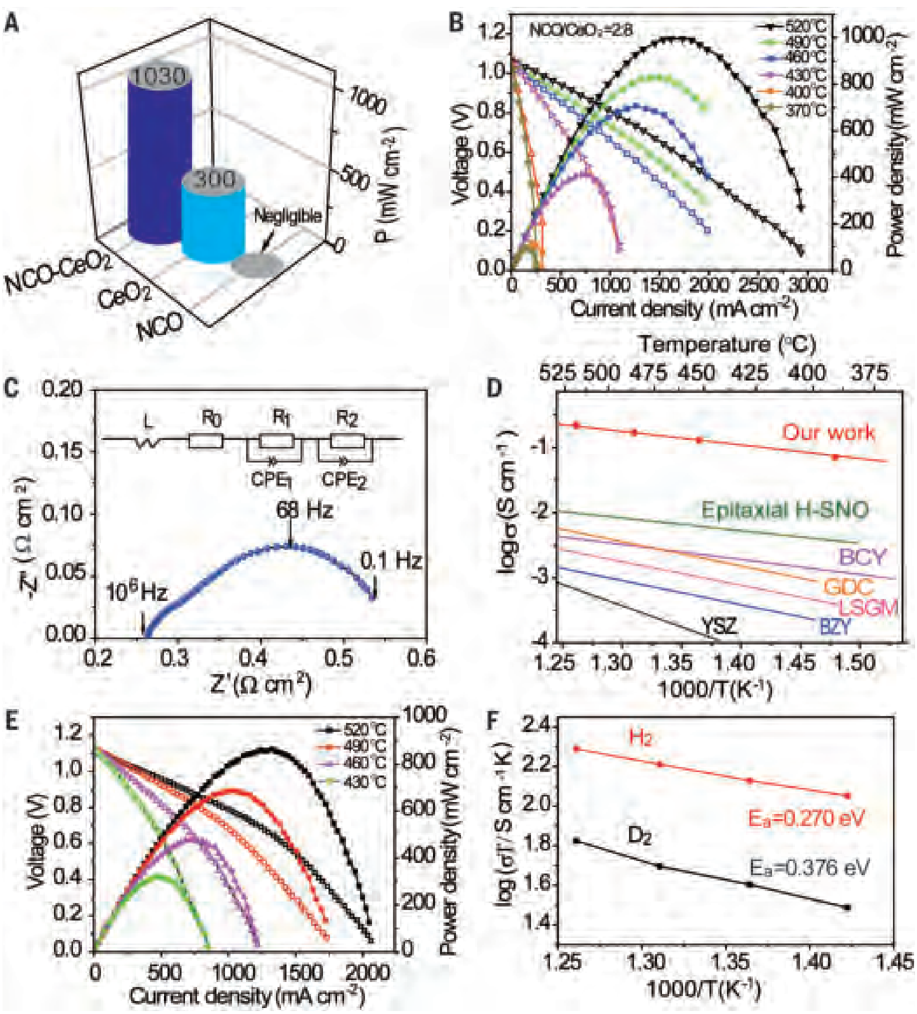

Fig. 3. Performance and proton transport measurement of NCO/CeO_2 cell. (**A**) Power output of NCO, CeO_2, and NCO/CeO_2 devices operated at 520°C. (**B**) *I-V* and *I-P* characteristics of the NCO/CeO_2 device operated at various temperatures. (**C**) Nyquist plot obtained under an OCV condition at 490°C for a Ni/NCAL/NCO/CeO_2/NCAL/Ni cell. Z, the complex impedance measured from the fuel cell; L, inductance; R_o, R_1, and R_2, resistors; CPE_1 and CPE_2, constant phase elements. (**D**) Ionic conductivity of NCO/CeO_2 compared with that of other oxygen ion–conducting electrolytes (dotted lines) and proton conductors (solid lines). H-SNO, hydrogenated samarium nickelate; BCY, barium-cerium/yttrium oxide; GDC, gadolinium-doped ceria; LSGM, lanthanum strontium gallate magnesite; BZY, yttrium-doped barium zirconate; YSZ, yttrium-stabilized zirconia. (**E**) *I-V* and *I-P* characteristics of the NCO/CeO_2 (2/8) device operated at various temperatures with proton filters. (**F**) Temperature dependence of conductivities in the NCO/CeO_2 (2/8) device operated in a 5% H_2/95% Ar mixture and a 5% D_2/95% Ar mixture at various temperatures.

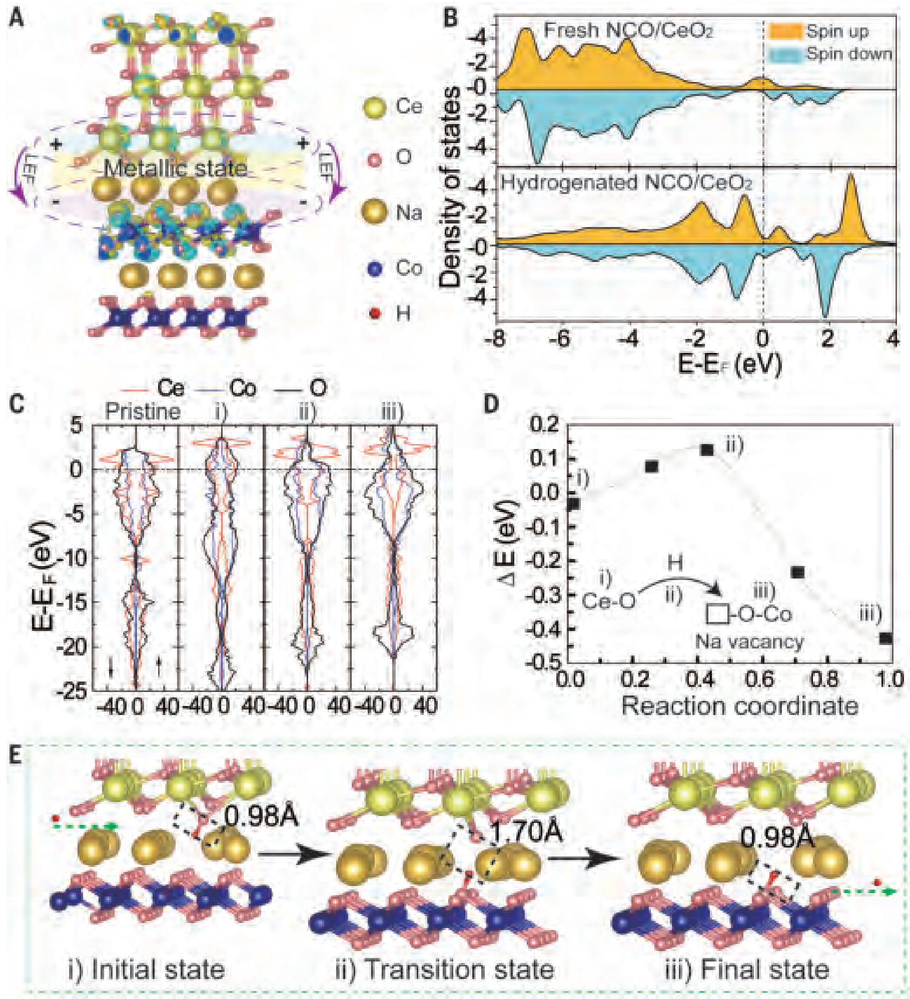

Fig. 4. Proton transport path. (**A**) Charge density differences at the NCO/CeO_2 interface. LEF, local electric field. (**B**) Spin-resolved density of states for fresh NCO-CeO_2 and hydrogenated NCO-CeO_2. (**C**) Spin-resolved partial density of states of H diffusion at the NCO-CeO_2 interface. (**D**) Energy diagram of H diffusion at the NCO/CeO_2 interface. (**E**) Corresponding charge transfer behavior for the initial (i), transition (ii), and final (iii) states of H absorption at the NCO/CeO_2 interface with a Na vacancy.

100-hour period, in which the operation voltage was improved from 0.9 to ~1.0 V by introducing an anode buffer layer (ABL) (fig. S12). The ABL can effectively enhance device performance and durability. This durability test can be further improved by exploring optimized electrode materials and device technology in future engineering efforts.

Theoretical calculations further reveal the proton conduction mechanism, as illustrated in Fig. 4 (see Fig. 4A for the distribution of charge density differences of the NCO/CeO_2 interface). At the NCO/CeO_2 interface, the unbalanced charge distribution between the Ce–O and Co–O layers induces a LEF within the interface region. Oxygen vacancies of CeO_2 and sodium vacancies of NCO can also cause an in-plane LEF, for which interfacial potential is verified by KPFM (Fig. 2F) and the LEF by the current-voltage (*I-V*) curve of the NCO/CeO_2 thin-film device (Fig. 2G). Proton transport states and paths are illustrated in Fig. 4, B and C. Proton intercalation leads to a pronounced spectral weight shift of the Co 3d and Ce 4f bands toward higher energy. Correspondingly, distributed orbitals cover a wide range of Fermi energies (E_F) from −3 to +1 eV, indicating the proton transport path with a lower barrier and resistance. Nudged elastic band calculations were carried out to understand proton migration pathways. The energy diagram of H diffusion at the interface (Fig. 4D) reveals the lowest energy barrier between protons and NCO. This is the optimal migration pathway for a proton moving from CeO_2 to the NCO surface. During the transport process, the proton driven by the LEF could incorporate with a lattice oxygen ion and move through the oxygen vacancy of CeO_2 (i: initial state) to form the H–OCe bond (bond length of 0.98 Å). Meanwhile, the LEF is confined in the heterostructure interface, which drives protons from the positively charged CeO_2 to the negatively charged NCO surface. (ii: transition state) (Fig. 4E and table S3). When the proton is close to NCO, Na experiences a large distortion that exerts a strong repulsive force on the proton. This causes deformation of the H···OCo bond (bond length 1.04 Å) and the H···OCe bond (1.70 Å). In addition, the energy barrier is too high for protons to be transported in the NCO and CeO_2 structure, so they are confined in the NCO/CeO_2 interface. Finally, protons spontaneously flow along the proton channel that results from the LEF-induced metallic state of NCO surface (iii: final state), of which the active energy (0.15 eV) is much lower than those of the bulk CeO_2 (3.17 eV) and NCO (3.89 eV). Such enhanced proton conduction is attributed to a synergic effect between the LEF and the metallic state of the NCO surface, which substantially accelerates proton transport.

Our approach may be used to improve proton transport by acceleration through a field-induced metallic state in the NCO/CeO_2 semiconductor heterostructure. The desired high proton conductivity, 0.1 to 0.3 S cm^{-1} (at 370 to 520°C), has been achieved with this system, and the NCO/CeO_2 fuel cell has exhibited a power density of 1000 mW cm^{-2} at 520°C. Our work offers a general methodology to develop functional semiconductor heterostructures with distinctive interfacial structure and properties. More broadly, this work lays the theoretical and experimental foundations for designing and exploiting novel materials in energy applications.

REFERENCES AND NOTES

1. C. Duan *et al.*, *Nature* **557**, 217–222 (2018).
2. S. Choi *et al.*, *Nat. Energy* **3**, 202–210 (2018).
3. C. Duan *et al.*, *Nat. Energy* **4**, 230–240 (2019).
4. J. B. Goodenough, *Nature* **404**, 821–823 (2000).
5. C. Duan *et al.*, *Science* **349**, 1321–1326 (2015).
6. R. Lan, S. W. Tao, *Adv. Energy Mater.* **4**, 1301683–1301689 (2014).
7. I. H. Kim *et al.*, *J. Mater. Chem. A* **7**, 21321–21328 (2019).
8. Y. Zhou *et al.*, *Nature* **534**, 231–234 (2016).
9. Y. Zheng *et al.*, *Adv. Mater.* **29**, 1700396 (2017).
10. T. Xia, W. Zhang, J. Murowchick, G. Liu, X. Chen, *Nano Lett.* **13**, 5289–5296 (2013).
11. M. Bañobre-López *et al.*, *Chem. Mater.* **17**, 1965–1968 (2005).
12. B. Y. Wang *et al.*, *J. Mater. Chem. A* **4**, 15426–15436 (2016).
13. A. Liscio *et al.*, *Adv. Funct. Mater.* **16**, 1407–1416 (2006).
14. F. Bocquet, L. Nony, C. Loppacher, T. Glatzel, *Phys. Rev. B* **78**, 035410 (2008).
15. C. Melzer, C. Siol, H. von Seggern, *Adv. Mater.* **25**, 4315–4319 (2013).
16. R. Berthelot, D. Carlier, C. Delmas, *Nat. Mater.* **10**, 74–80 (2011).
17. K. Takada *et al.*, *Adv. Mater.* **16**, 1901–1905 (2010).
18. M. I. Asghar, S. Jouttijärvi, R. Jokiranta, A.-M. Valtavirta, P. D. Lund, *Nano Energy* **53**, 391–397 (2018).
19. B. Zhu *et al.*, *Nano Energy* **19**, 156–164 (2016).
20. A. J. Jacobson, *Chem. Mater.* **22**, 660–674 (2010).
21. V. Esposito, E. Traversa, *J. Am. Ceram. Soc.* **91**, 1037–1051 (2008).

22. D. Pergolesi et al., Nat. Mater. 9, 846–852 (2010).
23. Y. Wu et al., ACS Appl. Energy Mater. 1, 580–588 (2018).
24. Y. Xing et al., ACS Energy Lett. 4, 2601–2607 (2019).
25. J. Garcia-Barriocanal et al., Science 321, 676–680 (2008).
26. C. Zhao et al., Energy Environ. Sci. 13, 53–85 (2020).

ACKNOWLEDGMENTS

We thank B. Y. Wang's group from Hubei University for verifying fuel cell results. We acknowledge Z. Y. Huang from Nanyang Technological University and J. Su from the Center for Nanoscale Characterization and Devices, WNLO, of the Huazhong University of Science and Technology (HUST) for high-resolution TEM characterization and discussion. We also thank J. Tang from HUST for helpful discussion. **Funding:** We acknowledge the support from the National Natural Science Foundation of China (grants 51774259 and 51772080). **Author contributions:** Y.W., H.B.S., and B.Z. conceived of the idea, designed the experiments, and analyzed the data. L.L. and Q.S. carried out most of the characterizations and device optimizations. M.H. performed the theoretical simulations and analyzed the results. Y.W., M.H., C.C., L.L., Q.S., J.S.K., H.B.S., and B.Z. participated in device optimization and data analysis. J.W. and J.F.L. carried out Raman characterizations and analyzed the results. L.R.Z. carried out XANES characterizations and analyzed the results. M.A. verified fuel cell results. Y.W., H.B.S., and B.Z. wrote the paper. All authors commented on the manuscript. **Competing interests:** The authors declare no competing interests. **Data and materials availability:** All data are available in the manuscript or the supplementary materials.

SUPPLEMENTARY MATERIALS

science.sciencemag.org/content/369/6500/184/suppl/DC1
Materials and Methods
Supplementary Text
Figs. S1 to S12
Tables S1 to S3
References (27–37)

19 October 2019; resubmitted 6 March 2020
Accepted 26 May 2020
10.1126/science.aaz9139

COGNITIVE MAPS

Cognitive map–based navigation in wild bats revealed by a new high-throughput tracking system

Sivan Toledo[1]*†, David Shohami[2]*†, Ingo Schiffner[2]‡, Emmanuel Lourie[2], Yotam Orchan[2], Yoav Bartan[2], Ran Nathan[2]*

Seven decades of research on the "cognitive map," the allocentric representation of space, have yielded key neurobiological insights, yet field evidence from free-ranging wild animals is still lacking. Using a system capable of tracking dozens of animals simultaneously at high accuracy and resolution, we assembled a large dataset of 172 foraging Egyptian fruit bats comprising >18 million localizations collected over 3449 bat-nights across 4 years. Detailed track analysis, combined with translocation experiments and exhaustive mapping of fruit trees, revealed that wild bats seldom exhibit random search but instead repeatedly forage in goal-directed, long, and straight flights that include frequent shortcuts. Alternative, non–map-based strategies were ruled out by simulations, time-lag embedding, and other trajectory analyses. Our results are consistent with expectations from cognitive map–like navigation and support previous neurobiological evidence from captive bats.

Goal-directed navigation, a fundamental component of animal movement involving a variety of sensory systems, stimuli, computational mechanisms, and memory encoding and retrieval, is essential for accomplishing many spatial tasks, ranging from nearly global migration of birds or whales to local foraging of ants or bees. The most sophisticated form, map-based navigation, does not require systematically following known routes or landmarks (piloting) or directly sensing some goal-emanating cue (beaconing), which are simpler forms of goal-directed navigation (*1*). Instead, map-based navigation requires a frame of reference for the animal's current position in relation to a known yet undetected goal (*1*).

For migratory and other animals moving through unfamiliar areas across large scales, such a frame of reference is thought to be provided by predictable environmental gradients such as Earth's magnetic field ["map-and-compass" navigation (*2*, *3*)]. Most animals, however, move much more frequently within their smaller-scale familiar home range. At these scales, the frame of reference for map-based navigation may be provided by an internal allocentric representation of space that supports self-localization and vector calculation, along with long-term memory of the spatiotemporal features of the environment—a "cognitive map" (sensu Tolman, O'Keefe, and Nadel) (*1*, *4*–*7*).

The neurobiological basis of spatial representation and navigation has been extensively studied in the laboratory (*5*, *8*), mostly on the traditional rodent model species and primates (*7*). The Egyptian fruit bat (*Rousettus aegyptiacus*, Pteropodidae) has recently become a model for many such studies, and lab-based evidence is mounting for its spatial cognitive abilities and their underlying neurobiology (*7*, *9*, *10*). Yet, field studies supporting these findings in this, or other, bat species have been limited to displacement experiments reporting successful homing of bats translocated well outside their familiar area, suggesting a map-and-compass navigation (*11*, *12*). The capacity of bats to navigate to multiple targets on a smaller, familiar-area scale relevant for a cognitive map (which may still be considerably large, spanning ~1000 km^2 for Egyptian fruit bats) has not yet been examined. Our previous GPS-tracking showed that bats of this species regularly fly far and straight to specific fruit trees within their home range, but the evidence was limited to partial tracking data collected over only a few nights (*11*).

In this study, we tagged and followed 172 free-ranging Egyptian fruit bats in the Hula Valley, Israel, for 3449 full nights (summed across all bats) using ATLAS—an innovative reverse-GPS system that localizes extremely light-weight, low-cost tags (*13*, *14*) (Fig. 1, inset). Each ATLAS tag transmits a distinct radio signal detected by a base-station network distributed in the study area. Tag localization is computed using nanosecond-scale differences in signal time-of-arrival to each station, enabling nearly real-time tracking and alleviating the need to retrieve the tag or to have some power-consuming remote-download capability. We were thus able to track wild bats at 0.125 to 1 Hz for up to 219 consecutive nights with 4-g tags, <4% of the bat's body weight, yielding ~18.2×10^6 localizations. On the basis of the neurobiological evidence obtained from laboratory animals, we hypothesized that Egyptian fruit bats use spatial memory to guide their routine foraging navigation in a manner compatible with possession of a cognitive map. We thus tested a set of predictions (elaborated below) comparing cognitive map to simpler alternative navigation mechanisms (random search, path integration, piloting and beaconing), applying multiple data analysis approaches to our dataset.

Bats were mist-netted on fruit trees or cave entrances and tagged with ATLAS in 38 capture sessions spanning all seasons between 2015 and 2019. Bats were tagged by gluing the tag to their back (138 individuals) or by a custom-made collar (34 individuals) (Fig. 1, inset), and were tracked for an average of 13 (maximum 38) and 47 (maximum 219) nights, respectively. We mapped every individual fruit tree (14,314) and an estimated 18,111 orchard fruit trees that can potentially be eaten by Egyptian fruit bats in a 19,000-ha area comprising the core area of bat foraging, where

[1]Blavatnik School of Computer Science, Tel-Aviv University, Israel. [2]Movement Ecology Lab, Department of Ecology, Evolution and Behavior, Alexander Silberman Institute of Life Sciences, Faculty of Science, The Hebrew University of Jerusalem, Israel.
*Corresponding author. Email: stoledo@tau.ac.il (S.T.); david.shohami@mail.huji.ac.il (D.S.); ran.nathan@mail.huji.ac.il (R.N.)
†These authors contributed equally to this work.
‡Present address: School of Natural Sciences, Bangor University, Deniol Road, Bangor LL57 2UW, UK.

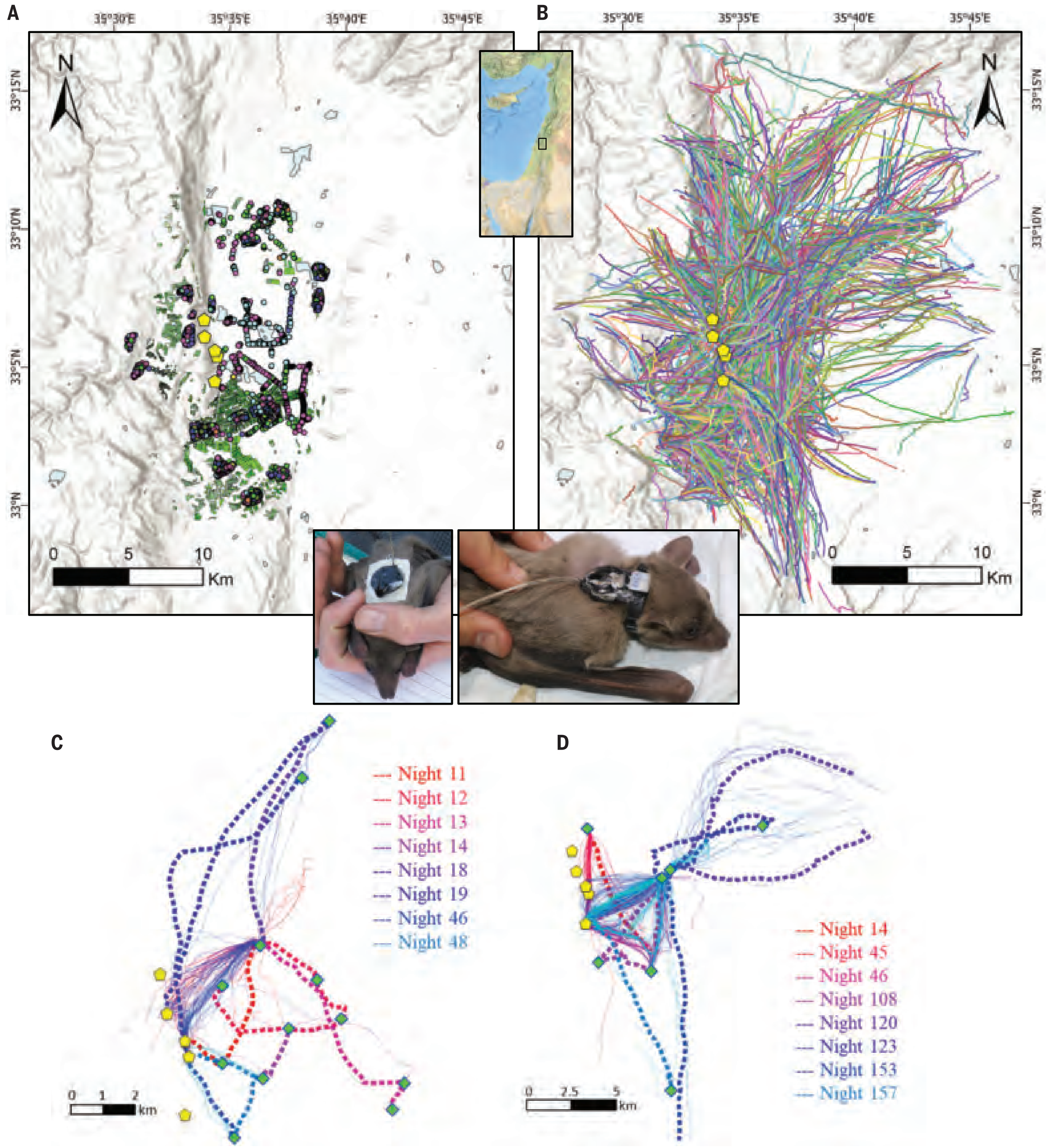

Fig. 1. The study system. (**A**) The study area in the Hula Valley, north Israel. Color points mark the location of 14,314 individually mapped fruit trees, and green polygons are fruit tree orchards (*15*). Yellow pentagons mark the five known bat colonies (caves) in the area. (**B**) ATLAS recording of 9218 movement tracks of 172 bats. Examples of (**C**) all 148 tracks of one bat over 54 consecutive nights, and (**D**) all 596 tracks of another bat over 219 consecutive nights. Dotted tracks were defined as shortcuts or unrecorded routes, nondotted tracks are regular tracks. The number in the legend indicates the night (after tagging) in which each particular shortcut was made. Tracks of the same color were made on nights between the previous shortcut and up to (including) the night of the shortcut of that color. Green diamonds mark the trees this bat flew to, or from, the shortcuts or unrecorded routes. Unrecorded routes not connected to a green diamond went or came back from out of ATLAS range. Insets show ATLAS tags deployed on adult Egyptian fruit bats using surgical glue (left) or a custom-made collar (right).

87% of localizations occurred (Fig. 1A) (*15*). We delineated individual tracks by defining >1 min stops as either start ("origin") or end ("goal") points, each classified as either cave, tree, or out of range type (*15*). In this way, 9218 individual movement tracks were identified (Fig. 1B). The overall ATLAS coverage area, where bats were successfully tracked at the Hula Valley and its surroundings, was 88,200 ha.

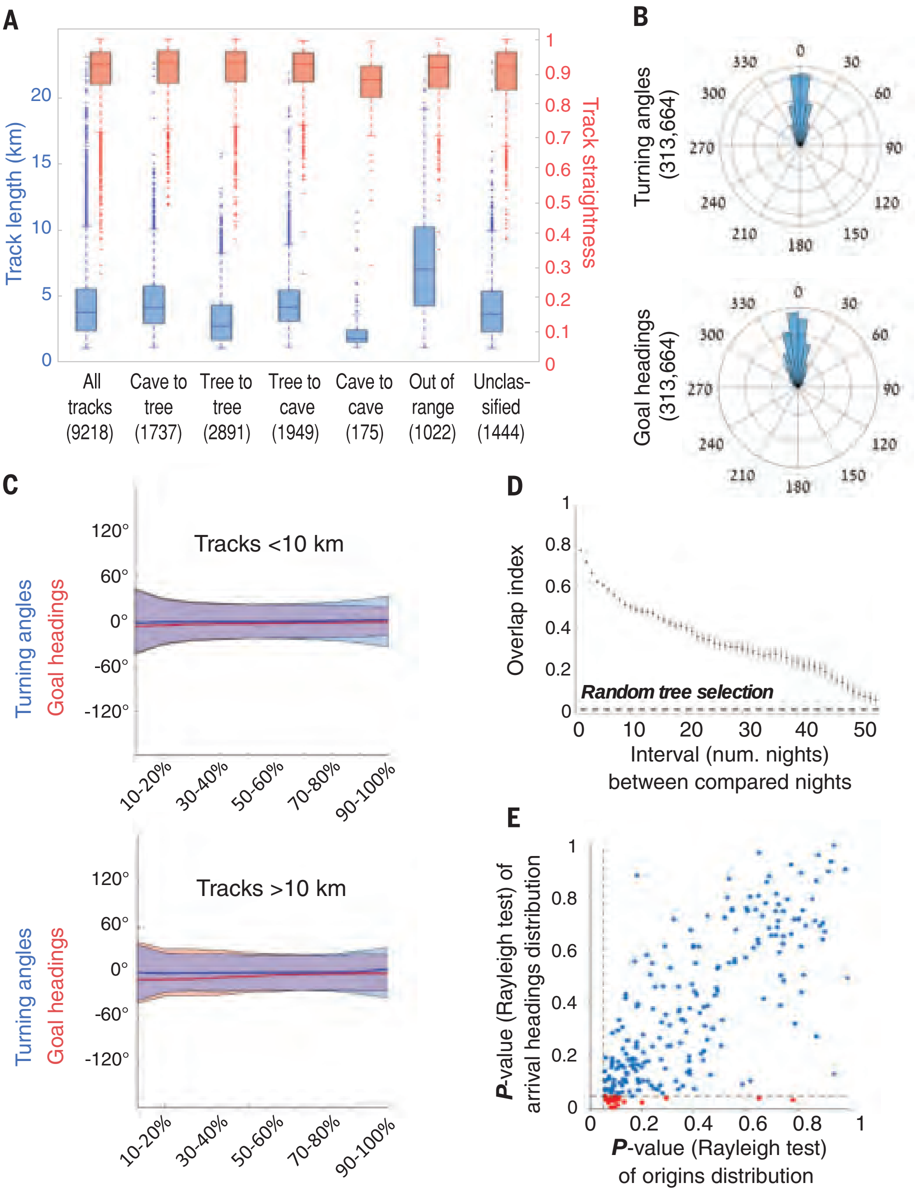

Fig. 2. Characteristics of Egyptian fruit bat flight tracks. (**A**) Boxplots of length (blue, left axis) and straightness index (red, right axis) of different track categories (number of tracks in parentheses). "Unclassified" could not be confidently categorized because of missing data at the track's beginning or end. (**B**) Distribution of (top) turning angles (angle relative to previous step) and (bottom) headings (angle relative to goal) of all nonstationary localizations. (**C**) Mean turning angles (red line) and headings (blue line) with circular SD (red and blue areas, respectively) for different track percentiles, for tracks shorter (top) or longer (bottom) than 10 km. (**D**) Pianka's overlap index (*17*) for mean ± SEM (across bats) overlap in tree visitations (within each bat) between different nights. Dotted line is the result of 10,000 bootstraps of random tree selections in each night, using only trees visited by bats during the same season as the tested bat. Compared to random, bats show significant fidelity to favorite fruit trees up to ~50 nights apart. (**E**) Scatterplot of *P* values of Rayleigh's test for circular nonuniformity, for all 239 target trees visited from multiple origins by the same bat. The *y* and *x* axes account for arrival headings and origins' angles to the target tree, respectively. Dotted lines show the 0.05 significance level for each axis. In red are 21 (9%) significant deviations from uniform for the *y* axis. The Hodges-Ajne nonparametric test found no significant deviations from uniform (fig. S1).

The bats exhibited typical, repetitive foraging movements characterized by straight flights (Fig. 1, B to D), with mean track straightness close to 1 regardless of origin or goal type (Fig. 2A and table S1) or of travel distance (linear regression, $r^2 < 0.01$, $P = 0.81$). Turning angles and headings were tightly distributed around zero (Fig. 2B and table S1), even for goals more than 21 km away. These parameters were consistent along the entire length of the tracks (Fig. 2C), implying that the bats, on average, depart already in the direction of their goal and stay on course for the duration of the flight. Straightness did not significantly differ between juveniles (3 to 8 months old) and adults (*t* test, $t = -0.19$, $P = 0.85$), nor was it affected by forearm length, a proxy for age (linear regression, $r^2 = 0.01$, $P = 0.25$). Although these straight tracks are substantially different from tortuous tracks expected from random searches, straight tracks alone might be insufficient to indicate goal-directed movement, because moving straight in a random direction is considered an efficient random search strategy (*16*). However, flight direction was far from random, as each bat flew every night to a few (mean ± SD, 4.13 ± 1.04) specific favorite fruit trees to which they returned on different nights [Pianka's modified niche overlap index (*17*), $P = 0.005$; Fig. 2D] and arrived from multiple directions (Fig. 2E). Altogether, our analyses show that Egyptian fruit bats seldom exhibit random search but rather traverse their home range in repeated, straight goal-directed flights to a few selected favored goals. Although such movements in the shortest or least-effort paths in multiple directions match predictions arising from spatial knowledge congruent with a cognitive map (*1*), further evidence is needed to support this conjecture (*18*).

The ability to take novel shortcuts between any two known locations that are not within detectable range of each other is considered the hallmark of a cognitive map and the strongest evidence for its existence (*1*, *18*). Lacking prior lifetime movement information on our captured wild bats, we defined a shortcut by a given bat as the first track between two previously recorded goals, and an unrecorded route as the first track to a previously unrecorded goal, that have not been traversed by this bat at least 10 nights after tagging; the mean number of nights was in fact much higher: 37.1 ± 40, median 18, maximum 158 nights. In total, 397 of the 9218 tracks (4.3%) were defined as shortcuts or unrecorded routes (Figs. 1, C and D, and 3A), observed in 70 of the 172 bats (41%), in equal proportions among age groups (Fisher's exact test, $P = 1.00$). Notably, though being somewhat longer, shortcuts and unrecorded routes did not otherwise differ significantly from regular tracks in straightness, turning angles, and headings (Fig. 3C). Furthermore, track straightness did not change

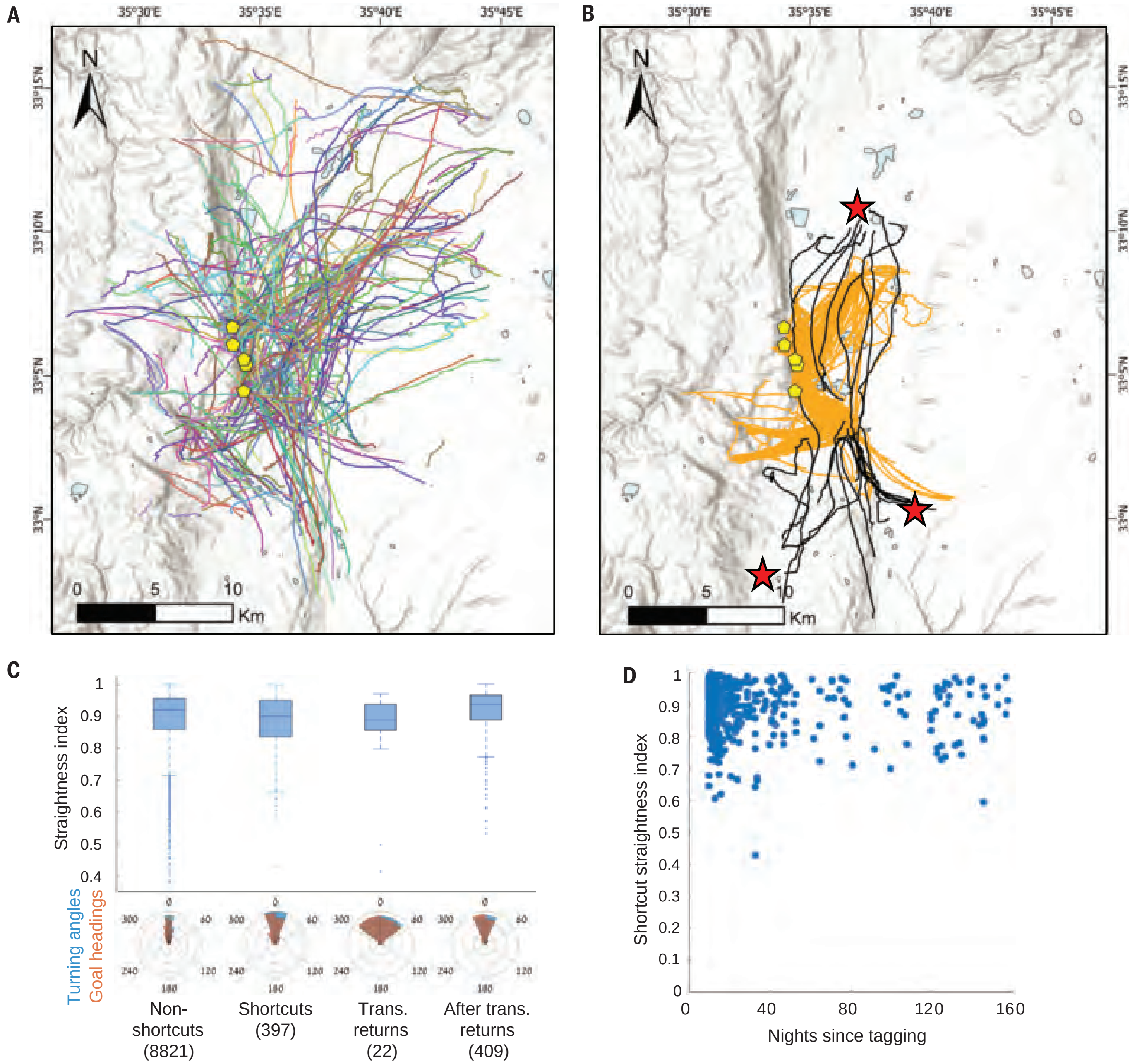

Fig. 3. Shortcuts and translocation experiments. (**A**) All tracks classified as shortcuts or unrecorded routes (n = 397) taken by 70 bats. (**B**) Movement tracks of translocated bats. Red stars mark the three release sites located 10, 14 and 16 km from the site of capture, in black are the return tracks and in orange are all the tracks subsequently made by these bats. Only one of the 22 translocated bats returned to the vicinity of the release site. (**C**) (Top) boxplots of straightness index for nonshortcut tracks, all shortcuts, return tracks of translocated bats, and tracks of translocated bats after returning (number of tracks in parentheses). (Bottom) turning angles (blue) and headings relative to goal (orange) of all nonstationary localizations within these categories. (**D**) Shortcut straightness index as a function of nights passed since tagging before the shortcut was made.

with increasing time since tagging (linear regression, r^2 = 0.001, P = 0.48; Fig. 3D) or differ among age groups (t test, t = –0.38, P = 0.72) or forearm lengths (linear regression, r^2 = 0.01, P = 0.47). Following an informed untagged conspecific as an alternative explanation for shortcutting is highly unlikely, given the very rare incidence in our dataset of two tagged individuals flying within reasonable distance (250 m) and time (10 s) of each other (37 track pairs were only partly overlapping within these parameters, totaling 0.4% of flight localizations). Overall, shortcuts or unrecorded routes were fairly common, very straight, and indistinguishable from the bats' regular repeated tracks between any two known locations for both juveniles and adult bats. These results matched our predictions and suggest superior map-like spatial knowledge with no decay in spatial memory for at least up to 158 nights, likely acquired within the first 3 months of life.

To reduce uncertainty about bats' previous experience within their home range, we

experimentally simulated shortcutting behavior by translocation experiments. Unlike translocations to far-off unfamiliar areas—aimed to examine map-and-compass navigation—we translocated bats to the periphery of the focal population's foraging area (Fig. 3B), yet within detection range of their familiar area as required for testing cognitive map–based navigation (*5*, *18*). As predicted, all 22 translocated bats returned to their regular foraging area immediately after release, in tracks that did not differ significantly in straightness and in turning angle and heading distributions from all other tracks, including the subsequent ones made by the same bats (Fig. 3C). Return flights very likely represent novel shortcuts because these release sites were rarely or never visited by any of the tracked bats of the focal population over the 4 years of our study.

We further investigated the bats' navigational process by applying time-lag embedding (*19*), a well-established method in dynamic systems theory for characterizing mechanical, physical, and mathematical systems [e.g., (*20*)] but also biological ones (*21*) using only the recorded time series and requiring no a priori knowledge of the underlying system (*15*). We determined both the correlation dimension (*19*, *22*), a measure of the system's number of degrees of freedom, and the largest Lyapunov exponent (*23*), measuring the system's degree of determinism or predictability. In animal navigation, degrees of freedom indicate the number of independent sensory modalities involved in the navigational process (*24*), much like the number of sensors or inputs necessary for a robot to navigate (*20*). The correlation dimension thus indicates the type of navigation strategy applied: Point-like information used in beaconing or piloting offers only one degree of freedom, hence is expected to result in a correlation dimension of 1. By contrast, map-based navigation requires multiple cues and therefore higher dimensionality; hence, we predicted a larger correlation dimension for the tracks made by the bats (*15*).

The mean correlation dimension estimated for the 1-Hz tracks ranged from 4.91 to 5.02 (Fig. 4A), suggesting a high-dimensional navigation process involving at least five independent navigational factors. The mean largest Lyapunov exponent ranged from 0.028 to 0.034 (Fig. 4B), suggesting that the same chaotic-deterministic process is in control throughout the entire track. This is similar to the process observed in homing pigeons, although here it appears to have one additional degree of freedom (*24*). Repeating these analyses for lower-resolution (0.5 to 0.125 Hz) tracks revealed very similar results (tables S4 and S5).

Taken together, the very high correlation dimension and very low largest Lyapunov exponent, along with shortcutting and characteristic goal-directed movements, are strongly consistent with cognitive map–based navigation; yet, we took additional approaches to examine the explanatory power of simpler point-like navigational processes (*1*, *15*, *18*). If bats were piloting, we expect strict movements consistent with following a set of local landmarks. Thus, when revisiting a target from multiple origins located in different directions, piloting should result in approach paths converging along a certain line of landmarks leading to the target, hence high directionality of arrival headings (*25*). By contrast, the same scenario under cognitive map navigation is predicted to allow for flexible approach paths, as was the case here: Approach paths from multiple uniformly distributed origins were flexible, with 91% of arrival headings having uniform rather than directional circular distribution (*15*) (Fig. 2E and fig. S1). Furthermore, despite their strong preference to return to the same cave that they emerged from (87% of nights), the bats did not follow the reverse sequence of trees going back to the cave in 91% of the nights in which ≥2 trees were visited. Such high flexibilities in goal-oriented movement do not fit predictions for piloting (or other models denoted as route-based navigation or topological map).

Beaconing to a specific goal-emanating cue was also unlikely, given the distribution of all fruit trees in the study area (*15*) (probability of a specific tree serving as beacon: 0.008; fig. S2) and—for olfactory beaconing—the local wind characteristics (fig. S3). An olfactory-based map navigation, similar to that suggested for pigeons and other birds (*2*, *26*), is also unlikely for the foraging fruit bats. The currently accepted paradigm for pigeon olfaction navigation necessitates remembering ratios of atmospheric trace compounds at the location of one goal—their home—and how these ratios change with wind direction and distance from that goal (*2*, *26*). Although each bat generally exhibited high fidelity to a small number of specific trees, they do track seasonal changes in fruiting and visit many other trees for much shorter durations (some for just a few minutes) (fig. S4). Under this model, foraging fruit bats must therefore remember the specific ratios of numerous goals, on the order of hundreds (fig. S4), which seems an unlikely memory load. Nevertheless, although olfactory-based navigation is unlikely, experiments manipulating the olfactory sense (*26*) are required to assess its role in routine foraging navigation of fruit bats.

Path integration, the only mechanism other than a cognitive map that allows for shortcuts, was also ruled out by several lines of evidence. First, observed trajectories failed to meet theoretical and empirical predictions (*15*), as return track straightness correlated neither with outbound straightness (Spearman's rho = –0.04, *P* = 0.31) nor with total excursion length (Spearman's rho = 0.10, *P* = 0.49). Second, in 13% of all nights, a bat returned to a different cave than the one it emerged from, 6.9 ± 5.5 km away from its cave of origin. In many of these cases, the bat returned to its previous cave only after several nights. Such a feat cannot be accomplished using only path integration.

This study reports research results based on data from the new wildlife tracking ATLAS system (*13*, *14*). The system's distinctive features—real-time high-resolution movement tracking of many small animals simultaneously for relatively long durations at low costs—revealed pervasive empirical evidence for cognitive map–based navigation in wild Egyptian fruit bats. ATLAS' main shortcomings—relatively high installation costs and limited spatial coverage compared to GPS—are less important once a fully operational ATLAS system is established (usually within several months), and in cases where most of the range relevant for the study population (here ~35 km by 25 km) can be covered by the system. Notably, by having smaller tags, ATLAS expands the range of trackable mammals and birds from 30 to 35% for the smallest currently commercially available

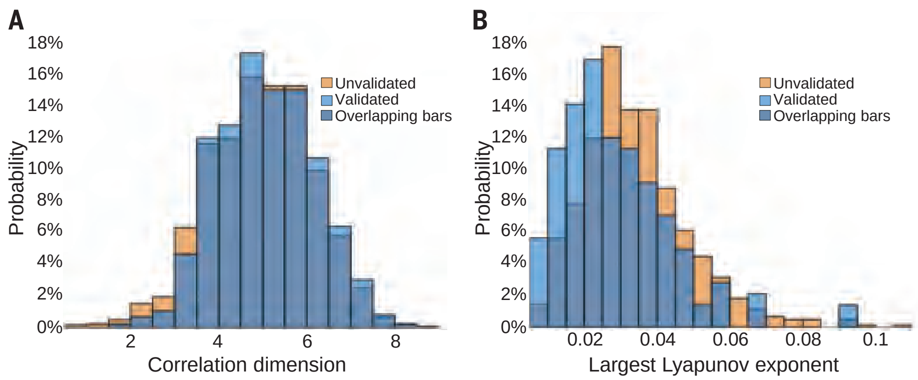

Fig. 4. Time-lag embedding analyses. Probability histograms for 1-Hz data before (light blue) and after (orange) a validation procedure to compensate for undersampling (*15*). Dark blue areas are estimates overlapping among the two categories. (**A**) Correlation dimension estimates. (**B**) Largest Lyapunov exponent estimates.

GPS to 80 to 90% (*27*), while maintaining high spatial accuracy. This is particularly important for small and nocturnal animals such as bats, for which solar-recharging technologies are impractical. Consequently, ATLAS opens new opportunities for investigating the movement ecology of bats, which account for ~25% of known mammal species and of which at least 25% are threatened (*28*). More generally, ATLAS suggests a promising new avenue for animal movement and navigation research.

Recent progress in neuroscience has yielded important insights into the cellular-level processes underlying animal behavior. Such lab experiments are vital but might not reveal how animals behave or utilize their cognitive potential in the wild (*29*, *30*). Using multiple approaches, analyses, and reasonings implemented on our high-resolution dataset, we have presented here several lines of evidence for the existence of a cognitive map in wild animals under natural settings, crucially complementing lab-based evidence (*7*, *9*, *10*). We caution, however, that although all these results are consistent with our interpretation, two main caveats [highlighted in (*18*)] should be carefully considered. First, lacking information on bats' tracks before we trapped and tagged them, shortcuts or unrecorded routes cannot be considered as strictly novel. Yet, they maintain the same properties (straight ab initio goal-directed flights) regardless of when the bats first traversed them: more than a month after tagging on average, and also after 5 months, across fruiting seasons, of continuous high-resolution tracking (Fig. 3D). Furthermore, 3- to 8-month-old juveniles also exhibited straight ab initio goal-directed shortcuts that were indistinguishable from those of the adults, and fruit bats in our study rarely (0.4%) fly together even for a short part of their commuting flights. We thus propose that a cognitive map is already present at an early stage and is likely acquired within the first 3 months of life. Having high-resolution lifetime (from birth to death) movement tracks of wild bats of various ages could greatly complement this study, to elaborate at which early stage of life a cognitive map is acquired (for juveniles) and for how long the spatial memory lasts across seasons and years (for adults). Second, tracked bats might still have used alternative (simpler) navigation mechanisms such as piloting and beaconing, as animals navigating in real-life environments likely use more than one navigation mechanism (*30*). Consequently, we do not claim that bats foraging within their familiar home range exclusively rely on a cognitive map, but rather that our results (i) are consistently compatible with multiple features expected from cognitive map–based navigation; (ii) are strictly incompatible with expectations of random search and path integration; and (iii) do not lend support to alternative navigation mechanisms that we examined, such as piloting and beaconing, although additional field experiments are needed to divulge whether, and to what extent, wild bats also use such mechanisms. We have previously employed such field experiments, revealing a key role for visual landmarks in large-scale homing of fruit bats (*11*). We thus hypothesize that a few visual landmarks might be sufficient for wild bats to anchor the cognitive map of their entire (relatively large) home range.

We suggest that such complex foraging navigation, considered to reflect high cognitive ability, may have evolved under selective forces similar to those proposed for long-lived, forest-dwelling frugivorous primates (*31*). Egyptian fruit bats feed on spatially patchy yet temporally predictable long-lived resources (fruit trees), have extreme longevity (25 years and more) relative to body size (*32*, *33*), and are social central-place foragers that return home to a cave at the end of the night rather than roost on trees within their foraging range. We suggest that these features may have selected for extended spatial memory and high foraging navigation performance of this and perhaps other similar species as well. It is interesting that Pteropodid bats have the largest relative brain size among bat families, surpassing even basal primates (*34*)—reminiscent of frugivorous primates that tend to have larger relative brain sizes than mostly folivorous primates (*31*). A genuine integration between lab-based neurobiology, experimental animal cognition research, and field-based movement ecology (*30*, *35*, *36*) could open new opportunities to further unravel the components of spatial cognition. Such integration may also help in understanding other long-lasting key questions on the neural, behavioral, and ecological mechanisms underlying cognitive performance of wild animals in their natural environments.

REFERENCES AND NOTES

1. J. Wiener *et al.*, in *Animal Thinking: Contemporary Issues in Comparative Cognition*, R. Menzel, J. Fischer, Eds. (MIT Press, Cambridge, MA, 2011).
2. H. G. Wallraff, *Animal Navigation: Pigeon Homing as a Paradigm* (Springer, Berlin, 2005).
3. G. Kramer, *J. Ornithol.* **94**, 201–219 (1953).
4. E. C. Tolman, *Psychol. Rev.* **55**, 189–208 (1948).
5. J. O'Keefe, L. Nadel, *The Hippocampus as a Cognitive Map* (Clarendon, 1978).
6. C. R. Gallistel, *The Organization of Learning* (MIT Press, 1990).
7. M. Geva-Sagiv, L. Las, Y. Yovel, N. Ulanovsky, *Nat. Rev. Neurosci.* **16**, 94–108 (2015).
8. E. I. Moser, E. Kropff, M.-B. Moser, *Annu. Rev. Neurosci.* **31**, 69–89 (2008).
9. A. Finkelstein *et al.*, *Nature* **517**, 159–164 (2015).
10. A. Sarel, A. Finkelstein, L. Las, N. Ulanovsky, *Science* **355**, 176–180 (2017).
11. A. Tsoar *et al.*, *Proc. Natl. Acad. Sci. U.S.A.* **108**, E718–E724 (2011).
12. S. Greif, I. Borissov, Y. Yovel, R. A. Holland, *Nat. Commun.* **5**, 4488 (2014).
13. A. Weller Weiser *et al.*, in *Proceedings of the 2016 ACM/IEEE International Conference on Information Processing in Sensor Networks (IPSN)*, Vienna, Austria, 12 to 14 April 2016, pp. 1–12.
14. S. Toledo, O. Kishon, Y. Orchan, A. Shohat, R. Nathan, Lessons and experiences from the design, implementation, and deployment of a wildlife tracking system, in *Proceedings of the 2016 IEEE International Conference on Software Science, Technology and Engineering (SWSTE)*, pp. 51–60.
15. Materials and methods are available as supplementary materials.
16. P. A. Zollner, S. L. Lima, *Ecology* **80**, 1019–1030 (1999).
17. E. R. Heithaus, T. H. Fleming, *Ecol. Monogr.* **48**, 127–143 (1978).
18. A. T. Bennett, *J. Exp. Biol.* **199**, 219–224 (1996).
19. F. Takens, "Detecting strange attractors in turbulence" in *Dynamical Systems and Turbulence, Warwick 1980* (Springer, 1981), vol. 898, pp. 366–381.
20. U. Nehmzow, *Scientific Methods in Mobile Robotics: Quantitative Analysis of Agent Behaviour* (Springer, London, 2006).
21. A. Hastings, C. L. Hom, S. Ellner, P. Turchin, H. C. J. Godfray, *Annu. Rev. Ecol. Syst.* **24**, 1–33 (1993).
22. J. E. Skinner, *Nat. Biotechnol.* **12**, 596–600 (1994).
23. M. T. Rosenstein, J. J. Collins, C. J. De Luca, *Physica D* **65**, 117–134 (1993).
24. I. Schiffner, J. Baumeister, R. Wiltschko, *J. Theor. Biol.* **291**, 42–46 (2011).
25. E. Normand, C. Boesch, *Anim. Behav.* **77**, 1195–1201 (2009).
26. A. Gagliardo, *J. Exp. Biol.* **216**, 2165–2171 (2013).
27. R. Kays, M. C. Crofoot, W. Jetz, M. Wikelski, *Science* **348**, aaa2478 (2015).
28. K. E. Jones, A. Purvis, J. L. Gittleman, *Am. Nat.* **161**, 601–614 (2003).
29. C. H. Janson, R. Byrne, *Anim. Cogn.* **10**, 357–367 (2007).
30. L. F. Jacobs, R. Menzel, *Mov. Ecol.* **2**, 3–3 (2014).
31. K. Milton, *Am. Anthropol.* **83**, 534–548 (1981).
32. G. Neuweiler, *The Biology of Bats* (Oxford Univ. Press, New York, 2000).
33. G. G. Kwiecinski, T. A. Griffiths, *Mamm. Species* **611**, 1–9 (1999).
34. P. Pirlot, H. Stephan, Encephalization in Chiroptera. *Can. J. Zool.* **48**, 433 (1970).
35. R. Nathan *et al.*, *Proc. Natl. Acad. Sci. U.S.A.* **105**, 19052–19059 (2008).
36. J. Morand-Ferron, E. F. Cole, J. L. Quinn, *Biol. Rev. Camb. Philos. Soc.* **91**, 367–389 (2016).
37. D. Shohami, R. Nathan, Cognitive map-based navigation in wild bats revealed by a new high-throughput tracking system, Dryad (2020); https://doi.org/10.5061/dryad.g4f4qrfn2.

ACKNOWLEDGMENTS

For valuable fieldwork assistance, we thank R. Lotan, A. Levi, S. Margalit, and other Movement Ecology Lab and the Minerva Center for Movement Ecology members. We thank N. Ulanovsky and A. Bennett for helpful comments on an earlier version, A. Ben-Nun for help with GIS analysis, and Y. Yovel for discussions on this topic; **Funding:** ATLAS development, maintenance, and studies have been supported by the Minerva Center for Movement Ecology, the Minerva Foundation, and ISF grant ISF-965/15; bat research in the movement ecology lab was supported also by grants from ISF-1316/05, ISF-1259/09, and GIF 1316/15. We also acknowledge support from Adelina and Massimo Della Pergola Chair of Life Sciences to R.N. and the Israel President Scholarship to D.S. **Author contributions:** D.S. and R.N. conceived the study; R.N. conceived and S.T. developed the ATLAS system, with the help of Y.O. and Y.B.; D.S. and E.L. carried out fieldwork; D.S. analyzed the data; I.S. conceived and performed the time-lag embedding analysis; D.S. and R.N. wrote the manuscript with input from all other coauthors; **Competing interests:** The authors declare no competing interests. **Data and materials availability:** All ATLAS localization data used in the analysis are available on Dryad (*37*).

SUPPLEMENTARY MATERIALS

science.sciencemag.org/content/369/6500/188/suppl/DC1
Materials and Methods
Figs. S1 to S4
Tables S1 to S4
References (*38*–*42*)

6 May 2019; accepted 29 May 2020
10.1126/science.aax6904

COGNITIVE MAPS

The ontogeny of a mammalian cognitive map in the real world

Lee Harten[1]*, Amitay Katz[1]*, Aya Goldshtein[1]*, Michal Handel[1], Yossi Yovel[1,2]†

How animals navigate over large-scale environments remains a riddle. Specifically, it is debated whether animals have cognitive maps. The hallmark of map-based navigation is the ability to perform shortcuts, i.e., to move in direct but novel routes. When tracking an animal in the wild, it is extremely difficult to determine whether a movement is truly novel because the animal's past movement is unknown. We overcame this difficulty by continuously tracking wild fruit bat pups from their very first flight outdoors and over the first months of their lives. Bats performed truly original shortcuts, supporting the hypothesis that they can perform large-scale map-based navigation. We documented how young pups developed their visual-based map, exemplifying the importance of exploration and demonstrating interindividual differences.

Since the introduction of the idea of a cognitive map (*1*), there has been an ongoing debate regarding which nonhuman animals have such a map (*2*–*4*). It is widely accepted that the most essential characteristic of map-based navigation is the shortcut, i.e., the ability to navigate between familiar points but in a new and direct path (*1*, *5*). When tracking an animal in the wild, one cannot know for certain that the animal has followed that path before the study period. That is, because we did not observe the first time the animal took this path, there is no way to know if it did so using cognitive map–based navigation or some other navigation strategy (Fig. 1A). In this study, we GPS tracked the full movement history of 22 Egyptian fruit bat (*Rousettus aegyptiacus*) pups from their first flight outside and over the first months of their lives.

The bats gradually increased their home range, which reached a mean of >60 km^2 after 70 days, similar to that of wild adult bats (*6*) (Fig. 1, B and C). While increasing their home ranges, the bats detected new fruit trees to which they returned to forage on later nights. Individuals' behavior typically included occasional exploratory nights that were spread between several nights of exploiting previously visited trees. On exploratory nights, the bats flew far beyond their home range and often detected new trees, whereas on exploitatory nights, the bats foraged on familiar trees mostly near the colony (fig. S1).

All bats performed shortcuts (for examples, see Fig. 1D and figs. S2 and S3). To make sure that these shortcuts were truly novel, we used a set of conservative criteria, defining shortcuts as movements for which at least 50% of the trajectory was original, i.e., >100 m away from any location where the bat had been previously (see the supplementary text, section S1). Note that these criteria assume that locations where a bat passed before (even for a brief moment) are familiar to it. This conservative assumption substantially reduced the number of shortcuts, but it increased our confidence that shortcuts were truly novel (doubling this criterion to 200 m did not change the results).

Several analyses suggested that the shortcuts were intentional, new, and direct, supporting the conclusion that they were derived from a cognitive map. First, shortcuts were almost as straight as flights in previously used routes, which we defined as "commutes" [the straightness index (SI) quartiles were 0.64 to 0.92 in shortcuts versus 0.78 to 0.96 in commutes; Fig. 2B]. Shortcuts were much straighter than exploration flights (i.e., events in which the bats moved to an unfamiliar location; the SI quartiles were 0.64 to 0.92 in shortcuts versus 0.04 to 0.60 in exploration; Fig. 2B and see

[1]School of Zoology, Faculty of Life Sciences, Tel Aviv University, 6997801 Tel Aviv, Israel. [2]Sagol School of Neuroscience, Tel Aviv University, 6997801 Tel Aviv, Israel.
*These authors contributed equally to this work.
†Corresponding author. Email: Yossiyovel@gmail.com

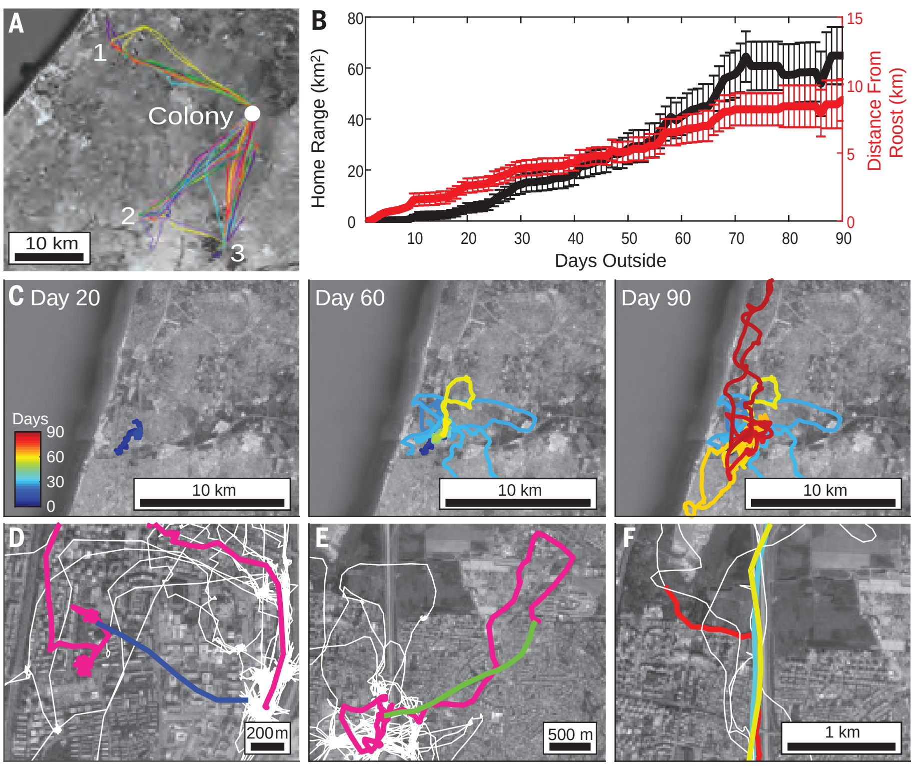

Fig. 1. Bats gradually increase their home range while mapping their environment. (**A**) Tracking of an adult fruit bat for >80 days. Around night 60, after flying to points 1, 2, and 3 on the map, the bat performed what is supposedly a shortcut between points 2 and 3 (yellow trajectory). Because we do not know the history of this bat, we cannot be sure that this trajectory is truly novel. For example, the bat might have moved between these two points a year earlier using random search navigation. (**B**) Average home range size (black) and maximum distance from the colony (red) over time for all 22 bats. Means and SEs are presented. (**C**) All flown trajectories of one individual bat after 20, 60, and 90 nights of navigation. (**D**) A novel shortcut is depicted in blue. The full movement of the bat on all previous nights is depicted in white. The movement on the same night before the shortcut is shown in pink. Additional examples are shown in figs. S2 and S3. (**E**) A long-cut is depicted in green. The full movement of the bat on all previous nights is depicted in white. The movement on the same night before the long-cut is shown in pink. Additional examples are shown in figs. S4 and S5. (**F**) Three examples (different colors) of bats flying along a highway. Additional examples are shown in fig. S6.

fig. S7 for a movement definitions). Second, bats headed toward their target from the beginning of the shortcuts, and take-off angles were centered around zero (i.e., they were significantly directional, $P < 10^{-6}$, Watson test, comparing with a uniform distribution between –90° and 90°; Fig. 2A). In the third analysis, the straightness of shortcuts could not be explained by a correlated random-walk model that was based on the bats' actual step size and turning angles [but without any navigational goal, $P < 10^{-46}$, Kolmogorov-Smirnov test comparing the SI distributions for the model and the real shortcuts; see null models in (*7*)].

Because we knew the exact home range of the animals on any day, we describe shortcuts performed from outside the home range as "long-cuts," and these typically occurred after long exploration flights. We make this distinction because long-cuts entail navigation in areas that were clearly unfamiliar to the bat, often many kilometers away from any location they had ever been before (see examples in Fig. 1E and figs. S4 and S5). Just as in the case of shortcuts, long-cuts were straight (fig. S4), and the bats embarked on them heading in the direction of the target (although this was not the case for exploration flights of similar range; Fig. 2, B and C, and fig. S8). Long-cuts were substantially straighter than exploration flights and only slightly less straight than shortcuts (SI quartiles were 0.52 to 0.81). Long-cut straightness could not be explained by a bat-like correlated random-walk model in which turning and step size were fit to the bats' actual movement [$P < 10^{-51}$; see null models in (*7*)]. Long-cut take-off angles were centered around zero and were significantly directional (P = 0.01, Watson test, comparing with a uniform distribution between –90° and 90°; Fig. 2C). Long-cuts could not be explained by simply heading back in the direction of the home range [$P < 0.001$, permutation analysis (*7*); fig. S9]. Although this suggests that bats were heading directly to their target during long-cuts, we cannot fully exclude the possibility that they sometimes first headed in the direction of the home range and then switched to map-based navigation to home in on their target.

It is difficult to determine the intention of the bats, but many of the movements were performed at the end of the night while returning to the colony (~65% of the long-cuts and ~35% of the shortcuts). We thus ran the same analysis (i.e., straightness and take-off heading) for this subset of movements and the results were identical (Fig. 2 and fig. S10).

In total, we observed 125 shortcuts and 121 long-cuts with an average distance of ~1500 and ~3300 m, respectively (fig. S11, A and B). We used a correlated random-walk model to test whether the frequency of performing long-cuts and shortcuts could be explained by a

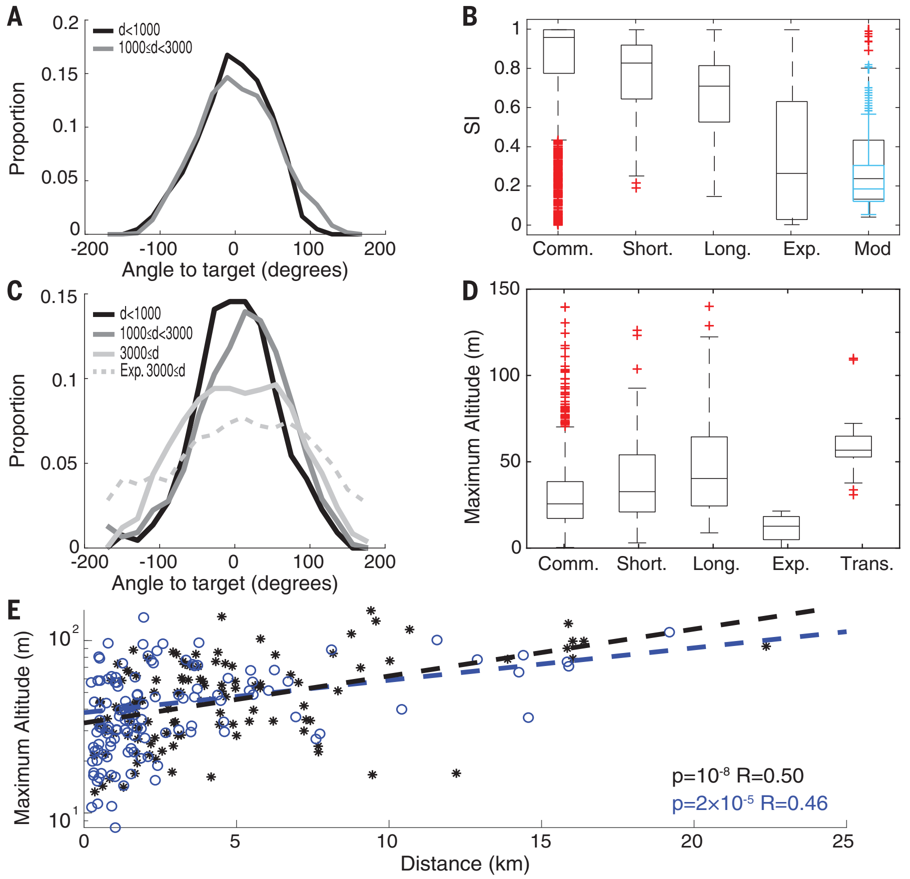

Fig. 2. Bats exhibit map-like navigation. (**A**) The distribution of shortcut take-off angles demonstrates that bats take off heading in the direction of the target. Gray levels separate shortcuts according to distance. (**B**) Flight straightness (SI) in four movement modes: commute, shortcuts, long-cuts, and exploration, and in two correlated random-walk movement models for shortcuts in blue and long-cuts in black (*7*). Boxplots in (B) and (D) show median, quartiles, and whiskers extending to the most extreme data points not including outliers depicted in red (see MATLAB for outlier definition). (**C**) The distribution of long-cut take-off angles demonstrates that bats take off heading in the direction of the target. We also show heading during exploration for comparison. Gray levels separate long-cuts according to distance. (**D**) Maximal flight altitudes reached during five different movement modes: commute, shortcuts, long-cuts, exploration, and translocation. (**E**) There was a significant positive correlation between the distance from which a shortcut or long-cut was performed and the maximum altitude to which the bat ascended (long-cuts are depicted in black and shortcuts in blue).

random-walk movement strategy. The model predicted fewer than one long-cut or shortcut compared with the 246 that we observed in reality [see null models in (*7*)]. Both shortcuts and long-cuts were performed in all possible directions (i.e., azimuths) without any directional preference (P = 0.22 and P = 0.10 for shortcuts and long-cuts, respectively, Rayleigh test; fig. S12). Bats performed both shortcuts and long-cuts from their first day outside, but it is noteworthy that the bats were at least 10 weeks old at this point (*7*). The rate of performing shortcuts and long-cuts did not increase over time, but their average distance increased substantially (fig. S13)

Our results suggest that the bats mostly relied on vision [the Egyptian fruit bat is extremely visual, whereas its echolocation can only sense up to a few dozens of meters ahead (*8*–*11*)]. First, bats flew significantly higher when performing shortcuts and long-cuts than when commuting in a familiar route [$P < 0.01$ and $P < 10^{-11}$ for the short- and long-cuts versus commute, respectively, generalized linear model (GLM), with altitude set as the explained variable and the type of navigation set as a fixed factor (*7*); Fig. 2D]. An increased flight altitude suggests the use of vision, especially in an urban environment, where the view is mostly blocked by nearby buildings. Second, the bats ascended just high enough to see beyond the buildings; there was a significant positive correlation between the maximum height of the buildings blocking the bats' view and the maximum altitude to which they ascended (P = 0.019, GLM with building height set as a fixed factor; fig. S14). An analysis of the visual input available for the bats once they

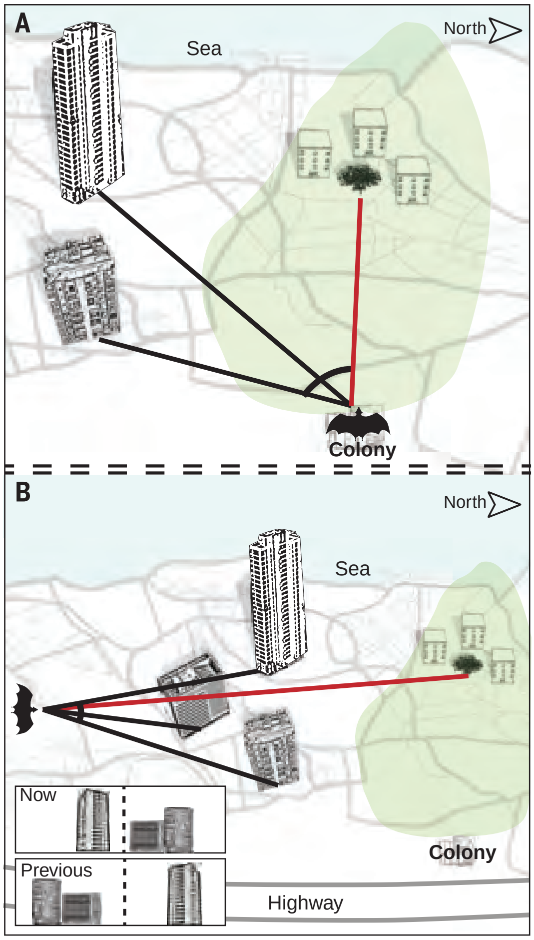

Fig. 3. Hypothetical schematic of bats' navigation strategy. Prominent visual landmarks such as buildings are used to move in shortcuts within the home range (**A**), and to home to familiar points of interest from outside the home range (**B**). Green shaded area represents the bat's home range. We propose that, when navigating, the bats set their heading relative to a spatial arrangement of familiar landmarks. The bats must have a map-like representation of these landmarks because they often see them from completely new angles and distances, e.g., when observing them from the south for the first time (inset, top) after only observing them from the north for many weeks (inset, bottom). Note how when observed from the south for the first time, both the right-left orientation of the landmarks and the relative distances between them on the retina change substantially.

ascended above the buildings using drone imaging confirmed that this behavior substantially increased the number of visible landmarks (see the supplementary text, section S2). Third, there was a positive correlation between the altitude above ground of the ascent and the distance of the shortcut or long-cut, as expected when orienting from a remote location while using vision (there was a significant positive correlation between the distance and the altitude, $P < 10^{-5}$ and $P < 10^{-8}$ for the shortcuts and long-cuts, respectively, GLM with the navigation strategy set as a fixed factor; Fig. 2E; also see supplementary text, section S2).

We performed several additional analyses to exclude the use of alternative, nonvisual input (fig. S15). First, to control for the potential use of an olfactory mosaic map (*12*, *13*), we compared wind direction with the straightness of all shortcuts and long-cuts, assuming that if bats were using olfaction, then they should navigate more accurately when flying upwind than when flying downwind. There was no correlation between wind direction and navigation straightness ($P = 0.66$, $r = 0.04$ and $P = 0.051$, $r = 0.18$ for the shortcuts and long-cuts, respectively, Pearson's correlation test; fig. S15D). The olfaction-gradient navigation hypothesis is probably not relevant for our bats because this navigation strategy has been shown to be relevant only when homing from long distances (beyond ~5 km), and most of our navigations were shorter (*14*). We do not entirely exclude the possibility that olfaction plays some role in fruit bat navigation but argue that it is probably used for short-distance orientation when searching for a tree with ripe fruit. Second, to control for use of sound cues, we analyzed continuous audio recordings performed onboard nine bats [see (*7*) and fig. S16]. Third, the use of echolocation for performing long-cuts or shortcuts is unlikely because echolocation is a short-ranged modality and bats can detect a large tree from a distance of no more than 50 m (*15*). Moreover, Egyptian fruit bats usually do not echolocate during their commute (*10*), a fact that we also confirmed in our audio recordings.

Although bats may use additional senses during foraging and navigation, our data suggest that vision is their main sense in map-based navigation (see the supplementary text, section S3). Our data also suggest that the bats had to represent navigational information in a viewpoint-invariant fashion (Fig. 3) to assess their location and desired heading, an ability that is considered to be a key feature of a cognitive map (*16*). We therefore suggest that the bats used the spatial arrangement of distal visual landmarks (e.g., using triangulation) before embarking on a navigation flight to determine their desired heading, and to some extent also distance (an analysis of their flight speed at the beginning of shortcuts and long-cuts suggested that they had some estimate of the distance; see the supplementary text, section S4). It is very unlikely that our bats followed other bats when performing shortcuts or long-cuts (see the supplementary text, section S5).

Individual bats varied in their degree of exploration (Fig. 4, A and B). As has been shown in other species (*17*, *18*), we hypothesized that bats that explored more would build a more complete cognitive map, thus allowing better navigation. Indeed, bats translocated to unfamiliar locations (*7*) showed more direct paths home when they had been more exploratory previously (Fig. 4, C and D).

Moreover, bats that flew higher on the nights preceding the translocation also homed in significantly straighter trajectories, supporting the vision-based navigation hypothesis ($P = 0.004$, GLM with altitude set as a fixed factor; Fig. 4E). Bats that were closer to the translocation release point before the translocation night did not necessarily navigate home better, once again contradicting the template-matching hypothesis ($P = 0.66$, GLM with the previous distance to translocation point set as a fixed factor; Fig. 4F). In other words, a bat that was near the translocation point on the previous night was not necessarily able to home back directly, whereas a bat that was never near this point but tended to fly high on previous nights homed in a straighter trajectory, supporting the use of map-like navigation. There was also no significant correlation between the day of the translocation or the age of the bat and the straightness of the return ($P = 0.9$, $r = 0.04$ and $P = 0.8$, $r = 0.05$, respectively, GLM), suggesting that it is not experience per se but specifically exploratory experience that is important for navigation (*19*).

In one of the most critical reviews, Bennet (1996) raised three main limitations that led him to conclude that no study had shown a cognitive map in a wild animal under natural conditions (*20*). In brief, Bennet claimed that (i) because the animal's history is unknown, reported novel shortcuts might not truly be novel; (ii) some studies did not rule out the use of path integration when performing the supposed shortcuts; and (iii) some studies can be explained by non-map-based, simpler navigation strategies (*21*) that could explain the animals' movement (e.g., beaconing or route following).

Our study allows us to exclude all of these possibilities. First, we tracked the animals' full

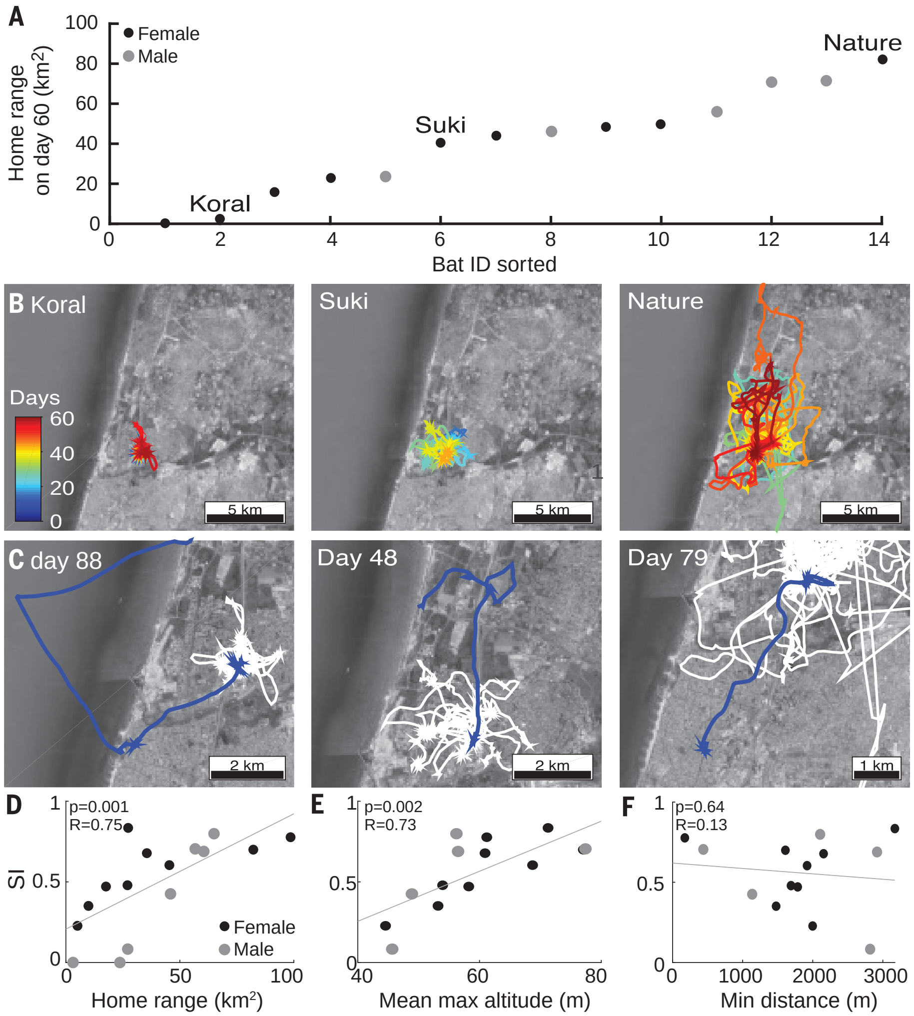

Fig. 4. Translocation experiments reveal individual navigation capabilities. (**A**) Different individuals (*x*-axis) tended to be more or less exploratory. The *y*-axis depicts the bat's home range on day 60. "Koral," "Suki," and "Nature" are bat names. (**B** and **C**) Three examples of translocations for a weak explorer (left column), an intermediate explorer (middle column), and an extreme explorer (right column). (B) Movements of the three bats before the translocation. (C) Return flights of the same three bats from the translocation point. (**D** and **E**) The straightness of homing back from the translocation point significantly correlated with: (D) the tendency to explore (depicted by the home range) and (E) the altitude flown by the bats on the nights before the translocation. (**F**) The straightness of homing back did not correlate with the nearest distance of previous trajectories to the point of translocation (i.e., how close the bat was to the translocation point on previous nights).

histories and were thus able to determine where a shortcut was truly novel. Second, we ruled out the use of path integration. Specifically, path integration, which does not require external sensory input, is notorious for its accumulation of error (*22*), and this is true in bats (*23*). If the animals were using path integration, then we would expect an increase in error when they flew farther from their starting point and when they turned more (*22*, *24*, *25*). We found no correlation between the straightness of the long-cuts and any of these parameters: accumulated flight duration, flight distance, or turning before the return (fig. S17). In addition, the animals' ability to return from the translocation sites (in straight trajectories) could not be explained by path integration.

Taken together, our results satisfy the requirements of demonstrating visual map–based navigation. That said, some caveats are in order. First, we do not claim that the map is Euclidean nor that the distances are accurately represented in the bat's brain. Second, navigation is a complex behavior that probably does not always rely on a single strategy (*2*, *26*). Bats occasionally switched from using map-based navigation to alternative strategies like flying along landscape elements such as highways (Fig. 1F, fig. S6, and supplementary text, section S6), but our data demonstrate that they have a map-like representation of their environment and can navigate according to this cognitive map when necessary.

REFERENCES AND NOTES

1. E. C. Tolman, *Psychol. Rev.* **55**, 189–208 (1948).
2. J. F. Cheeseman *et al.*, *Proc. Natl. Acad. Sci. U.S.A.* **111**, 8949–8954 (2014).
3. R. Menzel *et al.*, *Proc. Natl. Acad. Sci. U.S.A.* **102**, 3040–3045 (2005).
4. A. Tsoar *et al.*, *Proc. Natl. Acad. Sci. U.S.A.* **108**, E718–E724 (2011).
5. J. O'Keefe, L. Nadel, *The Hippocampus as a Cognitive Map* (Oxford Univ. Press, 1978).
6. K. Egert-Berg *et al.*, *Curr. Biol.* **28**, P3667–P3673 (2018).
7. Materials and methods are available as supplementary materials.
8. N. S. Bar, S. Skogestad, J. M. Marçal, N. Ulanovsky, Y. Yovel, *PLOS Biol.* **13**, e1002046 (2015).
9. A. Boonman, Y. Bar-On, N. Cvikel, Y. Yovel, *Front. Physiol.* **4**, 248 (2013).
10. S. Danilovich *et al.*, *Curr. Biol.* **25**, R1124–R1125 (2015).
11. Y. Yovel, M. Geva-Sagiv, N. Ulanovsky, *J. Comp. Physiol. A Neuroethol. Sens. Neural Behav. Physiol.* **197**, 515–530 (2011).
12. A. Gagliardo, *J. Exp. Biol.* **216**, 2165–2171 (2013).
13. S. Papi, F. Fiore, L. Fiaschi, V. Benvenuti, *Monit. Zool. Ital.* **6**, 85–95 (1972).
14. A. Gagliardo, P. Ioalè, M. Savini, H.-P. Lipp, G. Dell'Omo, *J. Exp. Biol.* **210**, 1132–1138 (2007).
15. W.-P. Stilz, H.-U. Schnitzler, *J. Acoust. Soc. Am.* **132**, 1765–1775 (2012).
16. D. A. Waller, L. Nadel, *Handbook of Spatial Cognition* (American Psychological Association, 2013).
17. L. K. Arvidsson, F. Adriaensen, S. van Dongen, N. De Stobbeleere, E. Matthysen, *Anim. Behav.* **123**, 151–158 (2017).
18. N. J. Dingemanse, C. Both, P. J. Drent, K. van Oers, A. J. van Noordwijk, *Anim. Behav.* **64**, 929–938 (2002).
19. R. M. R. Barclay, S. D. Jacobs, *Can. J. Zool.* **89**, 466–473 (2011).
20. A. T. Bennett, *J. Exp. Biol.* **199**, 219–224 (1996).
21. B. A. Cartwright, T. S. Collett, *Nature* **295**, 560–564 (1982).
22. A. Cheung, S. Zhang, C. Stricker, M. V. Srinivasan, *Biol. Cybern.* **97**, 47–61 (2007).
23. G. Aharon, M. Sadot, Y. Yovel, *Curr. Biol.* **27**, 3650–3657.e3 (2017).
24. M. Müller, R. Wehner, *Proc. Natl. Acad. Sci. U.S.A.* **85**, 5287–5290 (1988).
25. A. S. Etienne, R. Maurer, V. Séguinot, *J. Exp. Biol.* **199**, 201–209 (1996).
26. F. C. Dyer, J. L. Gould, *Science* **214**, 1041–1042 (1981).
27. L. Harten, A. Katz, A. Goldshtein, M. Handel, Y. Yovel, Data for: The ontogeny of a mammalian cognitive map in the real world, Version 1, Mendeley (2020); https://doi.org/10.17632/n9d8gbz3xr.1.

ACKNOWLEDGMENTS

We thank N. Ulanovsky, T. Eliav, and M. Geva for reading and commenting on the manuscript and M. Taub for assistance with graphics. **Funding:** This research was partially supported by the European Research Council (ERC–GPSBAT). **Author contributions:** L.H. and Y.Y. designed the experiment. Y.Y., A.K., and L.H. conceived the analysis. L.H. and M.H. conducted the experiment. Y.Y., A.K., and A.G. conducted the analysis. A.G. performed drone imaging and analysis. Y.Y. wrote the manuscript. L.H., A.K., and A.G. reviewed the manuscript. **Competing interests:** The authors declare no competing interests. **Data and materials availability:** All datasets included in the paper are available on Mendeley (*27*).

SUPPLEMENTARY MATERIALS

science.sciencemag.org/content/369/6500/194/suppl/DC1
Materials and Methods
Supplementary Text, Sections S1 to S6
Figs. S1 to S25
Captions for Movies S1 to S4
References (*28–38*)
Movies S1 to S4
GPS Tracking Data

11 June 2019; accepted 29 May 2020
10.1126/science.aay3354

ARCTIC PRODUCTIVITY

Changes in phytoplankton concentration now drive increased Arctic Ocean primary production

K. M. Lewis, G. L. van Dijken, K. R. Arrigo*

Historically, sea ice loss in the Arctic Ocean has promoted increased phytoplankton primary production because of the greater open water area and a longer growing season. However, debate remains about whether primary production will continue to rise should sea ice decline further. Using an ocean color algorithm parameterized for the Arctic Ocean, we show that primary production increased by 57% between 1998 and 2018. Surprisingly, whereas increases were due to widespread sea ice loss during the first decade, the subsequent rise in primary production was driven primarily by increased phytoplankton biomass, which was likely sustained by an influx of new nutrients. This suggests a future Arctic Ocean that can support higher trophic-level production and additional carbon export.

In response to anthropogenic climate change, the Arctic is warming faster than any other region, with the majority of the warming centered over the Arctic Ocean (AO) (*1*). Sea ice has radically decreased in concentration, volume, and duration, with summer sea ice predicted to disappear completely by mid-century (*1*). Correspondingly, annual phytoplankton net primary production (NPP) has significantly increased owing to a longer growing season and an expanded area of open water (OW) (*2–5*). However, scientists debate how continued sea ice declines will affect AO NPP in the future (*6*, *7*). Greater freshwater flux through precipitation, ice melt, and river outflow could intensify surface ocean stratification and inhibit the mixing of deep nutrients into surface waters, thus reducing AO NPP (*8*, *9*). Alternatively, greater OW area and more frequent storms (*5*) may increase NPP by promoting the upward delivery of new nutrients to the depleted euphotic zone through enhanced wind mixing (*10*), internal waves (*11*), and shelf break upwelling (*12*, *13*). Here, we present a two-decade-long time series of NPP in the AO that we parameterized using the largest and most complete dataset of in situ optics and phytoplankton biomass and physiology ever assembled for these waters to assess the current trajectory of NPP in response to ongoing changes in Arctic climate.

Satellite-derived estimates of chlorophyll *a* (Chl *a*), sea surface temperature (SST), and sea ice concentration were used as input to an AO NPP algorithm (*2*, *3*, *14*) to evaluate trends from 1998 to 2018. We used a modified version of the standard empirical NASA–Chl *a* algorithm to better account for the distinct bio-optical properties of the AO, which differ notably from the global ocean because of higher pigment packaging and chromophoric dissolved organic matter (CDOM) concentrations (*15*, *16*). The updated Chl *a* algorithm (*17*) was developed by using 501 coincident measurements of in situ remote sensing reflectance and Chl *a* from 25 different cruises that captured the spatial heterogeneity across the AO. Time series trends for mean surface phytoplankton biomass concentration (Chl *a*, milligrams per cubic meter), spatially integrated NPP (teragrams of carbon per year), SST (degrees Celsius), OW area (square kilometers), and OW duration (days) were statistically evaluated for the entire AO and 10 subregions (Fig. 1A) for the 21-year time period.

OW area (<50% sea ice cover) has increased by 27% in the AO between 1998 and 2018, with ~59,000 km^2 of OW added each year (Table 1). Subregions that experienced significant increases in OW area (24 to 123%) included the Basin, Kara, Siberian, Barents, and Chukchi (Table 1). Increases in OW area in the Laptev and Beaufort subregions were nonsignificant, and changes in the outflow shelves of the Nordic, Canada, and Baffin subregions were negligible (Table 1). However, the rate of OW increase in the AO and all subregions, except the Nordic, has slowed considerably since 2009 (Fig. 2A and Table 1).

At the same time, AO Chl *a* concentration increased significantly (22%) between 1998 and 2018 (Table 1), with almost all of the increase occurring since 2009 (Fig. 2B and Table 1). These changes were largely restricted to the

Department of Earth System Science, Stanford University, Stanford, CA 94305, USA.
*Corresponding author. Email: arrigo@stanford.edu

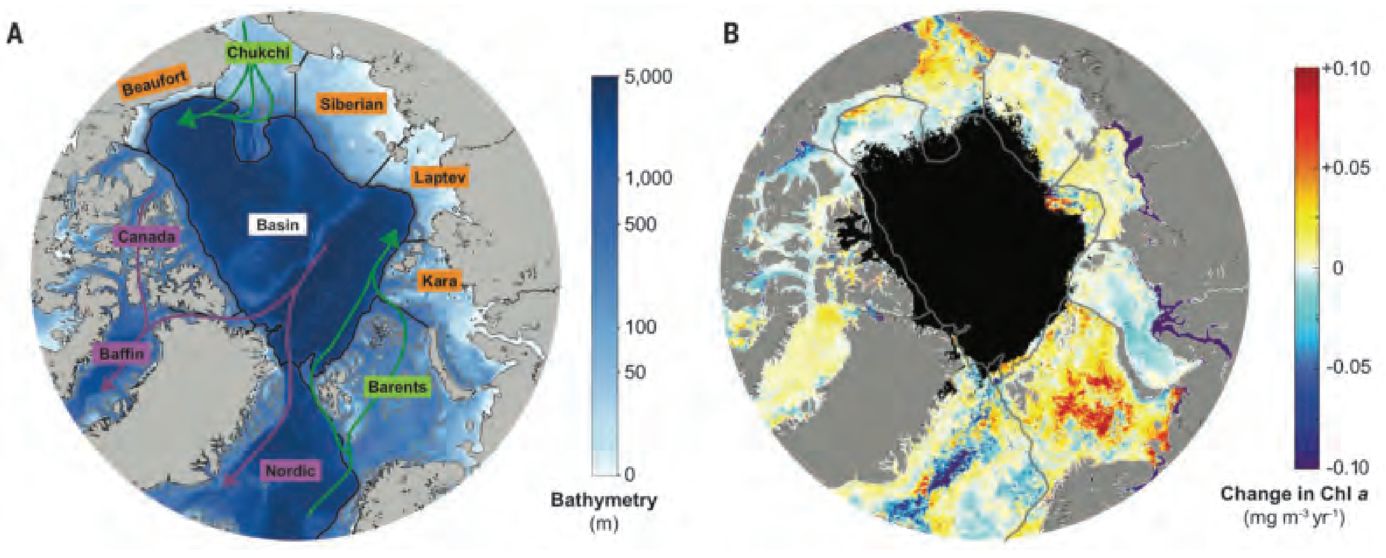

Fig. 1. Regions of interest and changes in phytoplankton biomass. (**A**) The AO with its shelf seas and basin. Subregions are bounded by black lines by using the 1000-m isobath and categorized as inflow (green), interior (orange), or outflow (purple) shelves. The 200-m isobath is shown in gray. Inflow and outflow currents are depicted as green and purple arrows, respectively. (**B**) The rate of change in Chl *a* (milligrams per cubic meter per year) between 1998 and 2018. Subregions are delineated by gray lines. Black pixels indicate no data.

Chukchi and Barents inflow shelves, where Chl *a* increased by 26 and 61%, respectively (Fig. 1B and Table 1). For both regions, three of the highest years of mean Chl *a* were measured in the past 4 years of the time series. Chl *a* also significantly increased in the smaller Baffin subregion (26%), with much of the increase occurring in recent years (Table 1). In all remaining subregions, Chl *a* showed no significant trend between 1998 and 2018 (Table 1). However, the slope of the Chl *a* trend in the shelf subregions shifted more positive between the first and second decades of the time series (Table 1). There were areas of intense increases in Chl *a* concentration along the shelf break of the interior seas, especially immediately north of the Beaufort, Laptev, and Barents shelf breaks (Fig. 1B).

Table 1. Time series trends. Regional time series trends for the AO and its subregions. Total percent change for the entire time series as well as slope of the regression (annual absolute change) for the entire time series (1998–2018), first decade (1998–2008), and the most recent decade (2009–2018) are shown. Values in parentheses for Chl *a* are rates of increase in the seasonal maximum Chl *a* concentrations, rather than the mean.

	1998–2018 (% change)	1998–2018 (change year^{-1})	1998–2008 (change year^{-1})	2009–2018 (change year^{-1})
OW area (km^2)				
Arctic	26.8*	58,952*	95,322*	31,961
Chukchi	30.0*	4545*	7387*	2666
Barents	24.4*	15,807*	26,184*	11,966
Siberian	63.6*	7604*	26,986*	1886
Laptev	20.7	1920	764	−4819
Kara	72.7*	8749*	12,722*	1366
Beaufort	21.7	788	650	−1174
Baffin	3.6	654	2721	−2355
Canada	7.4	944	−1286	−1000
Nordic	2.6	1990	277	8971*
Basin	123.1*	13,329*	19,567	6204
OW duration (days)				
Arctic	4.7	0.34	0.30	0.78
Chukchi	33.8*	1.77*	3.07*	3.70*
Barents	21.2*	3.34*	8.67*	0.58
Siberian	35.8*	1.22*	2.30	1.67
Laptev	61.7*	2.22*	2.29	−0.13
Kara	76.1*	3.18*	4.15*	−0.48
Beaufort	43.7*	2.18*	1.29	0.09
Baffin	4.5	0.32	1.23	−1.68
Canada	8.3	0.35	0.95	−0.85
Nordic	0.2	0.04	−0.20	0.02
Basin	0.0	0.00	1.09	1.52
Chl *a* (mg m^{-3})				
Arctic	21.5*	0.007*	−0.001	0.013 (0.052*)
Chukchi	26.2*	0.017*	−0.012	0.036 (0.387)
Barents	60.5*	0.022*	0.025	0.021 (0.061)
Siberian	−11.3	−0.003	−0.018*	0.003
Laptev	10.8	0.003	−0.003	0.001
Kara	−22.2*	−0.005*	−0.008	0.002
Beaufort	−17.0	−0.004	−0.008	0.001
Baffin	26.4*	0.005*	0.001	0.009
Canada	−8.7	−0.003	−0.010	0.005
Nordic	−9.8	−0.003	−0.022	0.019*
Basin	−15.3	−0.005	0.033	−0.052
Integrated production (Tg C year^{-1})				
Arctic	56.5*	6.79*	6.47*	8.39*
Chukchi	96.1*	1.06*	0.97	1.90*
Barents	87.6*	3.73*	4.45*	4.06*
Siberian	116.7*	0.37*	0.78*	0.44
Laptev	112.1*	0.26*	0.16	−0.02
Kara	100.2*	0.35*	0.54*	0.22
Beaufort	38.6*	0.05*	0.02	0.01
Baffin	26.3*	0.18*	0.17	−0.03
Canada	14.4	0.07	−0.08	0.02
Nordic	9.0	0.38	−1.22	2.66*
Basin	128.6*	0.37*	0.75*	−0.86

Continued to next page

	1998–2018 (% change)	1998–2018 (change year^{-1})	1998–2008 (change year^{-1})	2009–2018 (change year^{-1})
SST (°C)				
Arctic	13.4*	0.021*	0.021	0.040*
Chukchi	24.4	0.029	0.140	0.089
Barents	14.6*	0.027*	–0.009	0.083
Siberian	153.3	0.038	0.151	0.097*
Laptev	157.6*	0.078*	0.074	0.019
Kara	126.5*	0.085*	0.156*	0.041
Beaufort	68.7	0.074	0.111	–0.085
Baffin	47.4*	0.052*	0.073	–0.0120
Canada	78.4*	0.037*	0.051*	–0.033
Nordic	13.7*	0.029*	0.031	0.046
Basin	–40.8	–0.012	–0.013	0.006

*Significant trend; $P < 0.05$.

Since 1998, satellite-based NPP in the AO has increased by 57% (Fig. 2C and Table 1), far outpacing previously estimated rates (*2*–*4*, *6*). The most dramatic increases were on the eastern interior shelves (Siberian, Laptev, and Kara subregions), the inflow shelves (Chukchi and Barents subregions), and the Basin subregion (Table 1). The inflow shelves together contributed 70% of the AO NPP increase (Table 1), which is consistent with past studies that noted the importance of the Barents and Chukchi seas to AO NPP (*2*, *3*, *18*). A more modest yet statistically significant increase was seen on the western interior shelf (Beaufort subregion) (Table 1). The outflow shelves (Nordic, Canada, and Baffin subregions) exhibited the smallest percent increase in NPP, with the Nordic and Canada subregions showing no statistically significant trend (Table 1).

Historically, greater OW area and longer OW duration associated with sea ice decline have been the primary drivers of increased spatially integrated NPP across the AO (*2*–*5*). We found that although there were significant regional increases in OW duration (Table 1), there was no significant trend in OW duration across the entire AO, and OW duration was not a significant predictor of changes in AO NPP (Table 1). Although OW area significantly increased in the AO and most of its subregions (Table 1), these increases have slowed in recent years (Fig. 2A and Table 1). This recent deceleration in sea ice decline is likely due to internal climate variability temporarily masking human-induced changes (*19*). Regardless of the cause, although OW area explained 74% of the variance in AO NPP between 1998 and 2008 when sea ice was declining rapidly (Table 2), the relationship became less significant between 2009 and 2018, when rates of sea ice loss slowed, explaining only 20% of the variance in NPP (Table 2). This indicates that the recent increases in AO NPP were not driven by increases in OW area alone.

We found that increased Chl *a* explained 80% of variance in AO NPP between 2009 and 2018 compared with only 26% during the previous decade, when changes in OW area controlled the trend in NPP (Table 2). Within the Barents subregion, which contributed more than any other region to AO NPP, significant increases in Chl *a* since 1998 sustained greater NPP despite the slowing of OW expansion (Table 1). Clearly, changes in phytoplankton biomass over the past decade were largely responsible for the sustained increase in NPP across the AO (Fig. 2C), particularly in the inflow shelves (Fig. 1B), despite the slowing of sea ice loss.

There are a few possible causes for the observed increase in phytoplankton Chl *a* over the past decade. Photoacclimation can lead to altered cellular Chl *a* concentrations, but incident light, mixed-layer depth, and light attenuation within the water column did not change sufficiently during our study period to significantly alter C:Chl *a* ratios in areas where Chl *a* increased (fig. S1), so this possibility can be eliminated. Earlier phytoplankton blooms (*4*) could intensify the mismatch between grazing and phytoplankton growth, resulting in higher Chl *a* concentrations in recent years. However, this possibility is diminished by annual changes in Chl *a* being the same in spring (April through June) as they were in summer (July through September) (fig. S2), when grazing rates would be expected to be highest. Interannual variability in atmospheric factors such as cloud cover (fig. S3), the state of the North Atlantic Oscillation and AO (fig. S4), wind speed (fig. S5), and the number of upwelling-favorable wind days per year (fig. S6) were also unrelated to the measured increases in Chl *a*.

In the AO, nitrogen availability limits maximum phytoplankton biomass (*7*), so the increases in Chl *a* being restricted to the inflow shelves and to the central Arctic, where sea ice had receded back from the shelf break, points to nutrients playing a role. This is supported by seasonal maximum Chl *a* concentrations, which would be especially sensitive to additional nutrient input, having increased at more than three times the rate of mean Chl *a* concentrations from 2009 to 2018 in the AO and the Barents and Chukchi seas (Table 1). Increased advection of Atlantic Ocean waters into the Barents Sea (*20*) and Pacific Ocean waters into the Chukchi Sea (*21*) may supply enough additional nutrients to sustain the higher biomass observed on these inflow shelves (Fig. 1B and Table 2). The Pacific inflow through the Bering Strait, which provides most of the nutrients that fuel Chukchi Sea summer blooms (*22*), has increased by ~50% from 1999 to 2015 (*21*). The "Atlantification" of the Barents Sea may be associated with increased advection of phytoplankton and nutrients (*19*, *23*–*26*). In addition, the incoming warm Atlantic water reduces stratification, which has not increased since 1979 (*27*), and promotes vertical mixing (*28*) that increases nutrient availability to sustain substantial increases of phytoplankton biomass and production (*18*). Last, decreased sea ice cover and increased frequency and intensity of storms at high latitudes (*10*) result in episodic nutrient injections from the historically inaccessible deep water beneath the pycnocline through increased internal wave mixing (*11*) and storm-induced upwelling (*5*, *28*, *29*) throughout the shallow shelves. Increased Chl *a* along the interior shelf break (Fig. 1B) may be fueled by upwelling events that pull "new" nutrients from deep basin reservoirs into the nutrient-depleted upper euphotic zone and that are increasingly common

Table 2. Relative importance in predicting AO NPP. Multiple linear regression parameter estimates (± standard error) for the intercept (teragrams of carbon per year), OW area (ratio of teragrams of carbon per year to square kilometer), and Chl *a* concentration (ratio of teragrams of carbon per year to milligrams Chl *a* per cubic meter) in explaining the variance in mean annual NPP (teragrams of carbon per year) across the AO for entire time series (1998–2018), first decade (1998–2008), and the most recent decade (2009–2018).

	Parameter	Estimate β	*P* value	Relative importance (%)
Entire time series	Intercept	–247.7 ± 36.4		
Coefficient of determination (R^2) = 0.931	OW area	$6.92 \times 10^{-5} \pm 6.88 \times 10^{-6}$	<0.01	57.27
	Chl *a*	301.1 ± 37.09	<0.01	42.73
1998–2008	Intercept	–139.7 ± 58.43		
R^2 = 0.865	OW area	$6.10 \times 10^{-5} \pm 9.52 \times 10^{-6}$	<0.01	74.45
	Chl *a*	191.8 ± 47.9	<0.01	25.55
2009–2018	Intercept	–195 ± 69.84		
R^2 = 0.933	OW area	$4.86 \times 10^{-5} \pm 1.22 \times 10^{-5}$	<0.01	19.95
	Chl *a*	381.5 ± 4.28	<0.01	80.05

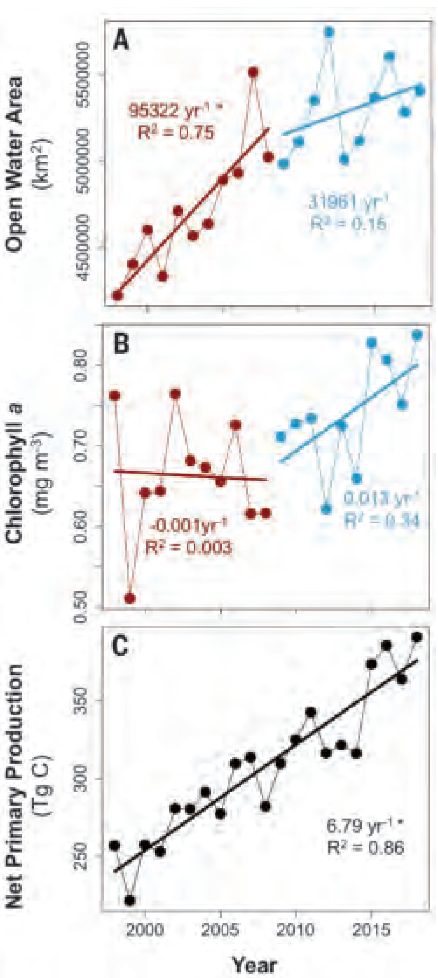

Fig. 2. AO time series trends. (**A** to **C**) Annual time series of AO (A) mean OW area, (B) mean Chl *a*, and (C) NPP. Results from regression analysis for the entire (1998–2018), early (1998–2008), and recent (2009–2018) parts of the time series are in black, red, and blue, respectively, with significant trends ($P < 0.05$) indicated by an asterisk.

now that the ice edge regularly retreats north of the shelf break (*12*, *13*, *30*) and storms have become more frequent and intense (*31*).

Despite substantial sea ice loss, there are still regions of the AO, including much of the interior and outflow shelves, where there was either no change or a decline in Chl *a* concentration between 1998 and 2018. Apart from the few areas of the shelf break where Chl *a* was enhanced, Chl *a* generally declined across most of the interior shelves (Fig. 1B and Table 1). These waters receive large volumes of low-nutrient and highly turbid river runoff (*30*, *32*), which suppresses NPP across the interior shelves (*30*). For example, the Kara subregion, which exhibited a significant 22% decline in Chl *a* (Fig. 1B and Table 1), has received an increasing amount of discharge from two of the three largest AO rivers (the Yenisey and the Ob) (*32*) that has been documented to suppress NPP on the Kara shelf (*33*). Similarly, the outflow and interior shelves may receive increasingly nutrient-depleted surface water from upstream consumption by phytoplankton on the productive inflow shelves, resulting in a decline in NPP downstream (*2*).

Previously, it was unclear whether NPP increases in the AO, which were linked only to increases in OW area and duration, were sustained by new or recycled nutrients (*2*, *3*). Our study documents sustained increases in NPP between 1998 and 2018 that are no longer being driven by increased OW area and duration alone; increased phytoplankton concentration is playing an increasingly important role. These biomass increases must be sustained by a larger supply of new nutrients to the system. To the extent that increases in new nutrient availability are driven by processes associated with anthropogenic climate change, the future AO may become not only more productive but also more able to support additional higher trophic-level production and carbon export (*34*).

REFERENCES AND NOTES

1. T. F. Stocker *et al.*, Eds., *Climate Change 2013: The Physical Science Basis. Contribution of Working Group I to the Fifth Assessment Report of the Intergovernmental Panel on Climate Change* (Cambridge Univ. Press, 2013).
2. K. R. Arrigo, G. L. van Dijken, *Prog. Oceanogr.* **136**, 60–70 (2015).
3. K. R. Arrigo, G. L. van Dijken, *J. Geophys. Res.* **116** (C9), C09011 (2011).
4. M. Kahru, V. Brotas, M. Manzano-Sarabia, B. G. Mitchell, *Glob. Change Biol.* **17**, 1733–1739 (2011).
5. J. Zhang *et al.*, *J. Geophys. Res.* **115** (C10), C10015 (2010).
6. S. Bélanger, M. Babin, J.-É. Tremblay, *Biogeosciences* **10**, 4087–4101 (2013).
7. J.-É. Tremblay, J. Gagnon, in *Influence of Climate Change on the Changing Arctic and Sub-Arctic Conditions* (Springer, 2009).
8. A. Nummelin, M. Ilicak, C. Li, L. H. Smedsrud, *J. Geophys. Res. Oceans* **121**, 617–637 (2016).
9. F. A. McLaughlin, E. C. Carmack, *Geophys. Res. Lett.* **37**, L24602 (2010).
10. X. Zhang, J. E. Walsh, J. Zhang, U. S. Bhatt, M. Ikeda, *J. Clim.* **17**, 2300–2317 (2004).
11. L. Rainville, R. A. Woodgate, *Geophys. Res. Lett.* **36**, L23604 (2009).
12. E. Carmack, D. C. Chapman, *Geophys. Res. Lett.* **30**, 1778 (2003).
13. J.-É. Tremblay *et al.*, *Geophys. Res. Lett.* **38**, L18604 (2011).
14. K. R. Arrigo, G. L. van Dijken, S. Bushinsky, *J. Geophys. Res.* **113** (C8), C08004 (2008).
15. K. M. Lewis, B. G. Mitchell, G. L. van Dijken, K. R. Arrigo, *Deep Sea Res. Part II Top. Stud. Oceanogr.* **130**, 14–27 (2016).
16. A. Matsuoka, Y. Huot, K. Shimada, S.-I. Saitoh, M. Babin, *Can. J. Rem. Sens.* **33**, 503–518 (2007).
17. K. M. Lewis, K. R. Arrigo, *J. Geophys. Res.* **125**, e2019JC015706 (2020).
18. L. Oziel *et al.*, *J. Geophys. Res.* **122**, 5121–5139 (2017).
19. N. C. Swart, J. C. Fyfe, E. Hawkins, J. E. Kay, A. Jahn, *Nat. Clim. Chang.* **5**, 86–89 (2015).
20. M. Årthun, T. Eldevik, L. H. Smedsrud, Ø. Skagseth, R. B. Ingvaldsen, *J. Clim.* **25**, 4736–4743 (2012).
21. R. A. Woodgate, *Prog. Oceanogr.* **160**, 124–154 (2018).
22. K. E. Lowry *et al.*, *Deep Sea Res. Part II Top. Stud. Oceanogr.* **118**, 53–72 (2015).
23. G. J. Hunt Jr. *et al.*, *Prog. Oceanogr.* **149**, 40–81 (2016).
24. L. Oziel *et al.*, *Nat. Commun.* **11**, 1705 (2020).
25. A. Randelhoff *et al.*, *Front. Mar. Sci.* **5**, 224 (2018).
26. M. Vernet *et al.*, *Front. Mar. Sci.* **6**, 583 (2019).

27. R. Yamaguchi, T. Suga, *J. Geophys. Res. Oceans* **124**, 8933–8948 (2019).
28. S. Lind, R. B. Ingvaldsen, T. Furevik, *Nat. Clim. Chang.* **8**, 634–639 (2018).
29. J. Yang, J. Comiso, D. Walsh, R. Krishfield, S. Honjo, *J. Geophys. Res.* **109** (C4), C04008 (2004).
30. W. J. Williams, E. C. Carmack, *Prog. Oceanogr.* **139**, 24–41 (2015).
31. R. S. Pickart *et al.*, *Deep Sea Res. Part I Oceanogr. Res. Pap.* **79**, 106–121 (2013).
32. A. Wagner, G. Lohmann, M. Prange, *Global Planet. Change* **79**, 48–60 (2011).
33. D. O. Hessen *et al.*, *Estuar. Coast. Shelf Sci.* **88**, 53–62 (2010).
34. R. W. Eppley, B. J. Peterson, *Nature* **282**, 677–680 (1979).
35. K. Lewis, G. van Dijken, K. Arrigo, Bio-optical Database of the Arctic Ocean. Dryad (2020).

ACKNOWLEDGMENTS

The authors thank M. Ardyna and M. M. Mills for their constructive comments on initial versions of the manuscript. **Funding:** This work is supported by NASA Earth and Space Science Fellowship grant NNX16AO08H awarded to K.M.L., NASA Earth and Space Science Fellowship grant RR175-257-4945576 awarded to K.R.A., and National Science Foundation grant 1304563 awarded to K.R.A. **Author contributions:** K.M.L. was responsible for formal analysis, funding acquisition, investigation, and writing (original draft). G.L.v.D. was responsible for data curation, investigation, software, formal analysis, and writing (reviewing and editing). K.R.A. was responsible for conceptualization, investigation, supervision, and writing (reviewing and editing). **Competing interests:** The authors have no competing interests. **Data and materials availability:** Bio-optical data used to develop the Arctic Chl *a* algorithm as well as time series data for Chl *a*, NPP, SST, OW area, and OW duration can be found on the Dryad data repository (*35*).

SUPPLEMENTARY MATERIALS

science.sciencemag.org/content/369/6500/198/suppl/DC1
Materials and Methods
Supplementary Text
Figs. S1 to S6
References (*36–44*)

24 July 2019; accepted 15 May 2020
10.1126/science.aay8380

IMMUNODEFICIENCIES

HEM1 deficiency disrupts mTORC2 and F-actin control in inherited immunodysregulatory disease

Sarah A. Cook[1]*, William A. Comrie[1,2]*, M. Cecilia Poli[3,4,5], Morgan Similuk[6], Andrew J. Oler[7], Aiman J. Faruqi[1], Douglas B. Kuhns[8], Sheng Yang[9], Alexander Vargas-Hernández[3,4], Alexandre F. Carisey[3,4], Benjamin Fournier[10,11], D. Eric Anderson[12], Susan Price[13], Margery Smelkinson[14], Wadih Abou Chahla[15], Lisa R. Forbes[3,4], Emily M. Mace[16], Tram N. Cao[3,4], Zeynep H. Coban-Akdemir[17,18], Shalini N. Jhangiani[18,19], Donna M. Muzny[18,19], Richard A. Gibbs[17,18,19], James R. Lupski[17,18,19], Jordan S. Orange[16], Geoffrey D. E. Cuvelier[20], Moza Al Hassani[21], Nawal Al Kaabi[21], Zain Al Yafei[21], Soma Jyonouchi[22,23], Nikita Raje[24,25], Jason W. Caldwell[26], Yanping Huang[27,28], Janis K. Burkhardt[27], Sylvain Latour[10,11], Baoyu Chen[9], Gehad ElGhazali[21], V. Koneti Rao[13], Ivan K. Chinn[3,4], Michael J. Lenardo[1]†

Immunodeficiency often coincides with hyperactive immune disorders such as autoimmunity, lymphoproliferation, or atopy, but this coincidence is rarely understood on a molecular level. We describe five patients from four families with immunodeficiency coupled with atopy, lymphoproliferation, and cytokine overproduction harboring mutations in *NCKAP1L*, which encodes the hematopoietic-specific HEM1 protein. These mutations cause the loss of the HEM1 protein and the WAVE regulatory complex (WRC) or disrupt binding to the WRC regulator, Arf1, thereby impairing actin polymerization, synapse formation, and immune cell migration. Diminished cortical actin networks caused by WRC loss led to uncontrolled cytokine release and immune hyperresponsiveness. HEM1 loss also blocked mechanistic target of rapamycin complex 2 (mTORC2)–dependent AKT phosphorylation, T cell proliferation, and selected effector functions, leading to immunodeficiency. Thus, the evolutionarily conserved HEM1 protein simultaneously regulates filamentous actin (F-actin) and mTORC2 signaling to achieve equipoise in immune responses.

Inborn errors of immunity (IEIs) can affect global cellular regulatory systems (*1*). The mechanistic target of rapamycin complex 1 (mTORC1) and mTORC2 are global regulators of metabolism and cell signaling. mTORC2, comprising the mTOR, RICTOR, mSIN1, mLST8, PROTOR1 and PROTOR2 (PROTOR1/2), and DEPTOR proteins, activates AGC kinases downstream of phosphoinositide 3-kinase (PI3K) to promote T cell survival, proliferation, and differentiation (*2–5*). Similarly, actin is a global regulator of cellular behavior and immune synapse (IS) formation (*6*, *7*). Signals activating the WAVE regulatory complex (WRC), which contains CYFIP1/2, HEM1/2, ABI1/2/3, HSPC300, and WAVE1/2/3, control the dynamics of Arp2/3-mediated branched filamentous actin (F-actin) nucleation and polymerization. In the WRC, HEM1/2 and CYFIP1/2 form a membrane-associated scaffold supporting the ABI1/2, HSPC300, and WAVE1/2/3 proteins and are directly activated by the small guanosine triphosphatases (GTPases) Rac1 and Arf1, although the Arf1 binding site is uncertain (*8*, *9*) (Fig. 1). Whether the WRC regulates the cortical actin network (CAcN) is unknown (*6–12*). Mutations affecting actin regulatory proteins underlie immunodeficiencies (table S1), but none have been reported yet for WRC components (*13*).

We investigated five patients from four unrelated families with recurrent bacterial and viral skin infections, severe respiratory tract infections leading to pneumonia and bronchiectasis (Fig. 1, A and B, left panels, and fig. S1A), and poor specific antibody responses (Fig. 1B, right panel, and table S2). Paradoxically, these patients also exhibited atopic and inflammatory disease alongside chronic hepatosplenomegaly and lymphadenopathy, sometimes with elevated immunoglobulin E (IgE) or IgG and autoimmune manifestations (Fig. 1B; fig. S1, B and C; and tables S2 and S3). FoxP3$^+$ T regulatory cells were normal (fig. S1D). All

[1]Molecular Development of the Immune System Section, Laboratory of Immune System Biology, and Clinical Genomics Program, National Institute of Allergy and Infectious Diseases (NIAID), National Institutes of Health (NIH), Bethesda, MD, USA. [2]Neomics Pharmaceuticals, LLC, Gaithersburg, MD, USA. [3]Department of Pediatrics, Baylor College of Medicine, Houston, TX, USA. [4]Section of Pediatric Immunology, Allergy, and Retrovirology, Texas Children's Hospital, Houston, TX, USA. [5]Program of Immunogenetics and Translational Immunology, Instituto de Ciencias e Innovación en Medicina, Facultad de Medicina, Clínica Alemana–Universidad del Desarrollo, Santiago, Chile. [6]Division of Intramural Research, NIAID, NIH, Bethesda, MD, USA. [7]Bioinformatics and Computational Biosciences Branch, Office of Cyber Infrastructure and Computational Biology, NIAID, NIH, Bethesda, MD, USA. [8]Neutrophil Monitoring Laboratory, Leidos Biomedical Research, Inc., Frederick National Laboratory for Cancer Research, Frederick, MD, USA. [9]Roy J. Carver Department of Biochemistry, Biophysics and Molecular Biology, Iowa State University, Ames, IA, USA. [10]Laboratory of Lymphocyte Activation and Susceptibility to EBV, INSERM UMR 1163, Paris, France. [11]University Paris Descartes Sorbonne Paris Cité, Institut des Maladies Génétiques-IMAGINE, Paris, France. [12]Advanced Mass Spectrometry Facility, National Institute of Diabetes and Digestive and Kidney Diseases (NIDDK), NIH, Bethesda, MD, USA. [13]Laboratory of Clinical Immunology and Microbiology, NIAID, NIH, Bethesda, MD, USA. [14]Biological Imaging Section, Research Technologies Branch, NIAID, NIH, Bethesda, MD, USA. [15]Department of Pediatric Hematology, Jeanne de Flandre Hospital, Centre Hospitalier Universitaire (CHU), Lille, France. [16]Department of Pediatrics, Columbia University Irving Medical Center, New York, NY, USA. [17]Baylor-Hopkins Center for Mendelian Genomics, Houston, TX, USA. [18]Department of Molecular and Human Genetics, Baylor College of Medicine, Houston, TX, USA. [19]Human Genome Sequencing Center, Baylor College of Medicine, Houston, TX, USA. [20]Section of Pediatric Hematology/Oncology/BMT, CancerCare Manitoba, University of Manitoba, Winnipeg, MB, Canada. [21]Sheikh Khalifa Medical City, Abu Dhabi Healthcare Company (SEHA), Abu Dhabi, United Arab Emirates. [22]Division of Allergy and Immunology, Children's Hospital of Philadelphia, Philadelphia, PA, USA. [23]Perelman School of Medicine, University of Pennsylvania, Philadelphia, PA, USA. [24]Division of Allergy, Immunology, Pulmonary, and Sleep Medicine, Children's Mercy Hospital, Kansas City, MO, USA. [25]Department of Internal Medicine and Pediatrics, University of Missouri Kansas City, Kansas City, MO, USA. [26]Section of Pulmonary, Critical Care, Allergy and Immunological Diseases, Wake Forest University School of Medicine, Winston-Salem, NC, USA. [27]Department of Pathology and Laboratory Medicine, Children's Hospital of Philadelphia Research Institute and Perelman School of Medicine, University of Pennsylvania, Philadelphia, PA, USA. [28]Department of Pathology, Anatomy, and Cell Biology, Thomas Jefferson University, Philadelphia, PA, USA.
*These authors contributed equally to this work.
†Corresponding author. Email: lenardo@nih.gov

five patients harbored biallelic *NCKAP1L* mutations encoding missense variants in HEM1, the hematopoietic-specific member of the WRC (Fig. 1, A and C, and table S4). The amino acid substitutions affected conserved residues that were not homozygous in the Genome Aggregation Database (gnomAD) or internal databases and were bioinformatically predicted to be damaging (fig. S2, A and B) (*14*). The altered residues clustered within the quaternary structure of the WRC near the distal Rac1-binding site located on CYFIP1/2 (fig. S2, A to D), which we call the HEM1 regulatory site (HRS). The human immune phenotype differs from the lymphopenia, neutrophilia, or bone marrow failure observed in HEM1-deficient mice (*12*, *15*, *16*).

Biochemical analyses showed that patients 1.1, 2.1, 2.2, and 4.1 lost HEM1, CYFIP1, and WAVE2, which indicates WRC destabilization, whereas patient 3.1 expressed normal levels of WRC proteins (Fig. 1D and fig. S3, A to C). Moreover, the HEM1 substitutions in patients 1.1 and 2.1, but not in patient 3.1, reduced affinity for WAVE2 (Fig. 1E and fig. S3D). The WRC could be restored in *NCKAP1L* CRISPR-Cas9 knockout (HEM1-KO) Jurkat cells by wild-type and patient 3.1 HEM1 but less so by the patient 1.1 and 2.1 variants (fig. S3E). Immunoprecipitation–mass spectrometry (IP-MS) showed that the Met^{371}→Val (M371V) HEM1 variant (patient 3.1) maintained association with HEM1- and WAVE2-interacting proteins (fig. S4 and table S5). We therefore hypothesized that M371V disrupted the activation by either Rac1 or Arf1, the small GTPases that activate the WRC. By reconstituting the WRC in vitro with recombinant proteins (containing HEM2 with the equivalent M373V substitution, but not HEM1, which had an insufficient yield), we observed that the HEM2-M373V protein interacted poorly with GST-Arf1 and could not promote F-actin polymerization upon stimulation with an Arf1-Rac1 dimer (Fig. 1F and fig. S3, F to H). Thus, the Met$^{371/373}$ residues located in the HRS of HEM1/2 are crucial for Arf1 binding and WRC activation, which is analogous to binding of Rac1 to CYFIP1/2 (*8*). Therefore, the patient HEM1 mutants either destabilize the WRC or disrupt its Arf1-mediated activation (fig. S2E).

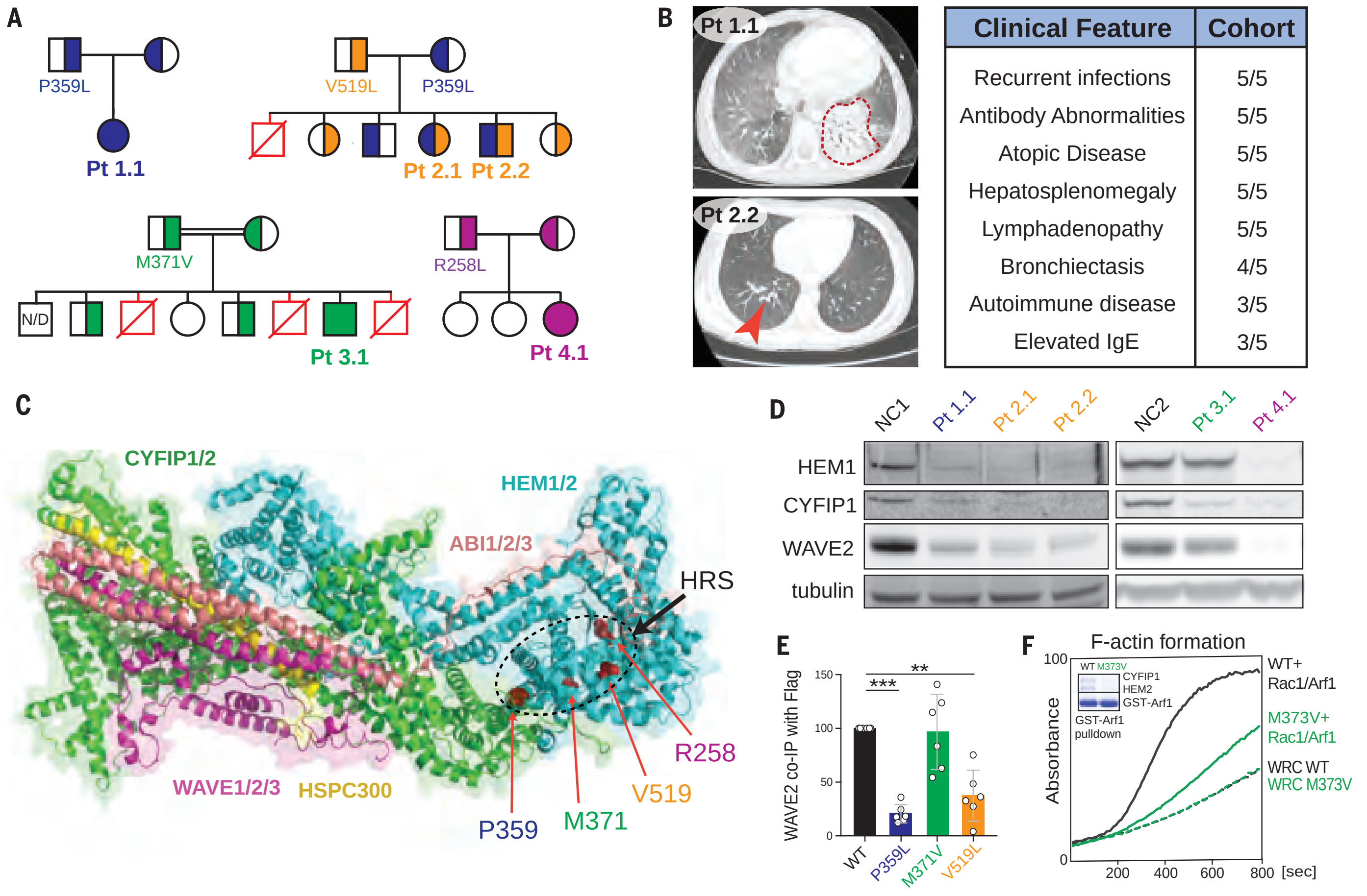

Clinical Feature	Cohort
Recurrent infections	5/5
Antibody Abnormalities	5/5
Atopic Disease	5/5
Hepatosplenomegaly	5/5
Lymphadenopathy	5/5
Bronchiectasis	4/5
Autoimmune disease	3/5
Elevated IgE	3/5

Fig. 1. Immunodysregulatory disorder caused by genetic HEM1 deficiency. (**A**) Patient (Pt) pedigrees showing recessive inheritance of disease and HEM1 amino acid substitutions. Red symbols indicate deceased affected siblings of unknown genotype. N/D, not determined. (**B**) Chest computed tomography (CT) scans showing ground glass opacity and pneumonia (red outline) in Pt 1.1 (upper left) and bronchiectasis (red arrow) in Pt 2.2 (bottom left). Key shared clinical features are also noted (right). (**C**) Structural location of patient variants in HEM1 in the WRC (Protein Data Bank: 3P8C; PubMed ID: 21107423). HRS, HEM1 regulatory site. (**D**) Immunoblot of WRC components in lysates derived from Pt and normal control (NC) CD4$^+$ (left) and CD8$^+$ (right) T cell blasts. (**E**) Quantification of WAVE2 coimmunoprecipitated (co-IP) by wild-type (WT) or mutant HEM1-Flag constructs in six independent experiments. Statistical analysis was performed using a one-sample *t* test. (**F**) Pyrene-actin polymerization assay with WRC230VCA containing HEM2 WT or M373V, with or without activation by a Rac1-Arf1 heterodimer preloaded with GMPPNP. (Inset) Coomassie blue–stained gel showing GST-Arf1 pull-down of WRC230VCA containing HEM2 WT or M373V and Rac1 (Q61L/P29S). Data are representative of four independent experiments. $^{**}P \leq 0.01$; $^{***}P \leq 0.001$. Single-letter abbreviations for the amino acid residues are as follows: A, Ala; C, Cys; D, Asp; E, Glu; F, Phe; G, Gly; H, His; I, Ile; K, Lys; L, Leu; M, Met; N, Asn; P, Pro; Q, Gln; R, Arg; S, Ser; T, Thr; V, Val; W, Trp; and Y, Tyr.

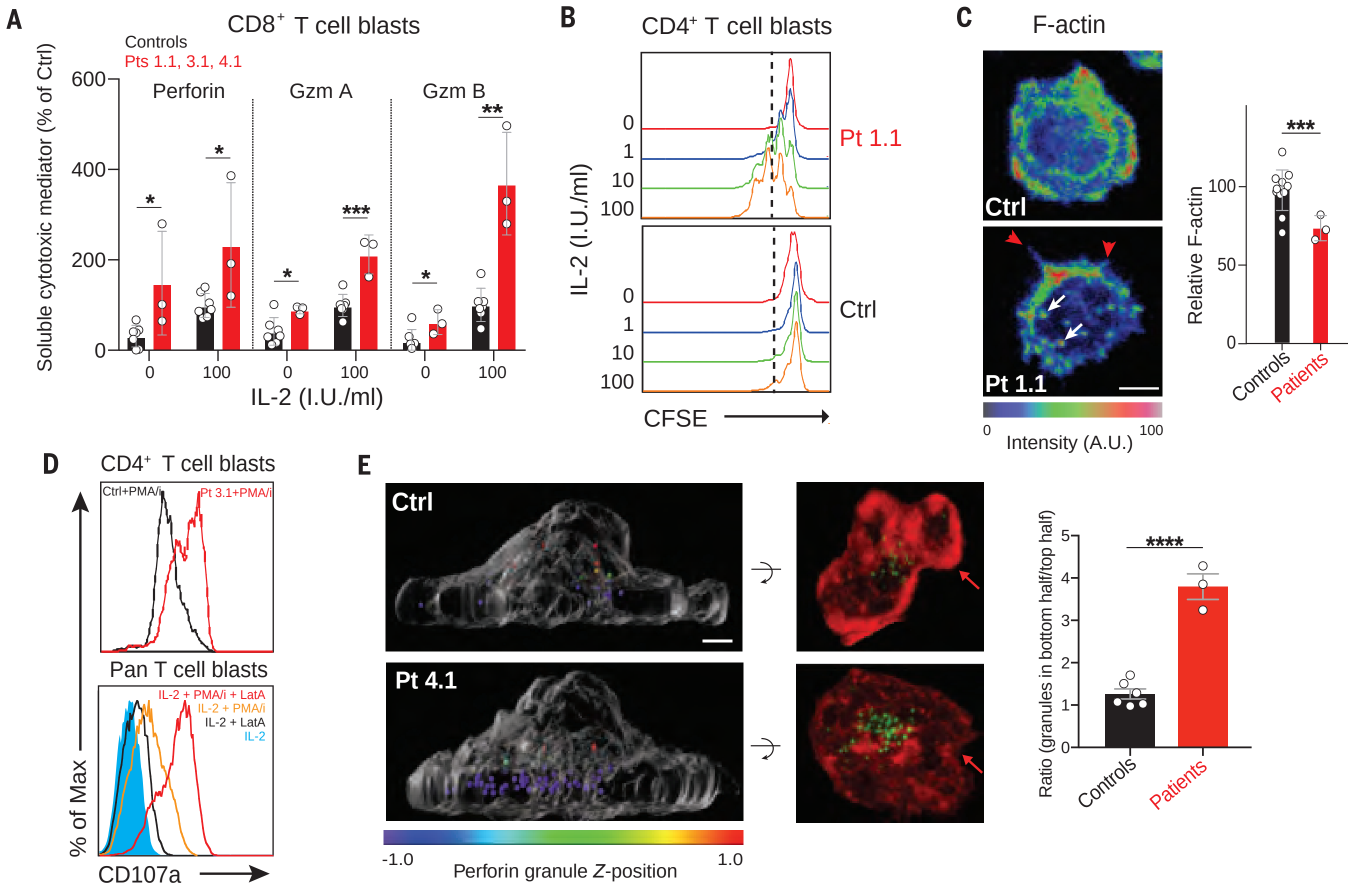

Fig. 2. HEM1 is essential for regulating cortical actin and granule release. (**A**) Release of granzymes (Gzm) A and B or perforin from Pt or control (Ctrl) CD8$^+$ T cell blasts after 18 hours of IL-2 stimulation in international units (I.U.) in three independent experiments. (**B**) Flow cytometric histograms measuring proliferation of rested CD4$^+$ T cell blasts from a normal control (Ctrl) or patient 1.1 (Pt 1.1) measured by carboxyfluorescein succinimidyl ester (CFSE) dilution after IL-2 restimulation for 96 hours. (**C**) (Left) Ctrl or Pt 1.1 CD4$^+$ T cell blasts spreading on coverslips coated with anti-CD3, anti-CD28, and ICAM-1 (1 μg/ml each), stained with phalloidin, and pseudocolored for F-actin. (Right) F-actin was quantified in three experiments. Red arrows indicate formin-mediated spikes, and white arrows indicate WASp-mediated actin puncta. Scale bar, 4 μm. (**D**) Surface CD107a on Ctrl and Pt 3.1 CD4$^+$ T cell blasts after 1 hour of phorbol myristate acetate (PMA)/ionomycin (I) stimulation (top) or stimulated pan T cells with 1 μM latrunculin A (LatA) (bottom). (**E**) (Left) Side view of perforin granules pseudocolored by *Z*-position relative to the cell center in Ctrl or Pt 1.1 CD8$^+$ T cell blasts. (Middle) Corresponding 90° forward rotation top views of F-actin (red) and perforin (green). Red arrows indicate lamellipodial F-actin density. Scale bar, 2 μm. (Right) Mean ratios of granules in the bottom half to top half of the cell, quantified in at least 30 cells per sample. Bars represent means ± SEM (control, *n* = 6; patient, *n* = 3). Data represent at least three repeat experiments. Statistical analyses for (A), (C), and (E) were performed using a *t* test without assuming equal variance. *$P \le 0.05$; **$P \le 0.01$; ***$P \le 0.001$; ****$P \le 0.0001$.

We observed that interleukin-2 (IL-2) stimulation caused patient and HEM1-knockdown cells to hypersecrete perforin and granzymes and hyperproliferate in response to IL-2 (Fig. 2, A and B, and fig. S5, A, B, and E). Proximal IL-2 signaling was normal, which implies that downstream processes, such as CAcN control of granule release, might have been affected (fig. S6) (*17*–*19*). We found evidence for an abnormal CAcN because patient cells displayed reduced cortical F-actin and aberrant membrane spikes and puncta caused by unregulated formin and WASp, respectively (Fig. 2C and movie S1) (*20*). We also observed defective cell spreading and lamellipodia (fig. S5C). Patient T cells expressed higher levels of surface CD107a (LAMP1), which indicates increased granule membrane fusion, especially after phorbol myristate acetate and ionomycin–induced degranulation (Fig. 2D and fig. S5D). Experimental reduction of HEM1 in primary T cells and NKL cells also increased the release of cytokines and granule contents, CD107a expression, or both (fig. S5, E to H). Three-dimensional imaging revealed a diminished CAcN and a notable accumulation of lytic granules at the IS of patient cells (Fig. 2E). Latrunculin A (LatA), which depolymerizes F-actin, increased exocytosis-based CD107a surface expression and the release of granzymes A and B in a dose-dependent manner (Fig. 2D, bottom, and fig. S5, I and J). Thus, the WRC containing HEM1 enables the CAcN to restrain excessive degranulation and granule release by T cells. Constitutive cytokine release was blocked by a Jak inhibitor (fig. S5E).

We next explored other F-actin functions using live-cell imaging of the T cell IS and found that patient cells and HEM1-KO Jurkat cells reconstituted with mutant HEM1 alleles cannot form symmetrical and stable synaptic contacts with the coverslip (movies S1 and S2) (*20*). We also observed abnormal formin spikes, WASp-mediated puncta, and defective lamellipodia. Because lamellipodia guide cell migration, we evaluated spontaneous T cell and neutrophil migration (*21*, *22*). We found that patient T cells exhibited defective membrane ruffling; loss of lamellipodial extensions; decreased F-actin density at the leading edge with abnormal puncta, spikes, and blebs; and reduced migratory

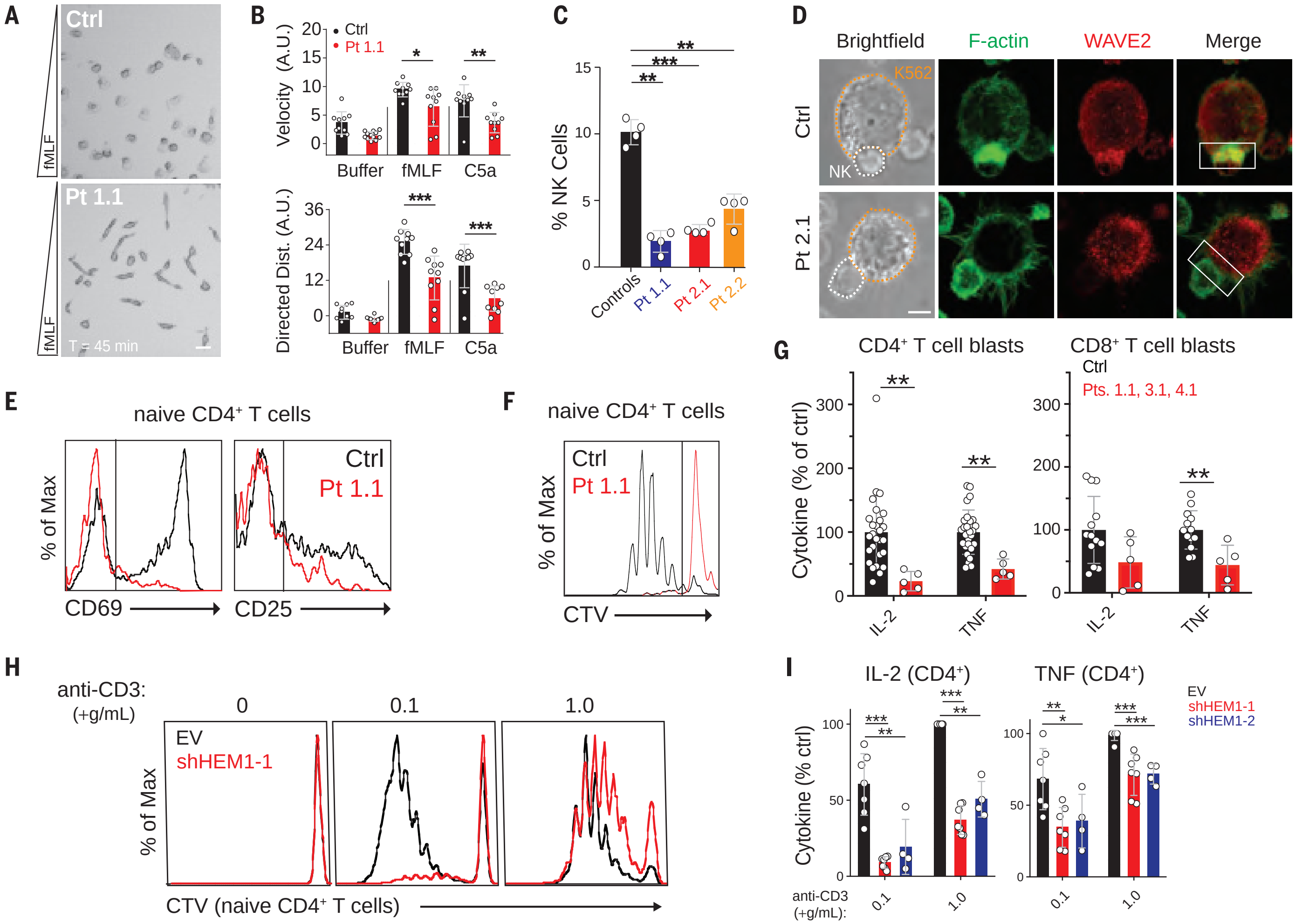

Fig. 3. HEM1 loss causes immunodeficiency by abnormal immune cell behavior and activation. (**A**) Single frame from movie S4 showing healthy Ctrl or Pt 1.1 neutrophils migrating in a gradient (bottom has the greatest concentration) of N-formyl-L-methionyl-L-leucyl-L-phenylalanine (fMLF). Scale bar, 20 μm. (**B**) Displacement velocity (top) and net directed distance (Dist.) (bottom) in arbitrary units (A.U.) of 10 randomly selected Ctrl or Pt 1.1 neutrophils migrating in chemoattractant gradients. (**C**) Percentage of NK cells in four peripheral blood samples. (**D**) Photomicrographs of immunological synapses between K562 target cells (orange outline) and NK cells (white outline) stained with phalloidin for F-actin and WAVE2 antibody. White boxes indicate area of synapse. Scale bar, 5 μm. (**E**) CD69 and CD25 up-regulation on Ctrl or Pt 1.1 naïve CD4$^+$ T cells after stimulation with immobilized anti-CD3/28 (1 μg/ml each). Max, maximum. (**F**) Cell trace violet (CTV) proliferation plots of cells as in (E), stimulated for 5 days. (**G**) IL-2 and TNF secretion by CD4$^+$ or CD8$^+$ T cell blasts after restimulation for 36 hours with immobilized anti-CD3/28 and ICAM-1 (1 μg/ml each) in three independent experiments. (**H**) CTV plots of naive CD4$^+$ T cells transduced with empty vector (EV) or small hairpin RNA against HEM1 (sh-HEM1), stimulated on immobilized ICAM-1/anti-CD28 (1 μg/ml each) and the indicated dose of anti-CD3. (**I**) IL-2 and TNF secretion by CD4$^+$ T cell blasts transduced with EV, sh-HEM1-1, or sh-HEM1-2 and stimulated as in (H). Neutrophil migration was analyzed for two independent donors; otherwise, data represent at least four independent trials of each assay. Statistical analyses for (B), (C), and (G) were performed using a *t* test without assuming equal variance. Statistical analysis for (I) was performed using a Wilcoxon matched-pairs signed-rank test. *$P \le 0.05$; **$P \le 0.01$; ***$P \le 0.001$.

velocity (fig. S7, A and B, and movie S3). Similarly, patient neutrophils migrating in chemokine gradients exhibited reduced velocity and directional persistence, unusual elongation, and misdirected competing leading edges (Fig. 3, A and B; movie S4; and fig. S7C). In patients for whom we had sufficient samples, we found decreased natural killer (NK) cell abundance along with defective F-actin accumulation at the IS and a corresponding defect in conjugate formation (Fig. 3, C and D, and fig. S7E). Additionally, HEM1-KO NKL clones displayed reduced effector function after stimulation (fig. S7, F and G).

We also found abnormal T cell activation manifested by reduced CD69 and CD25 expression, blunted proliferation, and decreased IL-2 and tumor necrosis factor (TNF) production (Fig. 3, E to G, and fig. S9, A and B). Additionally, patient T cells had defective integrin activation with lower soluble ICAM-1 binding, though adherence to immobilized ICAM-1 was largely intact, which indicates a defect in integrin affinity maturation. Notably, we found that CD8$^+$ T cell cytotoxicity and the release of granzyme A, granzyme B, and perforin were normal (fig. S8, A to C, and fig. S9, C and D) (*21*, *23*, *24*). Proliferation and cytokine defects were recapitulated by short hairpin RNA (shRNA) knockdown of HEM1 (Fig. 3, H and I).

Despite the IS abnormalities, proximal T cell receptor (TCR) signaling events in HEM1-deficient patient cells were normal (fig. S10, A to C) (*21*). Nevertheless, we found that both patient and HEM1-knockdown T cells showed

defective TCR-induced phosphorylation of a well-known substrate of the mTORC2 complex, AKT (protein kinase B), at Ser^{473} (Fig. 4A and fig. S11, A to C) (*25*). Phosphorylation of mTORC2-independent targets, including AKT Thr^{308} and ribosomal protein S6 Ser$^{235/236}$ and Ser$^{240/244}$, was moderately reduced in patient cells, but these defects were not recapitulated by HEM1 knockdown (Fig. 4B and fig. S11, C and D). Immunoblotting showed decreased phosphorylation of AKT Ser^{473} as well as decreased Ser^{21} of the downstream AKT substrate, glycogen synthase kinase (GSK) 3a (Fig. 4C). TCR-induced AKT Ser^{473} in T cells could be blocked by an mTOR catalytic inhibitor (Ku0063794), whereas inhibition of the actin network by LatA moderately enhanced AKT Ser^{473} phosphorylation. Thus, the AKT

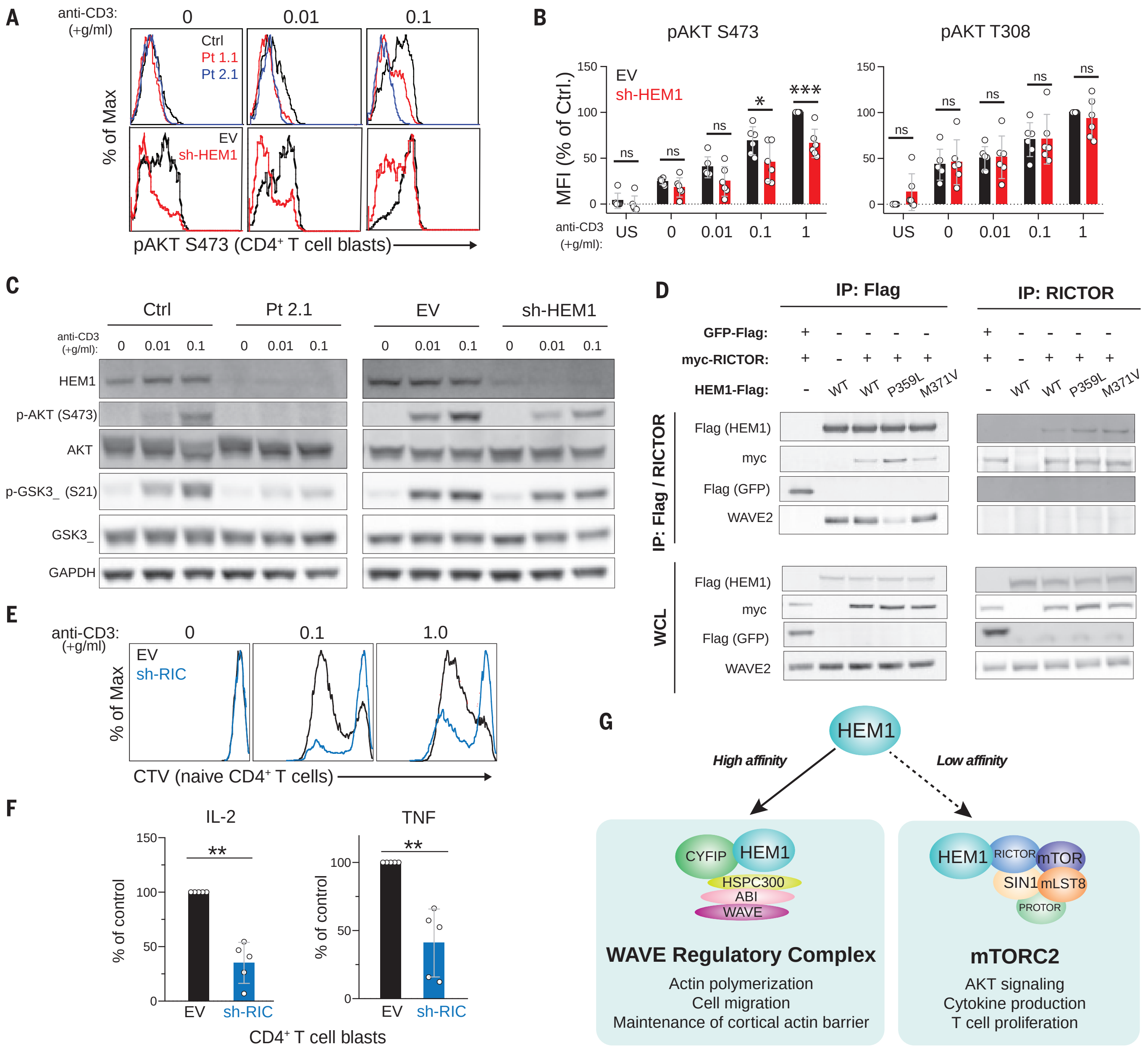

Fig. 4. HEM1 associates with RICTOR and governs mTORC2 activation. (**A**) Phospho-flow cytometry of purified CD4$^+$ T cell blasts from Ctrl or Pt (top row) or EV transduced or sh-HEM1 knockdown cells (bottom row) for AKT phosphorylated on Ser^{473} (pAKT S473). Cells were stimulated for 10 min with anti-CD28 and ICOS (1 μg/ml each) and the indicated dose of anti-CD3. (**B**) Mean fluorescence intensity (MFI) of pAKT S473 or AKT pAKT T308 in EV or sh-HEM1 CD4$^+$ T cell blasts stimulated as in (A) in six independent experiments. US, unstimulated; ns, not significant. (**C**) Immunoblot of Ctrl or Pt CD4$^+$ T cell blasts, or healthy CD4$^+$ T cell blasts cells transduced with EV or sh-HEM1. Cells were rested and restimulated with ICAM-1 and anti-CD28 (1 μg/ml each) and the indicated dose of anti-CD3. (**D**) Flag and RICTOR IP from 293T cells transduced with myc-RICTOR and either Flag-tagged GFP or Flag-tagged HEM1 (WT or mutant) and blotted. (**E**) CTV proliferation plots of naïve CD4$^+$ T cells transduced with EV or shRNA directed against RICTOR (sh-RIC). (**F**) Cytokine secretion by control and RICTOR knockdown (sh-RIC) CD4$^+$ T cell blasts after 18-hour restimulation in five independent experiments. (**G**) Provisional model of HEM1 independently regulating WRC- and mTORC2-mediated functions. Statistical analyses for (B) and (F) were performed using a Wilcoxon matched-pairs signed-rank test. *$P \leq 0.05$; **$P \leq 0.01$; ***$P \leq 0.001$.

Ser^{473} phosphorylation defect appears to be independent of HEM1 regulation of the CaCN (fig. S11, E and F).

To investigate how HEM1 regulates the phosphoinositide 3-kinase (PI3K)–AKT–mTORC2 pathway, we searched our IP-MS datasets and found that several mTORC2 components—including mTOR and RICTOR, the key scaffolding protein of mTORC2—were precipitated by HEM1 but not WAVE2 (fig. S4, fig. S12A, and table S5). This observation suggested the existence of a pool of HEM1 outside of the WRC that interacts with and regulates mTORC2 (*22*). Testing HEM1-Flag (wild-type, P359L, and M371V), Flag–green fluorescent protein (GFP), myc-RICTOR, or WAVE2 from 293T cells, we observed that HEM1, but not WAVE2, specifically coimmunoprecipitated with RICTOR (Fig. 4D and fig. S12, A and B). Notably, the P359L HEM1 is strongly associated with RICTOR, which suggests that the interaction occurs when HEM1 is not in complex with the WRC. Knockdown of RICTOR in CD4$^+$ T cells impaired proliferation and cytokine secretion (Fig. 4, E and F, and fig. S12D). Chemical inhibitors of the PI3K, AKT, or mTOR kinases also abrogated T cell proliferation and IL-2 and TNF secretion (fig. S12, E and F). Notably, specific inhibition of mTORC1 with rapamycin had little effect compared with inhibition of both complexes with an mTOR catalytic inhibitor, which suggests that mTORC2, but not mTORC1, is required. However, mTOR inhibition had little effect on the secretion of perforin and granzymes or on CD69 and CD25 up-regulation, essentially phenocopying the defects observed in patient cells (fig. S12, G to I). Thus, HEM1 plays an additional role in human T cells outside of the WRC as an upstream regulator of mTORC2 enzymatic activity (Fig. 4G).

Previous studies have shown that individual WRC components can have noncanonical roles in cellular processes beyond actin filament nucleation and that HEM1/2 exists, and likely functions, outside of the WRC complex (*11*, *22*). We now show that in human patients with immunodeficiency and immune hyperactivation, the loss-of-function mutations in *NCKAP1L*, the gene encoding HEM1, disrupt WRC-mediated actin polymerization and abrogate mTORC2 activation of AKT. The resulting autosomal recessive IEI affects multiple hematopoietic lineages and leads to bacterial and viral infections, atopic disease, autoimmunity, cytokine overproduction, and lymphoproliferative disease. We demonstrate that HEM1 and the WRC maintain the CAcN, which restricts cytokine secretion and lytic granule release. We also show that HEM1 plays a key binding role in Arf1-mediated WRC activation. Our findings suggest a broader effect of genetic HEM1 deficiency on the cytokine repertoire and cellular effector function that should be addressed in future work. Finally, we identify an interaction between HEM1 and RICTOR that is essential for mTORC2 regulation. HEM1 may have escaped detection in previous RICTOR precipitation experiments because the interaction appears to be weak and because commonly used 293T cells do not express the hematopoietically restricted HEM1. We posit that HEM1 independently coordinates WRC-mediated actin nucleation and mTORC2 catalytic activity in response to signals that activate both protein complexes—such as PI3K, Arf1, and Rac1—during T cell activation and possibly during B and NK cell activation. These data could explain how mTORC2 is activated downstream of actin-generated membrane tension and can negatively regulate the WRC (*26*). Because mTORC2 exerts similar roles in all lymphocytes, and because their activation involves actin-dependent regulation, it is likely that B and NK cell abnormalities contribute to immunopathology in the HEM1-deficient patients (*27*–*29*). Our study elucidates a human congenital disorder caused by loss of HEM1 and highlights potential routes for immunological therapy.

REFERENCES AND NOTES

1. C. Cunningham-Rundles, P. P. Ponda, *Nat. Rev. Immunol.* **5**, 880–892 (2005).
2. R. A. Saxton, D. M. Sabatini, *Cell* **169**, 361–371 (2017).
3. D. A. Guertin *et al*., *Dev. Cell* **11**, 859–871 (2006).
4. K. Lee *et al*., *Immunity* **32**, 743–753 (2010).
5. L. A. Van de Velde, P. J. Murray, *J. Biol. Chem.* **291**, 25815–25822 (2016).
6. B. Chen, S. B. Padrick, L. Henry, M. K. Rosen, *Methods Enzymol.* **540**, 55–72 (2014).
7. T. E. Stradal *et al*., *Trends Cell Biol.* **14**, 303–311 (2004).
8. B. Chen *et al*., *eLife* **6**, e29795 (2017).
9. Z. Chen *et al*., *Nature* **468**, 533–538 (2010).
10. A. M. Lebensohn, M. W. Kirschner, *Mol. Cell* **36**, 512–524 (2009).
11. C. Litschko *et al*., *Eur. J. Cell Biol.* **96**, 715–727 (2017).
12. L. Shao *et al*., *Nat. Commun.* **9**, 2377 (2018).
13. S. O. Burns, A. Zarafov, A. J. Thrasher, *Curr. Opin. Hematol.* **24**, 16–22 (2017).
14. M. Kircher *et al*., *Nat. Genet.* **46**, 310–315 (2014).
15. H. Park *et al*., *J. Exp. Med.* **205**, 2899–2913 (2008).
16. A. Leithner *et al*., *Nat. Cell Biol.* **18**, 1253–1259 (2016).
17. C. Basquin *et al*., *EMBO J.* **34**, 2147–2161 (2015).
18. A. F. Carisey, E. M. Mace, M. B. Saeed, D. M. Davis, J. S. Orange, *Curr. Biol.* **28**, 489–502.e9 (2018).
19. A. Gil-Krzewska *et al*., *J. Allergy Clin. Immunol.* **142**, 914–927.e6 (2018).
20. S. Murugesan *et al*., *J. Cell Biol.* **215**, 383–399 (2016).
21. J. C. Nolz *et al*., *Curr. Biol.* **16**, 24–34 (2006).
22. O. D. Weiner *et al*., *PLOS Biol.* **4**, e38 (2006).
23. J. C. Nolz *et al*., *Mol. Cell. Biol.* **27**, 5986–6000 (2007).
24. J. C. Nolz *et al*., *J. Cell Biol.* **182**, 1231–1244 (2008).
25. D. D. Sarbassov, D. A. Guertin, S. M. Ali, D. M. Sabatini, *Science* **307**, 1098–1101 (2005).
26. A. Diz-Muñoz *et al*., *PLOS Biol.* **14**, e1002474 (2016).
27. B. Treanor *et al*., *Immunity* **32**, 187–199 (2010).
28. T. N. Iwata, J. A. Ramírez-Komo, H. Park, B. M. Iritani, *Cytokine Growth Factor Rev.* **35**, 47–62 (2017).
29. C. Yang *et al*., *eLife* **7**, e35619 (2018).

ACKNOWLEDGMENTS

The authors thank the patients and family members for participating in this study and making this research possible. We thank H. Su for scientific input, discussions, and careful reading of the manuscript. The authors thank members of the Bioinformatics and Computational Biosciences Branch (BCBB), NIAID for bioinformatics support; the Office of Cyber Infrastructure and Computational Biology (OCICB), NIAID for high-performance computing support; and the Laboratory of Immune System Biology Flow Cytometry Core, NIAID for cell analysis. Finally, we thank the staff of the Advanced Mass Spectrometry Core, NIDDK. **Funding:** This work was supported by the Jeffrey Model Foundation Translational Research Award to I.K.C.; NIH-NIAID grant R01 AI120989 to J.S.O.; NIH-NIGMS (National Institute of General Medical Sciences) grant R35 GM128786 and start-up funds from the Iowa State University and the Roy J. Carver Charitable Trust to B.C.; NIH-NHGRI (National Human Genome Research Institute) grant UM1 HG006542 to the Baylor-Hopkins Center for Mendelian Genomics; and the National Cancer Institute, NIH, under contract no. HHSN261200800001E. Additional support came from the Division of Intramural Research, NIAID, NIH; the Division of Intramural Research, NIDDK; and the Deputy Director of Intramural Research, NIH, through the Clinical Center Genomics Opportunity. This work was also funded by a fellowship grant (1-16-PDF-025 to W.A.Co.) from the American Diabetes Association and a F12 postdoctoral fellowship (1FI2GM119979-01 to W.A.Co.) from the NIGMS, NIH. M.C.P. was supported by the Fondo Nacional de Desarrollo Científico y Tecnológico (FONDECYT no. 11181222). The content of this publication does not necessarily reflect the views or policies of the Department of Health and Human Services, nor does mention of trade names, commercial products, or organizations imply endorsement by the U.S. government. **Author contributions:** W.A.Co., S.A.C., and A.J.F. performed experiments related to WRC expression and function, T cell activation and function, and NKL cell analysis; analyzed data; and interpreted results. S.A.C. performed experiments related to the functional validation of P359L, M371V, and V519L; patient cell microscopy; and RICTOR interaction studies. M.C.P., A.V.-H., A.F.C., E.M.M., and J.S.O. directed or performed NK cell experiments and biochemical analysis of the mTORC2 complex, analyzed data, and interpreted results. D.B.K. performed neutrophil experiments and analyzed data. W.A.Co. prepared IP-MS samples, and D.E.A. performed MS analysis and generated the list of interacting proteins. S.Y. performed in vitro WRC reconstitution and pull-down and actin polymerization assays. M.Sm. acquired images and analyzed granule localization in patient cells. S.P., G.D.E.C., and V.K.R. oversaw care of Pt 1.1, and V.K.R., M.Si., and A.J.O. performed and interpreted whole-exome sequencing (WES) for kindred 1. J.W.C. and N.R. oversaw care of Pts 2.1 and 2.2, and T.N.C., Z.H.C.-A., S.N.J., D.M.M., R.A.G., and J.R.L. performed and interpreted WES to identify causal variants for kindred 2. M.A.H., N.A.K., Z.A.Y., S.J., and G.E. oversaw care of Pt 3.1. G.E. performed and G.E. and A.J.O. interpreted WES for kindred 3 to identify causal mutations. W.A.Ch., B.F., and S.L. oversaw care of Pt 4.1 and performed and interpreted WES to identify causal mutations. Patient clinical histories were prepared by W.A.Co., M.C.P., and attending physicians. J.S.O., L.R.F., J.K.B., S.L., B.C., G.E., V.K.R., I.K.C., and M.J.L. supervised various aspects of the project and project personnel. W.A.Co., S.A.C., M.C.P., I.K.C., and M.J.L. interpreted results and wrote the manuscript. W.A.Co. and S.A.C. took day-to-day responsibility for the study. M.J.L. coordinated the overall direction of the study. All authors read and provided appropriate feedback on the submitted manuscript. **Competing interests:** N.R. is a consultant for Horizon Therapeutics. **Data and materials availability:** All data needed to evaluate the conclusions in this paper are present either in the main text or the supplementary materials. WES data for the kindred of Pt 1.1 were submitted to the National Center for Biotechnology Information's (NCBI) database of Genotypes and Phenotypes (dbGaP) (accession no., phs001561). WES data for the kindred of Pts 2.1 and 2.2 were submitted to dbGaP (accession no., phs000711).

SUPPLEMENTARY MATERIALS

science.sciencemag.org/content/369/6500/202/suppl/DC1
Materials and Methods
Supplementary Text
Figs. S1 to S12
Tables S1 to S6
References (*30*–*42*)
Movies S1 to S4

30 June 2019; resubmitted 21 January 2020
Accepted 29 May 2020
10.1126/science.aay5663

CORONAVIRUS

Estimating the burden of SARS-CoV-2 in France

Henrik Salje[1,2,3]*, Cécile Tran Kiem[1,4]*, Noémie Lefrancq[1], Noémie Courtejoie[5], Paolo Bosetti[1], Juliette Paireau[1,6], Alessio Andronico[1], Nathanaël Hozé[1], Jehanne Richet[5], Claire-Lise Dubost[5], Yann Le Strat[6], Justin Lessler[3], Daniel Levy-Bruhl[6], Arnaud Fontanet[7,8], Lulla Opatowski[9,10], Pierre-Yves Boelle[11], Simon Cauchemez[1]†

France has been heavily affected by the severe acute respiratory syndrome coronavirus 2 (SARS-CoV-2) pandemic and went into lockdown on 17 March 2020. Using models applied to hospital and death data, we estimate the impact of the lockdown and current population immunity. We find that 2.9% of infected individuals are hospitalized and 0.5% of those infected die (95% credible interval: 0.3 to 0.9%), ranging from 0.001% in those under 20 years of age to 8.3% in those 80 years of age or older. Across all ages, men are more likely to be hospitalized, enter intensive care, and die than women. The lockdown reduced the reproductive number from 2.90 to 0.67 (77% reduction). By 11 May 2020, when interventions are scheduled to be eased, we project that 3.5 million people (range: 2.1 million to 6.0 million), or 5.3% of the population (range: 3.3 to 9.3%), will have been infected. Population immunity appears to be insufficient to avoid a second wave if all control measures are released at the end of the lockdown.

The worldwide pandemic of severe acute respiratory syndrome coronavirus 2 (SARS-CoV-2), the coronavirus that causes coronavirus disease 2019 (COVID-19), has resulted in unprecedented responses, with many affected nations confining residents to their homes. Much like the rest of Europe, France has been hit hard by the pandemic and went into lockdown on 17 March 2020. It was hoped that this lockdown would result in a sharp decline in ongoing spread, as was observed when China locked down after the initial emergence of the virus (*1*, *2*). In light of the expected reduction in cases, the French government has announced it will ease restrictions on 11 May 2020. To exit from the lockdown without escalating infections, we need to understand the underlying level of population immunity and infection, identify those most at risk for severe disease, and determine the impact of current control efforts.

Daily reported numbers of hospitalizations and deaths provide only limited insight into the state of the pandemic. Many people will either develop no symptoms or symptoms so mild that they will not be detected through health care–based surveillance. The concentration of hospitalized cases in older individuals has led to hypotheses that there may be widespread "silent" transmission in younger individuals (*3*). If most of the population were infected, viral transmission would slow, potentially reducing the need for the stringent intervention measures currently employed.

We present a suite of modeling analyses to characterize the dynamics of SARS-CoV-2 transmission in France and the impact of the lockdown on these dynamics. We elucidate the risk of SARS-CoV-2 infection and severe outcomes by age and sex, and we estimate the current proportion of the national and regional populations that have been infected and might be at least temporarily immune (*4*). These models support health care planning of the French government by capturing hospital bed capacity requirements.

As of 7 May 2020, there were 95,210 incident hospitalizations due to SARS-CoV-2 reported in France and 16,386 deaths in hospitals, with the east of the country and the capital, Paris, particularly affected (Fig. 1, A and B). The mean age of hospitalized patients was 68 years and the mean age of the deceased was 79 years, with 50.0% of hospitalizations occurring in individuals over 70 years of age and 81.6% of deaths within that age bracket; 56.2% of hospitalizations and 60.3% of deaths were male (Fig. 1, C to E). To reconstruct the dynamics of all infections, including mild ones, we jointly analyze French hospital data with the results

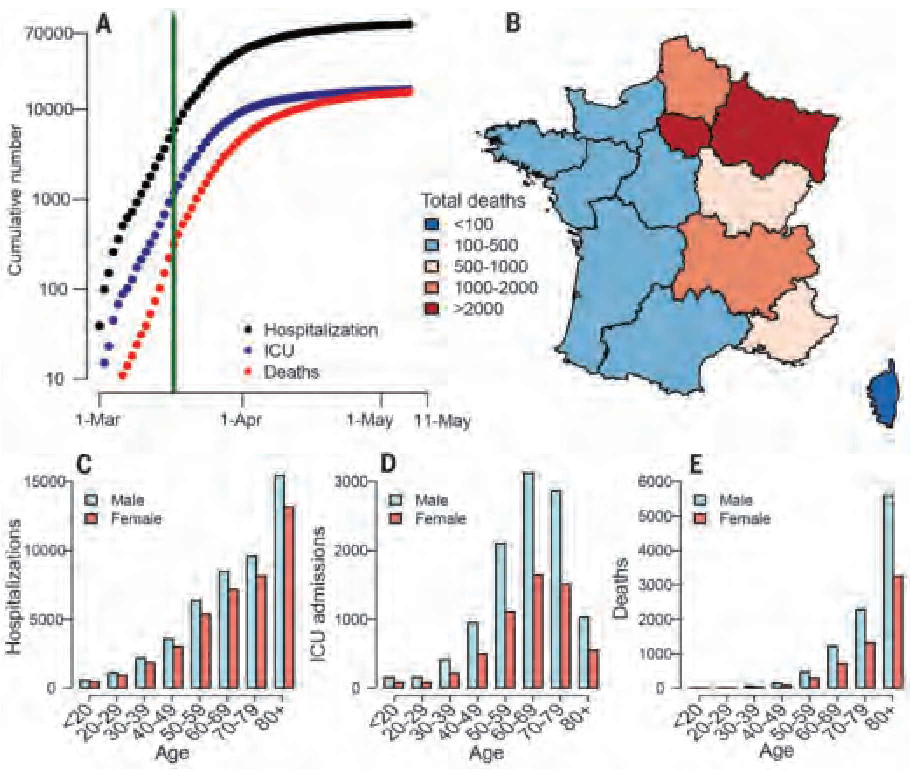

Fig. 1. COVID-19 hospitalizations and deaths in France. (**A**) Cumulative number of general ward and ICU hospitalizations, ICU admissions, and deaths from COVID-19 in France. The vertical green line indicates the time when the lockdown was put in place in France. (**B**) Geographical distribution of deaths in France. Number of (**C**) hospitalizations, (**D**) ICU admissions, and (**E**) deaths by age group and sex in France.

[1]Mathematical Modelling of Infectious Diseases Unit, Institut Pasteur, UMR2000, CNRS, Paris, France. [2]Department of Genetics, University of Cambridge, Cambridge, UK. [3]Department of Epidemiology, Johns Hopkins Bloomberg School of Public Health, Baltimore, MD, USA. [4]Collège Doctoral, Sorbonne Université, Paris, France. [5]DREES, Ministère des Solidarités et de la Santé, Paris, France. [6]Santé Publique France, French National Public Health Agency, Saint-Maurice, France. [7]Emerging Diseases Epidemiology Unit, Institut Pasteur, Paris, France. [8]PACRI Unit, Conservatoire National des Arts et Métiers, Paris, France. [9]Epidemiology and Modelling of Antibiotic Evasion Unit, Institut Pasteur, Paris, France. [10]Anti-infective Evasion and Pharmacoepidemiology Team, CESP, Université Paris-Saclay, UVSQ, INSERM U1018, Montigny-le-Bretonneux, France. [11]Institut Pierre Louis d'Epidémiologie et de Santé Publique, Sorbonne Université, INSERM, Paris, France.
*These authors contributed equally to this work.
†Corresponding author. Email: simon.cauchemez@pasteur.fr

of a detailed outbreak investigation aboard the Diamond Princess cruise ship where all passengers were subsequently tested [719 infections, 14 deaths currently, with one passenger still in the intensive care unit (ICU) after 2 months, who we assume will not survive his infection]. By coupling the passive surveillance data from French hospitals with the active surveillance performed aboard the Diamond Princess, we disentangle the risk of hospitalization for those infected from the underlying probability of infection (*5*, *6*).

We find that 2.9% of infected individuals are hospitalized [95% credible interval (CrI): 1.7 to 4.8%], ranging from 0.1% (95% CrI: 0.1 to 0.2%) in females under 20 years of age to 37.6% (95% CrI: 21.1 to 61.3%) in males 80 years of age or older (Fig. 2A and table S1). On average, 19.0%

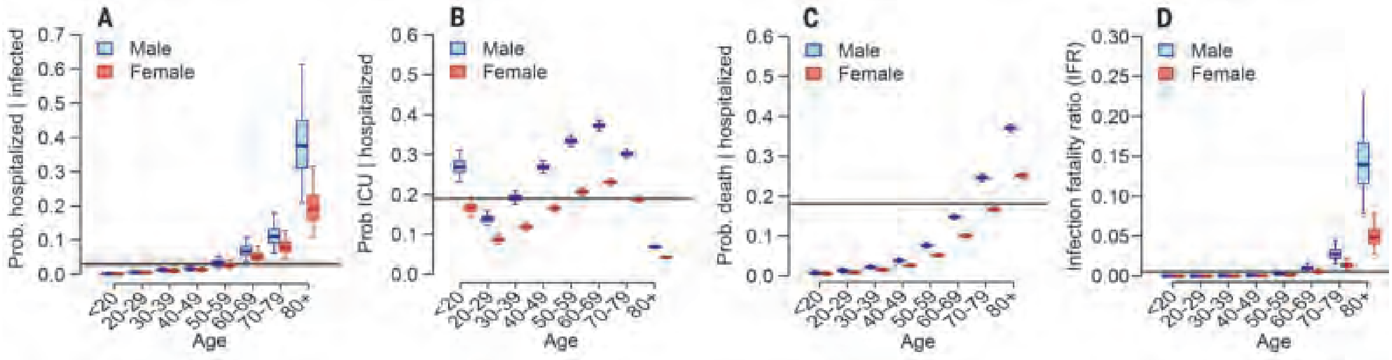

Fig. 2. Probabilities of hospitalization, ICU admission, and death. (**A**) Probability of hospitalization among those infected as a function of age and sex. (**B**) Probability of ICU admission among those hospitalized as a function of age and sex. (**C**) Probability of death among those hospitalized as a function of age and sex. (**D**) Probability of death among those infected as a function of age and sex. For each panel, the horizontal black line and gray shaded region represent the overall mean across all ages. The boxplots represent the 2.5, 25, 50, 75, and 97.5 percentiles of the posterior distributions.

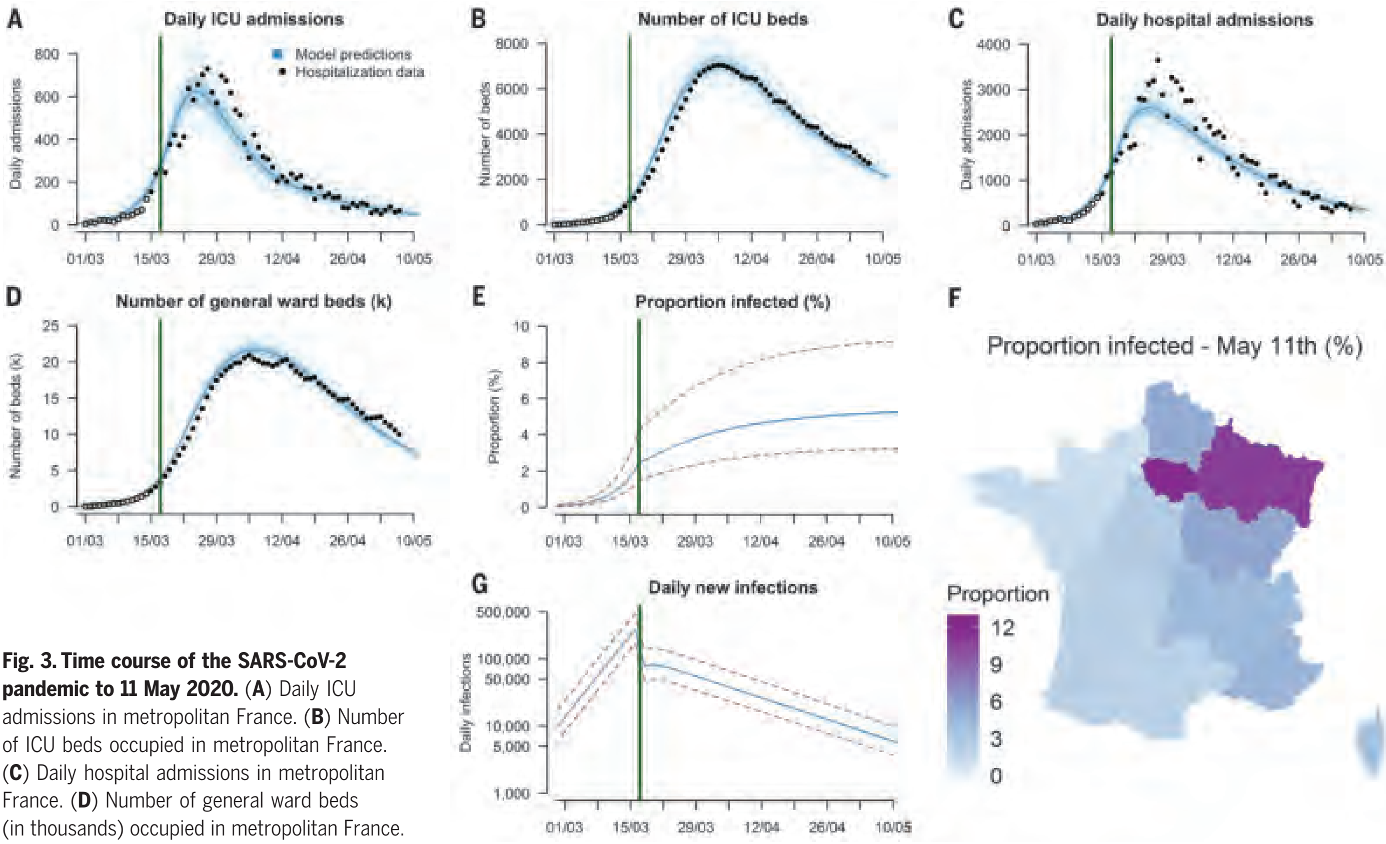

Fig. 3. Time course of the SARS-CoV-2 pandemic to 11 May 2020. (**A**) Daily ICU admissions in metropolitan France. (**B**) Number of ICU beds occupied in metropolitan France. (**C**) Daily hospital admissions in metropolitan France. (**D**) Number of general ward beds (in thousands) occupied in metropolitan France. (**E**) Daily new infections in metropolitan France (logarithmic scale). (**F**) Predicted proportion of the population infected by 11 May 2020 for each of the 13 regions in metropolitan France. (**G**) Predicted proportion of the population infected in metropolitan France. The solid circles in (A) to (D) represent hospitalization data used for the calibration, and the open circles represent hospitalization data that were not used for calibration. The dark-blue shaded areas correspond to 50% credible intervals, and the light-blue shaded areas correspond to 95% credible intervals. The dashed lines in (E) and (G) represent the 95% uncertainty range stemming from the uncertainty in the probability of hospitalization after infection.

(95% CrI: 18.7 to 19.4%) of hospitalized patients enter the ICU after a mean delay of 1.5 days (fig. S1). We observe an increasing probability of entering the ICU with age—however, this probability drops for those over 70 years of age (Fig. 2B and table S2). Overall, 18.1% (95% CrI: 17.8 to 18.4%) of hospitalized individuals do not survive (Fig. 2C). The overall probability of death among those infected [the infection fatality ratio (IFR)] is 0.5% (95% CrI: 0.3 to 0.9%), ranging from 0.001% in those under 20 years of age to 8.3% (95% CrI: 4.7 to 13.5%) in those 80 years of age or older (Fig. 2D and table S2). Our estimate of overall IFR is similar to other recent studies that found IFR values between 0.5 and 0.7% for the pandemic in China (*6*–*8*). We find that men have a consistently higher risk than women of hospitalization [relative risk (RR): 1.25; 95% CrI: 1.22 to 1.29], ICU admission once hospitalized (RR: 1.61; 95% CrI: 1.56 to 1.67), and death after hospitalization (RR: 1.47; 95% CrI: 1.42 to 1.53) (fig. S2).

We identify two clear subpopulations among hospitalized cases: individuals that die quickly after hospital admission (15% of fatal cases, with a mean time to death of 0.67 days) and individuals who die after longer time periods (85% of fatal cases, with a mean time to death of 13.2 days) (fig. S3). The proportion of fatal cases who die rapidly remains approximately constant across age groups (fig. S4 and table S3). Potential explanations for different subgroups of fatal cases include heterogeneous patterns of health care seeking, access to care, and underlying comorbidities, such as metabolic disease and other inflammatory conditions. A role for immunopathogenesis has also been proposed (*9*–*12*).

We next fit national and regional transmission models to ICU admission, hospital admission, and bed occupancy (both ICU and general wards) (Fig. 3, A to D; fig. S5; and tables S4 to S6), allowing for reduced age-specific daily contact patterns following the lockdown and changing patterns of ICU admission over time (fig. S18). We find that the basic reproductive number R_0 before the implementation of the lockdown was 2.90 (95% CrI: 2.81 to 3.01). The lockdown resulted in a 77% (95% CrI: 76 to 78%) reduction in transmission, with the reproduction number R dropping to 0.67 (95% CrI: 0.66 to 0.68). We forecast that by 11 May 2020, 3.5 million people (range: 2.1 million to 6.0 million; when accounting for uncertainty in the probability of hospitalization after infection) will have been infected, representing 5.3% (range: 3.3 to 9.3%) of the French population (Fig. 3E). This proportion will be 11.9% (range: 7.6 to 19.4%) in Île-de-France, which includes Paris, and 10.9% (range: 6.9 to 18.1%) in Grand Est, the two most affected regions of the country (Fig. 3F and fig. S5). Assuming a basic reproductive number of R_0 = 2.9, 66% of the population would have to be immune for the pandemic to be controlled by immunity alone. Our results therefore strongly suggest that, without a vaccine, herd immunity on its own will be insufficient to avoid a second wave at the end of the lockdown. Efficient control measures need to be maintained beyond 11 May.

Our model can help inform the ongoing and future response to COVID-19. National ICU daily admissions have gone from 700 at the end of March to 66 on 7 May. Hospital admissions have declined from 3600 to 357 over the same time period, with consistent declines observed throughout France (fig. S5). By 11 May, we project 4700 (range: 2900 to 7900) daily infections across the country, down from between 180,000 and 490,000 immediately before the lockdown. At a regional level, we estimate that 57% of infections will be in Île-de-France and Grand Est combined. We find that the length of time people spend in the ICU appears to differ across the country, which may be due to differences in health care practices (table S5).

Using our modeling framework, we are able to reproduce the observed number of hospitalizations by age and sex in France and the number of observed deaths aboard the Diamond Princess (fig. S6). As a validation, our approach is also able to correctly identify parameters in simulated datasets where the true values are known (fig. S7). As cruise ship passengers may represent a different, healthier population than average French citizens, we run a sensitivity analysis where Diamond Princess passengers are 25% less likely to die than French citizens (Fig. 4 and fig. S8). We also run sensitivity analyses for the following scenarios: longer delays between symptom onset and hospital admission; missed infections aboard the Diamond Princess; a scenario in which the final Diamond Princess patient in the ICU survives; equal attack rates across all ages; reduced infectivity in younger individuals; a contact matrix with unchanged structure before and during the lockdown; and a contact matrix with very high

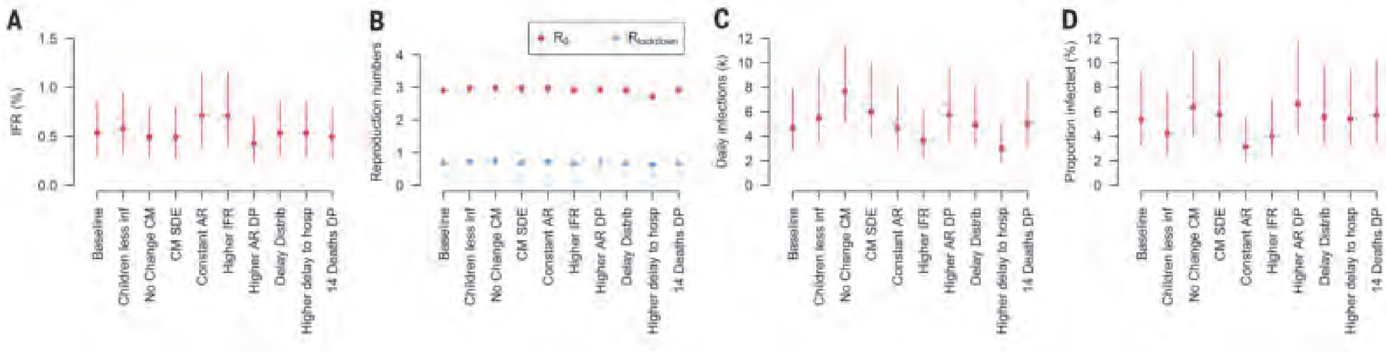

Fig. 4. Sensitivity analyses considering different modeling assumptions. (**A**) Infection fatality rate (%). (**B**) Estimated reproduction numbers before (R_0) and during lockdown ($R_{lockdown}$). (**C**) Predicted daily new infections on 11 May. (**D**) Predicted proportion of the population infected by 11 May. The different scenarios are as follows: "Children less inf," individuals under 20 years of age are half as infectious as adults; "No Change CM," the structure of the contact matrix (CM) is not modified by the lockdown; "CM SDE," contact matrix after lockdown with very high social distancing of the elderly; "Constant AR," attack rates are constant across age groups; "Higher IFR," French people are 25% more likely to die than Diamond Princess passengers; "Higher AR DP," 25% of the infections were undetected on the Diamond Princess cruise ship; "Delay Distrib,"single hospitalization to death delay distribution; "Higher delay to hosp," 8 days on average between symptom onset and hospitalization for patients who will require ICU admission and 9 days on average between symptom onset and hospitalization for the patients who will not; "14 Deaths DP," the final passenger of the Diamond Princess in ICU survives. For estimates of IFR and reproduction numbers before and during lockdown, we report 95% credible intervals. For estimates of daily new infections and proportion of the population infected by 11 May, we report the 95% uncertainty range stemming from the uncertainty in the probability of hospitalization given infection.

isolation of elderly individuals during the lockdown. These different scenarios result in mean IFRs from 0.4 to 0.7%, the proportion of the population infected by 11 May 2020 ranging from 1.9 to 11.8%, the number of daily infections at this date ranging from 1900 to 11,300, and a range of post-lockdown reproductive numbers of 0.62 to 0.74 (Fig. 4, figs. S8 to S15, and tables S7 to S12).

A seroprevalence of 3% (range: 0 to 3%) has been estimated among blood donors in Hauts-de-France, which is consistent with our model predictions (range: 1 to 3%) for this population if we account for a 10-day delay for seroconversion (*13*, *14*). Future additional serological data will help to further refine estimates of the proportion of the population infected.

Although we focus on deaths occurring in hospitals, there are also nonhospitalized COVID-19 deaths, including >9000 in retirement homes in France (*15*). We explicitly removed the retirement home population from our analyses, as transmission dynamics may be different in these closed populations. This omission means that our estimates of immunity in the general population are unaffected by deaths in retirement homes, however, in the event of large numbers of nonhospitalized deaths in the wider community, we would be underestimating the proportion of the population infected. Analyses of excess death will be important to explore these issues.

This study shows the massive impact that the French lockdown has had on SARS-CoV-2 transmission. Our modeling approach has allowed us to estimate underlying probabilities of infection, hospitalization, and death, which are essential for the interpretation of COVID-19 surveillance data. The forecasts we provide can inform lockdown exit strategies. Our estimates of a low level of immunity against SARS-CoV-2 indicate that efficient control measures that limit transmission risk will have to be maintained beyond 11 May 2020 to avoid a rebound of the pandemic.

REFERENCES AND NOTES

1. M. U. G. Kraemer *et al*., *Science* **368**, 493–497 (2020).
2. H. Tian *et al*., *Science* **368**, 638–642 (2020).
3. J. Lourenço *et al.*, medRxiv 2020.03.24.20042291 [Preprint]. 26 March 2020. https://doi.org/10.1101/2020.03.24.20042291.
4. L. Bao *et al.*, bioRxiv 2020.03.13.990226 [Preprint]. 14 March 2020. https://doi.org/10.1101/2020.03.13.990226.
5. J. Lessler *et al*., *Am. J. Epidemiol.* **183**, 657–663 (2016).
6. R. Verity *et al*., *Lancet Infect. Dis.* **20**, 669–677 (2020).
7. T. W. Russell *et al*., *Euro Surveill.* **25**, 2000256 (2020).
8. K. Mizumoto, K. Kagaya, G. Chowell, medRxiv 2020.02.12.20022434 [Preprint]. 13 March 2020. https://doi.org/10.1101/2020.02.12.20022434.
9. L. Peeples, *Proc. Natl. Acad. Sci. U.S.A.* **117**, 8218–8221 (2020).
10. D. Ricke, R. W. Malone, Medical Countermeasures Analysis of 2019-nCoV and Vaccine Risks for Antibody-Dependent Enhancement (ADE), 27 February 2020; https://ssrn.com/abstract=3546070.
11. J. Yang *et al*., *Int. J. Infect. Dis.* **94**, 91–95 (2020).
12. M. Bolles *et al*., *J. Virol.* **85**, 12201–12215 (2011).
13. A. Fontanet *et al.*, medRxiv 2020.04.18.20071134 [Preprint]. 23 April 2020. https://doi.org/10.1101/2020.04.18.20071134.
14. L. Grzelak *et al.*, medRxiv 2020.04.21.20068858 [Preprint]. 24 April 2020. https://doi.org/10.1101/2020.04.21.20068858.
15. French Government website, Info Coronavirus Covid 19 (in French); www.gouvernement.fr/info-coronavirus/carte-et-donnees.
16. H. Salje, C. Tran Kiem, Code and data for: Estimating the burden of SARS-CoV-2 in France, Version 1.1, Zenodo (2020); https://doi.org/10.5281/zenodo.3889894.

ACKNOWLEDGMENTS

Funding: We acknowledge financial support from the Investissement d'Avenir program, the Laboratoire d'Excellence Integrative Biology of Emerging Infectious Diseases program (grant ANR-10-LABX-62-IBEID), Santé Publique France, the INCEPTION project (PIA/ANR-16-CONV-0005), and the European Union's Horizon 2020 research and innovation program under grants 101003589 (RECOVER) and 874735 (VEO). H.S. acknowledges support from the European Research Council (grant 804744) and a University of Cambridge COVID-19 Rapid Response Grant. **Author contributions:** H.S., C.T.K., and S.C. conceived of the study, developed the methods, performed analyses, and co-wrote the paper. N.L., N.C., N.H., A.A., P.B., J.P., J.R., C.-L.D., L.O., P.-Y.B., A.F., J.L., D.L.-B., and Y.L.S. contributed to data collection and analysis. All authors contributed to paper revisions. **Competing interests:** The authors declare no competing interests. **Data and materials availability:** Code for the paper is available at (*16*).

SUPPLEMENTARY MATERIALS

science.sciencemag.org/content/369/6500/208/suppl/DC1
Materials and Methods
Supplementary Text
Figs. S1 to S18
Tables S1 to S12
References (*17*–*32*)

20 April 2020; accepted 11 May 2020
Published online 13 May 2020
10.1126/science.abc3517

PALEONTOLOGY

Marginal dentition and multiple dermal jawbones as the ancestral condition of jawed vertebrates

Valéria Vaškaninová[1,2]*, Donglei Chen[1], Paul Tafforeau[3], Zerina Johanson[4], Boris Ekrt[5], Henning Blom[1], Per Erik Ahlberg[1]*

The dentitions of extant fishes and land vertebrates vary in both pattern and type of tooth replacement. It has been argued that the common ancestral condition likely resembles the nonmarginal, radially arranged tooth files of arthrodires, an early group of armoured fishes. We used synchrotron microtomography to describe the fossil dentitions of so-called acanthothoracids, the most phylogenetically basal jawed vertebrates with teeth, belonging to the genera *Radotina*, *Kosoraspis*, and *Tlamaspis* (from the Early Devonian of the Czech Republic). Their dentitions differ fundamentally from those of arthrodires; they are marginal, carried by a cheekbone or a series of short dermal bones along the jaw edges, and teeth are added lingually as is the case in many chondrichthyans (cartilaginous fishes) and osteichthyans (bony fishes and tetrapods). We propose these characteristics as ancestral for all jawed vertebrates.

The origin of teeth was one of the key events in the evolutionary transition from jawless to jawed vertebrates. Stem osteichthyans (*1*, *2*) and most chondrichthyans (*3*) have transversely arranged whorl-like tooth files with lingual addition, whereas crown osteichthyans have longitudinal tooth rows (Fig. 1). In arthrodires, a clade of jawed stem gnathostomes, teeth are added in diverging files from a progenitor tooth or region; the number of files is highly variable, and addition can be labial as well as lingual or longitudinal (*4*–*9*). The recent discovery of osteichthyan-like marginal dermal jawbones combined with an arthrodire-like body plan in *Entelognathus* and *Qilinyu* (*10*, *11*) has resulted in a proposed evolutionary succession (*11*) in which these genera form a bridge between an arthrodire-like condition (assumed to be primitive for jawed vertebrates) and the osteichthyan condition (assumed to be primitive for crown gnathostomes). However, the dentitions of *Entelognathus* and *Qilinyu* are poorly understood.

In this work, we present dentitions of the Early Devonian acanthothoracid stem gnathostomes *Radotina*, *Kosoraspis*, and *Tlamaspis* from the Czech Republic, and we reexamine the only described acanthothoracid dentition, specimen CPW.9 from the Canadian Arctic (mistakenly assigned to *Romundina* by some authors) (*7*, *12*). Acanthothoracids, antiarchs, and *Brindabellaspis* (*13*) are the only jawed vertebrates with an anteriorly projecting precerebral trabecular region (*14*). This distinctive

[1]Department of Organismal Biology, Uppsala University, Norbyvägen 18A, SE-752 36, Uppsala, Sweden. [2]Institute of Geology and Palaeontology, Faculty of Science, Charles University, Albertov 6, Prague, 12843, Czech Republic. [3]European Synchrotron Radiation Facility, 71 avenue des Martyrs, 38043 Grenoble, France. [4]Department of Earth Sciences, Natural History Museum, Cromwell Road, London SW7 5BD, UK. [5]Department of Palaeontology, National Museum, Václavské náměstí 68, Prague, 11579, Czech Republic.
*Corresponding author. Email: va.vaska@gmail.com (V.V.); per.ahlberg@ebc.uu.se (P.E.A.)

facial geometry resembles that of jawless stem gnathostomes, especially galeaspids (*15*). Recent phylogenetic analyses have recovered antiarchs, *Brindabellaspis*, and acanthothoracids as basal to other jawed vertebrates (*11*, *14*, *16*), a position they retain when the (not previously analyzed) genera discussed herein are included in the analysis (fig. S1). The jaws and dentition of *Brindabellaspis* are unknown, whereas antiarchs lack teeth (*17*). Thus, the teeth of acanthothoracids have the unique potential to illuminate the origin of vertebrate dentition.

The tooth addition in the dentition of CPW.9, which comprises a pair of supragnathal plates on a snout (fig. S2) (*12*), has been described as concentric (*7*, *18*). As a result, a detached dermal tessera with concentrically arranged odontodes from the same formation was misinterpreted as an acanthothoracid supragnathal (*18*–*20*). Reanalyzing the micro–computed tomography (micro-CT) scans of CPW.9 reveals that the supragnathals suture labially with the dermal premedian plate. In fact, tooth addition is radial from a labial founder region, and there is no labial tooth addition (fig. S3). Instead, the oldest small teeth in the founder region become overgrown by larger dermal odontodes as has been observed in the stem osteichthyan *Andreolepis* (*2*).

Using propagation phase contrast synchrotron microtomography, we have discovered the previously unknown dentitions of *Radotina*, *Kosoraspis*, and *Tlamaspis* (*21*). All differ substantially from that of CPW.9. The dentition of *Radotina* (Fig. 2) comprises four rows of teeth carried on the ventral face of a large dermal cheekbone sutured to the external surface of the palatoquadrate. This ventral face forms a longitudinal trough, with the teeth carried on the labial flank and the floor of the trough marked by a row of vascular grooves. Thus, the dentition is unambiguously marginal, located inside the jaw margin but external to the palatoquadrate (Fig. 2C), and separated from the external surface of the cheek by a distinct labial edge of exposed bone (fig. S4). Tooth rows are added lingually (fig. S5), and a pronounced mineralization gradient is displayed from the oldest to youngest teeth (fig. S4). The teeth have an elongated bladelike stellate shape (Fig. 2E) that matches that of marginal dermal ornament odontodes on the tesserae of the cheek (fig. S6E). However, unlike those odontodes, the teeth are fused into rows by a distinct basal attachment tissue (fig. S7D). The arms of the stellate teeth, which consist of pallial mesodentine, attach to a central cone of circumpulpal semidentine (*22*, *23*). The large spaces of odontoblast clusters enclosed in the arms anastomose with the smaller and sparser cell spaces in the cone, across the boundary between pallial and circumpulpal dentine (fig. S7, A to C). Each arm is equipped with an enameloid-coated blade (fig. S7D). Well-developed wear facets on the teeth (fig. S5) show that this was a functional cutting dentition. There is no evidence of resorption or replacement of teeth, but a broken tooth in the lingualmost row has been repaired with a new crown inserted into the break (fig. S5, E and F).

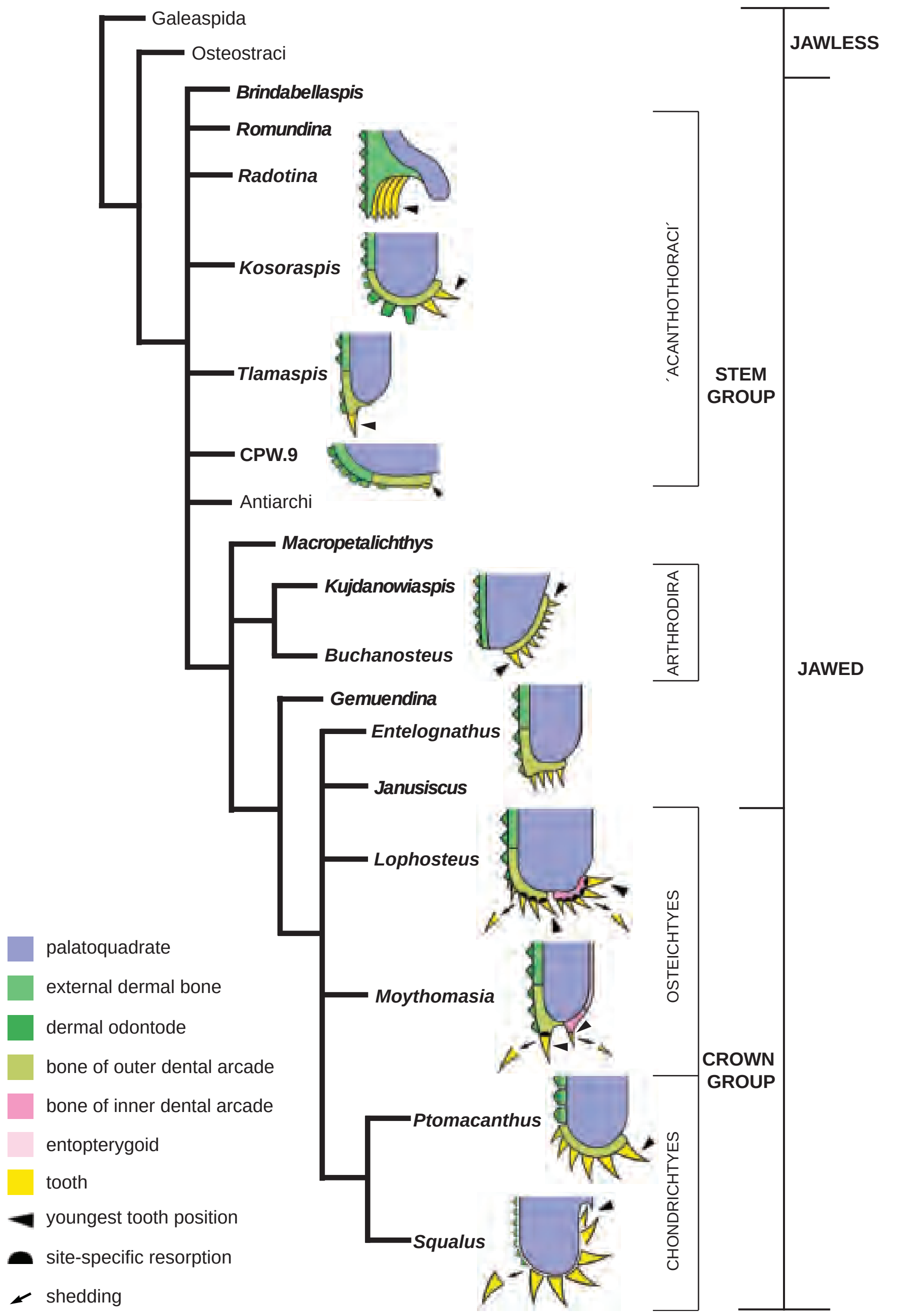

Fig. 1. Distribution of dentition types among gnathostomes. The images represent schematic transverse sections of palatoquadrate complexes, except for that of CPW.9, which represents the prenasal region. Genera with these schematic images are noted in bold. For strict consensus phylogeny, see fig. S1. The arthrodire and stem osteichthyan reconstructions are based on (*2*, *9*, *27*). The division between stem and crown is based on (*2*, *9*, *27*, *28*), which resolve *Lophosteus* as a stem osteichthyan and *Entelognathus* and *Janusiscus* as stem gnathostomes.

Kosoraspis (*24*) and *Tlamaspis* (*21*) have multiple short tooth–bearing dermal jawbones. They vary in length and shape according to their position (fig. S8) but invariably bear a prominent facial lamina. In *Kosoraspis*, the facial lamina carries toothlike odontodes that grade into recurved pointed teeth on the oral lamina (Fig. 3 and figs. S9 and S10), forming obliquely transverse whorl-like files that resemble the first-generation toothlike odontodes and nonshedding teeth in *Andreolepis* (*2*). They

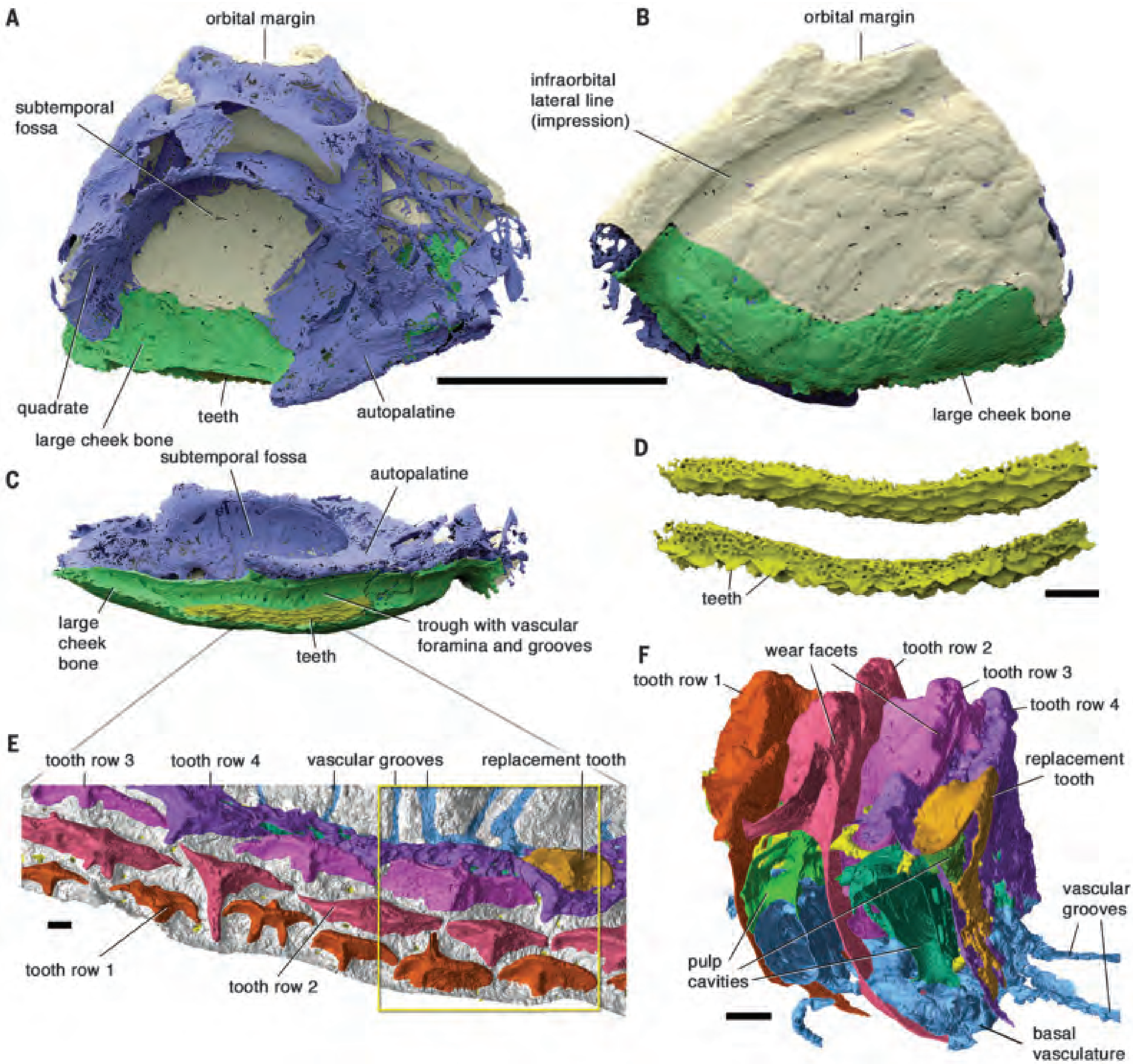

Fig. 2. Palatoquadrate complex and dentition of *Radotina tesselata*. (**A** to **C**) Palatoquadrate in internal (A), external (B), and ventral (C) views. (**D**) Dentition in mesoventral (top) and medial (bottom) views. (**E**) Detailed image of teeth in ventral view, with the relationship to (C) indicated with gray lines. (**F**) Block model of dentition in transverse view, showing the region indicated by the yellow box in (E). The scans shown in (A) to (D) have a voxel size of 13.49 μm, and the scans shown in (E) and (F) have a voxel size of 0.72 μm. In (A) to (D), green denotes external dermal bone, cream indicates natural mold of external dermal bone, blue indicates endoskeleton, and yellow indicates teeth and/or tooth-bearing dermal bone. In (E) and (F), red to purple tones denote different tooth rows, gold indicates a replacement tooth, green indicates pulp cavities, and blue indicates vasculature. Scale bars, 10 mm [(A) to (C)]; 1 mm (D); 0.1 mm [(E) and (F)].

differ in shape from the stellate odontodes on the cheek (Fig. 3A). Both the odontodes and teeth consist of pallial semidentine (*5*, *22*), and the circumpulpal dentine that infills the pulp cavity in mature teeth is an atubular dentinous tissue with fewer cell spaces enclosed (figs. S11 and S12). By contrast, the facial lamina of *Tlamaspis* is mostly unornamented labially (fig. S13), except for two or three rows of tubercles that transition abruptly into a single row of conical teeth, which are bordered lingually by a toothless flange (Fig. 4). This is reminiscent of the marginal jawbones of crown osteichthyans, even though the teeth are not shed or replaced. The tooth histology in this case is unknown.

In our phylogenetic analysis, acanthothoracids are separated from the gnathostome crown group node by four internodes (fig. S1). Nevertheless, there are distinct similarities between acanthothoracid and osteichthyan dentitions. Notably, multiple short dermal jawbones, similar to those of *Kosoraspis* and *Tlamaspis*, are present in the stem osteichthyan

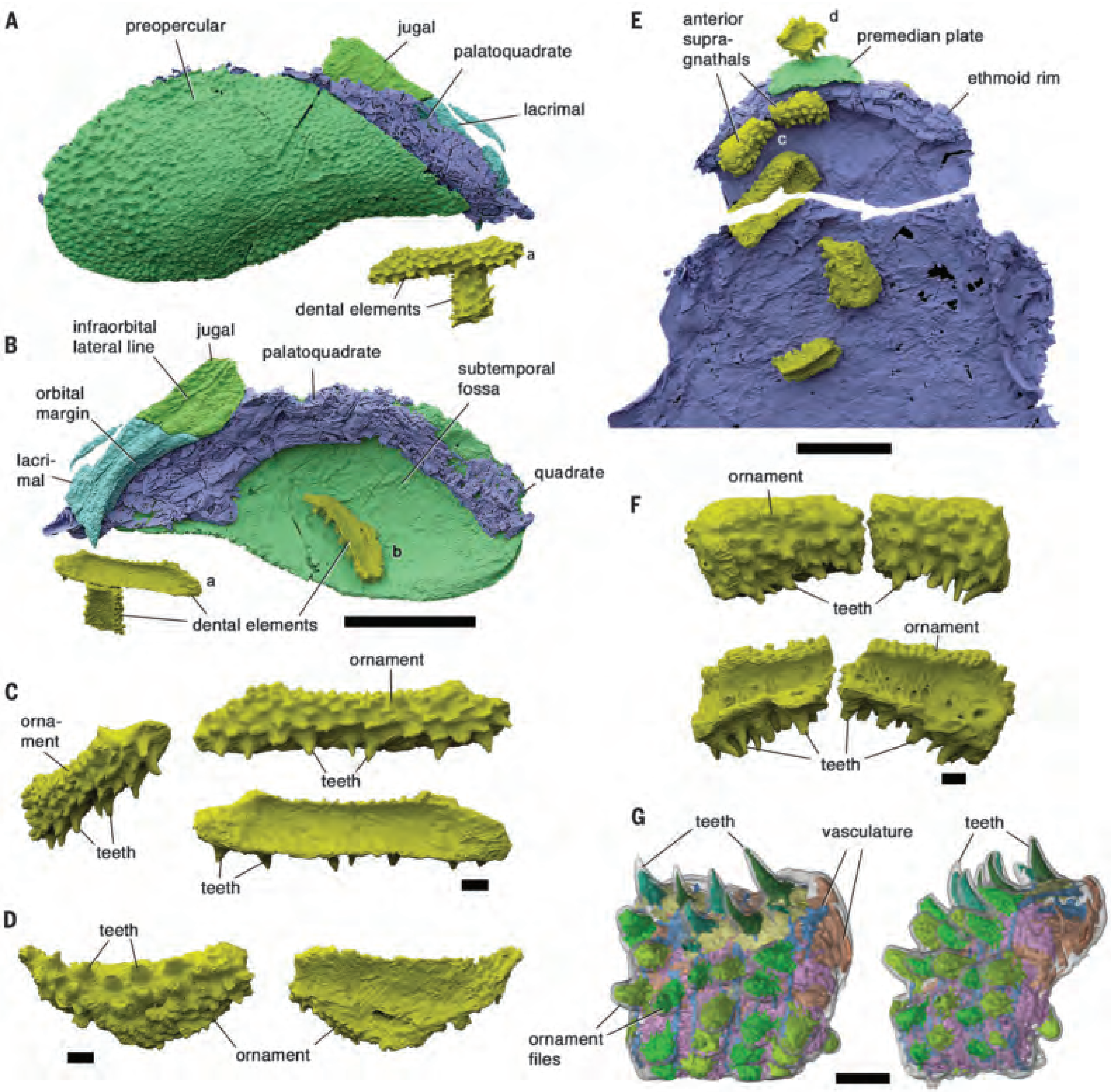

Fig. 3. Palatoquadrate complex, ethmoid, and dentition of *Kosoraspis peckai*. (**A** and **B**) Národní Muzeum (NM) specimen Lc 552 palatoquadrate complex in external (A) and internal (B) views, with associated tooth-bearing elements. Lowercase letters refer to detailed views of dental elements, as specified. (**C**) Dental element (a) in external (top), internal (bottom), and oblique anteroventrolateral (left) views. (**D**) Dental element (b) in occlusal (left) and basal (right) views. (**E**) NM Lc 16 ethmoid-trabecular region in ventral view with articulated premedian plate, two articulated supragnathals, and disarticulated dental elements. (**F**) Dental element (c) (supragnathals) in occlusal (top) and basal (bottom) views. (**G**) Dental element (d) in occlusal (left) and oblique (right) views. See fig. S9 for further details. Voxel size of (A) to (D) is 24.59 μm and that of (E) to (G) is 11.35 μm. The color coding used for (A) to (F) is the same as that in Fig. 2, A to D. Scale bars, 10 mm [(A), (B), and (E)]; 1 mm [(C), (D), (F), and (G)].

Lophosteus (fig. S14), which has acanthothoracid-like dermal ornament (*25*). The cheek pattern of *Kosoraspis* (fig. S10B) also closely approaches that of primitive crown osteichthyans (*26*). The possibility that the gnathostome crown is rooted close to acanthothoracids, with arthrodires and certain other so-called placoderm groups forming a divergent clade rather than a paraphyletic segment of the gnathostome stem, should be given serious consideration.

The newly described acanthothoracid dentitions exhibit a combination of shared characteristics and remarkable diversity. The diversity of the dentitions has functional and architectural aspects. Functionally, the dentition of CPW.9 appears to be adapted for crushing, that of *Radotina* adapted for cutting, and those of *Kosoraspis* and *Tlamaspis* adapted

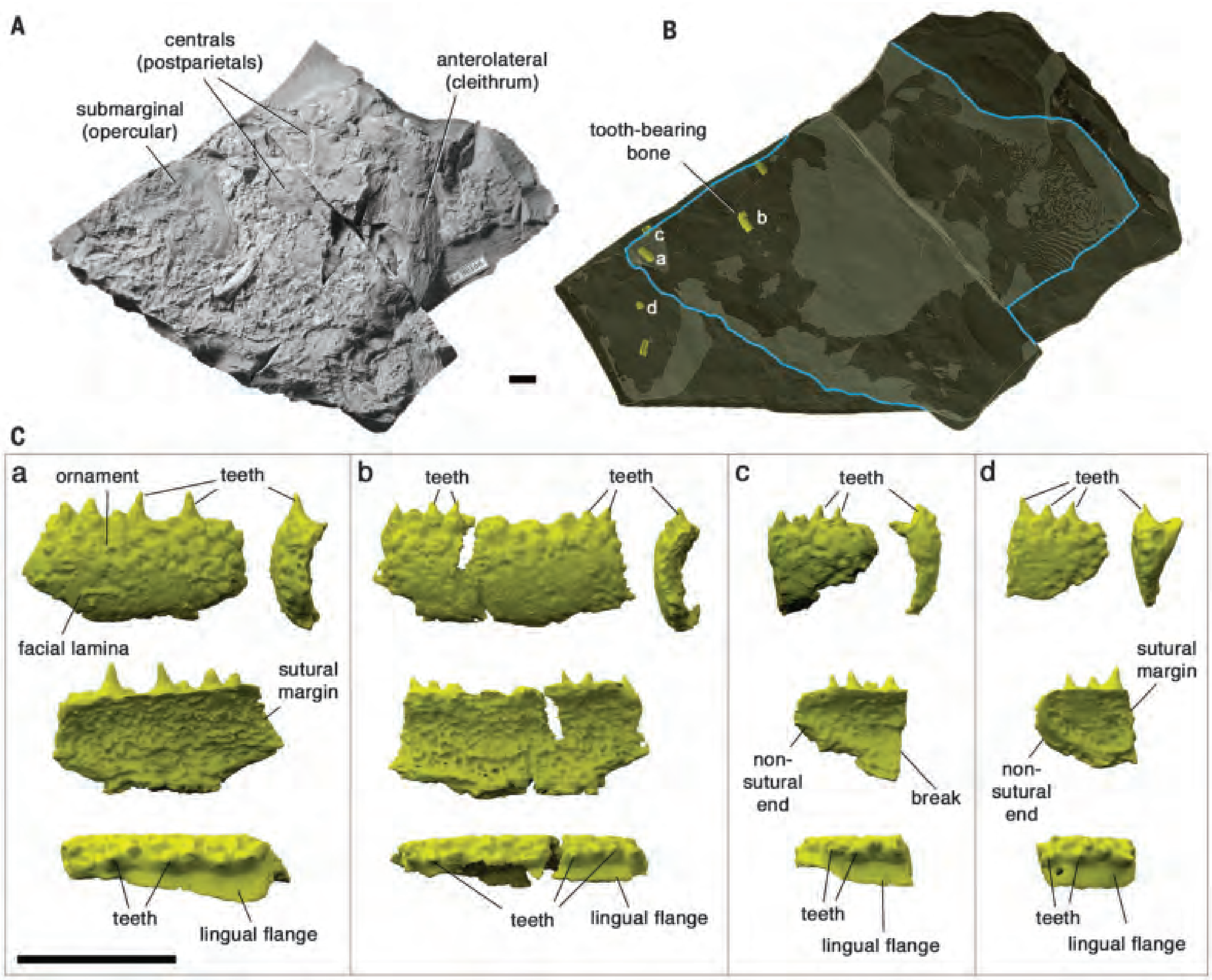

Fig. 4. Dentition of *Tlamaspis inopinatus*. (**A**) Photo of specimen NM Lc 166, a partly disarticulated head compressed in oblique left dorsolateral view, anterior to the left. (**B**) Scan model of assembled block Lc 166 plus 167 rendered semitransparent; Lc 166 is outlined in blue. Tooth-bearing bones are denoted in yellow, and other bones of the specimen are not shown. The tooth-bearing bones cluster in the anterior part of the head. Labeled bones are shown in (C). (**C**) Four tooth-bearing bones, each shown in labial (top left), end-on (top right), lingual (middle), and occlusal (bottom) views. Voxel size, 24.59 μm. Scale bars, 10 mm [(A) and (B)]; 5 mm (C).

for different styles of grasping and piercing. Architecturally, the most striking distinction is between *Radotina*—in which the teeth resemble ornament odontodes and are attached to the cheek plate—and the three other taxa, all of which have separate dermal jawbones and teeth that do not resemble their dermal ornament. In all of the dentitions, the teeth are nonshedding and lack evidence of resorption. All are carried by dermal bones that either have ornamented facial laminae or (as in the case of CPW.9) suture to facial bones; none show labial tooth addition. Their phylogenetic position among the least crownward jawed vertebrates strongly suggests that marginal teeth with lingual tooth addition, and possibly distinct marginal dermal jawbones, are ancestral for all gnathostome dentitions.

REFERENCES AND NOTES

1. H. Botella, H. Blom, M. Dorka, P. E. Ahlberg, P. Janvier, *Nature* **448**, 583–586 (2007).
2. D. Chen, H. Blom, S. Sanchez, P. Tafforeau, P. E. Ahlberg, *Nature* **539**, 237–241 (2016).
3. M. M. Smith, M. I. Coates, in *Major Events in Early Vertebrate Evolution*, P. E. Ahlberg, Ed. (Taylor and Francis, 2001), pp. 223–240.
4. M. M. Smith, *Evol. Dev.* **5**, 394–413 (2003).
5. T. Ørvig, *Zool. Scr.* **9**, 141–159 (1980).
6. M. M. Smith, Z. Johanson, *Science* **299**, 1235–1236 (2003).
7. M. M. Smith, Z. Johanson, *Science* **300**, 1661 (2003).
8. M. Rücklin *et al.*, *Nature* **491**, 748–751 (2012).
9. Y. Hu, G. C. Young, C. Burrow, Y. Zhu, J. Lu, *Palaeoworld* **28**, 525–534 (2019).
10. M. Zhu *et al.*, *Nature* **502**, 188–193 (2013).
11. M. Zhu *et al.*, *Science* **354**, 334–336 (2016).
12. D. Goujet, G. C. Young, in *Recent Advances in the Origin and Early Radiation of Vertebrates*, G. Arratia Fuentes, M. V. H. Wilson, R. Cloutier, Eds. (F. Pfeil, 2004), pp. 109–126.
13. G. C. Young, *Palaeontographica* **167**, 10–76 (1980).
14. V. Dupret, S. Sanchez, D. Goujet, P. Tafforeau, P. E. Ahlberg, *Nature* **507**, 500–503 (2014).
15. S. Kuratani, P. E. Ahlberg, *Zoological Lett.* **4**, 1–10 (2018).
16. T. Qiao, B. King, J. A. Long, P. E. Ahlberg, M. Zhu, *PLOS ONE* **11**, e0163157 (2016).
17. G. C. Young, *Palaeontology* **27**, 635–661 (1984).
18. M. M. Smith, B. Clark, D. Goujet, Z. Johanson, *Palaeontology* **60**, 829–836 (2017).
19. M. Rücklin, P. C. J. Donoghue, *Biol. Lett.* **11**, 20150326 (2015).
20. C. Burrow, Y. Hu, G. Young, *Biol. Lett.* **12**, 20160159 (2016).
21. V. Vaškaninová, P. E. Ahlberg, *PLOS ONE* **12**, e0174794 (2017).
22. T. Ørvig, in *Structural and Chemical Organization of Teeth*, A. Mills, Ed. (Academic Press, 1967), pp. 45–110.
23. T. Ørvig, *Colloq. Int. du Cent. Natl. la Rech. Sci.* **218**, 41–71 (1975).

24. W. Gross, *Palaeontographica* **113**, 1–35 (1959).
25. A. Jerve, Q. Qu, S. Sanchez, H. Blom, P. E. Ahlberg, *PeerJ* **4**, e2521 (2016).
26. M. Zhu, X. Yu, P. Janvier, *Nature* **397**, 607–610 (1999).
27. D. Chen *et al*., *R. Soc. Open Sci.* **4**, 161084 (2017).
28. S. Giles, M. Friedman, M. D. Brazeau, *Nature* **520**, 82–85 (2015).
29. M. M. Smith, B. Clark, D. Goujet, Z. Johanson, Data from: Evolutionary origins of teeth in jawed vertebrates: conflicting data from acanthothoracid dental plates ('Placodermi'), Dryad (2018); https://doi.org/10.5061/dryad.hr718.

ACKNOWLEDGMENTS

The fossils from the Národní Muzeum (NM) in Prague were scanned at the European Synchrotron Radiation Facility (ESRF) in Grenoble as parts of the proposals ES505 and ES673. We thank V. Fernandez for help during the scanning session ES673; D. Snitting for assistance with the segmenting and rendering software; M. M. Smith and D. Goujet for consultations concerning specimen CPW.9; F. Ahmed and A. Garbout (Image and Analysis Centre, Natural History Museum) for access and assistance with micro-CT scanning; G. Edgecombe for performing the phylogenetic analysis; and three anonymous reviewers for their comments. **Funding:** V.V. was supported by the Center for Geosphere Dynamics (UNCE/SCI/006). B.E. was supported by the Ministry of Culture of the Czech Republic via institutional financing of the National Museum (DKRVO 2019-2023/2.V.b, 00023272). V.V.'s access to ESRF was made possible by the Ministerstvo Školství, Mládeže a Tělovýchovy (MŠMT) funding 33914/2017-1. V.V. and D.C. were supported by a Wallenberg Scholarship from the Knut and Alice Wallenberg Foundation, awarded to P.E.A. **Author contributions:** Conceptualization: V.V., P.E.A., and D.C.; Data curation: P.T. and B.E.; Formal analysis: P.T., Z.J., V.V., D.C., and P.E.A.; Funding acquisition: P.E.A.; Investigation: V.V., P.E.A., and D.C.; Methodology: V.V., D.C., and P.E.A.; Project administration: V.V.; Resources: B.E., Z.J., and H.B.; Software: Z.J.; Supervision: P.E.A.; Validation: V.V., D.C., and P.E.A.; Visualization: V.V., D.C., and P.E.A.; Writing – original draft: V.V., P.E.A., and D.C.; Writing – review and editing: all authors. **Competing interests:** The authors declare no competing interests. **Data and materials availability:** Synchrotron data for the NM material are available at http://paleo.esrf.eu, and CT data for CPW.9 are available on Dryad (*29*). The fossils are available in the NM, except for CPW.9 (which is deposited at the Museum National d'Histoire Naturelle in Paris) and the *Lophosteus* material (which is registered to the Geological Institute in Tallinn and currently stored at Uppsala University).

SUPPLEMENTARY MATERIALS

science.sciencemag.org/content/369/6500/211/suppl/DC1
Materials and Methods
Supplementary Text
Figs. S1 to S14
Table S1
References (*30–33*)
MDAR Reproducibility Checklist

22 October 2019; accepted 18 May 2020
10.1126/science.aaz9431

CALL FOR APPLICATIONS

International call to recruit 68 junior researchers for the new leonardo labs

Leonardo SpA, the largest multinational high tech company of Italy, worldwide leader in aerospace and defence, is launching the Leonardo Labs: an international network of Corporate R&D Laboratories dedicated to advanced research and technology innovation.

For 2020, we plan to open our first 6 Leonardo Laboratories in Italy in the area of Milan, Turin, Genoa, Rome, Naples and Taranto and to recruit 68 researchers (Leonardo Research Fellows).

We search for enthusiastic and bright young researchers having STEM degree and/or PhD, with skills in the following research areas: 36 positions in Artificial Intelligence and Autonomous Intelligent System, 15 in Big Data Analytics, 6 in High Performance Computing, 4 in Electrification of Aeronautical Platforms, 5 in Materials and Structures and 2 in Quantum Technologies.

Contracts duration is up to 5 years, renewable, with European standard salary.

The application form, the details of the job profiles and the mission of the 6 Leonardo Laboratories can be found in www.leonardocompany.com/LeonardoLabs-CallToRecruit.
Candidates should submit the application form and the updated CV to the following email address: LeonardoLabs@Leonardocompany.com by July 31st, 2020.

Leonardo SpA has a gender policy in place: woman scientists are strongly encouraged to apply. We encourage candidates from around the world to apply.

For further info, contact us at
LeonardoLabs@Leonardocompany.com

Leonardo Labs

LEONARDO

Visionary mind wanted

Game changer wanted

Forward-thinker wanted

CAREER FEATURE:

Postdoctoral Careers

Issue date: August 21
Reserve ad space by August 6
Ads accepted until August 14 if space allows

To book your ad, contact:
advertise@sciencecareers.org

The Americas
202 326 6577
Europe
+44 (0) 1223 326527
Japan
+81 3 6459 4174
Greater China, South Korea, Singapore, Thailand
+86 131 4114 0012

Produced by the *Science*/AAAS Custom Publishing Office.

Why choose this feature for your advertisement?

- Relevant ads lead off the career section with a special postdoctoral banner.

Expand your exposure by posting your print ad online:

- Additional marketing driving relevant job seekers to the job board
- *Science* online job postings are now being served to thousands of passive job seekers in the Wiley Online Library.

FOR RECRUITMENT IN SCIENCE, THERE'S ONLY ONE *SCIENCE*.

Science Careers
AAAS
ScienceCareers.org

By **Kelsey Hodge-Hanson**

The day I left the lab

I finished my experiment and hurried to store my samples. I had a train to catch, and I was cutting it close. “Ugh, I should just stay in the lab to get a few more experiments done. I’m not even sure what I’ll get out of the career development symposium,” I thought to myself. I had started a postdoc position 8 months earlier and needed to gather preliminary data to bulk up a fellowship application and extend my postdoc appointment. But I also knew that I needed to cultivate contacts in industry, in case I wanted to pursue a career outside academia. A friend working in biotechnology had told me, “Sometimes you need to get out of the lab to make meaningful connections.” He was right, I decided. I washed my hands and headed to the train.

When I started my postdoc, I aimed to become a professor at a liberal arts college. But as time wore on, I had doubts. I didn’t want to do a second postdoc, which I feared would be necessary to land a faculty position. My partner and I were also settled in Chicago after 5 years of juggling a long-distance relationship, so the prospect of moving to a new city didn’t appeal to me.

Yet cultivating connections and exploring career options outside the lab proved difficult. My weekly calendar was always filled with seminars, student presentations, and lab meetings. I felt guilty taking time away from my work—but just as guilty about neglecting my future. So when an email circulated about the career development symposium, I signed up.

“Cultivating connections and exploring career options outside the lab proved difficult.”

As I stood awkwardly in the lunch line that day, I chatted with a technology transfer specialist. We found a table together and met a medical science liaison, who told me about how much he enjoys communicating medical research with health care providers. That piqued my interest because I’d always enjoyed communicating science, but I hadn’t seriously considered it as a career option. He told me to check out a science writing panel that afternoon, where he’d be a panelist.

A few hours later, I spotted him up on the stage. He and the other panelists—all of whom had Ph.D.s—clearly loved their jobs. They made frequent use of skills they had honed through their graduate training: critical thinking, project management, and the ability to learn quickly. I sat in the audience feeling I, too, could be a medical writer—and that it would suit me.

I knew that I needed a varied, intellectually stimulating career that would keep me on my toes. I wanted to spend time thinking about how to present data, because that’s something I enjoyed doing in academia. The more I thought about it, the more I felt science communication might be the perfect fit for me.

It took me 2 months, but eventually I reached out to a medical writer who had served on the panel, and she agreed to meet for tea. As she spoke about her job at a medical communications agency, time flew by and I wanted to know more. I asked her for advice about how I could launch my own medical writing career, and she responded by asking for my resume. One week later, I had a phone interview with her agency. Two months later, I started a new job as a medical writer working alongside her.

I’ve been at the company for 1.5 years now, and I’m thankful I found a career that’s such a good fit. I work collaboratively with my colleagues on projects that communicate medical research for our clients, mainly pharmaceutical companies. And I use many core skills from my scientific training, such as rapidly sifting through the literature to find relevant information and communicating data visually.

During my postdoc, it was challenging to figure out where my career path would take me next. For me, the catalyst was talking to people. I realize it can be hard to get out and network in person these days. But virtual networking is always an option—and you won’t even have to worry about missing a train. ■

Kelsey Hodge-Hanson is a medical writer at AMICULUM. She’s based in Chicago. Do you have an interesting career story that you would like to share? Send it to SciCareerEditor@aaas.org.

ILLUSTRATION: ROBERT NEUBECKER